Molecular Gold Clusters as Precursors to Heterogeneous Catalysts

A thesis presented to the University College London in partial fulfillment of the requirements for the degree of Doctor of Philosophy

John Kilmartin

University College London

April 2010

Declaration

I hereby declare that the work described within this thesis is entirely my own, except where specifically acknowledged in the text.

John Kilmartin – Thesis submitted April 2010

Abstract

This work of this thesis covers a number of different aspects of chemistry. Initially, the relationship between the number of atoms at the core of molecular clusters of gold and the steric bulk of the stabilising phosphine ligands is explored. A range of gold clusters was prepared through the use of increasingly bulky phosphine ligands. Theses clusters were characterised using a number of techniques to gain an insight into their structures.

Catalysis chemistry was investigated by using the clusters to synthesise heterogeneous catalysts. The effect of varying the loading and calcination temperature of the catalysts on their catalytic activity for the oxidation of benzyl alcohol was researched. A number of standard (XRD, TEM) and advanced characterisation (*in situ* XAS) methods were utilised to determine the effect on the catalyst structure by calcination temperature and gold loading. The relationship between the catalytic activity and the size of the cluster used to prepare the catalyst, as well as the type of catalyst support used, was also examined.

Synchrotron radiation allowed for *in situ* experiments to be designed and utilized in order to learn about a new low temperature peroxide assisted ligand removal process as an alternative to calcination. This method proved to enable more control over the rate of phosphine loss and could possible be used to activate other ligand-stabilised clusters for catalysis.

Table of contents

Table of figures

Table of tables

Table of appendices

Acknowledgements

I would like to thank my supervisors Prof. Gopinathan Sankar and Dr. Graeme Hogarth for their guidance, knowledge and understanding throughout the course of my research. It has been a pleasure working with both of them and I appreciate them taking me on for this project.

I would also like to thank Dr. Abil Aliev who was incredibly obliging and patient with collecting NMR data. Thank you to Dr. Steve Firth and Dr. Ian Watts who were always so helpful with their TEM and XRD knowledge.

Dr. Steve Fiddy at the SRS and Dr. Carmelo Prestipino at the ESRF were invaluable in their efforts to keep the beamlines functional throughout the course of XAS data collection and I am grateful for the long hours they put in.

Discussions with Dr. Chris Blackman, Dr. Russell Binions, Dr. Geoff Hyett and Dr. Charlie Dunnill were very useful and I would like to thank them for their help and advice.

I am grateful to Rozie Sarip, Christian Matjecka and Dr. Ruth Ballesteros whose contributions were a huge help to me in various areas of the work.

I would like to thank the other members of my group, Kerry, Martin, Vladmir, Chris Wright, Babis and Ben for brightening up the lab. Special thanks to Andy Smith for his amazing script.

Thanks to Paolo Melgari for all his help, particularly with Macs, Dr. Ashkan Salamat and Dr. Raul Quesada for lunch and friendship and Dr. Caroline Knapp for, among other things, printing and submitting my thesis. You are all awesome. Thanks also to the guys in the lab and office.

Thank you to my parents, Marian and Peter, and sister Katie, for your love and encouragement. Thank you for being a wonderful family.

A final thank you to my amazing wife Mekhla, for all of the love, patience and support that you gave throughout the course of researching and writing this thesis. Thank you for all the time you spent helping me with it. You're the best.

This thesis is dedicated to my mother, Marian.

1. Introduction

1.1. Catalysis

In a catalytic process, the rate of reaction for a given reaction is accelerated (or decelerated) by the presence of a separate component that does not react. This separate component is a catalyst and it speeds up the rate of a chemical reaction by lowering the activation energy of the reaction pathway to provide easier access to the transition state for the substrate. The catalyst does not allow for thermodynamically forbidden reactions to occur, it only enables reactions to occur at higher rates until equilibrium is reached.

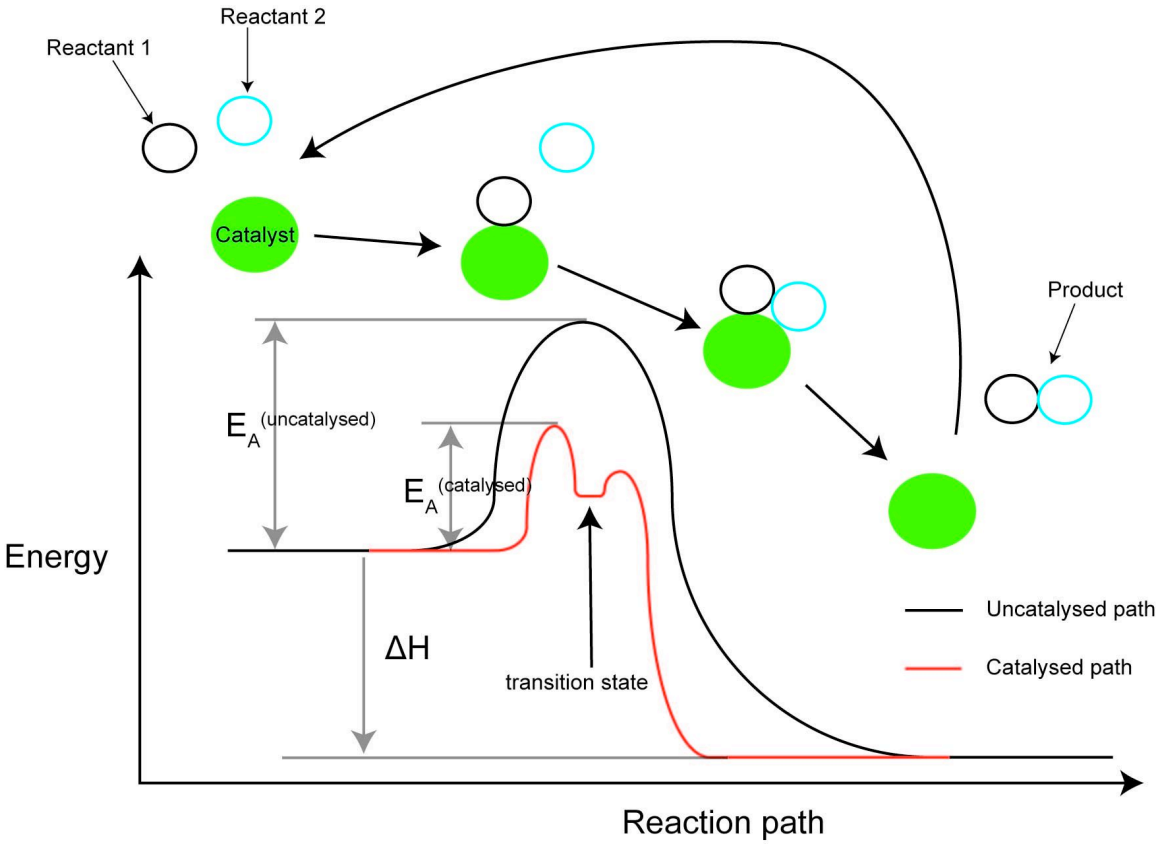

Figure 1.1. The reaction pathway of a catalytic cycle for the reaction between reactants 1 and 2 ($E_A^{(uncatalysed)}$ = activation energy of uncatalysed reaction, $E_A^{(catalysed)}$ = activation energy of catalysed reaction, ΔH = total enthalpy change).

Figure 1.1 shows how the activation energy of the reaction path is lowered to allow the transition state to be reached more easily, before forming the combined product of reactants 1 and 2. The overall change in energy is the same whether the catalyst is present or not. At the end of the reaction, the catalyst can be recovered unchanged, as it does not react and only facilitates the reaction of the substrate(s). The figure also illustrates the cyclic nature of a catalytic reaction, where once the product has desorbed, reactants are free to adsorb on to the catalyst again and continue the reaction.

In 1834, Berzelius[1] first described in a review the tendency of some compounds, such as sulphuric acid in the conversion of alcohol to ether, to affect a change in other compounds without themselves transforming. He named this the catalytic force and the decomposition of the compounds was named catalysis.

In modern times, catalysts are used for countless applications, from everyday uses such as catalytic converters in cars, to large-scale industrial applications like the contact process for the synthesis of sulphuric acid. Due to the high importance of catalytic materials, a large volume of academic and industrial research is dedicated to exploring this area. There is growing pressure, in the wake of environmental concern, that environmentally friendly alternatives be used in place of to the use of stoichiometric quantities of chemicals in industrial reactions, as well as catalysts that reduce harmful emissions. This means that existing processes must either adapt or be completely re-designed to comply with these issues, which may be difficult when also trying to remain financially viable.

In catalyst synthesis there are three main requirements; the first being that it must exhibit high activity or conversion in a reaction. The second is that it must show good selectivity of a desired product, as it may be difficult (and costly) to separate out the side-products. The final

requirement is that the catalyst must show good durability without deterioration or loss of activity under reaction conditions.

1.1.1. Types of catalysts

There are three key types of catalysts; heterogeneous catalysts, homogeneous catalysts and enzymes. Enzymes are biological catalysts with highly specific active sites that give excellent conversions and selectivities for a given reaction that they are designed for. Millions of years of evolution has made enzymes perfectly adapted to the conditions under which they operate (usually ambient temperatures and pressures) and for the processes that they catalyse. They are excellent model catalysts, but are extremely difficult to replicate due to the complex protein structures surrounding the active site. For this reason, synthetic analogues are highly simplified versions of the enzymes they are based on. Synthetic homogeneous and heterogeneous catalysts aim to replicate or improve on the activity and selectivity of enzymes in a wide range of reactions.

1.1.1.1. Homogeneous catalysis

Homogeneous catalysts are those that are in the same phase as the substrate, which is generally a liquid. These catalysts therefore have the advantage of mixing with the substrate better than heterogeneous catalysts. In homogeneous catalysis, the speed at which the reaction takes place is proportional to the concentration of catalyst present. The active molecules tend to be mononuclear species with labile ligands. Homogeneous catalysts have been found to be particularly useful for asymetric synthesis as the ligands on the active centre can be carefully selected to allow only one stereoisomer to be formed. These catalysts are frequently used in organic synthesis. The problem with homogeneous

catalysts is that they are potentially difficult to separate from the reactants as they are in the same phase. An example of a homogeneous catalyst is shown in figure 1.2, where $[IrI_2(CO)_2]^-$ catalyses the carbonylation of methanol to acetic acid in the Cativa™ process. The catalytic cycle proceeds through three steps before the original catalyst is recovered.

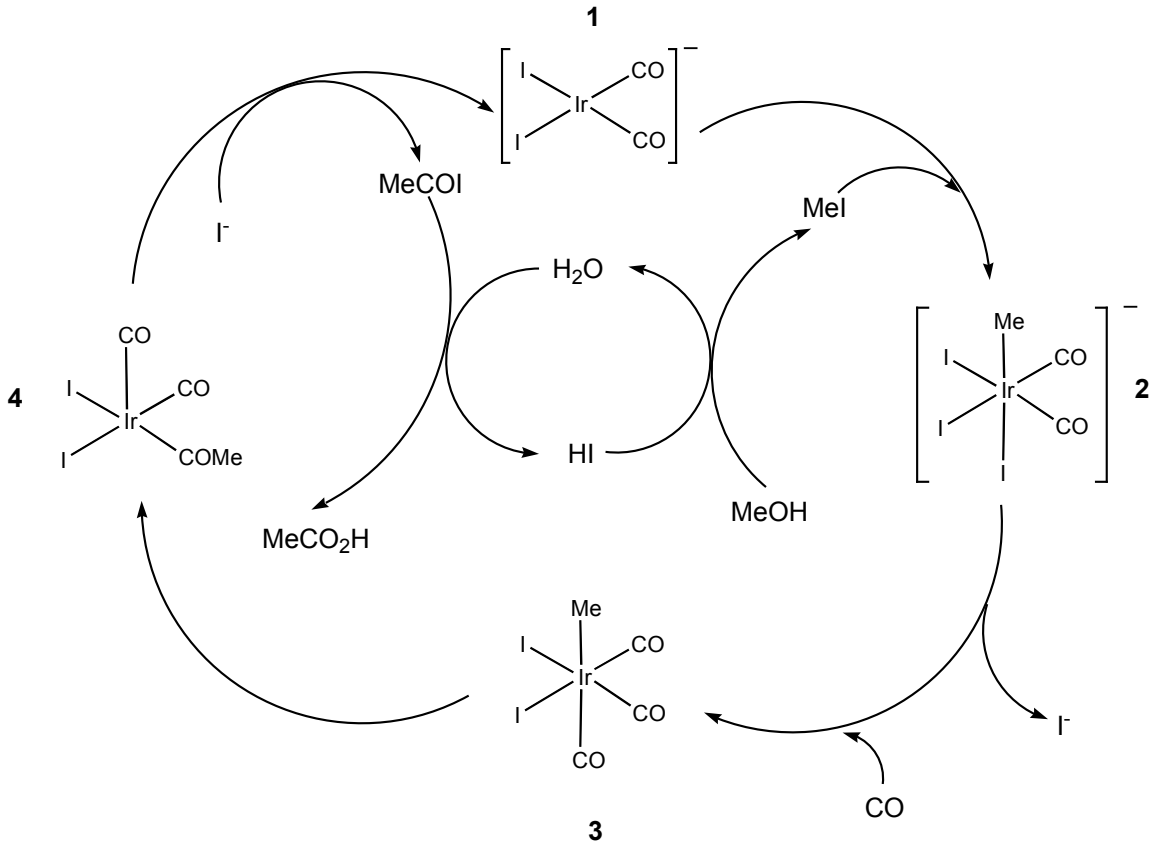

Figure 1.2. The Cativa™ process[2] for the carbonylation of methanol to acetic acid uses a homogeneous iridium catalyst.

1.1.1.2. Heterogeneous catalysis

A heterogeneous catalyst is one that is in a different phase to the reactants.

The catalysts are usually solid with the substrates in either gas or liquid form. In heterogeneous catalysis, the speed at which the reaction takes place is proportional to the area of the catalytic surface. The rates of diffusion of the reactants on to, and products off of the catalytic surface,

as well as the rate of activity at the site of the catalyst are all important factors in heterogeneous catalysis. It is usually the case that the rate of diffusion is slow, but the rate of reaction is high. In homogeneous catalysts, only the rate of reaction at the site of the catalyst is important with diffusion rates not being an issue. Another important factor in heterogeneous catalysts is how stable they are, or how stable the reaction centres are. The advantage of heterogeneous catalysts is that they are easily separated from the reactants or products. This allows for continuous flow reactors to be used instead of only batch reactors.

There are two main types of heterogeneous catalyst; bulk catalysts and supported catalysts. Bulk catalysts are typically oxides (both stoichiometric and non-stoichiometric) in composition, with surfaces providing sites for activity..

1.1.1.2.1. Bulk catalysts

Some examples of bulk catalysts that have been extensively researched are presented below. Bulk catalysts are a huge area of research with many groups investigating the catalyst's structures and observing how modifications to them affect the activity.

Vanadium phosphorus oxides[3, 4]

Vanadium phosphorus oxide (VPO) catalysts are used industrially for the synthesis of maleic anhydride through the selective oxidation of n-butane (70-85 % conversion). Maleic anhydride is used for a number of purposes including the synthesis of unsaturated resins and pharmaceuticals. Though it can also be synthesised from benzene, it is preferential to synthesise it from n-butane as it is a cheaper feedstock and the process has less environmental impact. There are a number of different forms of VPO that are active for this reaction, but studies have found that vanadyl^{IV} pyrophosphate ($(VO_2)P_2O_7$) is present in the most selective catalysts. VPO catalysts are synthesised through the thermal degradation

of vanadyl^{IV} hydrogen phosphate hemihydrate ($VOHPO_4 \cdot 0.5H_2O$) and it is a characteristic of VPOs that they undergo conversions to different phases throughout their lifetime.

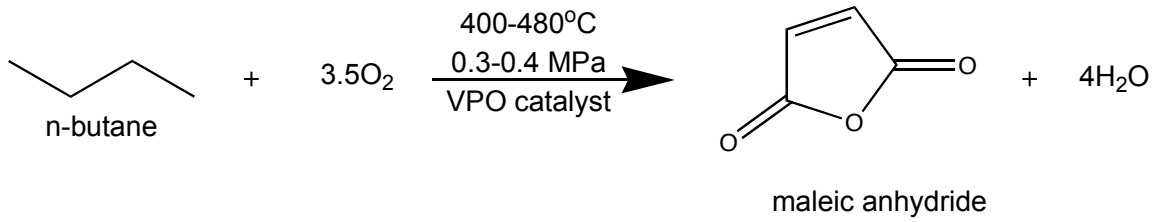

Figure 1.3. Reaction scheme of the selective oxidation of n-butane over a VPO catalyst to form maleic anhydride.

Bismuth molybdates[5]

Bismuth molybdate catalysts are used for the selective oxidation of hydrocarbons and are usually composed of $x(Bi_2O_3)y(MoO_3)$ with varying ratios of *x* to *y*. Though it started as only bismuth molybdate present in the catalyst, improvements to the activity have been made through the addition of iron and nickel oxides as well as other metal oxides. This catalyst is particularly well known for the oxidation of propene to the unsaturated aldehyde, acrolein. This is a highly reactive compound used in the synthesis of other molecules and polymers (see figure 1.4).

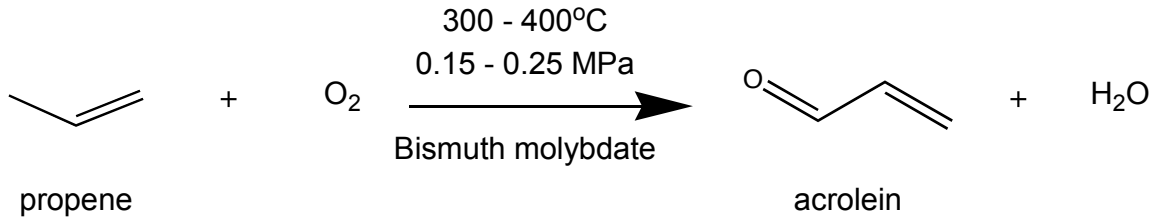

Figure 1.4. Reaction scheme of the partial oxidation of propene to acrolein over bismuth molybdate.

Zeolites[6]

Zeolites are structured aluminosilicate compounds with either porous or channelled frameworks. They are acknowledged for their activity in

catalytic cracking[7] and are made up of tetrahedral AlO_4 and SiO_4 units linked through common oxygen atoms. The pores can be 1 nm or less in size, which make them ideal for shape selective catalysis with similarly sized hydrocarbons. The negatively charged porous framework of zeolites means that they can host cationic species such as Na^+, H^+ or catalytic metal ions. When H^+ is present, zeolites act as solid acids which makes them suitable for acid catalysed reactions. The presence of the pores means that bulk or branched hydrocarbons cannot enter the zeolite so linear particles are preferentially reacted. Zeolites also make excellent supports for catalytic metal particles which opens up the possibility for a range of catalytic reactions.[8]

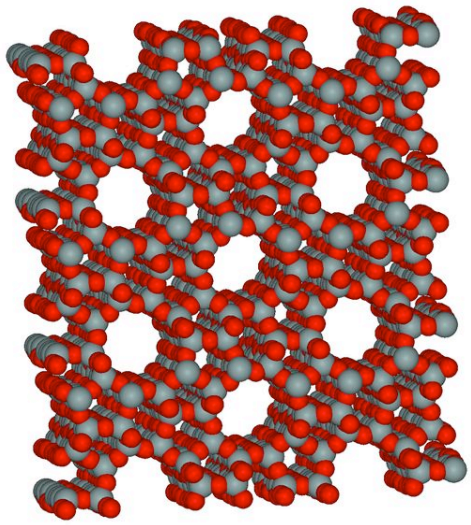

Figure 1.5. The porous structure of zeolite ZSM-5.

1.1.1.2.2. Supported catalysts

Supported catalysts tend to consist of dispersed metal particles deposited on to a surface of a high surface area metal oxide support where the metal particles are the activity centres. There are also many examples of supported heterogeneous catalysts. More will be discussed in later sections. The example shown here is probably the first thing most people think of when they hear of catalysts.

The catalytic converter

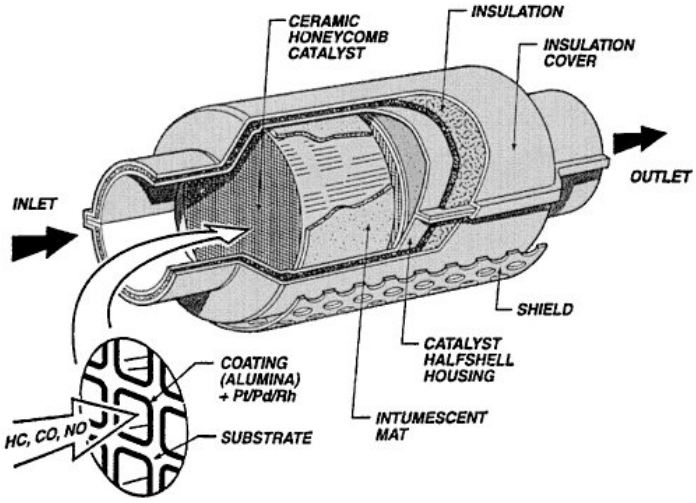

Figure 1.6. A diagram of a catalytic converter.[9]

This revolutionary device was introduced to the automotive industry in the 1970's by Johnson Matthey as a response to Environmental Protection Agency legislature that aimed to decrease the levels of harmful emissions from automobiles. These emissions are unburned hydrocarbons, CO and NO_x. The hydrocarbons and CO are released because the combustion efficiency is less than 100%. The three-way catalytic converter (illustrated in figure 1.6) is used for the reduction of these emissions through the reactions shown in figure 1.7.

Oxidation:

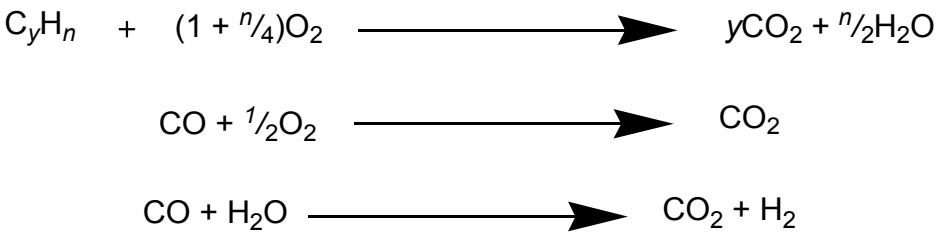

Reduction:

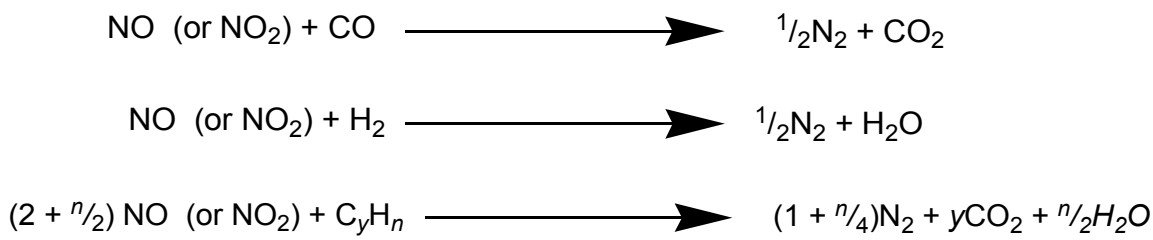

Figure 1.7. The oxidation and reduction reactions that occur inside an operating catalytic converter.

The active phases are supported on an alumina coated cordierite (roughly $2MgO : 5SiO_2 : 2Al_2O_3$) monolith. The active phases originally consisted of rhodium promoted platinum and palladium promoted platinum. Modern catalytic converters have all three metals supported separately from each other.[10]

1.1.1.3. Supported heterogeneous catalyst synthesis

There are a number of methods for attaching the active phase of the catalyst to a support.

Impregnation – This involves the support being brought into contact with a precursor solution of the active metal. This method is commonly used, as it allows for the active phase to be deposited on to a specially shaped or structured support such as a monolith. There are a number of different

ways of depositing the precursor on to the support in impregnation. The precursor can either react with the support surface OH groups or adsorb on to a prepared surface. The surface can be tuned through reaction with an acid or base to be either anionic (deprotonated) or cationic (protonated). This means that cationic precursor species will adsorb on to an anionic support surface and anionic precursors adsorb on to a cationic support surface.

Co-precipitation - Whereas impregnation deposits the active precursor on to a pre-formed support, co-precipitation involves the simultaneous precipitation of both the support and the active phase of the catalyst out of a precursor solution through adjustment of the solutions pH. This results in a dispersion of metal particles throughout the support.

Deposition precipitation - In this process a precursor solution is mixed with a solid support. The pH is then carefully increased (either through the use of a base or the heat enabled decomposition of urea) to bring about precipitation of the precursor on to the support.

Homogeneous catalyst immobilisation - This method is a way of counteracting the difficulty of separating a homogeneous catalyst from the reactants and products. Homogeneous catalysts are deposited on to a solid support, but often with a substantial loss in activity compared to the original catalyst.

Chemical vapour deposition - In chemical vapour deposition, a volatile catalyst precursor is deposited on to a heated support surface. On contact with the surface, the precursor reacts or decomposes resulting in the deposition on to the support. If the support surface is flat, a film of the precursor is formed. A common use of this technique is in materials synthesis.

Colloidal deposition - This method involves a solid support being dipped into a colloidal dispersion of the active phase resulting in the colloidal particles being deposited on the support surface. If carried out

successfully, there should be little increase in the size of the metal particles.

Usually drying and calcination follows the deposition of the active phase precursor on to the support. This part is very important, as it is where the particles are bound strongly to the support surface.

Large active metal particles are sometimes undesirable in supported heterogeneous catalysts as often, smaller particles give higher activities. Large particle formation can lead to less active catalysts which can be costly if precious metals are used. An ideal catalyst would have a dispersion of identically sized active particles bound to the support surface. Unfortunately, though these methods are commonly used for the preparation of supported metal catalysts, each of them has their own disadvantages, with differently sized active metal particles obtained through each. Generally, each of these methods leads to the formation of a dispersion of active particles. There is always some variation in the size of the particles, and though this variation can be very narrow, there is always some heterogeneity in the metal particle size. Also, if, when calcining the catalyst the rate of temperature increase is too high, particle aggregation can occur. However, this is highly dependent upon the support and the metal precursor.

Cluster deposition- Another method that has been used to successfully synthesise highly active supported metal catalysts is through deposition of ligand-stabilised clusters. This method differs from colloidal deposition as when ligand stabilised clusters are synthesised, they have no size variation, with each of the cluster molecules the same size and shape. This level of monodispersity is rare in colloidal disersions and cannot be gained with the same ease as the synthesis of molecular clusters.[11] Some examples of catalysts obtained using this method are presented below.

$[Ru_{12}C_2(CO)_{32}Cu_4Cl_2]^{2-}$ on mesoporous silica

Thomas *et al* reported the synthesis of copper-ruthenium bimetallic catalysts supported on mesoporous silica (MCM-41) for the hydrogenation of hex-1-ene.[12] The cluster precursor $[Ru_{12}C_2(CO)_{32}Cu_4Cl_2]^{2-}$ was grafted on to the inside of the pores of the support and the carbonyl ligands were carefully removed by heating under high vacuum. This resulted in loss of the carbonyl ligands and the formation of Cu_4Ru_{12} particles 1.5-2.0 nm in size on the surface of the support. Characterisation revealed that the ruthenium atoms were supported on the silica surface through the copper atoms. There was very little sintering during the ligand removal process and during the catalytic reaction, where high conversions of hex-1-ene were achieved.

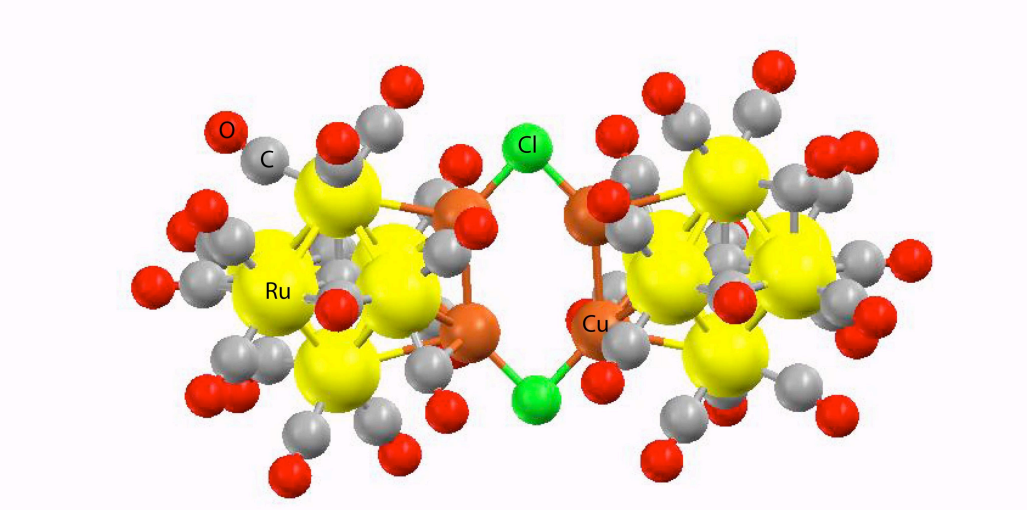

Figure 1.8. X-ray structure of $[Ru_{12}C_2(CO)_{32}Cu_4Cl_2]^{2-}$.

Au_{55} on silica

Johnson *et al* reported the use of triphenylphosphine stabilised Au_{55} clusters for the oxidation of styrene using molecular oxygen.[13] The clusters were deposited on to the silica support by stirring a dichloromethane solution of the cluster with the silica and removing the solvent under vacuum. The catalyst was then calcined to 200°C under vacuum. The supported catalysts gave narrow particle size distributions

of 1.0-2.0 nm in diameter. It was found that increasing the loading led to larger, inactive gold particle formation.

These examples demonstrate the use of molecular clusters in catalyst preparation. The latter example is of particular interest as it shows the use of a previously considered inert element, gold. At present, gold is widely researched as a catalyst due to its unique ability to oxidise CO at sub-zero temperatures. It can also be highly active for a range of other catalytic reactions, which are discussed in Chapter 4. Here, some general background information on gold will be examined.

1.2. Gold

1.2.1. History of gold

Gold has long been considered precious due to its unique colour, and was the first metal utilised by man. It was used from as early as 1500 B.C. in ancient Egypt for Pharaohs death masks and statues and was referred to as "the flesh of the Gods.[14]" Other early uses were in jewellery and coinage. Lydian merchants in what is now west Turkey were the first to gold as a form of money in 700 B.C. In later years, its value became too high for regular circulation so cheaper metals such as copper replaced gold. Eventually even the value of copper increased past the value of the coins pressed. Today gold is used as a standard in monetary exchange and as an element, has one of the highest values of metals.

Table 1.1. Table of prices compared to Pt, Pd, other precious metals (*as of 08/07/09 from kitco.com, 1 troy oz. = 31.103 g).

	GOLD	SILVER	PLATINUM	PALLADIUM	RHODIUM	COPPER
Price (£/troy oz.)*	575	8	705	149	799	0.1
Mass fraction (kg/kg of earths crust)[15]	4×10^{-9}	8×10^{-8}	1×10^{-8}	1.5×10^{-8}	1×10^{-10}	6.8×10^{-5}

Though it is not as rare or expensive as some metals such as platinum or rhodium, gold is still highly prized and coveted for its noble character as it does not tarnish. More recent applications include its use in electronic circuitry[16, 17] and in medicine as anti-arthritis treatments.[18]

Most of the history of gold has focused on its metallic state. Early gold chemistry that was investigated was generally carried out as a means of purifying or recovering metallic gold with any compounds isolated merely being intermediates. Only in the past 30 years has the chemistry of gold really been thoroughly explored, with a lot of the recent research focusing on the use of gold in advanced materials and catalysts.

1.2.2. Properties of gold

Gold exhibits typical metal qualities. It has a shiny lustre and high electrical and thermal conductivities. It is also one of the most malleable and ductile metals with just 1g being enough to be hammered into 1 m^2. However, it is not a very hard metal and pure gold can easily be scratched with a knife. The electronic arrangement of gold is [Xe]$4f^{14}5d^{10}6s^1$. Like metallic copper and silver, metallic gold has a face centred cubic structure. The melting and boiling points of gold are higher than silver due to stronger interatomic bonding. The metallic radius of gold is smaller than that of silver. This is due to its location in the periodic table after the lanthanide contraction, meaning that it experiences relativistic effects more so than other elements.

Table 1.2. **A table comparing the properties of copper, silver and gold.**

Property	Cu	Ag	Au
Atomic Number	29	47	79
Electron Configuration	[Ar]$3d^{10}4s^1$	[Kr]$4d^{10}6s^1$	[Xe]$4f^{14}5d^{10}6s^1$
Solid structure	fcc	fcc	fcc
Lattice constant (nm)	0.361	0.409	0.408
Metallic radius (nm)	0.128	0.14447	0.14420
Density (g cm^{-3})	8.95	10.49	19.32
Melting point (K)	1356	1234	1337
Boiling point (K)	2843	2428	3081
Sublimation enthalpy (kJ mol^{-1})	337 ± 6	285 ± 4	343 ± 11
1^{st} ionisation energy (kJ mol^{-1})	745	731	890

Platinum and mercury, located either side in the periodic table in groups 10 and 12 respectively share some similar properties to gold. Platinum also has a face centred cubic structure in the metallic state, whereas mercury is a liquid at room temperature due to relativistic effects. Gold has far lower melting and boiling points than platinum though.

Table 1.3. **Table comparing the properties of platinum, gold and mercury.**

Property	Pt	Au	Hg
Atomic Number	78	79	80
Electron Configuration	$[Xe]4f^{14}5d^{9}6s^{1}$	$[Xe]4f^{14}5d^{10}6s^{1}$	$[Xe]4f^{14}5d^{10}6s^{2}$
Solid structure	fcc	fcc	fcc
Lattice constant (nm)	0.392	0.408	0.299
Metallic radius (nm)	0.1385	0.14420	0.299
Density (g cm^{-3})	21.41	19.32	13.53
Melting point (K)	2042	1337	234.1
Boiling point (K)	443	3081	630
Sublimation enthalpy (kJ mol^{-1})	469 ± 25	343 ± 11	59.1 ± 0.4
1^{st} ionisation energy (kJ mol^{-1})	866	890	1007

Gold has the lowest electrochemical potential of any metal due to significant contraction and stabilisation of the 6*s* orbital in metallic state. It is also the most electronegative metal.

The 2^{nd} and 3^{rd} ionisation energies of gold are lower than those of the Group 1 alkali metals. For this reason it can form the salt like compound, AuCs, with a structure similar to caesium iodide rather than an alloy. Another halogen similarity is the observation of diatomic Au_2 species in vaporised gold.

Table 1.4. **Table showing the accessible oxidation states of copper, silver and gold**

	+1	+2	+3	+4	+5	-1
Copper	common	common	rare ($[CuF_6]^{3-}$)	rare ($[CuF_6]^{2-}$)	no	no
Silver	common	rare	rare (AgF_3)	no	no	no
Gold	common	known	common	known	rare (AuF_5)	known (AuCs)

1.2.3. Relativistic effects

A lot of the differences in the chemistry of gold compared to other metals are due to, or indirectly related to relativistic effects. In heavy post–lanthanide elements there are a large number of protons in the nucleus of the atom. This means that the electrons in the core orbitals experience a very high nuclear charge causing them to move at speeds close to the speed of light. As the electron approaches the speed of light, according to Einstein's theory of relativity, its mass increases (i.e. its relativistic mass is higher than that of an electron at rest). This affects the electrons in s-orbitals much more than those in other orbitals as they are closer to the nucleus. This increased mass causes the core s orbitals to be contracted, decreasing the distance between the electron and the nucleus and giving them higher ionisation energies. The more strongly bound s-electrons shield the nuclear charge from the electrons in the d (and f) orbitals.

Whereas the s-orbitals, and to a lesser extent the p-orbitals, undergo direct relativistic contraction, the d and f-orbitals experience the opposite effect and are expanded and destabilised with respect to hypothetical non-relativistic analogues. This is due to the shielding effect of the outer shell s and p-orbitals and is known as indirect relativistic orbital expansion.

Gold being a third row transition metal, has a full 4f orbital, and thus the effective nuclear charge experienced by its valance electrons is higher than it would be if only s, p, and d orbitals were present. This is called the lanthanide contraction and it occurs because the 4f orbital is a poor shield of the nuclear charge. Computational studies investigating the consequence of relativistic effects on the 4f orbitals have found some interesting results; namely the contraction of the 6s orbital in gold was not a direct relativistic effect as experienced by the ($n \leq 5$) ns orbitals, but was in fact due to the 4f shell. This is because the 4f electrons themselves experience indirect relativistic orbital expansion, which reduces their screening ability of the nuclear charge. It was concluded that the lanthanide contraction was a result of both relativistic effects and the structure of the electron shells. Research by other groups has shown that the 5d orbitals also play a large role in the stabilisation of the 6s orbital as they also undergo indirect relativistic expansion leading to poorer charge shielding abilities. This relativistic expansion of the 4f and 5d orbitals leading to a reduction in nuclear screening is the reason for the 6s orbital contraction.[19]

These effects are only seen in post lanthanide elements and for the elements from gold to bismuth, the impact on energies is close to bond energies.[20] Due to the position of gold following the filling of the 5d orbital after the lanthanide contraction, it is the element that exhibits the most influence from the relativistic effect.

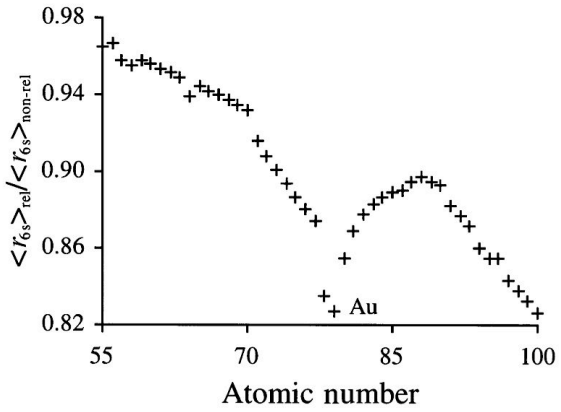

Figure 1.9. **A plot to show the relativistic contraction of the 6s orbital of the elements Cs to Fm. This is calculated from $(radius_{6s})_{relativistic}/(radius_{6s})_{non\text{-}relativistic}$[19-21] and shows a maximum contraction at gold.**

The influences of relativistic effects are seen in many of the properties of gold. The most striking and obvious example is that of gold's unique colour. Gold strongly absorbs blue (and violet) light in the band-gap of 2.38 eV, due to electronic excitation from the filled 5d to the Fermi level. Due to the absorption of these wavelengths of light, gold appears yellow. This transition can only occur as the 5d and the 6s orbitals are so close together in terms of energy. An analogous transition occurs in silver from the 4d to the 5s level. However, the difference in energy between these two levels in silver is far greater than between the 5d and 6s in gold due to relativistic effects so no visible light is absorbed. In silver the 4d to 5s transition is in the ultraviolet region at approximately 2.7 eV. Non-relativistic gold would appear white in colour.

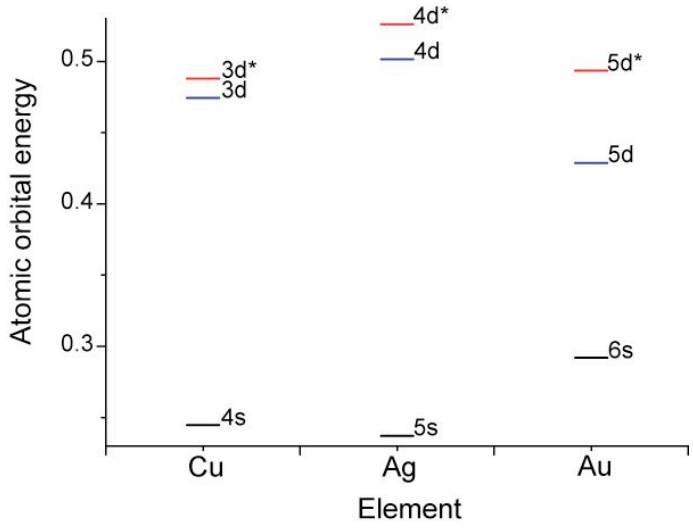

Figure 1.10. **A comparison of the atomic orbital energies for metallic copper, silver and gold[22].**

There are a number of other consequences of relativistic effects seen in the chemistry and physical properties of gold. The stabilisation of the s electrons in gold due to relativistic effects in bond distance compared to those expected for non-relativistic gold. The stabilisation of the s electrons also contributes to the higher melting point of gold compared to silver as mentioned earlier.

One of the most distinctive characteristics resulting from relativistic effects is the ability of low coordinate gold(I) complexes to associate with each other to form dimers, trimers, oligomers and even polymers. This is done through direct gold-gold interactions termed “Aurophilicity” by Schmidbaur.[23-25] These gold-gold interactions are unique in that they occur through closed shell metal centres, in the case of gold(I) through the $5d^{10}$ electrons. In aurophilic interactions, the gold atoms reach an equilibrium distance between 2.7 and 3.3 Å. Though this type of bonding through electron correlation is similar to van der Waals interactions, they are much stronger due to relativistic effects. These types of bonds are not confined to mononuclear gold(I) complexes. Similar contacts have been observed in polynuclear molecules in which gold atoms appear drawn together to within 3 Å of each other. It has also been observed that

multinuclear complexes adopt unusual conformations so that the gold atoms present can become nearest neighbours.[23, 26-28] These are sometimes known as hypercoordinate or polyaurated complexes because the interstitial cation at the centre of the complex exceeds its standard coordination number. Examples are given in figure 1.11.

Formation of 2-coordinate linear complexes occurs more readily with gold(I) than silver(I) due to the small differences in energy between the s, p and d orbitals. Silver(I) preferentially forms 3- and 4-coordinate analogues.

Gold has access to more oxidation states than silver due to the destabilisation of the 5d orbital. This explains the ease at which gold can exist in the +3 oxidation state, which is difficult to achieve with silver. Silver(III) only exists in fluoride compounds. Gold(-1) can also be formed owing to the stabilisation of the 6s orbitals, whereas the -1 oxidation state is not know for silver.

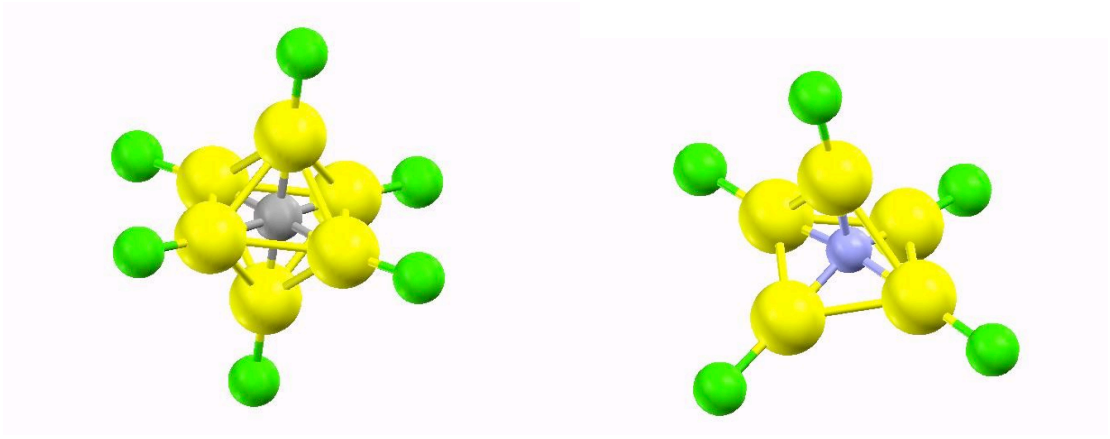

1 *2*

Figure 1.11. Examples of hypercoordination of carbonium (1)[14] and ammonium dications (2).[23, 29-31]

1.3. Gold complexes

Initially, the chemistry of gold was dominated by research on linear, two coordinate gold(I) complexes and square planar, gold (III) complexes. Now much work has been carried out on other compounds in this area that do not fall into either of these categories. This section will provide an overview of the different conformation that the different oxidation states of gold can adopt.

1.3.1. Gold(I) complexes

Of all the areas of research on gold, the chemistry of gold(I) is the most developed. Gold(I) has a closed shell electron configuration (Xe)$4f^{14}5d^{10}$ and so the complexes formed are diamagnetic.

Many 14 electron gold(I) compounds of the type [AuXL] are known where L is a neutral donor ligand such as a phosphine or amine . Depending on the nature of L, the molecules are capable of accommodating short intermolecular gold-gold bonds through aurophilic interactions. This means that the monomeric complexes can associate into dimers and higher ordered units.

It is a lot more common for gold(I) to form linear 2 coordinate complexes than copper(I) or silver(I). Linear gold(I) complexes can be cationic (example), anionic, or neutral.

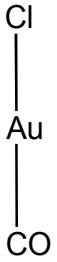

1

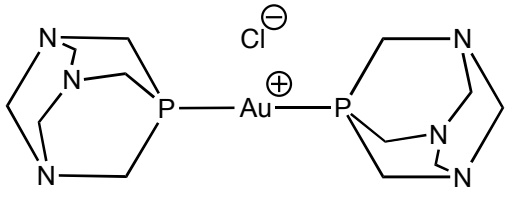

2

Figure 1.12. **Examples of linear gold(I) complexes, [(OC)AuCl] (1)[32] and bis(1,3,5-triaza-7-phosphaadamantane-*P*) gold(I) chloride (2).[33]**

Copper (I) and silver (I) have a greater tendency to form complexes with higher coordination numbers. For example, when gold is bound to triethylphosphine in $AuI(PEt_3)$, it exists as a monomer. However, the equivalent copper and silver complexes exist as tetramers with iodide ligands bridging the metals, giving them coordination numbers of 4. Higher coordination numbers are also known for gold(I). It forms trigonal planar and tetrahedral conformations for three and four coordinate complexes respectively. It is known that the stabilities of the gold-phosphine complexes given in the example below are low. However, they will readily lose ligands to form the favoured 2- coordinate compounds. A similar trend is observed in group 12 where mercury(II) preferentially forms linear 2 coordinate compounds whereas its co-geners, zinc and cadmium do not when in the same oxidation state.

There are a number of possible reasons as to why gold(I) preferentially forms complexes with linear 2 coordinate arrangements. Steric factors are unlikely to be important when considering low coordination number complexes. It must therefore be electronic factors that are responsible. If only simple electrostatic effects are considered, it can be said that a small, highly charged metal ion with a high polarising power should have a high coordination number. This means that if the charge on the metal ion remains the same, then there will be an increased likelihood of forming a higher coordination number complex if the metal ion is smaller. Comparing the ionic radii of gold(I) (1.37 Å), silver(I) (1.26 Å) and copper(I) (0.96 Å)[34], it can be seen that copper is far smaller than the others. With the previous assumptions, it could be said that due to the difference in size, the copper(I) would form higher coordinate complexes. The problem is that due to the similarity of silver(I) to gold(I) in size, it

would be expected that silver(I) would have a far higher possibility of forming 2 coordinate complexes than copper(I), which is untrue.

Taking into account valence shell electron pair repulsion theory, it could be seen as logical that gold(I) forms linear 2 coordinate complexes with ligands bounds to the s orbital, as the coordinated species will repel each other. If one considers that this would also be true for copper(I) and silver(I), then it is obvious that a more complex explanation is required.

If the nature of the orbitals used in the bonding of the ligands to the metal is considered, more insight is to be gained into gold(I)'s linear preference. In linear complexes, hybrid *sp* orbitals are used in bonding. The ease at which the s and p orbitals hybridize depends on their energy separation. The closer they are in energy, then the more hybridization can occur to higher coordination complexes. If the s and p orbitals have a large energy gap that allows for less hybridization as in gold(I), then only *sp* hybrid orbitals will form giving linear complexes.

By looking at the energy separation of the s and p orbitals in gold, silver, and copper, a larger energy gap is present for gold to allow for hybridization to occur. This means that more hybridization will occur for copper and silver more readily than for gold, and thus there will be a larger preference for copper(I) and silver(I) to form higher coordinate complexes.

1.3.2. Gold(I) phosphine complexes

A huge number of gold(I) phosphine complexes are known.[35, 36] They are almost always linear 2 coordinate compounds in the form [LAuX] where L is a phosphine ligand and X is an anionic species. These are commonly synthesised by the reaction of gold(III) chloride with 2 equivalents of phosphine. This gives the gold phosphine complex *via* the initial formation

of a gold (III) intermediate, for example, $AuCl_3(PPh_3)$. This is then reduced by another phosphine to give the desired product.[37]

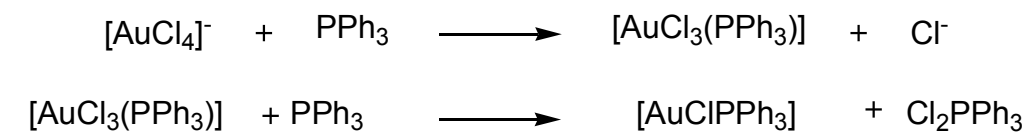

Figure 1.13. **Reaction scheme showing the two-step formation of $[AuClPPh_3]$.**

Another method that has been utilised is the replacement of a weaklier bound group by a phosphine ligand. This preparation technique can be employed to minimise the amount of phosphine required to make the gold phosphine complex.

As mentioned earlier, gold(I) can accommodate up to 4 triphenylphosphine ligands, thus forming an 18 electron complex. These compounds are synthesised through the addition of an excess of the ligand to a solution of $[PPh_3AuCl]$. Analogous reactions with $AsPh_3$ have also been carried out which have shown that $[AuL_4]^+$ compounds can also be obtained with these ligands.[38] Gold bonds more strongly to phosphines than to the analogous arsine or stibine compounds. This reaction is also possible with a range of other phosphines. The Cl^- anion can usually be replaced by another counterion through a metathesis reaction.

Phosphorus-31 NMR has been a useful tool in confirming that 2, 3 and 4 coordinate gold(I) complexes are formed in solution. Low temperature NMR can be used to identify individual complexes, as at room temperature they are labile and rapidly interconvert.[35]

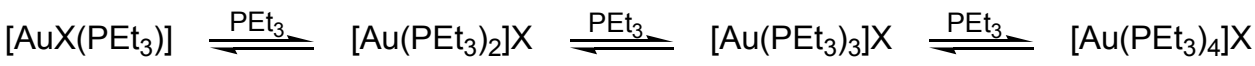

Figure 1.14. Reaction schemes for the addition of phosphine to gold up to $[AuL_4]^+$.

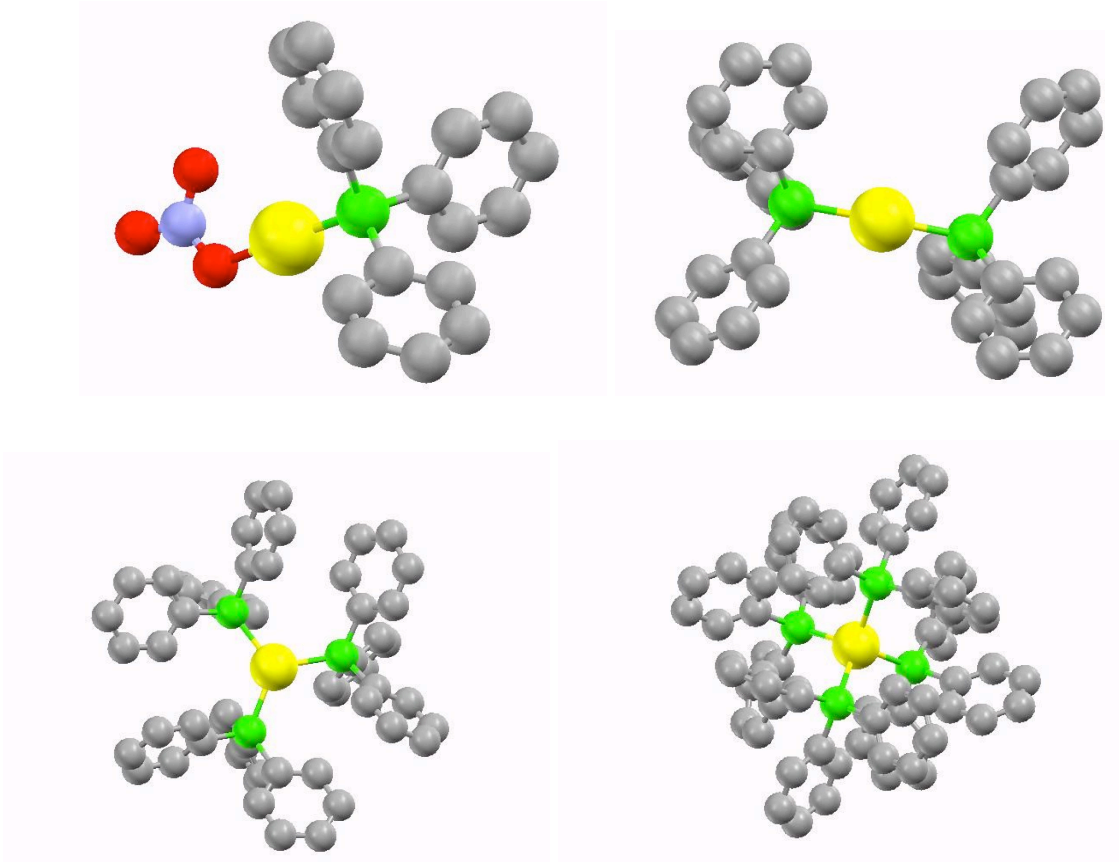

Figure 1.15. Crystal structures of gold(I) with varying triphenylphosphine coordination numbers[39-42] (hydrogen atoms omitted for clarity). Before the crystal structure was obtained in 1980, evidence of $[Au(PPh_3)_4]^+$ was observed through ^{97}Au Mössbauer spectroscopy[43] and elemental analysis.[44]

Gold(I) complexes with two phosphine ligands can have either linear or trigonal planar geometries, depending upon the coordinating power of the anion and the steric properties of the phosphine. In $[Au(PPh_3)_2]^+$, the presence of more strongly coordinating counterions such as Cl^- give trigonal planar $[Au(PPh_3)_2Cl]$. However, if a less strongly coordinating anion such as NO_3^- or PF_6^- is present, the complex is essentially linear.[35]

Gold(I) complexes with three phosphine ligands again can be in one of two geometries, depending on the ligands and the anion. Complexes of the type $[AuL_3]^+$ are trigonal planar, with the anion sometimes causing slight perturbation of the structure. Four coordinate complexes of $[AuL_3X]$

can also be formed. These usually have slightly distorted tetrahedral arrangements, though trigonal pyramidal complexes have been reported.

Gold(I) with four phosphine ligands, $[AuL_4]^+$, is coordinatively saturated (L= PPh_3, PEt_3, $PMePh_2$). Here, the geometric arrangement of the phosphines around the gold is dependent on the cone angle of the ligands. For phosphines with large cone angles, such as triphenylphosphine, there are larger steric interactions occurring between the ligands. In $[Au(PPh_3)_4]$ BPh_4, it has been observed that the gold forms an almost trigonal planar structure with 3 of the triphenylphosphine units 2.4 Å from the gold.[42] The fourth phosphine ligand is bound to the gold with an elongated bond of 3.95 Å. Phosphines with smaller cone angles like $PMePh_2$ can allow for gold(I) to form truly tetrahedral complexes such as in$[Au(PMePh_2)_4]PF_6$.[45]

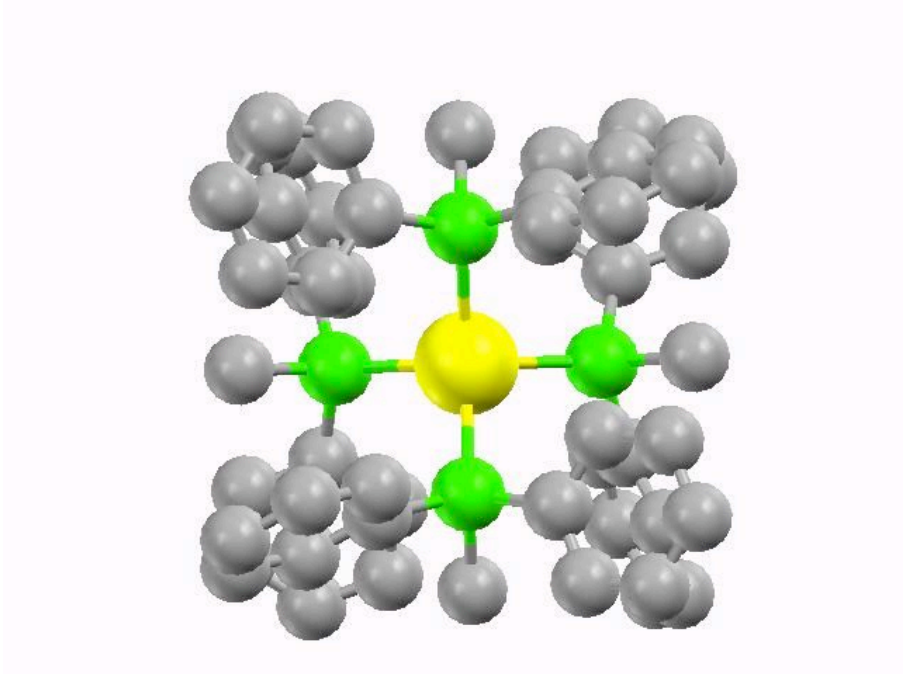

Figure 1.16. **$[Au(MePPh_2)_4]^+$ with tetrahedral coordination geometry.**[45]

1.3.2.1. Gold Phosphine Bonds

It has been observed through single crystal X-ray diffraction that in general, as more phosphines coordinate to the gold(I) centre, the gold-phosphorus bonds increase in length as they become weaker and weaker. This is explained by the effect of π bonding occurring in linear complexes with filled 5d orbitals of π symmetry (d_{xz} and d_{yz}) in gold overlapping with vacant phosphorus 3d orbitals. This π bonding is much weaker in the trigonal planar and tetrahedral complexes. Also, as the number of ligands around the gold increases, more s and p orbital hybridization occurs. Gold(I) in linear complexes is *sp* hybridized, whereas in trigonal planar complexes, it is sp^2 hybridized. This means that as the s orbital character of the gold- phosphorus bond decreases, so does the σ bond strength.

1.3.3. Other gold(I) complexes

There are many other examples of gold(I) phosphine complexes. A vast amount of research has been conducted looking at the ways in which diphosphines, triphosphines and higher phosphines interact with gold(I). It is worth mentioning the use of diphosphines in the synthesis of gold(II) complexes. Compounds with gold in this oxidation state are rare compared to those with gold(I) or gold(III). They usually oxidise or disproportionate very readily compared to common copper(II) complexes. Many compounds that suggested the presence of gold(II) were later found to contain both gold(I) and gold(III). Ligands that can form gold(II) complexes tend to be bidentate. For example, a diphosphine that can form a complex with gold(II) is bis(diphenylphosphino)methane (dppm).[46] Many of the most stable gold(II) complexes are synthesised with ylide and bis-ylide ligands.

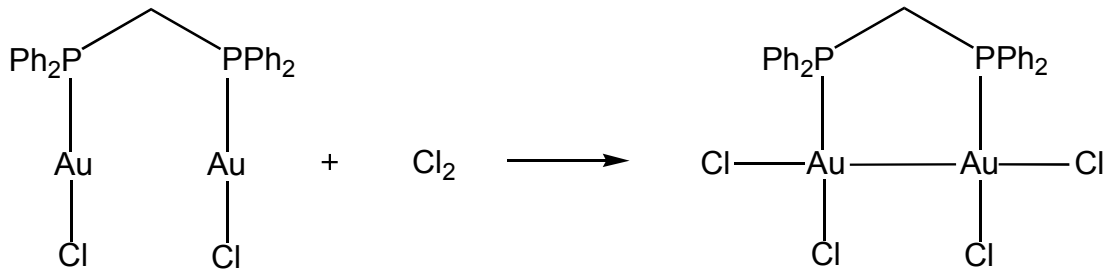

Figure 1.17. **Reaction scheme of [(dppm)Au_2Cl_2] with Cl.**[47]

1.4. Gold(III) compounds

As with gold(I) compounds, a huge amount of research as been carried out into gold(III) complexes. Gold(III) differs from gold(I) in that it can accommodate hard donor ligands such as nitrogen and oxygen as well as the softer ligands that dominate the complexes researched in gold(I).This is because gold(III) is in a higher oxidation state so can be considered a harder Lewis acid. Also, its ionic radius is also smaller (0.85 Å) than gold(I) (1.37 Å) which make it much less polarisable.[48] Generally, gold(III) complexes are more stable than gold(I) complexes which can be more susceptible to oxidation and disproportionation to gold(III) and metallic gold.

1.4.1. Gold Chlorides

The chemical generally used to provide a route into gold(III) chemistry is $HAuCl_4 \cdot 3H_2O$. This complex can be dissolved in a number of solvents including ether and water, to give $[AuCl_4]^-$. The compound, $HAuCl_4$, is also used in the purification of 99.5% purity gold through electrolysis where it is used as an electrolyte dissolved in HCl. The impure gold is the anode and pure gold is the cathode. Upon the application of a current,

pure gold is deposited onto the cathode and palladium and platinum that are usually present as impurities can be recovered from the anode. $HAuCl_4 \cdot 3H_2O$ can be obtained by dissolving gold in aqua regia and evaporating the solvent. Under heating, it decomposes with the release of HCl, to the dimeric complex $AuCl_3$. This reaction is reversible by dissolving $AuCl_3$ in concentrated hydrochloric acid again. $AuCl_3$ can also be synthesised from the direct reaction of gold with chlorine gas at high temperatures. In chloride solutions it gives the square planar anion $[AuCl_4]^-$ and in water it gives the hydrolysed species $[AuCl_3(OH)]^-$.

$$Au + 5H^+ + 4Cl^- + NO_3^- \longrightarrow HAuCl_4 + NO + 2H_2O$$

$$2\,Au + 3\,Cl_2 \xrightarrow{423\ K} 2\,AuCl_3$$

$$AuCl_3\,(aq) + HCl\,(aq) \longrightarrow H[AuCl_4]$$

$$2\,H[AuCl_4] \xrightarrow{>527\ K} 2\,AuCl_3 + HCl$$

Figure 1.18. **Shown here are the reaction schemes showing the formation and decomposition of hydrogen tetrachloroaurate and gold(III) chloride.**

$AuCl_3$ can decompose to give the metastable compound AuCl and Cl_2. AuCl has a polymeric structure with each gold(I) having a linear coordination environment. AuCl slowly undergoes disproportionation at room temperature to give metallic gold and $AuCl_3$. Heating AuCl to 563 K causes its full decomposition to gold(0) and Cl_2.[47]

$$AuCl_3 \xrightarrow{heat} AuCl + Cl_2$$

$$2AuCl \xrightarrow{563\ K} 2Au + Cl_2$$

Figure 1.19. **Reaction schemes showing the decomposition of $AuCl_3$ to AuCl and then metallic gold.**

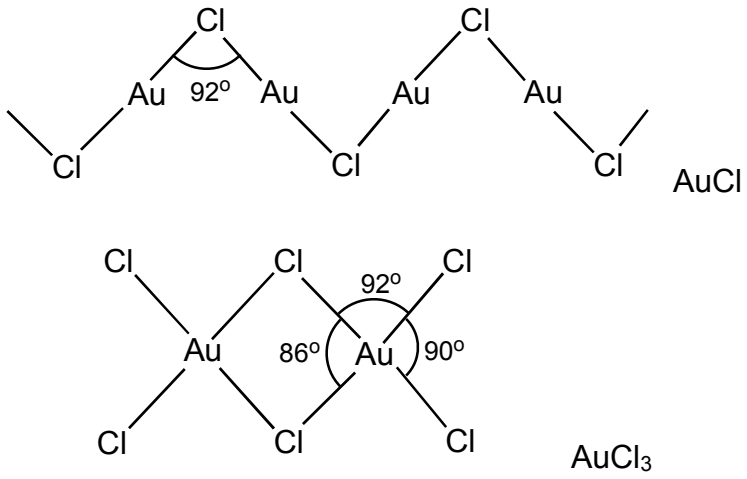

Figure 1.20. **The planar structures of AuCl and $AuCl_3$.**[47]

In the structure dimeric of $AuCl_3$, the chlorine bridges present between the gold atoms are easily broken by neutral ligands, such as phosphines, to give highly reactive complexes such as $AuCl_3(PPh_3)$. With the presence of such easily oxidised ligands in $AuCl_3$, it can also act as a chlorinating agent. In the case of the reaction of PPh_3 with $AuCl_3$, Cl_2PPh_3 is formed as well as $AuCl_3PPh_3$. $AuCl_3$ can therefore be used in the in the synthesis of linear [LAuCl] gold(I) complexes (where L is a neutral ligand) such as the gold- phosphine complexes mentioned earlier, as well as being useful in the synthesis of $[LAuCl_3]$ compounds.

Gold(III) compounds have a diamagnetic $5d^8$ electron configuration. This means that most of the complexes formed with gold(III) have the expected square planar geometry. σ bonding occurs in these compounds using 4 hybrid orbitals from $5d_x^2\text{-}_y^2$, 6*s*, $6p_x$ and $6p_y$. As mentioned earlier, the σ bonds in gold(I) compounds have predominantly s character and get weaker as more hybridization with p orbitals occur. The σ bonds in gold(III) complexes are different in that p orbitals have a far greater presence in the hybrid orbitals than in gold(I) compounds. It has also

been observed that the 5d orbitals play a much smaller role in the bonding of gold(III) complexes compared to gold(I).[47]

5[49] and 6[50] coordinate gold(III) compounds have also been reported, though they are far rarer than 4 coordinate square planar gold(III) complexes.

1.5. Gold clusters

Clusters fall into the category between molecules and nanoparticles. They can be considered as large molecules or small, monodisperse nanoparticles. Gold clusters have been known since the 1960's, but it has only been recently that they have started to potentially have real applications. Water-soluble gold clusters have been used as an electron dense biological label in electron microscopy studies of proteins.[51, 52] More recently, it has been found that clusters of gold can catalyze the conversion of CO to CO_2 under low temperature conditions.[53] This will be covered more in Chapter 4.

1.6. Scope of this thesis

The work within this thesis aims to build upon two areas of chemistry; catalysis and cluster chemistry. In order to investigate the effect of gold particle size on catalytic activity, the steric effects of the stabilising ligand on the particle size has first been explored. A series of phosphine ligands with slight variations from each other were used to synthesise a range of gold clusters. These clusters were characterised extensively to understand the effects of the phosphines used to stabilise them.

These clusters were then used to synthesise novel supported gold catalysts by depositing them on to silica nanospheres. The catalysts were

then investigated for their activity in liquid phase oxidation reactions. By varying both the loading of the gold on the support, and the temperature at which it the catalyst was calcined, the effect of these variables, along with the size of cluster used to synthesise the catalyst, could be related to the activity achieved.

Through investigating the activity of uncalcined catalysts, a novel method for the low temperature removal of phosphine ligands from the gold clusters has been estabilshed. This improves upon the original calcination process by offering more control over the rate at which the phosphines are lost, leading to decreased aggregation of the gold, which was an issue for the uncalcined catalysts.

The final part of the thesis discusses the initial findings of supporting the clusters on other supports, in particular, anatase phase and mesoporous titania. Some structural characterisation and catalytic activity data is reported and compared to the silica supported catalysts.

2. Characterisation methods

A number of different methods were used for the characterisation of the compounds and catalysts described within this work. The first part of this chapter discusses laboratory-based techniques routinely used for catalytic studies. The second part of the chapter details the characterisation methods used, in particular X-ray absorption spectroscopy. This chapter will also discuss some of the theory behind the techniques.

2.1. Catalytic reactor setup

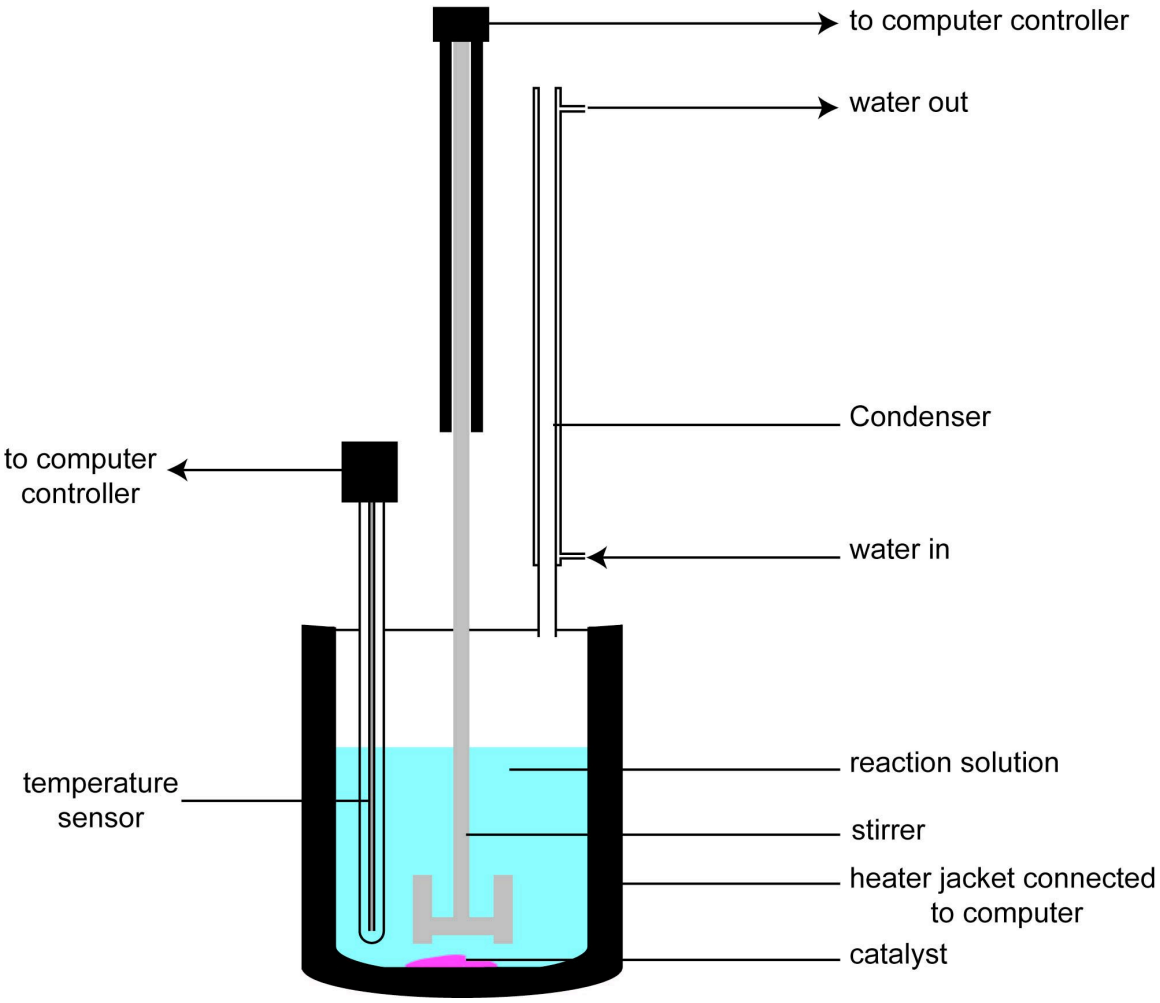

Figure 2.1. A diagram of the catalytic reactor vessel.

In order to test the activity of the catalysts that were synthesised, catalytic oxidation reactions were carried out. Using a "Mettler Toledo Multimax Reactor Box," up to four parallel reactions could be run independently. The reactor box allowed for the temperature, rate of temperature change and stirrer speed to be programmed by computer. The computer also displayed the temperature and stirrer speed whilst the reaction was occurring. The setup for each reactor is illustrated in figure 2.1. Each reactor was fitted with a top-down stirrer, a temperature sensor to

constantly monitor the reaction temperature and a condenser to prevent loss of any solvent or volatile compounds.

2.2. X-ray diffraction (XRD)

X-ray diffraction is commonly used to characterise samples that have long-range order. From the interaction between X-rays and a crystalline solid, a diffraction pattern is obtained that can reveal structural information about the solid such as the unit cell size and shape.

When the wavelengths of the X-rays are similar in size to the distance between atoms, it is possible for diffraction to occur. In an ordered lattice like a crystalline solid, the ordered atoms form planes and it is these planes that diffract the X-rays. Bragg[54] demonstrated in 1913 the relationship between the incident angle (or Bragg angle, θ) of the incoming X-ray beam and the distance between the diffracting planes (d). This simple relationship is shown in equation 1 and is known as Bragg's law.

$$n\lambda = 2d\sin\theta \qquad \textbf{Equation 1.}$$

Where: λ= wavelength of the incident X-rays, d= distance between the planes, θ= incident angle of X-rays.

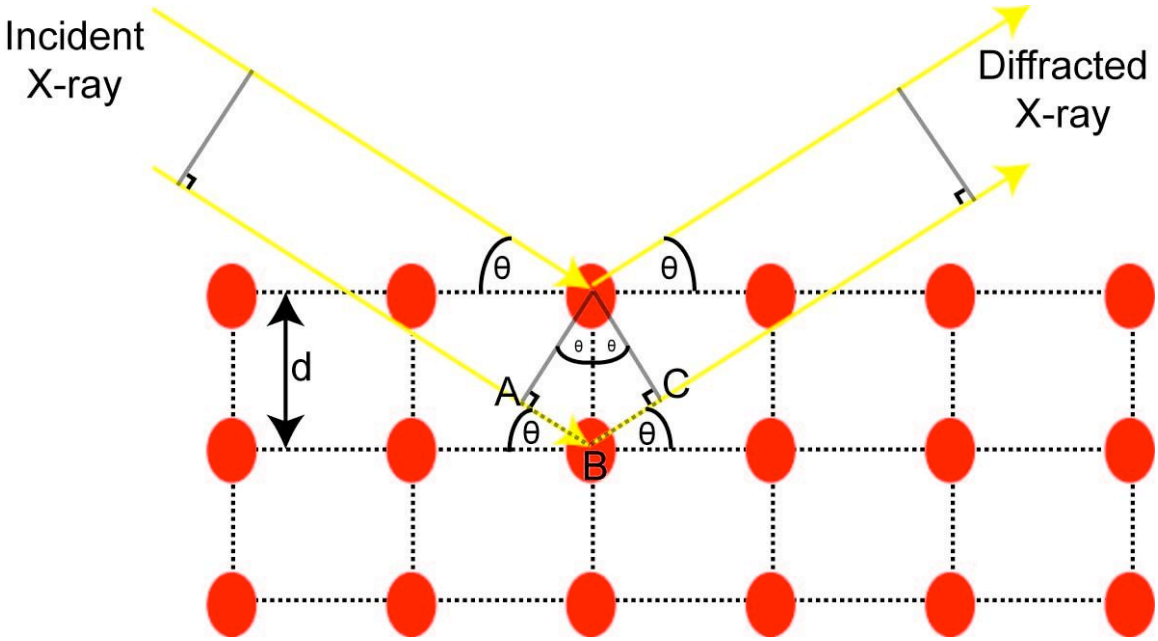

Figure 2.2. The diffraction of an X-ray by an ordered lattice of atoms.

Figure 2.2 illustrates how the Bragg's law is calculated by showing the path difference in the reflected X-rays arises as a result of the top of the incident X-ray reaching the diffracting atom before the bottom. The path difference (δ) is equal to the sum of AB and BC and explains the interference between the diffracted X-rays. Constructive interference occurs at a maximum when the path difference is equal to a whole number of wavelength ($n\lambda$) as shown in equation 1. This constructive interference allows a diffraction pattern to be collected by moving the position of the detector relative to the sample.

X-ray diffraction was not used to its fullest extent for the work within this thesis. Whereas it can be used for phase identification and the arrangement of atoms within a solid, it functioned as a highly useful means of identifying the average size of the gold crystallites on the surface of a support. This is possible due to the broadening of peaks when diffraction is carried out on small (<0.1 μm) particles. To calculate the average particle size of silica supported gold particles, powder XRD patterns were collected and peaks corresponding to gold reflections were identified. The full width half maximum (FWHM) values for the peaks of

interest were determined and the values were used, along with the known values of λ, θ and *K*, to obtain an approximate mean gold particle size using the Scherrer equation[55] (equation 2).

$$\tau = \frac{K\lambda}{\beta \cos\theta} \qquad \textbf{Equation 2.}$$

The Scherrer equation, where: τ= the mean size of crystallite domains, *K*= the shape factor, λ= the wavelength of the X-rays, β= the full width half maximum value of the crystallite peak and θ= the Bragg angle.

The components of the equation can all be obtained from XRD data and the shape factor, *K*, is a value between 0.89 (for spherical particles) and 0.94 (for cubic). *K* is set to 0.90 for unknown particle shapes. This gives a rough particle diameter. Instrumental peak broadening can also occur, but this can be accounted for by finding the FWHM values of large gold particles that do not present any line broadening. This FWHM value is then subtracted from the experimental value to give a more accurate mean particle diameter. This made very little difference to the values observed.

2.3. Nuclear magnetic resonance

Nuclear magnetic resonance (NMR) spectroscopy is quite a unique technique in that it explores the nuclei of a sample and not the electrons. NMR takes advantage of the magnetic properties of specific nuclei to yield chemical information. Nuclei that have an overall spin can be probed by NMR spectroscopy. When a magnetic field is applied to an atom, the magnetic moment of the nucleus will either align with or against the applied magnetic field. The lower energy state is that aligned with the magnetic field. If a sample is irradiated with radio waves of the correct frequency, the atoms absorb the energy and are the nuclei promoted to

the less energetically favourable (higher energy) antiparallel spin state. When this occurs it is known as resonance.

The nuclei have a Boltzmann distribution of spin states; that is to say that not all of the nuclei are in the lower energy spin state. There is an almost even distribution of the spin state populations of ^{1}H at room temperature, with only a slight excess of nuclei in the lower energy, aligned, state. As this difference in population states is small, it means that in order to achieve a sufficient signal to noise ratio, many signals must be averaged.

A sample is pulsed with radio waves in the correct frequency range, promoting the nuclei to higher energy spin state. After the pulse, the nuclei relax and return to their equilibrium positions. The process of the spin states switching back and forth generates a radio-frequency signal that is detected. In the process of relaxing, the signal decays. The sum of all of the frequencies of the target nuclei in the sample makes up the decaying signal. The frequencies are recorded and transferred into chemical shift values relative to a standard.

The electrons present in the atoms also generate magnetic field through their motion. The presence of these electron generated magnetic moments means ^{1}H, and other NMR active nuclei will have different resonant frequencies depending on the chemical environment of the atom.

2.4. Infrared spectroscopy

Infrared (IR) spectroscopy uses absorption of IR radiation by a compound to identify the types of bonds present. A compound will only absorb specific energies of IR radiation that correlate to energies of the bond or group vibrations within the sample molecule. IR spectroscopy can therefore be employed to observe the presence of different bonds or groups within a compound. IR active bonds must have a permanent

dipole (i.e. the atoms bonded to each other must have different electronegativities).

The mid infrared (4000-400 cm^{-1}) radiation was employed, together with an attenuated total reflection (ATR) accessory to analyze gold clusters that had undergone counterion metathesis. The ATR accessory meant than samples did not have to be dissolved into a solution or pressed into a pellet to obtain a spectrum as the samples could be pressed on to a small window of an IR transmitting crystal with a high refractive index. IR radiation then bounces off the inside of the crystal against the surface of the sample and is then directed back out of the crystal and back into the machine. Using this method, IR spectroscopy was able to confirm the exchange of NO_3^- groups with PF_6^- as both of these groups have IR active bond vibrations.

2.5. Gas Chromatography

Gas chromatography (GC) is used as a means of determining the compositions of mixtures of compounds as a result of a catalytic reaction. In this technique, a sample liquid is injected into the GC where it is vapourised and carried through a very long, narrow chromatography column by a flow of inert gas such as helium. This is known as the carrier gas (mobile phase). The column contains an immobilised solvent (the stationary phase) that the components of the sample adsorb on to. Different compounds will have different strengths of adsorption on to the stationary phase and this is what causes the separation.

At the end of the column is a detector that is concentration sensitive. There are different types of detectors that can be used depending upon the nature of the compounds being analysed. Throughout this work, a flame ionization detector (FID) was used that burns organic compounds

in air and hydrogen producing ions that register as a current (which is proportional to concentration).

The column is inside a highly accurate oven that can be programmed to ramp to different temperatures to accelerate the rate at which the compounds pass through the column. The flow rate of the carrier gas can also be adjusted to increase or decrease the rate at which the samples pass though the column.

As the components of the sample mixture will separate depending on their strength of adsorption to the stationary phase, the compounds will take different lengths of time to pass through the column. This is known as the retention time of a compound. The output of a GC is a plot of the retention time vs. the ionization current. This is given as a series of peaks with areas proportional to the amount of compound present in a sample.

Before analysis of mixed samples is carried out, pure standard samples of known compounds present in the mixture are injected into the GC to find the individual compounds retention time. The corresponding peaks in the mixed sample can then be identified. Also, if equal quantities of pure compounds are injected into the GC, they should in theory give the same sized peaks with equal areas. However, some compounds have a better response than others and this is known as the response factor. Through injection of mixtures of known quantities or ratios of compounds, the relative response factors of each compound can be calculated and then results normalised.

To find the relative quantities of compounds in a sample mixture, the area underneath peaks that correspond to compounds of interest are normalised with respect to a known quantity of one compound that does not vary throughout a reaction. This is the internal standard. Throughout the catalysis experiments carried out in this thesis, decane was used as an internal standard as its quantity remained constant relative to the rest of the compounds.

2.6. Electron microscopy

Electron microscopy was an invaluable tool throughout this work. It uses a beam of electrons to illuminate a sample and magnify it up to and greater than 100,000x. Two different types of electron microscopy were employed to analyse samples, transmission electron microscopy (TEM) and scanning electron microscopy (SEM).

2.6.1. TEM

A TEM uses an electron gun to generate a beam of electrons that are accelerated through an electric field and, using electromagnetic lenses, are focused on to a sample. The electrons are slightly scattered as they pass through the sample. The degree of scattering depends on the electron density of the sample being viewed. The electrons are then focused on to a fluorescent screen as a magnified image of the sample being analysed. Photographs can be obtained through focusing the electrons on to a photographic film beneath the fluorescent screen, though in modern TEMs, there is a digital camera sensor that the electrons are focused on to allowing the images to be viewed on a computer monitor. As the elements with more electron density scatter the electrons more, this means that heavier elements appear darker in the images. The magnification levels that the images were recorded at allows for the sizes of particles observed in the images to be calculated.

2.6.2. SEM

SEM differs from TEM in that the electron beam does not provide an image of the whole sample, only a point on the sample. An electron beam

is generated by an electron gun, accelerated through an electric field and focused on to a single spot on the sample using electromagnetic lenses. Scanning coils or deflector plates then scan the beam across a rectangular surface of the sample. The electron beam causes the emission of secondary electrons from the sample as a result of inelastic scattering. Elastic scattering can also occur giving back-scattered electrons that are higher in energy than secondary electrons. The secondary electrons allow for high-resolution images to be obtained that also give an insight into the morphology of the sample. Though they provide lower resolution images, back-scattered electron images can provide information about the distribution of heavier elements throughout a sample. X-rays are also emitted as a result of the electron beam's interaction with the sample. The energy of the X-rays corresponds to energy differences between electronic shells in the sample. Thus, the X-rays emitted by the sample are element specific and detection of these X-rays can be used as a form of elemental analysis for the scanned area. This is known as energy dispersive X-ray spectroscopy.

2.7. Synchrotron radiation

Synchrotron radiation has been an invaluable tool throughout this work as it allowed for the use of otherwise unattainable techniques. Synchrotron radiation is a product of a synchrotron, where electric fields are applied to accelerate electrons to close to the speed of light inside a storage ring. Magnetic fields are used to change the direction of the ultrarelativistic particles within the storage ring resulting in energy loss in the form of synchrotron radiation. This consists of electromagnetic radiation ranging from infrared to high energy (hard) X-rays. The light is emitted from the position where the path of the charged particle was deflected (by a bending magnet), into an experimental hutch where it can be utilising. Before reaching the experimental hutch, the light first passes through an

optics hutch where it is collimated and focused. This is illustrated in figure 2.1.

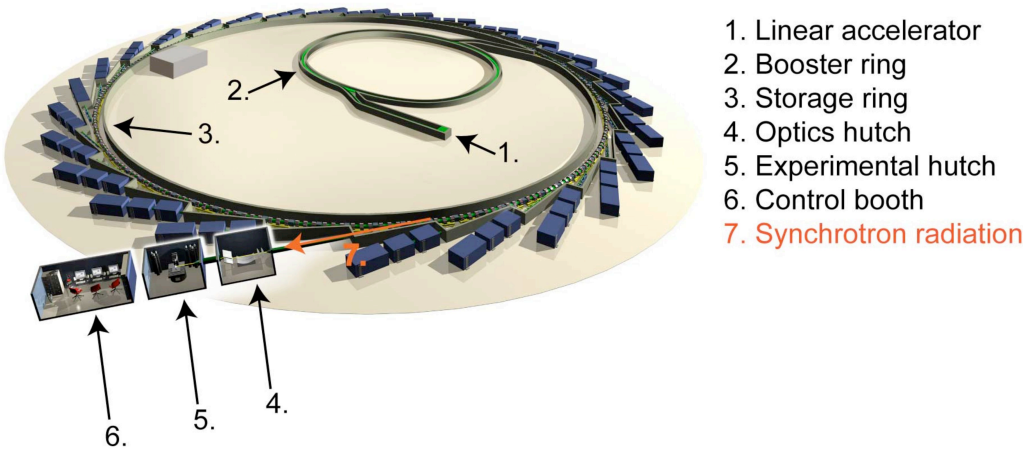

Figure 2.3. A diagram of a synchrotron with labelled components.[56]

Due to the intensity of the X-rays (many orders of magnitude greater than the X-rays generated by X-ray tubes), it is possible to collect data that would take at least an hour in a laboratory, in less than a minute. This means that scientists can accumulate vast quantities of data at a synchrotron whereas in the lab it would take several weeks or maybe even months. The beam intensity also means that specialist techniques that require high intensity and tuneable energy X-rays, such as X-ray absorption spectroscopy, can be carried out. In particular, Synchrotron Radiation provides (a) high-intensity, (b) coherent radiation and (c) tuneable energy (or wavelength) over a wide range. For these reasons, more researchers are turning to Synchrotron Radiation. The X-ray absorption spectroscopy data discussed within this work was collected at the now closed Synchrotron Radiation Source (SRS) in Daresbury and the European Synchrotron Radiation Facility (ESRF) in Grenoble, France.

2.7.1. X-ray absorption spectroscopy

X-ray absorption spectroscopy (XAS) is a characterisation technique that gives local information on the probed elements such as the coordination number and bond distances of the coordinated atoms. It is an element specific technique, which means that it is an invaluable tool for gaining information of active species in catalysts. Even when in very low concentrations or embedded within a support, due to the penetrating nature of the X-rays used in XAS it is possible to record data under these conditions. Long-range order is not required in XAS, so it is one of the few characterisation techniques that can be used on non-crystalline materials, even solutions. Another benefits of XAS is that *in situ* studies can be carried out using this technique.

XAS functions by measuring the X-ray absorption of a material or element as a function of X-ray energy. XAS operates on the basis that when X-rays are emitted on to a material, some of the photons are absorbed. This causes the intensity of the incident X-ray beam to decrease. The absorption of the photons causes the excitation of core level electrons to vacant energy levels. When the energy of the X-ray matches the energy difference between the core level and unoccupied or partially unoccupied levels, X-ray absorption takes place. The amount of absorption that occurs at a given energy is characteristic for each compound, hence this technique is termed as being "atom-specific." The X-ray absorption coefficient, $\mu(E)$, is determined from the decrease in X-ray beam intensity, I, with distance, x.[57] This is shown in equation 3.

$$\mu(E) = -d\ln I / dx \qquad \textbf{Equation 3.}$$

Where: $\mu(E)$= the absorption coefficient, I= intensity and x= distance.

After the x-ray has passed through the sample, the change in I from the incident intensity, I_0, is calculated in equation 4.

$$I = I_0 e^{-\mu(E)x} \qquad \textbf{Equation 4.}$$

Where: I= intensity after passing through sample, I_0= incident intensity, $\mu(E)$= the absorption coefficient and x= sample thickness.

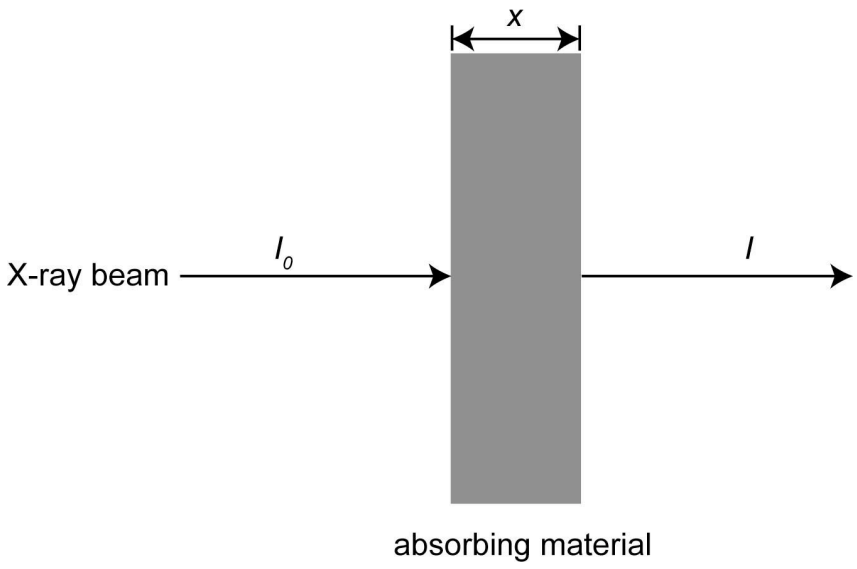

Figure 2.4. Diagram illustrating X-ray absorption of a sample where I_0 is the incident X-ray intensity, I is the transmitted intensity and x is the thickness of the absorbing material.

Plotting the change in absorption coefficient against energy shows the features of interest. What is observed is an overall decrease in X-ray absorption as the energy increases. There are also sharp increases in the absorption coefficient as the energy increases and these are known as edges. Just beyond the edges in energy are a series of oscillatory features.

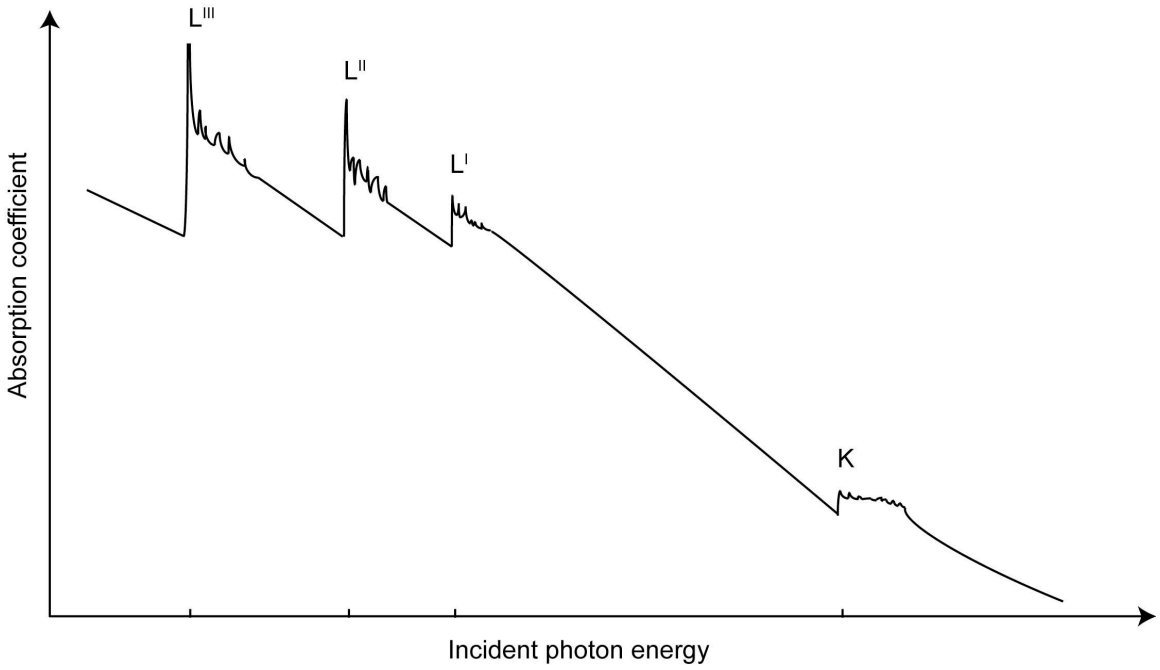

Figure 2.5. Diagram illustrating the variation in absorption coefficient with incident photon (X-ray) energy.

Table 2.1. Table of the absorption edges and the relating transitions.

Absorption edge	Transitions to Fermi level
K	1s
L^{I}	2s
L^{II}	$2p_{(1/2)}$
L^{III}	$2p_{(3/2)}$
M^{I}	3s

The absorption spectrum of an atom has three main features. The pre-edge and post-edge regions are the X-ray absorption near edge structure (XANES) and beyond that is the extended X-ray absorption fine structure (EXAFS). These are illustrated in figure 2.6.

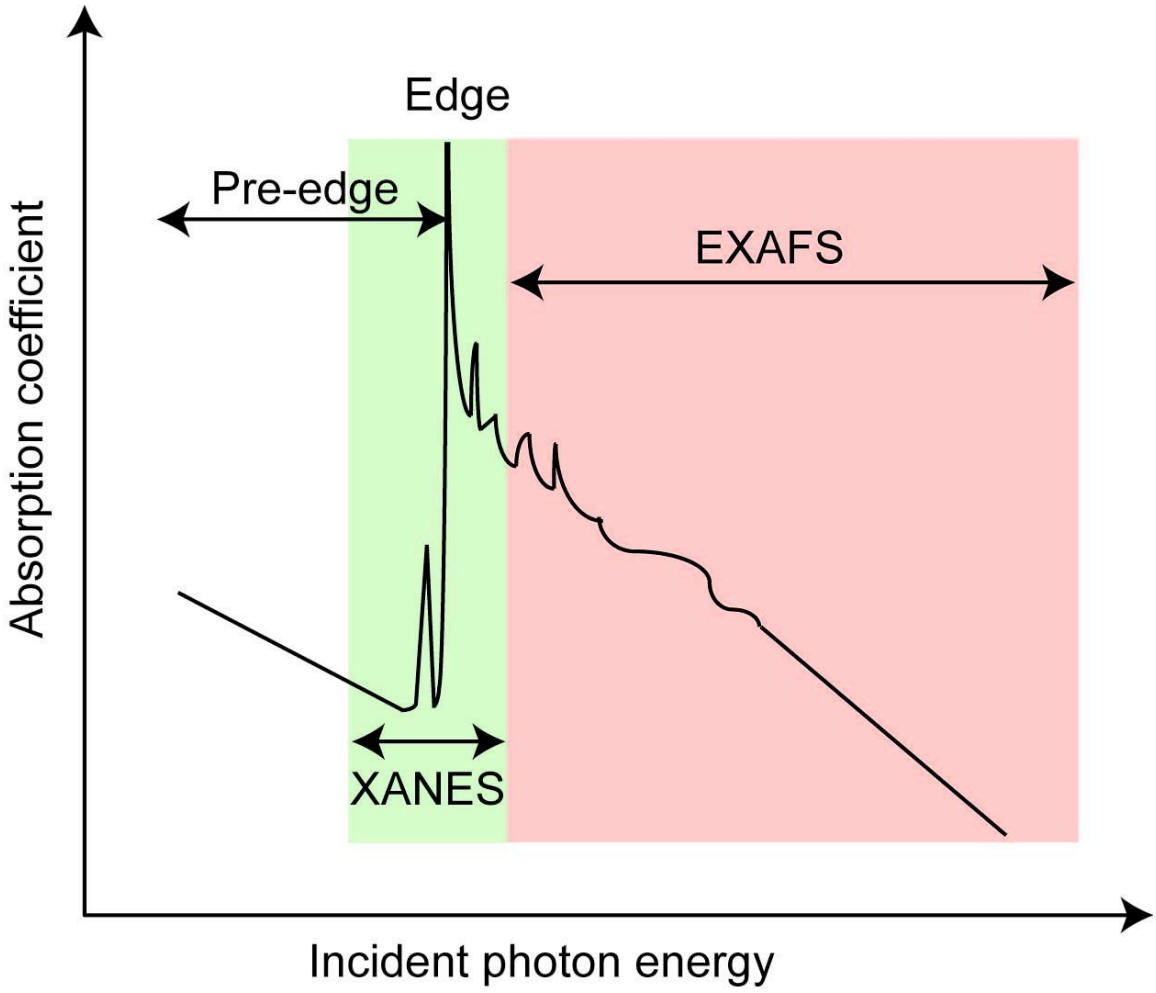

Figure 2.6. Diagram to show the different regions in an X-ray absorption spectroscopy spectrum.

Upon absorption of an X-ray photon, the atom is said to be in an excited state. This means that one of the core electron levels is left empty by the promotion of an electron to a higher energy level as a photoelectron. The excited state can decay in one of two ways, X-ray fluorescence or Auger emission. X-ray fluorescence occurs when a higher energy core level electron fills the core hole resulting in the emission of an X-ray of well-defined energy. Auger emission occurs when an electron from a higher energy level drops to fill the core hole with the emission of an electron. When hard X-rays are being employed, it is more likely that X-ray fluorescence will occur whereas with lower energy X-rays, Auger emissions will predominate.

2.7.2. XANES

This region is located in an absorption spectrum roughly 50 eV before (pre-edge), and 100 eV above the edge. After the initial decrease in intensity due to mass absorption, a sudden increase in intensity follows as the X-rays promote electronic transitions to partially full or vacant energy levels. XANES data can provide information about the oxidation state of a sample, as well as its coordination environment. Peaks in the pre edge are due to core transitions to partially occupied states. These can indicate the presence of a particular oxidation state in an element. For example, Thomas and Sankar revealed that the Ti^{+4} active sites were four-coordinate tetrahedral in titanosilicate catalysts for the epoxidation of propylene by the position and intensity of the pre-edge peak.[58]

2.7.3. EXAFS

EXAFS is observed as oscillations from 50 to 1000 eV above the edge. When a material absorbs X-rays at this energy range, photoelectrons are ejected that carry kinetic energy. These ejections of photoelectrons can be thought of as spherical waves emanating from the absorbing atoms. When the photoelectron reaches a neighbouring atom, backscattering occurs, meaning that the wave bounces back towards the original absorbing atom. This is pictured in figure 2.7.

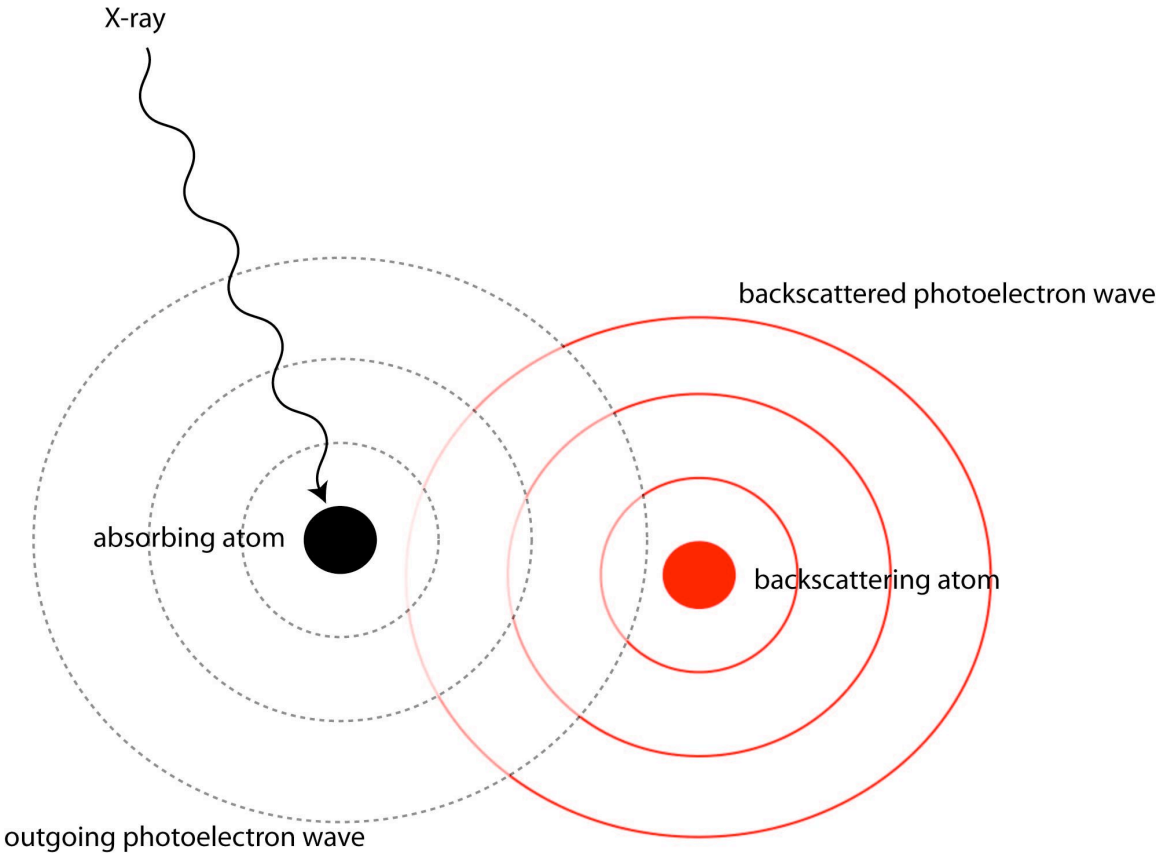

Figure 2.7. Diagram of the outgoing and backscattered photoelectron waves after X-ray absorption by an atom.

The sum of the outgoing waves and the backscattered waves (interfering either constructively or destructively) are what is observed in the absorption coefficient variations with energy (EXAFS spectra).[59] This is described in equation 5.

$$\mu_{total} = \mu_0[1 + \chi_{EX}] \qquad \textbf{Equation 5.}$$

Where: μ_{total}= the absorption coefficient above the edge, μ_0= atomic background and χ_{EX}=sum of outgoing and backscattered photoelectron waves.

χ_{EX} is also known as the EXAFS function. It can be simply described by considering the waves as planar rather than spherical, and with one scattering shell of atoms. The EXAFS function can then be expressed as in equation 6.

$$\chi(k) = \sum_{j=1}^{Shells} A_j(k) \sin\Phi_j(k)$$ **Equation 6.**

Where: $\chi(k)$= the EXAFS function of wave vector (k), $A_j(k)$= the amplitude of wave vector(k) and $\sin\Phi j(k)$= sine function of interference pattern.

The relationship between the wave vector, *k*, and energy, E, is given in equation 7.

$$k = \sqrt{\frac{2m(E - E_0)}{(h/2\pi)^2}}$$ **Equation 7.**

Where: k= the wave vector, m= the mass of an electron, E= energy, E_0= threshold energy and h= Planck' constant.

Equation 6 can be broken down into two parts to explain the amplitude of the wave vector and the sine function of the interference pattern between the emitted photoelectron and the backscattered photoelectron.

$$\sin\Phi_j(k) = \sin[2kR_j - \phi_j(k)]$$ **Equation 8.**

Where: R_j= inter-atomic distance between the absorbing and backscattering atoms, $\phi_j(k) = 2\phi_{absorber}(k) + \phi_{scatterer}(k)$= the phase shift, dependent on the absorbing and scattering atoms.

Equation 8 shows how the phase part of the interference pattern contains in inter-atomic distance between the absorbing and the scattering atoms and also the phase shift. The sine function is the related to the time taken by a photoelectron wave to travel to a neighbouring backscattering atom and return to the absorbing atoms. The phase shift accounts for the change in speed of the photoelectron as a result of the positive charge of the nucleus.

$$A_j(k) = \frac{N_j}{kR_j^2} S_0^2 F_j(k) e^{-2k^2\sigma^2} e^{-2R_j/\lambda k}$$ **Equation 9.**

Where: N_j= coordination number, R_j= inter-atomic distance, S_0^2= amplitude reduction factor, $F_j(k)$= backscattering amplitude, σ^2= disorder factor (mean

square displacement of the neighbouring atom over an average distance, this consists of both static and thermal disorder), λ= mean free path of photoelectron.

Equation 9 shows how the amplitude of the wave vector is dependent upon a number of factors. The coordination number (N_j), inter-atomic distance (R_j) and disorder factor (σ^2) of a compound can be obtained by fitting recorded EXAFS data to model data. What makes EXAFS so useful is the fact that the backscattering amplitude ($F_j(k)$) is element specific, so even more information can be acquired using this technique. The amplitude reduction factor (S_0^2) takes into account the reduction in amplitude wave vector due to inelastic scattering. The mean free path of the photoelectron (λ) is an exponential term that accounts for the finite lifetime of the excited state.

2.7.4. Data collection

It is possible to collect EXAFS data in one of two ways, either in transmission geometry, or fluorescence geometry. Transmission data is recorded using ion chambers. These are airtight chambers containing a carefully measured mixture of noble gases separating two highly (oppositely) charged parallel plates. Windows in the chamber allow the X-ray to pass through. When this occurs, the X-rays ionize the gases, causing an ionization current, which is recorded. Ion chamber are placed before and after a sample in the path of the X-ray beam to record the difference in current either side of the sample, which relates to the changes in X-ray beam intensity.

Fluorescence data is recorded through the use of highly sensitive detector arrays. These detectors record the X-rays emitted from the sample. Fluorescence data is often recorded if the sample contains low, or even trace levels of the element being observed. In this work, all of the data was collected using transmission mode.

2.7.5. Data analysis

The first step of EXAFS data analysis is to subtract the background of the pre-edge from the collected data. This is done by fitting a smooth line to the pre-edge which, when subtracted from the original data, removes any instrumental background and absorption from other edges. Normalised XANES are obtained by normalising the edge jump increase in $\mu(E)$ from 0 to 1. The threshold energy, E_0, is energy of the maximum derivative of $\mu(E)$ (usually the mid point of the edge jump). The EXAFS, $\chi(k)$, data is obtained by plotting a smooth line background function through the post-edge (representing the absorption by 1 atom), and subtracting it from the recorded data (figure 2.8).

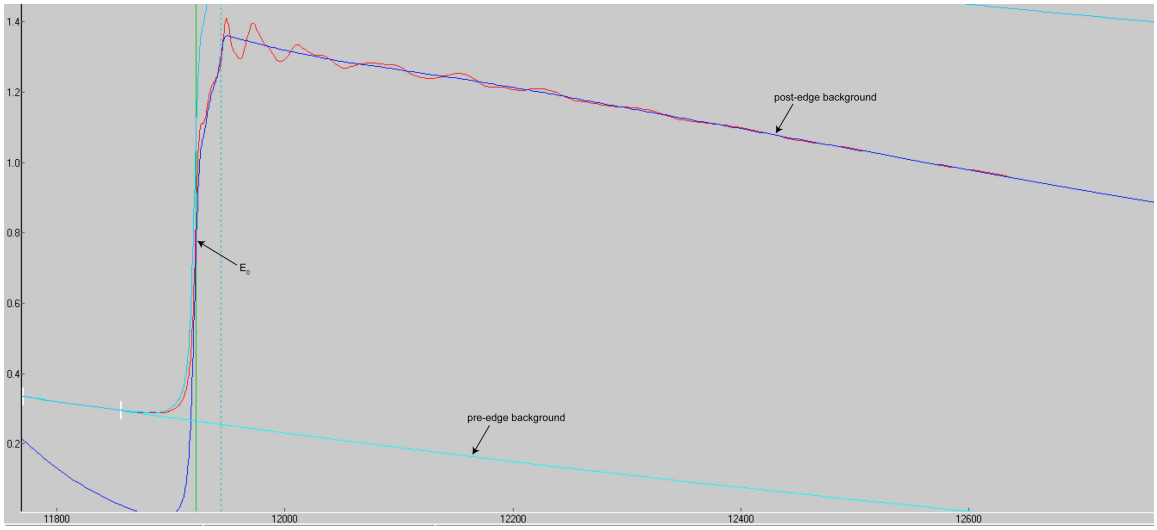

Figure 2.8. Background subtraction of raw EXAFS data using the program VIPER.

Due to the fast decay of EXAFS, in order to amplify the oscillations at higher k values, they can be plotted with higher k weightings such as k^3. The EXAFS data shown in figure 2.9 are k^3 weighted.

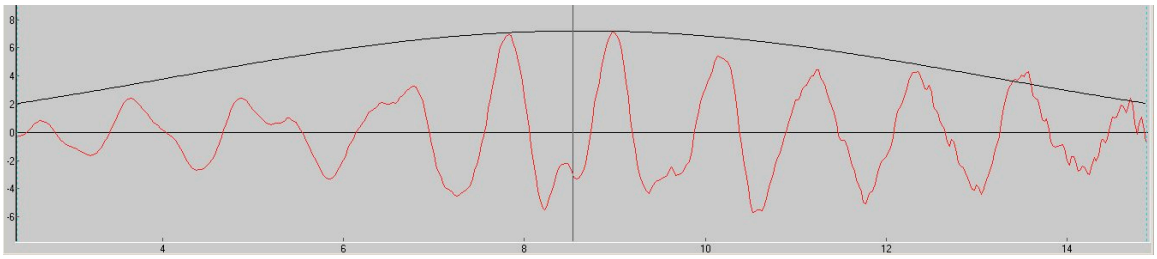

Figure 2.9. EXAFS data extracted after background subtraction using the program VIPER.

The EXAFS data can be Fourier transformed to convert χ(k) into *R*-space. Fourier transformed (FT) data shows the number and distance of atoms from the atom absorbing X-rays. An example can be seen in figure 2.10. The background subtraction program VIPER[60] was used during EXAFS analysis of the data presented in this work.

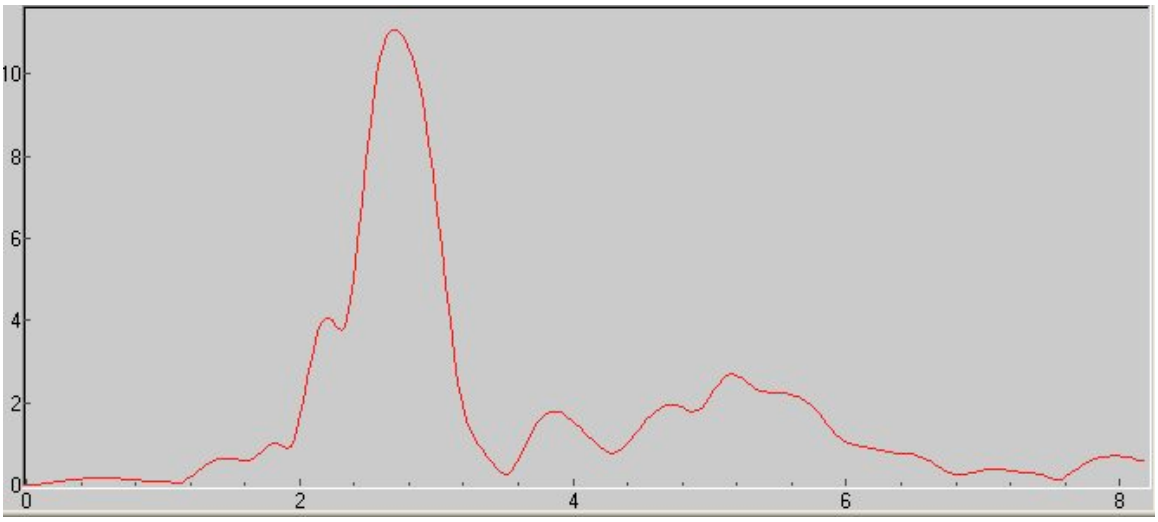

Figure 2.10. Fourier transformed EXAFS data from the program VIPER.

To calculate from the data what elements are bound to the X-ray absorbing atom, how many atoms of that type and the bond distances, structural models must be built and refined to fit the recorded EXAFS data. The program used for this work was EXCURVE,[61] which operates using the rapid curved wave theory. This program simulates EXAFS spectra from the parameters of the radial shells of atoms surrounding the central atom. An example is shown in figure 2.11.

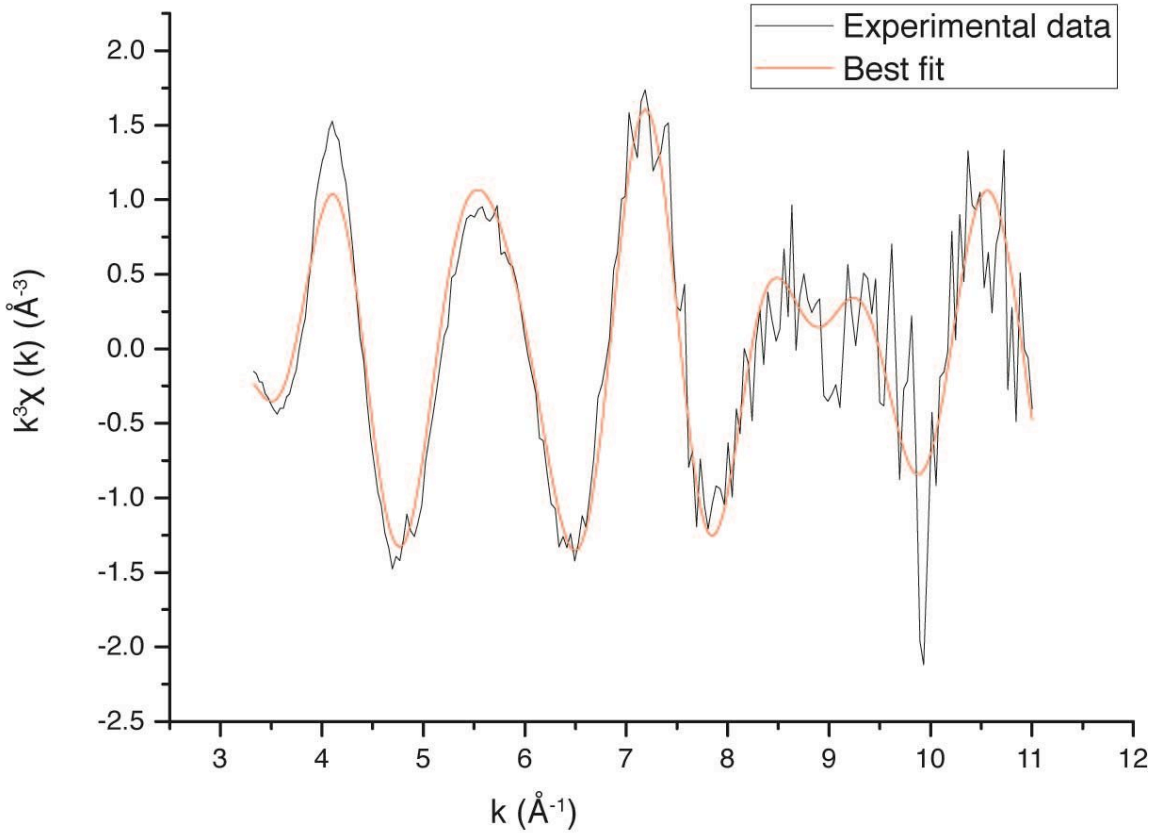

Figure 2.11. Example of k^3 weighted EXAFS data fitted to a model using EXCURVE.

3. Cluster synthesis using varying arylphosphines

Abstract

This part of the project investigated the effects of altering the size of the phosphine ligands on the size of the gold clusters formed after reduction of the precursor with $NaBH_4$. Though previous work in this area has demonstrated that increasing the steric bulk of the ligand decreases the size of the cluster formed, none have investigated a series of ligands with such small variations between them. Using a range of techniques to characterise the clusters, previously unidentified clusters have been observed.

3.1. Gold Clusters

Clusters can be considered as large molecules, or small monodispersed nanoparticles and can generally be classed into two different types; those stabilised by phosphine ligands and those which are stabilised by thiol or other ligands.

3.1.1. Gold- phosphine clusters

Gold- phosphine clusters were first reported in 1965 by Naldini and coworkers[62] who reacted PPh_3AuCl with sodium borohydride. Whereas in previous experiments with the copper and silver complexes, $[(PPh_3)_2M(BH_4)]$ (M= Cu, Ag) were formed, the gold complex reacted differently to give a red crystalline precipitate. It was believed at the time that this red compound was $Au_5(PPh_3)_4Cl{\cdot}5H_2O$.[44] It was not until the partial crystal structure of $[Au_{11}(PPh_3)_7(SCN)_3]$ was reported[63] in 1969 that it was apparent that the structures of the species formed were more complex than first thought. Following this there was large amount of research carried out exploring the effects of different ligands on the cluster, leading to many novel crystal structures being reported (see table 3.1). There are also many gold cluster compounds known that can be prepared using diphosphines, for example, the reduction of $[(AuCl)_2(dppe)]$ by $NaBH_4$ in ethanol give the cluster $[Au_6(dppe)_2Cl_2]$.[64]

Table 3.1. Table of different cluster compounds and preparation methods used.

CLUSTER	PREPARATION METHOD	REFERENCE
$[Au_4(PPh_3)_4(\mu\text{-}I)_2]$	Reaction of $[Au_9(PPh_3)_8]^{3+}$ with KI	65
$[Au_4(dppm)_3I_2]$	Reaction of $[Au_4(PPh_3)_4(\mu\text{-}I)_2]$ with dppm	66
$[Au_5(dppm)_3(dppm\text{-}H)]^{2+}$	Metal evaporation into dppm	67, 68
$[Au_6(PCyPh_2)_8]^{2+}$	Reduction of $[Au(PCyPh_2)(NO_3)]$ by $NaBH_4$	68
$[Au_6(P(o\text{-tolyl})Ph_2)_8]^{2+}$	Reduction of $[Au(P(o\text{-tolyl})Ph_2)(NO_3)]$ by $NaBH_4$	68
$[Au_6(PPh_3)_6]^{2+}$	Reaction of $[Au_8(PPh_3)_8]^{2+}$ with $K[Ag(CN)_2]$	68
$[Au_6(dppe)_2Cl_2]$	Reduction of $[Au_2(dppe)Cl_2]$ by $NaBH_4$	64
$[Au_6(dppp)_4]^{2+}$	Reaction of dppp with $[Au_9(PPh_3)_8]^{3+}$ or $[Au_4(PPh_3)_4(\mu\text{-}I)_2$	69
$[Au_7(PPh_3)_7]^{2+}$	Metal evaporation into PPh_3	70
$[Au_8(PPh_3)_6I]^{+}$	Reaction of $[Au_9(PPh_3)_8]^{3+}$ with NBu_4I	70
$[Au_8(PPh_3)_7]^{2+}$	Reaction of $[Au_8(PPh_3)_8]^{2+}$ with $[RhCl(C_8H_{14})_2]_2$	71, 72
$[Au_8(PPh_3)_8]^{2+}$	Reaction of $[Au_9(PPh_3)_8]^{3+}$ with PPh_3	73
$[Au_9(PCy_3)_5(SCN)_3]$	Reduction of $[Au(PCy_3)(SCN)]$ by $NaBH_4$	74
$[Au_9(P(p\text{-}OMe)_3)_8]^{3+}$	Reduction of $[Au(P(p\text{-}OMe)_3)(NO_3)]$ by $[Ti(\eta\text{-}C_5H_5Me)_2]$	75
$[Au_9(P(p\text{-}OMe)_3)_8]^{3+}$	Reduction of $[Au(P(p\text{-}OMe)_3)(NO_3)]$ by $NaBH_4$	76
$[Au_9(P(p\text{-tolyl})_3)_8]^{3+}$	Reduction of $[Au(P(p\text{-tolyl})_3)(NO_3)]$ by $NaBH_4$	77, 78
$[Au_9(PPh_3)_8]^{3+}$	Reduction of $[Au(PPh_3)(NO_3)]$ by $NaBH_4$	78-80
$[Au_{10}(PCy_2Ph)_6Cl_3]^{+}$	Reduction of $[Au(PCy_2Ph)(NO_3)]$ by $NaBH_4$	81
$[Au_{11}(PPh_3)_7(SCN)_3]$	Reduction of $[Au(PPh_3)Cl]$ by $NaBH_4$	44, 82
$[Au_{13}(PMe_2Ph)_{10}Cl_2]^{+}$	Reaction of $[Au_{11}(PMe_2Ph)_{10}]^{3+}$ with NEt_4Cl	83
$[Au_{39}(PPh_3)_{14}Cl_6]^{2+}$	Reduction of $HAuCl_4$ by $NaBH_4$ in presence of PPh_3	84
$[Au_{55}(PPh_3)_{12}Cl_6]$	Reduction of $[Au(PPh_3)Cl]$ by B_2H_6	85

These clusters are not only easy to prepare and isolate in good yield, but can often undergo facile rearrangements through reactions with other

reagents (see figure 3.1) or ligands, such as phosphines[71] and diphosphines.[66]

$$[Au_8(PPh_3)_8](NO_3)_2 \xrightarrow{[RhCl(C_8H_{14})_2]_2} [Au_8(PPh_3)_7](NO_3)_2$$

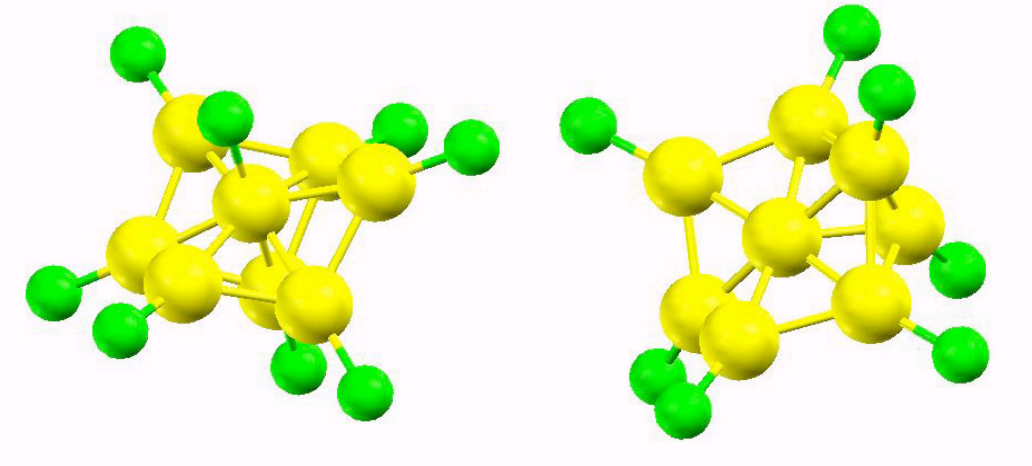

Figure 3.1. Shown here is an example of the gold cluster $[Au_8(PPh_3)_8](NO_3)_2$ reacting with the phosphine scavenging species $[RhCl(C_8H_{14})_2]_2$ to form $[Au_8(PPh_3)_7](NO_3)_2$. The crystal structures for the cationic cluster cores are shown below the reaction.

Geometric rearrangement has also been demonstrated through electrochemical reduction.[86] $[Au_9(PPh_3)_8]^{3+}$ can be reduced by a two step charge transfer at a platinum electrode to give $[Au_9(PPh_3)_8]^{+}$. Using single crystal x-ray diffraction, it was shown that the solid structure of the cluster had reordered significantly as a result of the reduction process. $[Au_9(PPh_3)_8]^{+}$ is illustrated in figure 3.2.

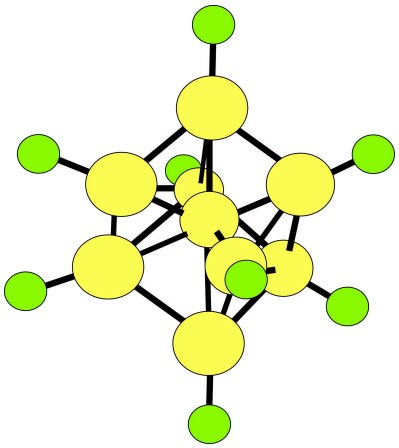

Figure 3.2. Diagram of $[Au_9(PPh_3)_8]^+$, obtained through the reduction of $[Au_9(PPh_3)_8]^{3+}$.[86]

Another unique feature of phosphine stabilised gold clusters is way that the size and geometry adopted by the cluster is highly dependent upon the ligands in the complex. By slight alteration of the phosphine group on the gold(I) precursor, a large change can be seen in the cluster core. For example, the reduction of $[Au(PPh_3)(NO_3)]$ by $NaBH_4$ gives the cluster compound, $[Au_9(PPh_3)_8](NO_3)_3$,[78] whereas under the same conditions $[Au(PCyPh_2)(NO_3)]$ yields $[Au_6(PCyPh_2)_6](NO_3)_2$[68] (figure 3.3).

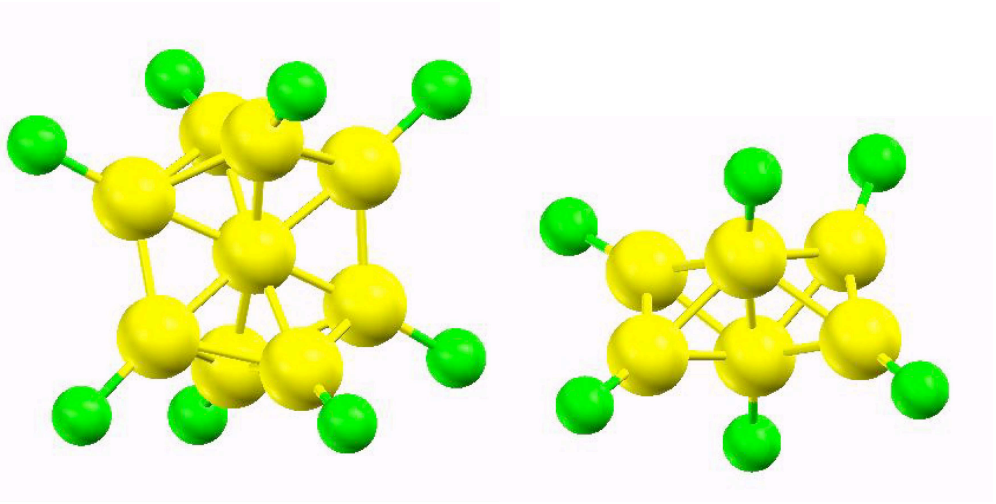

$[Au_9(PPh_3)_8](NO_3)$ $[Au_6(PCyPh_2)_6](NO_3)$

Figure 3.3. Shown above are the cluster cores of the clusters $[Au_9(PPh_3)_8](NO_3)_3$[78] and $[Au_6(PCyPh_2)_6](NO_3)_2$[87] with the carbon and hydrogen atoms omitted.

An important factor to consider when using phosphine ligand's is the ligands cone angle. The cone angle is a measure of the size of a ligand and was first used to describe ligands by Tolman in 1977.[88] It describes the angle formed on the metal by the substituents of the phosphine.

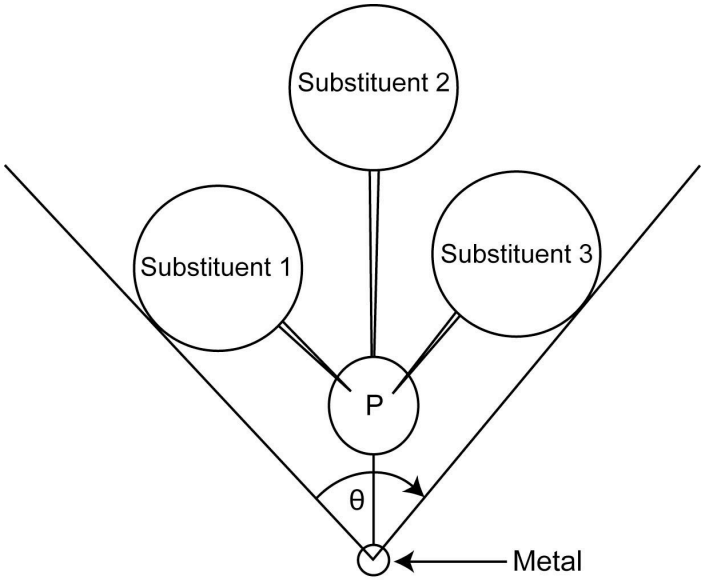

Figure 3.4. Diagram of how the Tolman cone angle is obtained.

Ligands with large cone angles are more sterically inhibiting. The affect of having more sterically inhibiting ligands present can be seen in table 3.2. It is generally observed that the size of the phosphine ligand has a direct bearing on the size of the cluster formed.

Table 3.2. A table to show how the number of gold atoms within the core of a cluster is affected by the size of the phosphine ligands stabilising them.

Stabilising Ligand	Ph_2PCy	$Ph_2P(o\text{-tolyl})$	PPh_3	$PhPMe_2$
Number of Au atoms in cluster core	6	6	9	13
Tolman Cone Angle	155^o	185^o	145^o	122^o
Reference	[68, 89]	[68]	[78, 79, 88]	[83, 88]

Table 3.2 illustrates how ligands of different sizes (and varying Tolman cone angles) yield clusters with varying numbers of gold atoms within the cluster core. This shows that by increasing the Tolman cone angle of the phosphine ligand, a significant change in the core of the cluster synthesised is observed. There is a strong correlation between the size of the cluster core and the steric demands of the ligands. From the table 3.2, it can be seen that the phosphine with the larger cone angle, $PCyPh_2$ (155^o), gives a smaller sized cluster core than if PPh_3 with a lower cone angle is used (145^o). If phosphines are replaced by smaller, less bulky ligands such as Cl^-, then the cluster can increase in nuclearity. This is observed in the synthesis of the cluster $[Au_{13}(PMe_2Ph)_{10}Cl_2]$[83] shown in figure 3.5.

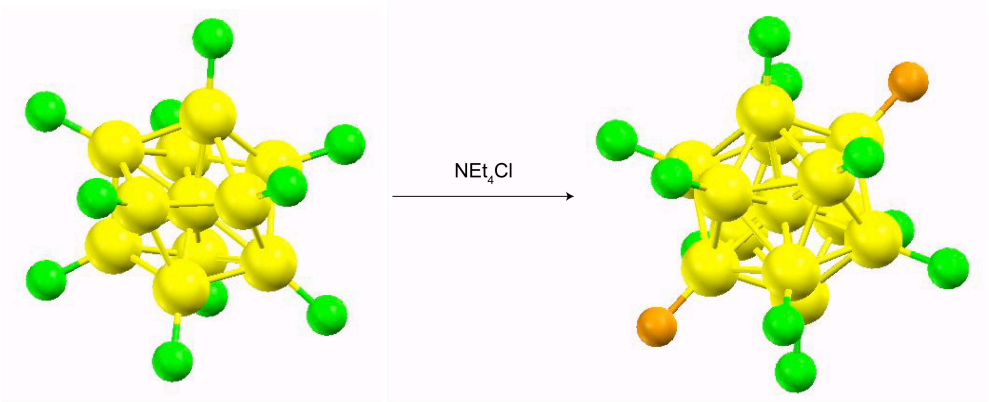

$$[Au_{11}(PMe_2Ph)_{10}]^{3+} \xrightarrow{NEt_4Cl} [Au_{13}(PMe_2Ph)_{10}Cl_2]^{3+}$$

Figure 3.5. The crystal structure of the core of $[Au_{13}(PMe_2Ph)_{10}Cl_2]$ and the reaction to synthesize it from $[Au_{11}(PMe_2Ph)_{10}]^{3+}$.[83]

Besides the phosphine ligand, the nature of the X group in the precursor $[AuPR_3X]$ also plays a role in the size and shape of the cluster obtained. If X is a strongly bonding ligand, such as a halide, then the cluster formed will tend to be of the type $[Au_{11}(PR_3)_7X_3]$[90] whereas if X is a poor ligand such as nitrate then the cluster formed will be of the type $[Au_9(PR_3)_8](NO_3)_3$[78]. Therefore the cluster will be larger to accommodate the strong bonding X anion; the larger the cluster, the more ligands are

able to bind directly to gold atoms. Weakly bound anions such as PF_6^- and BF_4^- can be exchanged through simple metathesis reactions (see figure 3.6).

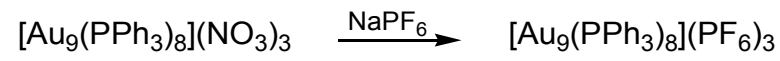

Figure 3.6. This is an example of a counterion exchange reaction in which the nitrate group on the cluster is replaced by a hexafluorophosphate group.[78]

The reducing agent also makes a huge difference to the geometry of the cluster formed. Even from the same gold-phosphine precursor, a number of different complexes can be obtained. The reduction of $[(PPh_3)AuCl]$ by $[Ti(\eta\text{-}C_5H_5Me)_2Cl_2]$ leads to the formation of $[Au_9(PPh_3)_8]^{+3}$ [91] whereas reduction of the same compound with B_2H_6 gives the largest gold phosphine cluster known, $[Au_{55}(PPh_3)_{12}Cl_6]$[85]. A lot of work has been carried out in characterising[92, 93] this cluster, as a single crystal structure cannot be obtained due to degradation and cluster agglomeration during crystallization. This cluster is of interest because of its properties as a small, monodisperse nanoparticle (with a gold core diameter of ~1.4 nm) and potential applications in catalysis,[13] supramolecular assemblies,[21] nanoelectronics,[94] and cytotoxicity.[95]

One of the most widely studied clusters is $[Au_9(PPh_3)_8](NO_3)_3$. This cluster was first reported in 1971[77] and has been studied extensively.[65, 69] Reasons for research being carried out on this specific cluster are the availability and low cost of PPh_3 along with the ease of cluster synthesis. Some examples the reactions that this cluster can undergo to form other clusters is shown in figure 3.7. This cluster has also been explored in catalytic reactions, which will be discussed in Chapter 4.

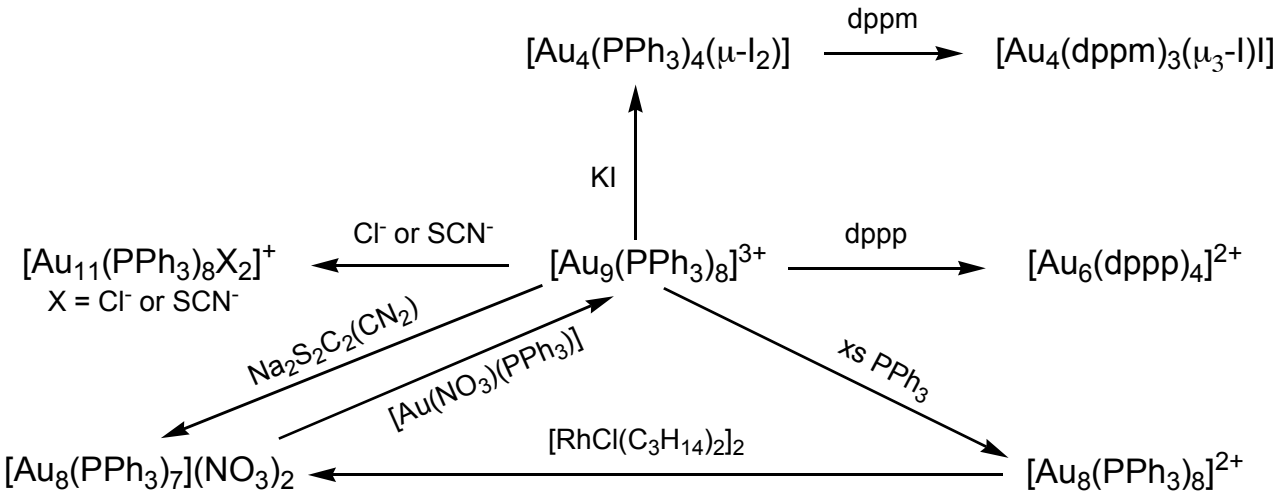

Figure 3.7.Reaction scheme to show some of the clusters accessible from $[Au_9(PPh_3)_8]^{3+}$.

Phosphine stabilised gold clusters are usually cationic or neutral, depending on whether strong or weak bonding anions are present. The oxidation state of the gold present in the cluster is between 0 and +1. Research has looked at the charges on specific gold atoms in certain clusters.[96] In these calculations, it was observed that in the cluster type $[Au_{11}(PPh_3)_7X_3]$, the negatively charged ligands bond to the more positively charged gold atoms. The charges calculated for this cluster where X= I is shown in figure 3.8.

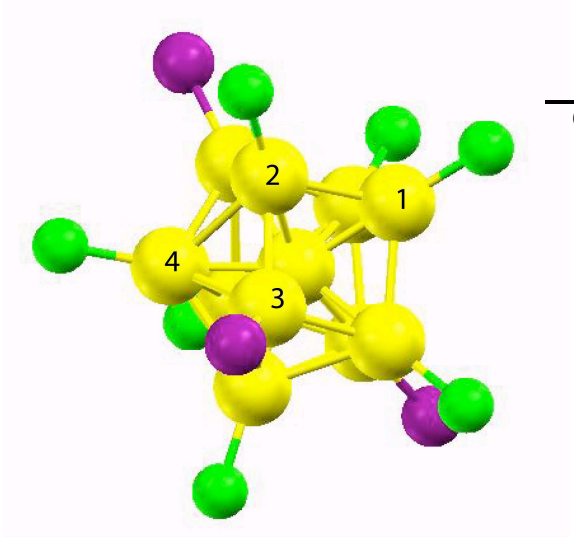

	Calculated charge (Huckel)
Central	0.53
1	0.04
2	0.21
3	0.32
4	0.27

Figure 3.8. The structure of the core of $[Au_{11}(PPh_3)_7I_3]$ with the corresponding charges on the numbered gold atoms.[96]

3.1.2. Bonding in clusters

The main form of bonding occurring within gold clusters is the overlap of the 6s orbitals and is of a multicentre nature. Therefore, for the clusters to be at their most stable, bonding is multidirectional, leading to the shapes of clusters of low nuclearity being condensed deltahedral polyhedra. Molecular orbital analysis of $[Au_x(PH_3)_x]$ clusters has shown that cluster metal-metal bonding is maximised for polyhedra with triangular faces as such geometries generate the largest number of next neighbour interactions between the $Au(PH_3)$ fragments.[97]

In higher nuclearity clusters, such as $[Au_{13}(PMe_2Ph)_{10}Cl_2]$, and $[Au_9(PPh_3)_8]^{3+}$, a gold atom is usually present at the centre of the cluster core. This is important in providing stability within the cluster as it forms radial bonds to all the peripheral gold atoms. It has been observed that the central gold atom-peripheral gold atom bonds are some 0.1-0.2 Å[79, 83] shorter than those between the peripheral gold atoms and subsequently the central gold atom bonds more strongly to the surrounding gold atoms than peripheral gold atoms bond to each other.

Mingos stated that gold-centred higher nuclearity cluster could be divided into two categories; i) those with a closed (almost spherical) structure and ii) those with a more open toroidal (doughnut shaped) structure.[98-100] These structures were associated with small electronic differences. Those with a spherical structure generally obey the rule of 12n+18 electrons whereas the toroidal structures had 12n+16 electrons (n= the number of peripheral gold atoms). This small difference in electron counts agrees with the aforementioned work on the electrochemical reduction of $[Au_9(PPh_3)_8]^{3+}$; i.e. that a toroidal cluster may be reduced to a spherical cluster. From this it can be seen that gold clusters do not obey the rules

of Polyhedral Skeletal Electron Pair theory set out by Wade and Mingos,[101] unlike metal carbonyl clusters.

Molecular orbital calculations have shown that there is very little d-d orbital overlap in non-centred gold clusters due to the contraction of the orbitals[96] which can be attributed to relativistic effects.[19] For example, in an octahedral structure there is some $6p_\sigma$-$6p_\sigma$ overlap but very little 6s-6s and $6p_\pi$-$6p_\pi$ overlap, which is more effective in lighter elements. Theoretical calculations found that a 'naked' cluster of 6 gold atoms in an octahedral arrangement would be very weakly bound as only 1 electron pair would be present in a strongly bonding orbital; the remaining electrons would occupy non-bonding and mildly antibonding orbitals (d-band). It was found that the presence of phosphine ligands greatly stabilised the cluster as they promote gold-gold bonding. This is done as the phosphines bonds to the golds 6s, 6p and 5d orbitals, which encourages orbital hybridization of the gold. These hybridized orbitals overlap better with each other. Also, the extra pairs of electrons coming from the phosphines allow filling of gold-gold and gold-phosphine bonding orbitals. The s-d_z^2 hybrid orbitals are particularly important in these bonding modes and allow strong radial bonding to occur. Later, it was found that both the naked cluster $[Au_6]^{2+}$ and the ligand stabilised cluster $[Au_6(PR_3)_6]^{2+}$ (R=H, Me) could be stabilised further by the presence of an interstitial atom[102] such as carbon[23] or nitrogen[103] through favourable overlap of the s and p valence orbitals of the interstitial element and the inward pointing gold hybrid orbitals. The electrons from the interstitial atom contribute to a very stable closed electron configuration.

It was also predicted that the presence of a central gold atom in a naked $[Au_9]^{3+}$ cluster allows the formation of a bonding molecular orbital below the level of the d-band. This orbital is primarily 6s in character for the central gold atom and a hybrid of 6s and 5d for the peripheral atoms. The core gold atom therefore stabilises the cluster. The presence of phosphine ligands in $[Au_9(PPh_3)_8]^{3+}$ stabilises the molecule further.

Mingos[99, 100] concluded that the geometries of gold clusters was extremely flexible and can easily undergo skeletal rearrangements through a number of different processes (such as electrochemical reduction, reaction with another ligand or gold-phosphine fragment). This was said to be an important factor to consider when depositing clusters and gold crystallites onto support materials, as they would not necessarily maintain their arrangement.

A more recent theory that has been proposed to explain the bonding in ligand- stabilised clusters is the consideration of the clusters as superatoms.[104] This theory suggests that spherical clusters behave as single atoms with spherical shells of electrons encompassing all of the atoms with the cluster, rather than combinations of each atom's electron shells.

3.1.3. Non-phosphine stabilised gold clusters

There are many example of gold clusters stabilised by ligands other than phosphines. A cluster molecule worth noting is the recently described neutral arsine stabilised cluster $[Au_{16}(AsPh_3)_8Cl_6]$[105] (figure 3.9). This is synthesised through the same method of many of the the phosphine stabilised clusters, by means of the reduction of $[Au(AsPh_3)Cl]$ by $NaBH_4$. This cluster is of interest because it has a centred icosahedral structure very similar to $[Au_{13}(PMe_2Ph)_{10}Cl_2]$[83] but with a tetrahedral pendant bound by one corner to the gold core surface fitting with the structures defined by Mingos.[99] The As-Au bond are longer and weaker than P-Au bonds meaning that it may be easier to remove the arsine ligands to form metallic particles.

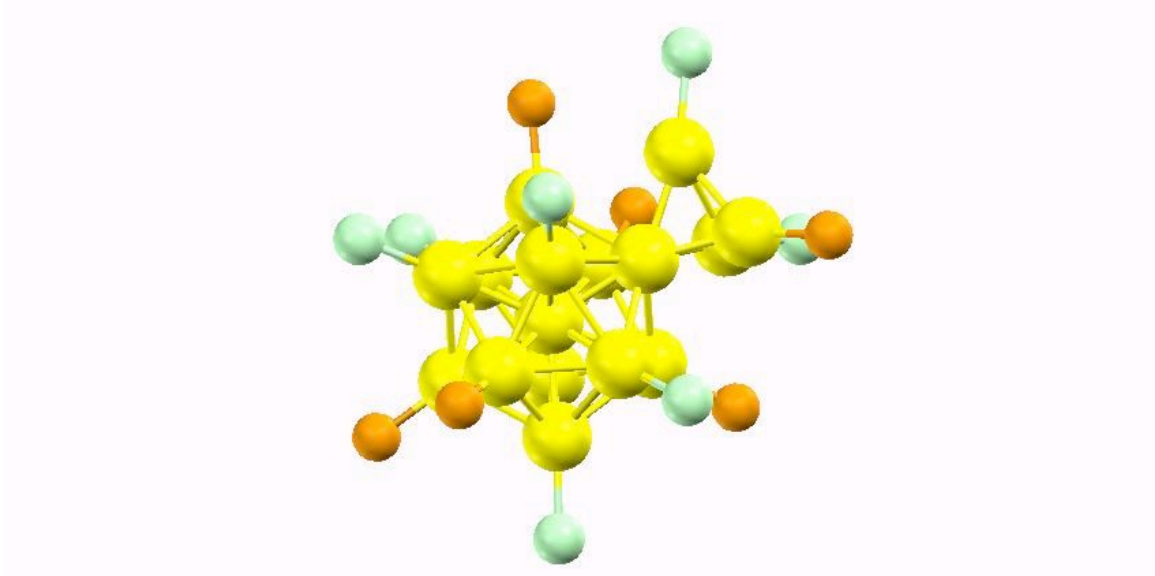

Figure 3.9 X-ray structure of the gold core $[Au_{16}(AsPh_3)_8Cl_6]$ consisting of a centred icosahedron with a tetrahedral pendant.[105]

Research has also been carried out on clusters stabilised by other ligands, particularly thiolates. The largest gold cluster structure known is that of $[Au_{102}(p\text{-mba})_{44}]$ (*p*-mba = *para*-mercapto benzoic acid)[106] and was synthesised by the reduction of $[HAuCl_4]$ with $NaBH_4$ in the presence of *p*-mba at pH 2.5. The surface coverage of the thiol ligands is realtively large at 70% of the 23 surface gold atoms. The thiol monolayer is not only stabilised by bonds with the gold surface, but also by interactions between the *p*-mba ligands. At centre of the 79 atom core, the gold is arranged in an fcc arrangement also found in metallic gold.

This cluster was discovered whilst researching thiol-stabilised nanoparticles, which are similar to clusters only larger and generally less uniform in size and geometry. The cluster $[Au_{102}(p\text{-mba})_{44}]$ is of great importance because it was the first reported monoatomically disperse nanoparticle. This is a huge area of research[107, 108] due to gold nanoparticles' unique optical,[109] electrochemical[110] and photophysical[111] properties. Thiol-stabilised gold nanoparticles are usually prepared through the reduction of AuSR species by $NaBH_4$ but usually give a range of particle sizes.[112] Control over the average core size can be exhibited by monitoring the ratio of Au:SR.[113] The size of the particles formed is

highly sensitive to the reactions conditions during their synthesis. The length of the SR ligands is another major factor controlling the particle size.[114]

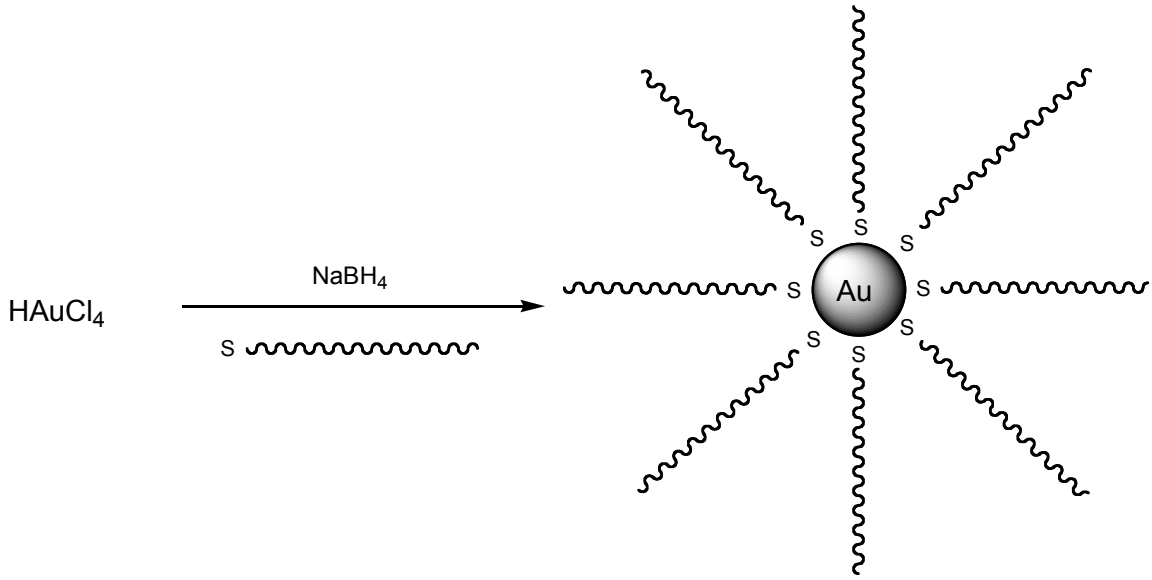

Figure 3.10 Example reaction for the synthesis of gold nanoparticles

3.1.4. Cluster Characterisation Techniques

A wide range of techniques have been employed to characterise these clusters. When crystal structures are not available, techniques such as EXAFS, IR and ^{31}PNMR can be used to gain more information about the possible geometries of the clusters. These techniques and their uses in cluster chemistry are discussed in Chapter 2. Other techniques that have been used include XPS[115] and MössBauer spectroscopy.[69]

3.1.5. Current Work

A range of phosphines were synthesised that differed by only a small amount in size. The phosphines used are shown in figure 3.11. These phosphines were employed to synthesise linear mononuclear gold

complexes, which could in turn be used for the generation of clusters. As all the reactions were carried out under the same conditions, it is possible to directly associate the clusters formed with the phosphine ligands used in making them.

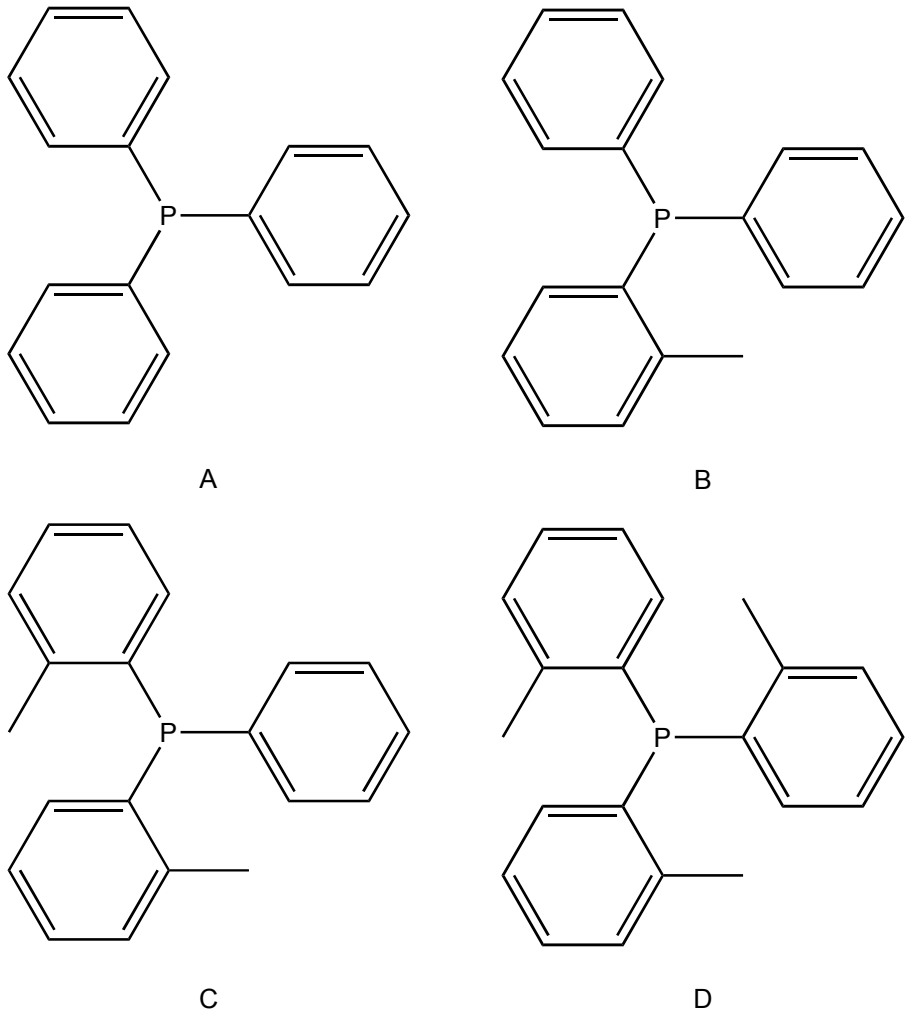

Figure 3.11. Diagrams of the phosphines used to synthesise the range gold clusters; A= triphenylphosphine, B= diphenyl *o*-tolyl phosphine, C= phenyl di-*o*-tolyl phosphine, D= tri-*o*-tolyl phosphine.

3.2. Experimental

3.2.1. Synthesis of PPh_3AuCl[116]

Figure 3.12. Synthesis of PPh_3AuCl.

To a stirred solution of PPh_3 (1.39 g, 5.29 mmol) dissolved in ethanol (~25 ml), a solution of $HAuCl_4 \cdot 3H_2O$ (1.04 g, 2.64 mmol) dissolved in ethanol (~5 ml) was added. The mixture of the two clear solutions immediately turned cloudy white. The reaction mixture was allowed to stir for 10 minutes to allow to as more conversion to the desired product. The white precipitate was then filtered off under vacuum and washed with a little ethanol. The product was isolated as a fine white crystalline powder. 95% yield (1.24 g).

Spectroscopic data:

^{1}H NMR δ: 7.55-7.44 (m, 15H, 3xPh on PPh_3). ^{31}P NMR δ: 33.6 (s, 1P, PPh_3).

3.2.2. Alternative synthesis of PPh_3AuCl with 2,2'-dithioethanol

$HAuCl_4 \cdot 3H_2O$ (1.00 g, 2.54 mmol) was dissolved in a small amount of distilled water (12 ml) to give a clear yellow solution. Drop-wise, 2,2'-thiodiethanol (0.94 g, 7.6 mmol) was added to the stirring solution. As it was added, the solution formed a cloudy white precipitate that would redissolve on stirring. After the addition of the 2,2'-thiodiethanol, a clear and colourless solution was formed. To this, a solution of PPh_3 (0.67 g, 2.54 mmol) dissolved in ethanol (35 ml) was added and allowed to stir.

White PPh_3AuCl precipitated out of the solution ,which was then filtered off, washed with ethanol and dried under vacuum. 98% yield (1.23 g).

3.2.3. Synthesis of $PPh_3Au(NO_3)$[44]

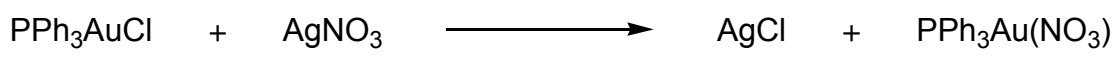

Figure 3.13. Synthesis of $PPh_3Au(NO_3)$.

$AgNO_3$ (1.06 g, 6.26 mmol) was dissolved in ethanol (~30 ml) heated with hot water. This was added to a stirring solution of dichloromethane (~8 ml) containing PPh_3AuCl (1.24 g, 2.50 mmol). This was followed by the immediate precipitation of white AgCl. The precipitate was filtered off under gravity and the solution was evaporated to dryness under vacuum to form an off-white solid. In order to remove and remaining AgCl, the solid was redissolved in dichloromethane (~15 ml) and filtered. A dry white solid was obtained through the removal of dichloromethane under reduced pressure.If the solid collected was still grey in colour, it was redissolved in dichloromethane and filtered again before removing the solvent. 77% yield (1.08 g).

Spectroscopic data:

^1H NMR δ: 7.49-7.56 (m, 15H, 3xPh on PPh_3). ^{31}P NMR δ: 27.7 (s, 1P, PPh_3).

3.2.4. Synthesis of $[Au_9(PPh_3)_8](NO_3)_3$[78]

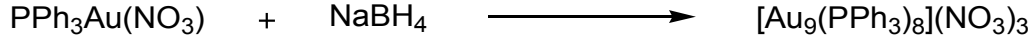

Figure 3.14. Synthesis of $[Au_9(PPh_3)_8](NO_3)_3$.

To a stirring slurry of $PPh_3Au(NO_3)$ (0.87 g, 1.66 mmol) in ethanol (~20 ml), an ethanolic solution (~30 ml) of $NaBH_4$ (0.016 g, 0.42 mmol) was

added. The solution immediately turned dark red/brown and was allowed to stir until the initial white was no longer visible. The solution was then evaporated under vacuum to give a brown solid. This solid was dissolved in a small amount of tetrahydrofuran (~10 ml) to form a dark brown/ red solution. Hexane (~2 ml) was added to this solution to precipitate out a dark green/brown solid. This solid was filtered off and washed with hexane under vacuum. The solid was then dried under vacuum and isolated as a dry dark green/brown solid. 66% yield (0.50 g).

Spectroscopic data:

^{1}H NMR δ: 7.23-6.70 (m, 120H, 8xPPh_3). ^{31}P NMR δ: 57.3 (s, 8P, PPh_3).

3.2.5. Synthesis of $[Au_9(PPh_3)_8](PF_6)_3$[78]

$$[Au_9(PPh_3)_8](NO_3)_3 \quad + \quad \text{xs } NaPF_6 \longrightarrow [Au_9(PPh_3)_8](PF_6)_3$$

Figure 3.15. Synthesis of $[Au_9(PPh_3)_8](PF_6)_3$.

$[Au_9(PPh_3)_8](NO_3)_3$ (0.21 g, 5.18 mmol) was dissolved in ethanol (~10 ml) and mixed with a solution of $NaPF_6$ (0.02 g, 0.145 mmol) dissolved in ethanol (~10 ml). The dark reaction mixture became a cloudy dark solution. This solution was filtered under vacuum yielding a black precipitate. The filtrate was red/orange in colour. Attempts were made to recrystallise the precipitate from dichloromethane and ethanol. 92% yield (0.20 g).

Spectroscopic data:

^{1}H NMR δ: 7.23-6.70 (m, 120H, 8xPPh_3). ^{31}P NMR δ: -143 (sept, P, PF_6^-), 57.3 (s, 8P, PPh_3).

IR DATA: $\nu(PF_6^-)$ 838 cm^{-1} (medium and broad).

3.2.6. Synthesis of Ph_2P(*o*-tolyl)

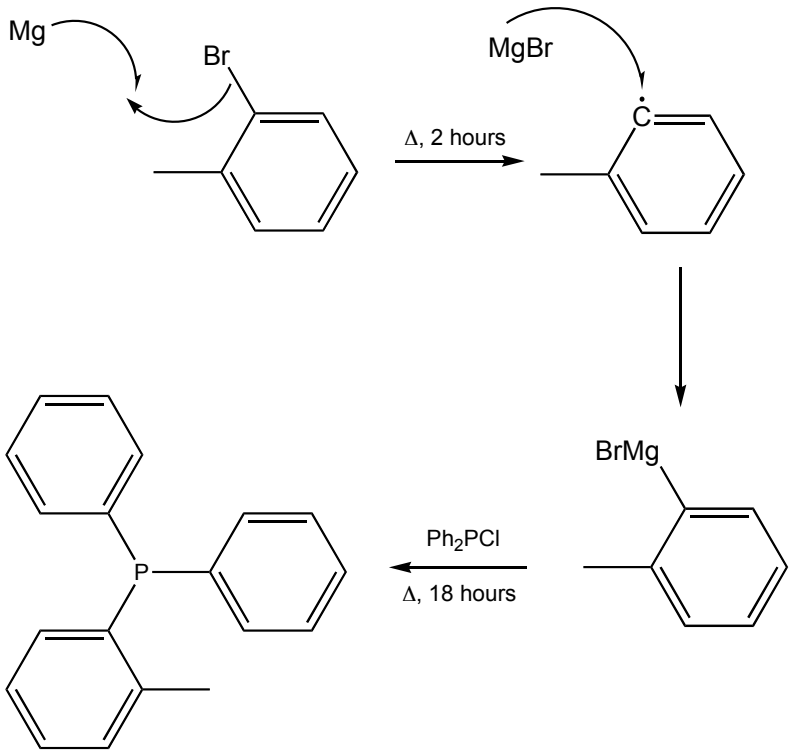

Figure 3.16. Synthesis of Ph_2P(*o*-tolyl).

Under a nitrogen atmosphere, a small amount of 2-bromotoluene (1 ml) was added to a stirring slurry of magnesium turnings (3.14 g, 128.00 mmol) in dry tetrahydrofuran (~40 ml), along with a crystal of iodine. The mixture was refluxed until it turned black. The remaining 2-bromotoluene (28.44 ml, 117.00 mmol) was then added drop-wise as a solution in tetrahydrofuran. The reaction mixture was then left to reflux for 2 hours under nitrogen. After cooling in an ice bath, a solution of Ph_2PCl (21.72 g, 98.00 mmol) in tetrahydrofuran (~30 ml) was added drop-wise. Once the addition was complete, the mixture was refluxed under nitrogen overnight, turning very dark red. The reaction mixture was then transferred to a separating funnel and extracted with ether (3x80 ml). The clear pink organic layer was then isolated and dried over anhydrous $MgSO_4$. The ether solution was filtered and evaporated under vacuum leaving an orange oil. Some petrol (~ 10 ml) was used to triturate the oil

before placing the mixture in a freezer for 2-3 hours. After this time small spheres of a white solid formed. This precipitate was isolated through filtration and the remaining solution was placed in the freezer to obtain more of the product. 34% yield (9.27 g).

Spectroscopic data:

^{1}H NMR δ: 2.41 (s, 3H, CH_3), 6.60 (m, 1H, aromatic H), 7.10 (t, 1H, aromatic H), 7.28 (m, 12H, aromatic H). ^{31}P NMR δ: -12.9 (s, 1P, of Ph_2P(*o*-tolyl)).

3.2.7. Synthesis of Ph_2P(*o*-tolyl)AuCl

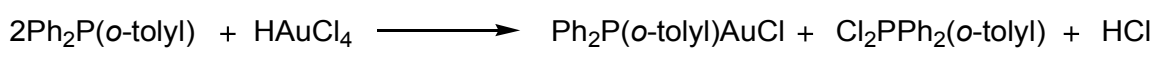

Figure 3.17. Synthesis of Ph_2P(*o*-tolyl)AuCl.

To a stirring solution of $HAuCl_4 \cdot 3H_2O$ (0.50 g, 1.27 mmol) in ethanol (~10 ml), a solution of Ph_2P(o-tolyl) (0.70 g, 2.55 mol) dissolved in ethanol (~20 ml) was added. After 10 minutes of stirring, the solution had turned cloudy yellow. The mixture was left to stir for a further 20 minutes before filtering off the white precipitate under vacuum. The precipitate was then washed with ethanol and dried in air yielding a fine white crystalline powder. 52% yield (0.34 g).

Spectroscopic data:

^{1}H NMR δ: 2.53 (s, 3H, CH_3), 6.73 (m, 1H, aromatic H), 7.17 (t, 1H, aromatic H), 7.26 (t, 11H, aromatic H), 7.53 (m, 12H, aromatic H's). ^{31}P NMR δ: 26.8 (s, 1P, of Ph_2P(*o*-tolyl)).

3.2.8. Synthesis of Ph_2P(*o*-tolyl)AuCl with 2,2'-dithioethanol

$HAuCl_4 \cdot 3H_2O$ (0.78 g, 1.98 mmol) was dissolved in a small amount of distilled water (12 ml) to give a clear yellow solution. Drop-wise, 2,2'-thiodiethanol (0.72 g, 5.89 mmol) was added to the stirring solution. As it was added, the solution formed a cloudy white precipitate that would redissolve on stirring. After the addition of the 2,2'-thiodiethanol, a clear and colourless solution was formed. To this, a solution of Ph_2P(*o*-tolyl) (0.55 g, 1.98 mmol) dissolved in ethanol (20 ml) was added and allowed to stir. White PPh_3AuCl precipitated out of the solution which was then filtered off, washed with ethanol and dried under vacuum. 96% yield (0.97 g).

3.2.9. Synthesis of Ph_2P(*o*-tolyl)Au(NO_3)

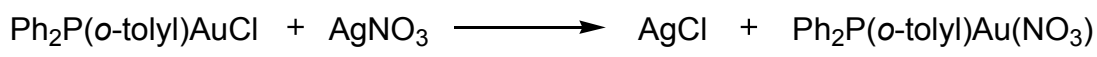

Figure 3.18. Synthesis of Ph_2P(*o*-tolyl)Au(NO_3).

Ph_2P(*o*-tolyl)AuCl (0.30 g, 58.90 mmol) was dissolved in dichloromethane (~10 ml) and added to a solution of $AgNO_3$ (0.25 g, 1.47 mmol) in ethanol (~20 ml). Upon addition of the gold complex, AgCl precipitated. This was filtered off and the solution was pumped down to give an off-white solid. This solid was redissolved in dichloromethane. The solution formed was then filtered to remove any remaining AgCl. The filtered solution yielded a dry white solid after removing the solvent on a rotary evaporator. 68% yield (0.22 g).

Spectroscopic data

^1H NMR δ: 2.53 (s, 3H, CH_3), 6.75 (q, 1H, aromatic H), 7.20 (t, 1H, aromatic H), 7.34 (t, 11H, aromatic H), 7.52 (m, 11H, aromatic H's). ^{31}P NMR δ: 19.9 (s, 1P, of Ph_2P(o-tolyl)).

3.2.10. Synthesis of $[Au_6(Ph_2P(o\text{-tolyl}))_6](NO_3)_2$

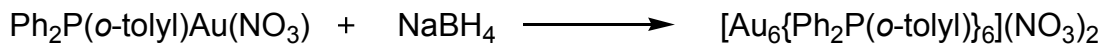

Figure 3.19. Synthesis of $[Au_6(Ph_2P(o\text{-tolyl}))_6](NO_3)_2$.

$Ph_2P(o\text{-tolyl})AuNO_3$ (0.20 g, 0.38 mmol) was placed in ethanol (~20 ml) to form a slurry to which a solution of $NaBH_4$ (0.0036 g, 0.096 mmol) dissolved in ethanol (~30 ml) was added. The mixture turned dark green/yellow at first but soon turned dark brown/red. After stirring for 20 minutes, no more of the white starting material remained. The solution yielded a dry dark brown solid after removing the solvent on a rotary evaporator. The solid was dissolved in tetrahydrofuran (~ 2 ml) and hexane (~10 ml) was added to this solution, causing a dark precipitate to form. The precipitate was filtered off under vacuum and washed with hexane. After drying the solid under vacuum, a dark brown powder was obtained. 69 % yield (0.13 g).

Spectroscopic data:

^{1}H NMR δ: 2.56 (s, 18H, CH_3), 6.75 (q, 6H, aromatic H), 7.20 (m, 6H, aromatic H), 7.30 (m, 6H, aromatic H), 7.57 (m, 66H, aromatic H's). ^{31}P NMR δ: 38.4 (s, 1P, of Ph_2P(o-tolyl)).

Elemental analysis: C 40.18% (46.20%), H 3.11% (3.47%), N 2.18% (0.95%), P 4.99% (6.27%).

3.2.11. Synthesis of $[Au_6(Ph_2P(o\text{-tolyl}))_6](PF_6)_2$

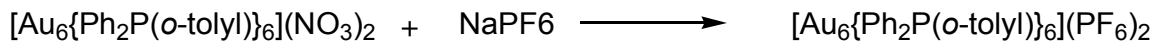

Figure 3.20. Synthesis of $[Au_6(Ph_2P(o\text{-tolyl}))_6](PF_6)_2$.

$[Au_6(Ph_2P(o\text{-tolyl}))_6](NO_3)_3$ (0.10 g, 0.33 mmol) was dissolved in ethanol (~10 ml) and added to a solution of $NaPF_6$ (12.00 mg, 0.0.38 mmol) in

ethanol (~10 ml). The solution turned from very dark red to cloudy brown/green in colour after the addition. This was allowed to stir for 15 minutes before filtering off the precipitate, and drying it under vacuum. This yielded a green powder that we attempted to recrystallise from dichloromethane and ethanol. 5% yield (0.53 g).

Spectroscopic data:

^{1}H NMR δ: 2.56 (s, 18H, CH_3), 6.75 (q, 6H, aromatic H), 7.20 (m, 6H, aromatic H), 7.30 (m, 6H, aromatic H), 7.57 (m, 66H, aromatic H's). ^{31}P NMR δ: -143 (sept, P, PF_6^-), 38.4 (s, 1P, of Ph_2P(*o*-tolyl)).

IR DATA: $\nu(PF_6^-)$ 836 cm^{-1} (medium and broad).
Crystal Structure: See Appendix 1.

3.2.12. Synthesis of (PhP(*o*-tolyl)$_2$)AuCl

Figure 3.21. Synthesis of (PhP(*o*-tolyl)$_2$)AuCl.

Previously synthesised PhP(*o*-tolyl)$_2$ (0.78 g, 2.54 mmol) was dissolved in ethanol (~30 ml). This required some heating with hot water. A clear yellow solution of $HAuCl_4 \cdot 3H_2O$ (0.50 g, 1.27 mmol) in ethanol (~10 ml) was added to this. Upon addition, the solution turned from clear to pale yellow. The reaction mixture was cooled in a cold-water bath at which time fine crystals began to appear in the solution. After a few minutes, the ethanol solution had turned cloudy with the precipitating solid. The reaction mixture was allowed to stir for a further 15 minutes before filtering off and washing the white solid under vacuum. The solid was dried in air to form a fine white crystalline powder. The remaining solution was concentrated on a rotary evaporator and placed in a fridge overnight yielding more solid. 62% yield (0.41 g).

Spectroscopic data:

^{1}H NMR δ: 2.66 (s, 3H, 2xCH_3), 6.7-7.1 (q, 2H, aromatic H's), 7.19 (t, 2H, aromatic H's), 7.35 (t, 2H, aromatic H's), 7.43-7.58 (m, 7H, aromatic H's).

^{31}P NMR δ: 17.4 (s, 1P, (*o*-tolyl)$_2$PPh).

3.2.13. Synthesis of (PhP(*o*-tolyl)$_2$)Au(NO_3)

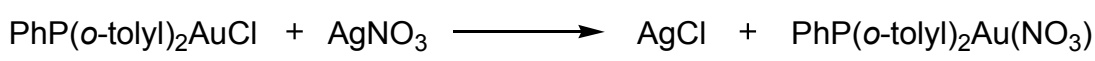

Figure 3.22. Synthesis of (PhP(*o*-tolyl)$_2$)Au(NO_3).

To a solution of $AgNO_3$ (0.31g, 1.88 mmol) dissolved in ethanol (~30 ml), (PhP(*o*-tolyl)$_2$)AuCl (0.39 g, 0.75 mmol) dissolved in dichloromethane (~20 ml) was added. The mixture turned cloudy and after stirring for 5 minutes, the white AgCl precipitate was filtered off. The remaining solution was then pumped down to give an off-white solid. This solid was then dissolved in a little dichloromethane and filtered to remove any remaining AgCl. The dichloromethane was then removed from the solution using a rotary evaporator yielding a dry off-white powder. 72% yield (0.28 g).

Spectroscopic data:

^{1}H NMR δ: 2.67 (s, 6H, 2xCH_3), 6.83 (q, 2H, aromatic H's), 7.21 (t, 2H, aromatic H's), 7.38 (t, 2H, aromatic H's), 7.38-7.72 (m, 7H, aromatic H's).
^{31}P NMR δ: 8.9 (s, 3P(*o*-tolyl)$_2$PPh).

3.2.14. Synthesis of [Au_4(PhP(*o*-tolyl)$_2$)$_4$](NO_3)$_2$

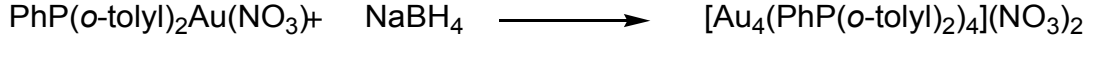

Figure 3.23. Synthesis of [Au_4(PhP(*o*-tolyl)$_2$)$_4$](NO_3)$_2$.

To a suspension of stirring (PhP(*o*-tolyl)$_2$)AuNO$_3$ (0.27 g, 0.49 mmol) in ethanol (~15 ml), solution of NaBH$_4$ (0.0051 g, 0.12 mmol) dissolved in ethanol (~20 ml) was added. This caused the solution to turn from cloudy white to dark brown/red. The reaction mixture was then stirred until no more white solid remained. The red/brown solution was pumped down to a dry solid on a rotary evaporator before dissolving the solid in tetrahydrofuran (~10 ml). When hexane (~8 ml) was added to the tetrahydrofuran solution, a dark brown solid precipitated out. The solid was filtered off under vacuum and washed with hexane. 43% yield (0.11 g).

Spectroscopic data:

^{1}H NMR δ: 2.54 (s, 6H, 2xCH$_3$), 6.88 (q, 2H, aromatic H's), 7.29 (t, 2H, aromatic H's), 7.46 (q, 2H, aromatic H's), 7.58 (m, 6H, aromatic H's) 7.67 (t, 1H, aromatic H). ^{31}P NMR δ: 30.3 (s, 3P(o-tolyl)$_2$PPh).

Elemental analysis: C 30.20% (46.32%), H 2.50% (3.70%), N 5.12% (1.35%), P 3.84% (5.98%).

3.2.15. Synthesis of [Au$_4$(PhP(*o*-tolyl)$_2$)$_4$](PF$_6$)$_2$

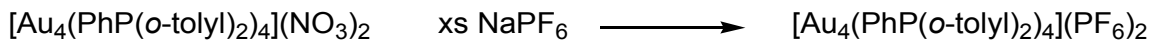

Figure 3.24. Synthesis of [Au$_4$(PhP(*o*-tolyl)$_2$)$_4$](PF$_6$)$_3$.

Clusters formed from (PhP(*o*-tolyl)$_2$)AuNO$_3$ (99.00 mg, 47.7 x10^{-3} mmol) were dissolved in ethanol (~10 ml) and added to a solution of NaPF$_6$ (0.011 g, 6.8x10^{-5} mol) in ethanol (~10 ml). This caused the precipitation of a green solid in the solution. This was filtered off and dried under vacuum. Recrystallisation was attempted on the green solid using dichloromethane and ethanol. 64% yield (0.068 g).

^{1}H NMR δ: 2.54 (s, 6H, 2xCH$_3$), 6.88 (q, 2H, aromatic H's), 7.29 (t, 2H, aromatic H's), 7.46 (q, 2H, aromatic H's), 7.58 (m, 6H, aromatic H's) 7.67

(t, 1H, aromatic H). ^{31}P NMR δ: -143 (sept, P, PF_6^-), 30.3 (s, 3P(o-tolyl)$_2$PPh)

IR DATA: $\nu(PF_6^-)$ 840 cm^{-1} (medium and broad).

3.2.16. Synthesis of P(*o*-tolyl)$_3$

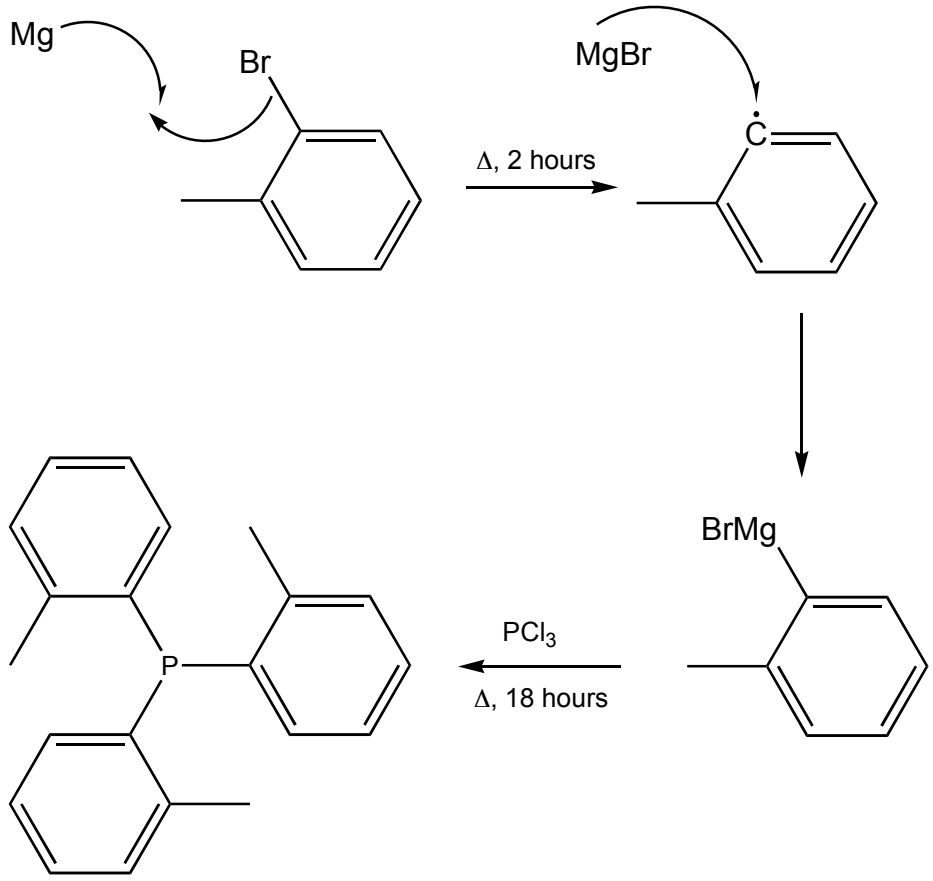

Figure 3.25. Synthesis of P(*o*-tolyl)$_3$.

To a slurry of magnesium turnings (3.11 g, 0.13 mol) in dry tetrahydrofuran under a nitrogen atmosphere, a small amount of 2-bromotoluene (1 ml) was added along with one crystal of iodine. The reaction mixture was heated up until initiation occurred. The rest of the 2-bromotoluene (28.456 ml intotal, 0.12 mmol) was then added drop-wise as a solution in tetrahydrofuran. The reaction mixture was allowed to

reflux for 2 hours forming a very dark solution. The reaction mixture was then cooled to 0°C in an ice bath and a solution of PCl_3 (3.248 ml, 0.36 mol) in tetrahydrofuran was added drop-wise. Upon addition of the PCl_3 solution, a white mist formed within the reactor vessel. Once all of the PCl_3 had been added, the reaction mixture was allowed to reflux under nitrogen for 18 hours after which time it turned very dark green/black in colour. Aluminium chloride (1.17 g, 19.00 mmol) dissolved in water (~ 25 ml) was added to the solution at room temperature. A white solid formed as the aqueous solution was added but it soon redissolved back into solution. The resulting solution was then extracted with ether. The organic layer was then dried over anhydrous $MgSO_4$, filtered and then concentrated on a rotary evaporator. The resulting oil was then cooled in an ice bath forming a white solid. This was filtered off under vacuum and washed with hexane leaving a bright white product. 61% yield (6.84 g).

Selected Spectroscopic data:

^{1}H NMR δ: 2.39 (s, 9H, 3xCH_3), 6.72 (m, 3H, aromatic H's), 7.07 (m, 3H, aromatic H's), 7.24 (m, 6H, aromatic H's). ^{31}P NMR δ: -29.2 (s, 1P, (*o*-tolyl)$_3$P).

3.2.17. Synthesis of P(*o*-tolyl)$_3$AuCl

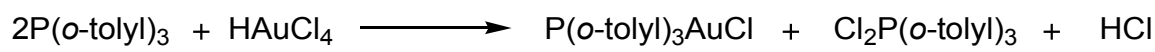

Figure 3.26. Synthesis of P(*o*-tolyl)$_3$AuCl.

To a solution of $HAuCl_4 \cdot 3H_2O$ (0.50 g, 1.27 mmol) in ethanol (~10 ml), a solution of P(*o*-tolyl)$_3$ (0.77 g, 2.54 mmol) in ethanol (~20 ml) was added. As the reaction mixture was stirred, it turned cloudy white/yellow. After 15 minutes of stirring, the white precipitate was filtered off under vacuum and washed with a little ethanol to obtain a dry white crystalline solid. The remaining ethanol solution was concentrated on a rotary evaporator and

placed in a fridge overnight to obtain more of the precipitate. 91% yield (0.62 g).

Spectroscopic data:

^{1}H NMR δ: 2.68 (s, 9H, 3xCH_3), 6.92 (q, 3H, aromatic H's), 7.18 (t, 3H, aromatic H's), 7.36 (t, 3H, aromatic H's), 7.67 (t, 3H, aromatic H's). ^{31}P NMR δ: 8.6 (s, 1P, P(*o*-tolyl)$_3$).

3.2.18. Synthesis of P(*o*-tolyl)$_3$Au(NO$_3$)

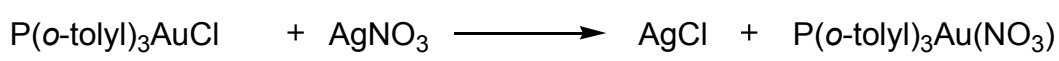

Figure 3.27. Synthesis of P(*o*-tolyl)$_3$Au(NO$_3$).

P(*o*-tolyl)$_3$AuCl (0.55 g, 1.06 mmol) was dissolved in dichloromethane (~10 ml) and this solution was added to a solution of $AgNO_3$ (0.77 g, 4.57 mmol) in ethanol (~20 ml). AgCl immediately precipitated out of the reaction solution. This was filtered off and the solution was evaporated to dryness on a rotary evaporator. The remaining solid was then dissolved in a little dichloromethane (~15 ml) and filtered to remove any remaining AgCl. The dichloromethane was then removed from the solution under vacuum yielding a dry white solid. 79% yield (0.47 g).

Spectroscopic data:

^{1}H NMR δ: 2.70 (s, 9H, 3xCH_3), 6.92 (q, 3H, aromatic H's), 7.22 (t, 3H, aromatic H's), 7.34 (t, 3H, aromatic H's), 7.50 (t, 3H, aromatic H's). ^{31}P NMR δ: -1.7 (s, 1P, P(*o*-tolyl)$_3$).

3.2.19. Synthesis of [Au$_4$(P(*o*-tolyl)$_3$)$_4$](NO$_3$)$_2$

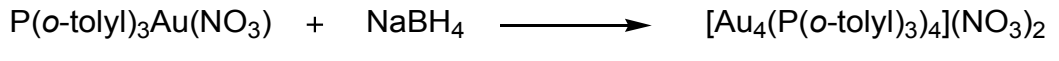

Figure 3.28. Synthesis of $[Au_4(P(o\text{-tolyl})_3)_4](NO_3)_2$.

A slurry of $(o\text{-tolyl})_3PAuNO_3$ (0.41 g, 0.72 mmol) in ethanol (~20 ml) was stirred with a solution of $NaBH_4$ (7.00 mg, 1.80 mmol) in ethanol (~30 ml). The caused the solution to turn dark brown in colour. The reaction mixture was stirred until there was no longer any white solid remaining. The solvent was then evaporated from the solution on a rotary evaporator yielding a dry solid. The remaining solid was then dissolved in a little tetrahydrofuran (~20 ml). Hexane (~10 ml) was added to this solution, precipitating out a dark brown solid. The solid was filtered off and washed with hexane under vacuum yielding a dark brown powder. 73% yield (0.28 g).

Spectroscopic data:

^{1}H NMR δ: 2.47 (s, 9H, 3xCH_3), 6.91 (q, 3H, aromatic H's), 7.30 (t, 3H, aromatic H's), 7.344 (d, 3H, aromatic H's), 7.60 (t, 3H, aromatic H's). ^{31}P NMR δ: 21.8 (s, $(o\text{-tolyl})_3P$).

Elemental analysis: C 44.80% (47.36%), H 3.85% (3.98), N 1.76% (1.32%), P 5.39% (5.82%).

3.2.20. Synthesis of $[Au_4(P(o\text{-tolyl})_3)_4](PF_6)_2$

$$[Au_4(P(o\text{-tolyl})_3)_4](NO_3)_2 \quad + \quad \text{xs } NaPF_6 \longrightarrow [Au_4(P(o\text{-tolyl})_3)_4](PF_6)_2$$

Figure 3.29. Synthesis of clusters $[Au_4(P(o\text{-tolyl})_3)_4](NO_3)_2$.

A small amount of the cluster formed from $(P(o\text{-tolyl})_3)AuNO_3$ (0.16 g, 75.1 x10^{-3} mmol) was dissolved in ethanol (~10 ml). To this solution, a solution of $NaPF_6$ (0.019 g, 0.114 mmol) was added causing the appearance of a brown precipitate. This solid was filtered off and dried under vacuum. Attempts to recrystallise the precipitate were carried out using dichloromethane and ethanol. 48% yield (0.085 g).

Spectroscopic data:

^{1}H NMR δ: 2.47 (s, 9H, 3xCH_3), 6.91 (q, 3H, aromatic H's), 7.30 (t, 3H, aromatic H's), 7.344 (d, 3H, aromatic H's), 7.60 (t, 3H, aromatic H's). ^{31}P NMR δ: -143 (sept, P, PF_6^-), 21.8 (s, (*o*-tolyl)$_3$P).

3.2.21. Characterisation techniques

EXAFS and XANES -

EXAFS data of all of the gold complexes synthesised except $[Au_6(Ph_2P(o\text{-tolyl}))_6](NO_3)_2$ was collected at station 9.3 of the SRS in Daresbury. The fine powder was mounted on to adhesive tape and placed into an aluminium sample holder. Alternatively, samples were ground as a mixture with silica using a pestle and mortar. This was then pressed into a disc and mounted on an aluminium sample holder. Au L_{III} edge data was recorded in transmittance mode from 11.6 to 13 keV. 5 scans were collected, each over 5 minutes, and were combined to minimise error.

EXAFS data for $[Au_6(Ph_2P(o\text{-tolyl}))_6](NO_3)_2$ was collected on the DUBBLE beamline at the ESRF in Grenoble. 100 mg of Au_6 cluster was mounted on adhesive tape and mounted on an aluminium sample holder. Au L3 edge fluorescence data was collected at room temperature from 11.6 to 12.8 keV.

Background subtraction of data collected at both the SRS and ESRF was performed using VIPER[60] and the extracted EXAFS data was analysed using EXCURV[61].

Mass Spectroscopy -

FAB mass spectroscopy with positive ions was used to identify the masses of the unknown clusters synthesised from Au(PhP(*o*-tolyl)$_2$)(NO$_3$) and Au(P(*o*-tolyl)$_3$)(NO_3). This is a very useful technique as the

identification of a molecular ion peak in the mass spectrum can greatly assist in the structural elucidation of the unknown clusters.

NMR -

All NMR spectra were recorded on a Brüker AMX 400 instrument using either $CDCl_3$ or CD_3OD.

IR Spectroscopy -

All IR spectroscopy was recorded on a Perkin Elmer FTIR spectrophotometer with an ATR accessory.

Single Crystal X-ray diffraction -

All single crystal X-ray diffraction data was collected on a Brüker SMART APEX diffractometer.

3.3. Results and discussion

A range of clusters were synthesised using the same stepwise methodology. By altering the size of the phosphine ligands present on the cluster precursors, the effect of ligand bulk on cluster size was investigated. The clusters and precursors were characterised using a range of techniques including NMR, XANES, EXAFS and infra-red spectroscopy. EXAFS and mass spectroscopy were particularly useful in identifying the clusters obtained through the reduction of (PhP(*o*-tolyl)$_2$)Au(NO_3) and (P(*o*-tolyl)$_3$Au(NO_3). The results of the experiments will be discussed in this section.

3.3.1. NMR data

^{1}H NMR was less useful than ^{31}P NMR as the positions of the aromatic and methyl hydrogen chemical shifts did not vary much with the different complexes as they were all at least 3 atoms away from the gold atoms. The integral values from the ^{1}H NMR spectra were useful as they could be used to confirm the presence and number of *o*-tolyl groups relative to the phenyl groups.

The ^{31}P NMR spectra of both the cluster and precursor complexes show only one singlet peak. This is true even for the cluster complexes that have been crystallographically resolved as having non-equivalent gold-phosphine sites present. The singlet peaks observed could be due to dynamic equilibria of the phosphine ligands on the surface of the cluster. It is also possible that the gold atoms within the cluster allow for electronic charge to be evenly distributed throughout the molecule, which would result in the phosphine ligands being bound to electronically equivalent gold atoms.

By comparing the position of the singlet in the ^{31}P NMR spectrum, it is possible to observe the change in electron density on the phosphorus when changing the anion, coordinating the ligand to gold, reducing the complex, and exchanging the phenyl groups for *o*-tolyl groups. By looking at the plot below (Figure 3.30), it can be seen that on going from a free ligand to a gold-phosphine complex, there is a (down-field) shift in the position of the phosphorus singlet as the electron density on the phosphorus atom is reduced. This is due to the donation of the loan pair of electrons on the phosphorus to the gold s-orbital.

It is generally observed that the presence of *o*-tolyl groups in the place of phenyl groups on the phosphorus results in a down-field shift of the singlet. This is seen in both the linear AuLCl and $AuL(NO_3)$ complexes, as well as the cluster complexes formed. The compounds all follow the trend in δ value with compounds of PPh_3 > $Ph_2P(o\text{-tolyl})$ > $PhP(o\text{-tolyl})_2$ > $P(o\text{-tolyl})_3$. This is because *o*-tolyl groups push more electron density on to the phosphorus atom than phenyl groups, which accept electron density into the delocalised ring more readily.

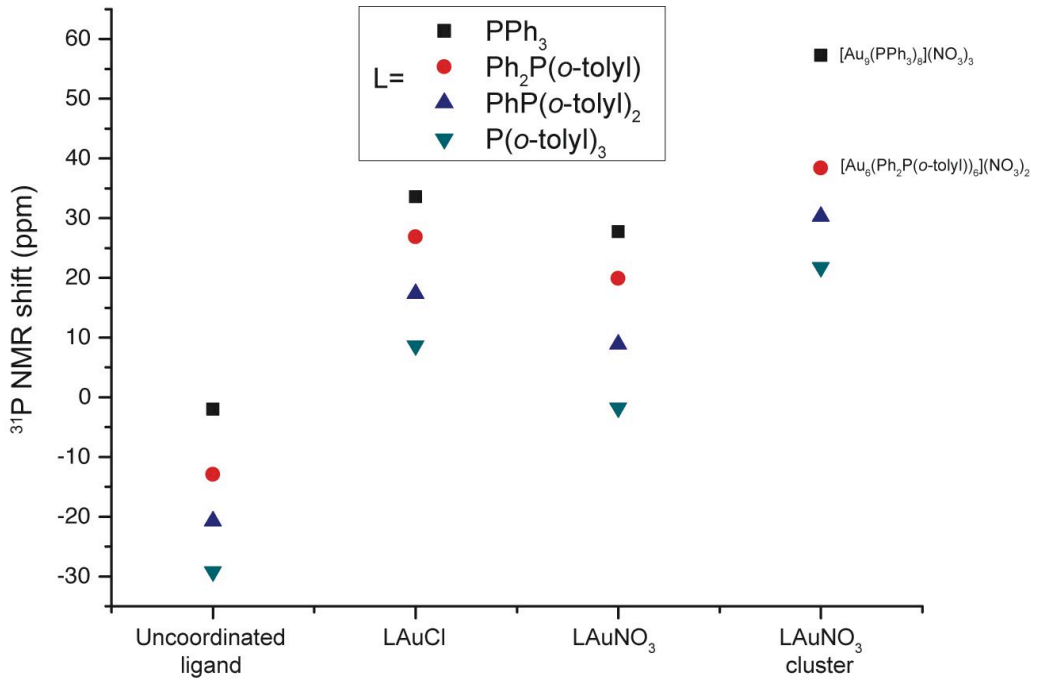

Figure 3.30. The chemical shifts of the singlet peaks from ^{31}P NMR of uncoordinated and gold-coordinated phosphines.

When looking at the change in NMR shift on going from AuLCl to $AuL(NO_3)$, it can be seen that the chemical shift moves up-field by about 7 ppm. This change in chemical shift is a characteristic feature of these compounds.

Reduction of $AuL(NO_3)$ with $NaBH_4$ leads to the formation of phosphine stabilised clusters. On going from $AuL(NO_3)$ to their respective cluster compounds, there is a down-field shift of δ ~20 ppm for the compounds where L= $Ph_2P(o\text{-tolyl})$, $PhP(o\text{-tolyl})_2$ and $P(o\text{-tolyl})_3$. When L= PPh_3, the cluster δ value is shifted down-field by ~ δ30 ppm. This change in chemical shift is due to the increased σ donation from the phosphines to the gold atoms in the cluster. This happens because the redistribution of electron density from the gold atoms to surrounding gold atoms within the cluster means that the phosphines are able to donate more electron density to the gold atoms.

3.3.2. XANES data

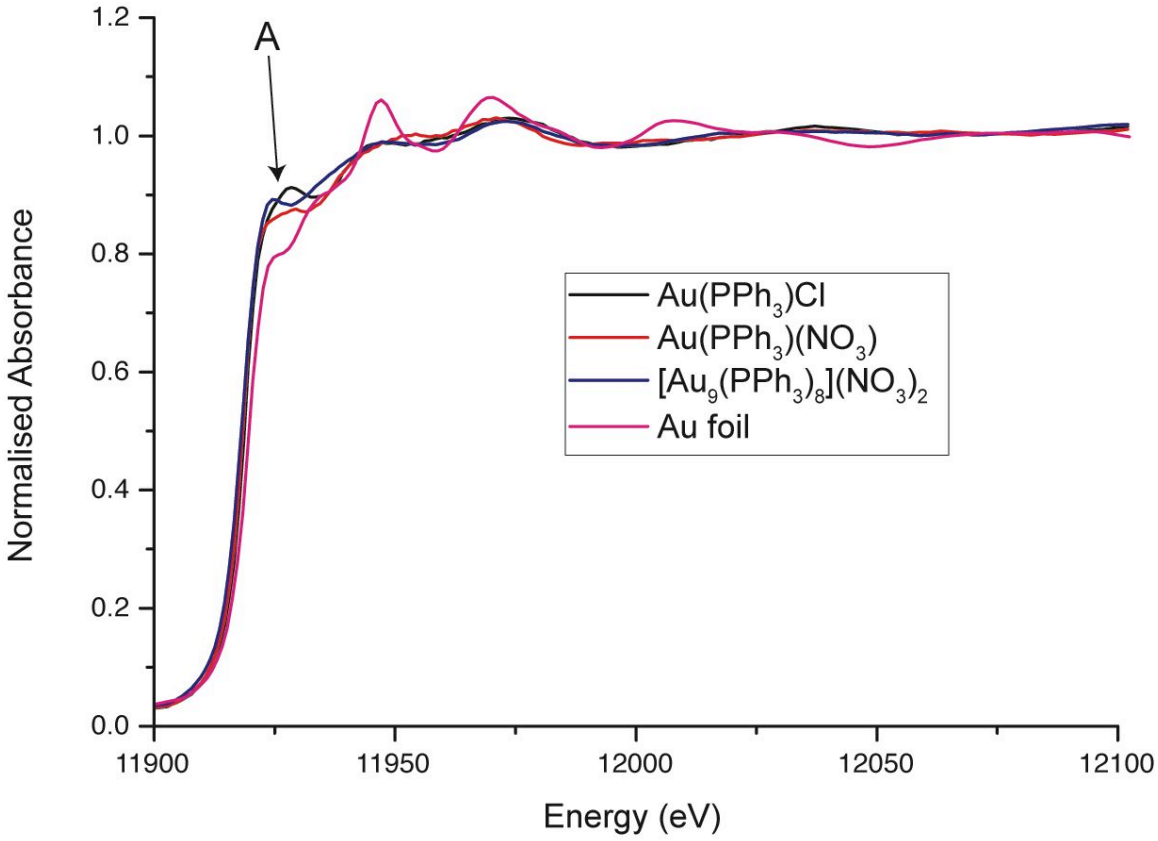

Figure 3.31. XANES Au L3 edge data for $[Au_9(PPh_3)_8](NO_3)_3$ and its precursors with gold foil for reference.

XANES can provide information about the oxidation state of the gold and in other materials, it can provide coordination environment information. The small peaks marked A in figure 3.31 are due to the transitions from the $2p_{2/3}$ to the 5d level. From the figure, it can be seen that the peak's intensity is lowest for gold foil. This is because the intensity of this peak is dependent on the unoccupied d states. This means that because the gold in the precursors $Au(PPh_3)Cl$ and $Au(PPh_3)(NO_3)$ is in the +1 oxidation state, the peak will be more prominent than for bulk gold (foil). The charge of the cluster $[Au_9(PPh_3)_8](NO_3)_3$ is +3 giving the gold atoms a charge of $+^1/_3$ each. The partial oxidation states of the gold atoms in the cluster results in a larger peak at this position in the XANES spectra than bulk gold.

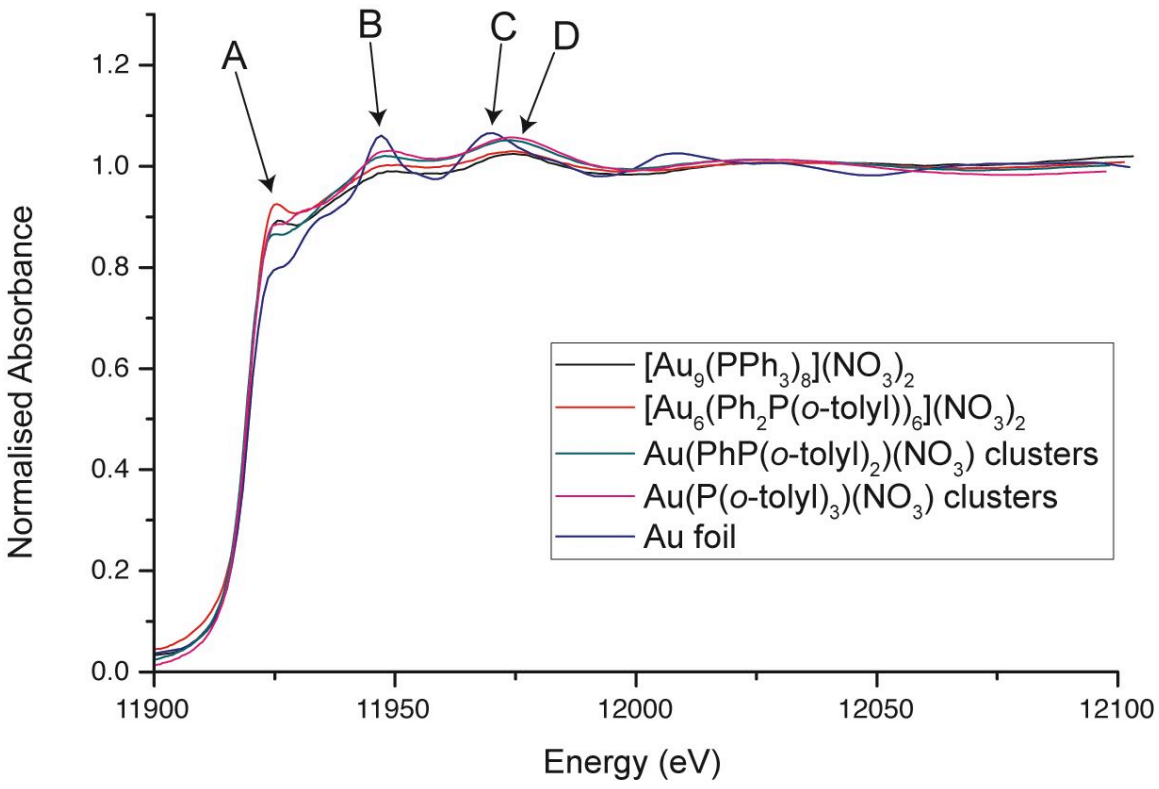

Figure 3.32. Au L3 edge XANES data of all the clusters synthesised with different phosphine ligands with gold foil for as a reference.

The XANES spectra shown in figure 3.32 compares the XANES for all of the synthesised clusters with bulk gold. It can be seen that the peak at about 20 eV past E0, marked A, is largest for $[Au_6(Ph_2P(o\text{-tolyl})_2)_6](NO_3)_2$, with $[Au_9(PPh_3)_8](NO_3)_3$ and the cluster formed from $AuP(o\text{-tolyl})_3$ having similarly sized peaks. The cluster synthesised from $Au(PhP(o\text{-tolyl})_2)$ had a marginally smaller peak, but it is still larger than that of gold foil. These peaks indicate that there is a positive charge on the gold in the clusters and the gold within is in a positive oxidation state. Features labelled B and C in figure 3.32 are the most prominent for the gold foil. Whilst B is present in all of the XANES of the cluster species, it is much sharper for the gold foil. The broad feature labelled D on the XANES of the clusters is shifted slightly higher in energy from peak C of the gold foil XANES. These features (D), along with the broad features B are characteristic of

the XANES of all the phosphine stabilised gold clusters synthesised that we have characterised in this way.

3.3.3. EXAFS data

In figure 3.33 Fourier transformed data of the Au L_{III} EXAFS data of all the gold clusters synthesised are shown. The Fourier transformed data shows the presence of two distinct peaks in all of the samples. These peaks can be attributed to Au-P and Au-Au bonds. However, this assignment can be confirmed by detailed analysis of the EXAFS data using refining methods (described in Chapter 2).

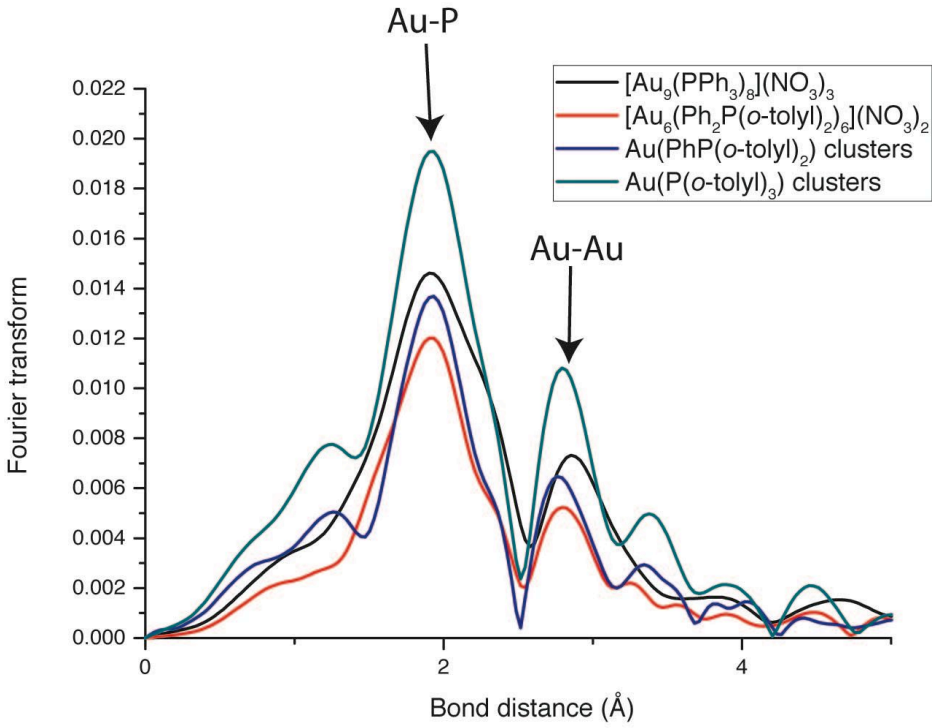

Figure 3.33. Non-phase shift corrected Fourier transformed data showing presence of both Au- and Au-Au bonds in the analysed molecular clusters.

EXAFS data gives us local information about the gold atoms. Through analysis of the recorded data, the coordination number of the gold, the type of atoms bonded to the gold and the bond distances can be found.

Best fits of the calculated EXAFS and the experimental data from the refinement with EXCURVE are shown in figure 3.34.

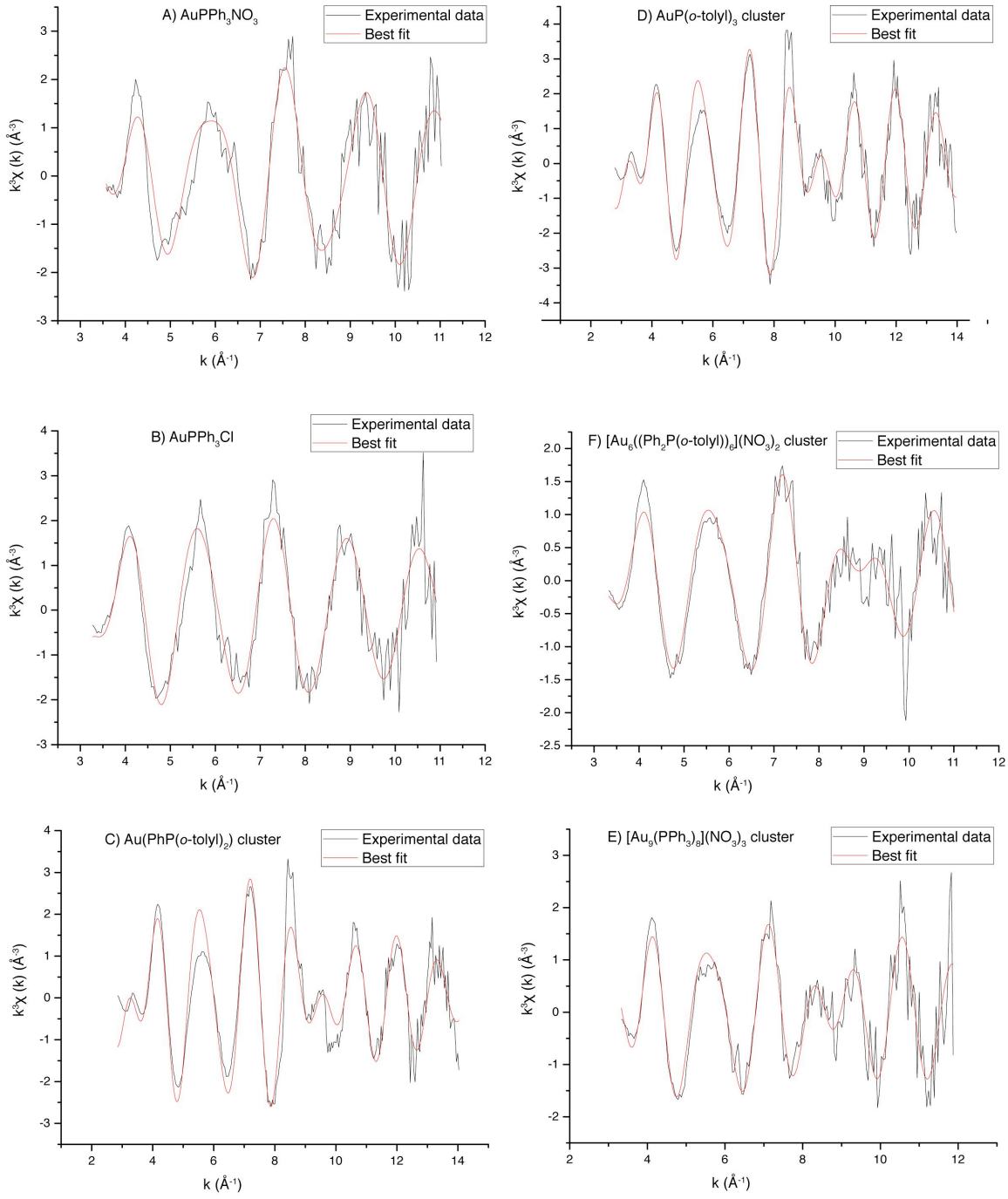

Figure 3.34. Au L_{III} background subtracted EXAFS data showing the experimental data and the best fits after carrying out analysis with EXCURVE.

Table 3.3. Table showing the coordination number (N), bond distance ®, and Debye-Waller factor (σ^2) of the Au-P and Au-Au interactions in the gold precursors and clusters taken from EXAFS data. Single crystal X-ray diffraction data is also presented.

	Au-P			Au-Au			Au-X*		
	N	r (Å)	σ^2 (Å^2)	N	r (Å)	σ^2 (Å^2)	N	r (Å)	σ^2 (Å^2)
PPh_3AuCl (EXAFS)	0.68	2.19	0.018	-	-	-	0.97	2.26	0.007
PPh_3AuCl (Crystal)[117, 118]	1	2.23	-	-	-	-	1	2.28	-
$PPh_3Au(NO_3)$ (EXAFS)	1	2.22	0.007	-	-	-	1	2.13	0.008
$PPh_3Au(NO_3)$ (Crystal)[119]	1	2.20	-	-	-	-	1	2.07	-
$[Au_9(PPh_3)_8](NO_3)_3$ (EXAFS)	0.4	2.29	0.003	3.51	2.74	0.024	-	-	-
$[Au_9(PPh_3)_8](NO_3)_3$ (Crystal)[79]	0.88	2.28	-	4.44	2.78	-	-	-	-
$[Au_6(Ph_2P(o\text{-tolyl}))_6](NO_3)_2$ (EXAFS)	0.70	2.30	0.01	0.63	2.71	0.01	-	-	-
$[Au_6(Ph_2P(o\text{-tolyl}))_6](NO_3)_2$ (Crystal)	1	2.29	-	3.66	2.78	-	-	-	-
$Au(PhP(o\text{-tolyl})_2)$ cluster (EXAFS)	1	2.30	0.010	3	2.68	0.020	-	-	-
$Au(P(o\text{-tolyl})_3)$ cluster (EXAFS)	1	2.30	0.007	3	2.68	0.017	-	-	-

***For PPh_3AuCl, X= Cl and for $PPh_3Au(NO_3)$, X= O.**

The EXAFS data shows that the Au-P bond distance is shorter by almost 1 Å for the mononuclear gold-phosphine precursor compounds. PPh_3AuCl and $PPh_3Au(NO_3)$ both have very similar Au-P bond lengths, with that of PPh_3AuCl being only slightly longer. The data shows excellent agreement with the reported bond lengths from the crystal structure of $PPh_3Au(NO_3)$ but there is a small difference with that of PPh_3AuCl.

Of the clusters, that obtained from $AuP(o\text{-tolyl})_3$ has the largest Au-P distance and $[Au_9(PPh_3)_8](NO_3)_3$ has the smallest. There is however very little difference in the values of the Au-P distances in the clusters (>0.3 Å). Also, the values of the Au-P distances for the PPh_3 and $PPh_2(o\text{-tolyl})$

stabilised clusters obtained from the EXAFS data are in excellent agreement with those from the crystal structure data.

The average Au-P coordination numbers of $[Au_9(PPh_3)_8](NO_3)_3$ and $[Au_6(Ph_2P(o\text{-tolyl}))_6](NO_3)_2$ are not in close agreement with the figures obtained from the crystal structures (0.88 and 1.0 respectively). This difference could be due to the close link that the Debye-Waller factor has to the coordination number values.

Of particular interest are the average Au-Au bond length values from the clusters. These range from 2.679-2.731 Å. These bond lengths are substantially shorter than those reported for metallic gold (2.86 Å). Similar examples of Au-Au bond contractions have been reported from other gold cluster compounds, for example, $Au_{55}(PPh_3)_{12}Cl_6$ with 2.78 Å[120] and $Au_{11}(SCN)_3(PPh_3)_7$ with 2.60 Å.[84, 121] When a cationic charge is present on the gold, these reduced bond distances are observed.

3.3.4. Crystal Structures

A

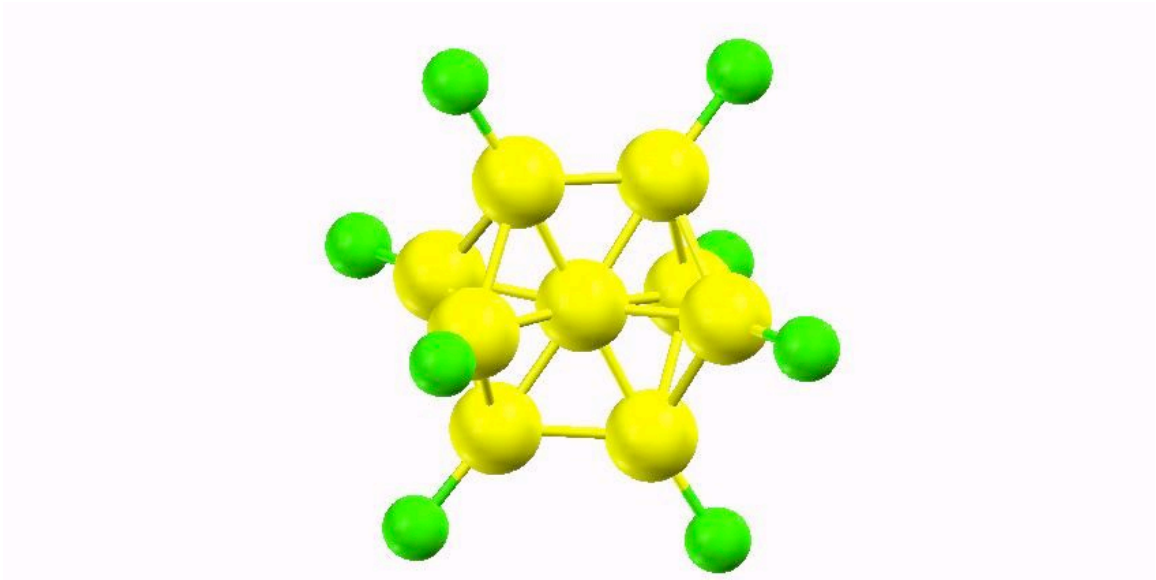

B

Figure 3.35. Crystal structures of $[Au_6(Ph_2P(o\text{-tolyl}))_6](PF_6)_2$ (A) and $[Au_9(PPh_3)_8](NO_3)_3$[79] (CCDC number: 645243)(B). The gold core (yellow) and the phosphorus atoms (green) bound to the surface are shown and the hydrogen and carbon atoms have been omitted for clarity.

Concerning the crystal structures of $[Au_9(PPh_3)_8](NO_3)_3$ and $[Au_6(Ph_2P(o\text{-tolyl}))_6](PF_6)_2$ (see figure 3.35), there are many differences between them. The most obvious difference is the presence of a single gold atom at the

centre of $[Au_9(PPh_3)_8](NO_3)_3$. This central atom is bound to all the other gold atoms in the cluster with bond lengths ranging from 2.708 to 2.675 Å. The rest of the Au-Au bond distances on the molecule were longer than these (between 2.772 and 2.855 Å). Generally, compared to the Au-Au contacts in metallic gold (2.876 Å)[120] those present in $[Au_9(PPh_3)_8](NO_3)_3$ were much shorter, averaging 2.776 Å. The average bond distance in $[Au_6(Ph_2P(o\text{-tolyl}))_6](PF_6)_2$, is slightly shorter, at 2.755 Å. Au-Au bond contractions are characteristic of gold clusters a have been previously identified.[84, 120, 122] The crystal structures are in good agreement with the aforementioned EXAFS data. Selected crystallographic data for $[Au_6(Ph_2P(o\text{-tolyl}))_6](PF_6)_2$ is presented in Appendix 1.

3.3.5. Structures of $[AuP(o\text{-tolyl})_3](NO_3)$ and $[Au(PhP(o\text{-tolyl})_2)](NO_3)$ clusters

Analysis of the EXAFS data collected for the cluster stabilised by P(*o*-tolyl)$_3$, strongly suggests that the structure of the cluster formed is tetrahedral with 4 stabilising phosphine ligands (see figure 3.34 and table 3.3), one bound to each gold atom. This structure is in agreement with the prediction by Mingos[97] that it is most energetically favourable for the clusters to arrange themselves in tetrahedra. The elemental analysis data was in agreement with this structure, with the slight differences in recorded and calculated numbers attributable to solvent contamination of the sample.

From the mass spectroscopy data, peaks have been identified that correspond to $Au_4(P(o\text{-tolyl})_3)_4$ and its stepwise break-up through the alternate loss of phosphines and gold atoms. Peaks at m/z 2005, 1700, 1503, 1199, 1002 a.m.u. relate to $[Au_4(P(o\text{-tolyl})_3)_4]^+$, $[Au_4(P(o\text{-tolyl})_3)_3]^+$, $[Au_3(P(o\text{-tolyl})_3)_3]^+$, $[Au_3(P(o\text{-tolyl})_3)_2]^+$, $[Au_2(P(o\text{-tolyl})_3)_2]^+$ respectively. After this, gold is lost and $[Au(P(o\text{-tolyl})_3)_2]^+$ is formed (m/z 806 a.m.u.) ,

which loses another phosphine to form $[Au(P(o\text{-tolyl})_3)]^+$ (m/z 501 a.m.u.). This is illustrated in figure 3.36.

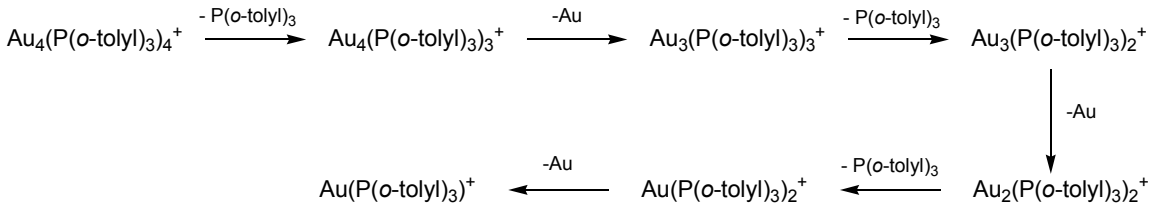

Figure 3.36.Fragmentation pattern of $[Au_4(P(o\text{-tolyl})_3)_4]^+$ during positive ion fast atom bombardment mass spectroscopy.

The EXAFS data (see figure 3.34 and table 3.3) also suggests that the structure of the cluster synthesised from $[Au(PhP(o\text{-tolyl})_2)](NO_3)$ is a tetrahedral arrangement of gold atoms, each stabilised by one phosphine ligand, though the fit of this data to the model is marginally better for the cluster synthesised from $[Au(P(o\text{-tolyl}_3)](NO_3)$. Elemental analysis data also indicated the tetrahedral structure, with the ratios of C:H:P consistent with those in $[Au_4(PhP(o\text{-tolyl})_2)_4](NO_3)_2$. A large excess of nitrate from an unknown source accounts for the differences in the recorded and calculated numbers. Mass spectroscopy only provided a vague idea of the composition of the cluster.

It should also be noted that Matrix assisted, laser desorption ionisation mass spectroscopy was also used to try to identify the new clusters. This method provided no useful information about the possible structures. Significant peaks were at large molecular masses that could have corresponded to larger cluster structures. It is likely that this technique was generating new clusters, possibly with the support matrix material, which is why it was so difficult to assign any peaks. This method has been used for synthetic purposes.[123]

3.4. Conclusion

It has been demonstrated that increasing the steric bulk of the phosphine ligands in mononuclear Au-phosphine precursors corresponds to lower nuclearity clusters.

From the EXAFS and mass spectroscopy data, there is good evidence to suggest that increasing the steric bulk of the stabilising phosphine ligand decreases the size of the resulting cluster formed. The crystal structures of both $[Au_9(PPh_3)_8](NO_3)_3$ and $[(Au_6(Ph_2P(o\text{-tolyl})_{)6}](NO_3)_2$ corroborate this.

By comparing the known structure of the cluster obtained through the reduction of $AuPPh_3(NO_3)$, $[Au_9(PPh_3)_8](NO_3)_3$, to that obtained from the reduction of $Au(Ph_2P(o\text{-tolyl}))(NO_3)$, it s clear that the change in phosphine ligand has greatly affected the cluster structure. By increasing the cone angle of the phosphine from 145^o to 185^o, a large change can be observed in the core of the cluster obtained. Whereas in $[Au_9(PPh_3)_8](NO_3)_3$ a central gold atom is present, surrounded by other gold atoms bonded to the phosphines, no central atom is present in $[Au_6(Ph_2P(o\text{-tolyl}))_6](NO_3)_2$. In $[Au_6(Ph_2P(o\text{-tolyl}))_6](NO_3)_2$, all of the gold atoms are bound to a phosphine.

Evidence has been provided for the structure for the cluster formed from the reduction of $Au(P(o\text{-tolyl})_3(NO_3)$ and it suggests that it forms a tetrahedral cluster with each of the 4 gold atom present bound to 3 other gold atoms and 1 phosphine. Characterisation data also suggests that the structure formed from the reduction of $Au(PhP(o\text{-tolyl})_2)(NO_3)$ is also tetrahedral. These clusters are the first monodentate phosphine stabilised gold clusters to be reported with tetrahedral geometry.

4. Cluster deposition, ligand removal and catalytic activity testing

Abstract

This section focuses on the deposition of the clusters on to a metal oxide support. Heterogeneous gold catalysts were synthesised from the clusters described in chapter 3. After depositing the clusters on to the support material to give a range of gold loadings, the catalysts were calcined at different temperatures to remove the phosphines. Extensive characterisation was carried out including *in situ* EXAFS, which was used to follow the ligand removal process. The catalysts were then tested for their oxidation activity to find the optimum gold loading and calcination temperature.

4.1. Introduction

4.1.1. Catalysis using gold

Gold has been investigated as a catalyst for a range of reactions. The first suggestion of the potential activity of gold was in 1906 when the uptake of hydrogen by gold was studied in the presence of oxygen at 600^{o}C.[124] Some years later, in 1950, it was demonstrated that gold surfaces could convert nuclear spin isomer para-hydrogen into ortho-hydrogen.[125]

4.1.1.1. Hydrogenation

Following on from the nuclear spin isomer work, it was shortly reported that both gold foil[126, 127](hydrogen-deuterium exchange) and supported gold catalysts[128-130] were active for exchange reactions above 200^{o}C. Due to this activity, a large amount of research has focused on the use of gold in the hydrogenation of different unsaturated hydrocarbons.

$$H_2 + D_2 \xrightarrow{\text{Gold surface}} HD$$

Figure 4.1.Hydrogen-deuterium exchange reaction over a gold surface.

As our area of interest lies within heterogeneous catalysis, this section will focus only on supported gold catalysis. A very large volume of work has also been carried out into looking at homogeneous catalysis using gold, most of which focuses on gold in nucleophilic addition to π systems. These molecular catalysts have been found to be highly effective and growth continues in the number of groups studying this area. The example illustrated in figure 4.2 was the first reported example of a reaction using gold as a homogenous catalyst for nucleophilic addition to alkynes[131] and reportedly gave a 570% yield for the desired ketone

product when the catalytic reaction was carried out using a 15 fold excess of substrate.

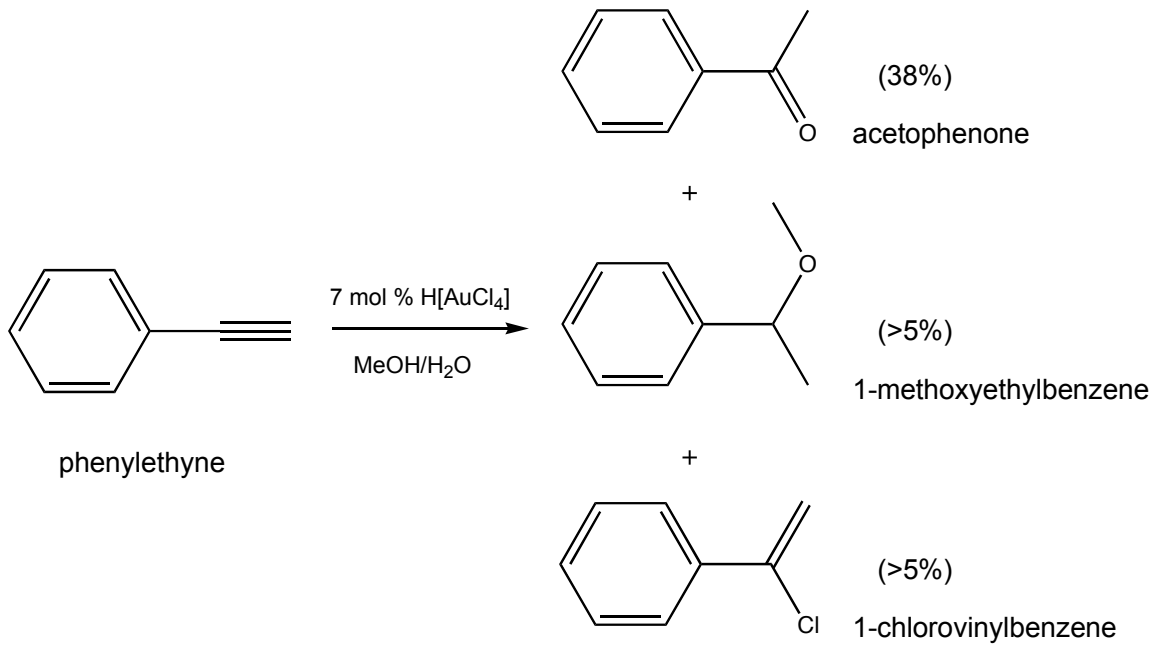

Figure 4.2. **Reaction scheme to show the selectivity of homogenous gold(III) catalyst to form a ketone (acetophenone) from an alkyne substrate (phenylethyne) along with the side products, 1-methoxyethylbenzene and 1-chlorovinylbenzene.**

The use of gold for the hydrogenation of cyclohexene was the starting point of research investigating gold as a hydrogenation catalyst. In the 1960's it was reported that both gold foil and gold powder could be used to catalyse the reaction in which cyclohexene was converted to cyclohexane and benzene at high temperatures.[132] In this reaction, cyclohexene acted as both the substrate and the source of hydrogen. By either increasing the temperature of the reaction or by decreasing the hydrogen pressure, the amount of benzene produced increases. Benzene is the major product due to the activation energy of the hydrogenation reaction being far higher than that of the dehydrogenation.

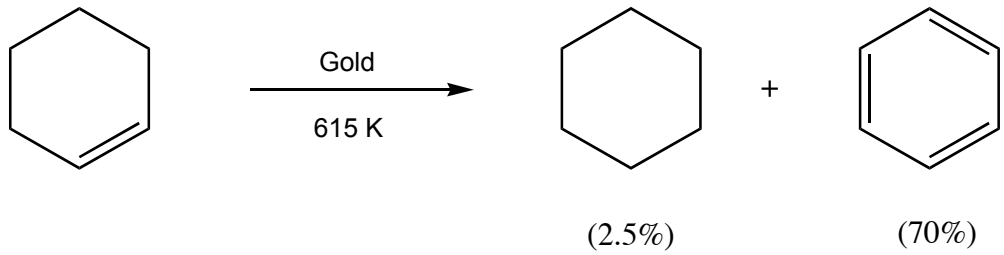

Figure 4.3. **The conversion cyclohexene to benzene and cyclohexane.**

In 1973, it was demonstrated for the first time that gold could be used as an efficient hydrogenation catalyst without the need for high temperatures[133] (figure 4.3). At temperatures as low as 373 K, gold particles supported on silica and alumina could convert pent-1-ene into pentane.[129] Gold was also shown to exhibit selectivity for the first time in terms of both diastereoselectivity and chemoselective hydrogenation for the hydrogenation of both 1,3-butadiene and 2-butyne. Figure 4.4 shows how *trans* but-1-ene and *cis* but-2-ene are preferentially formed over the other possible products for the hydrogenation of *trans* but-1-ene and *cis* but-2-ene respectively.

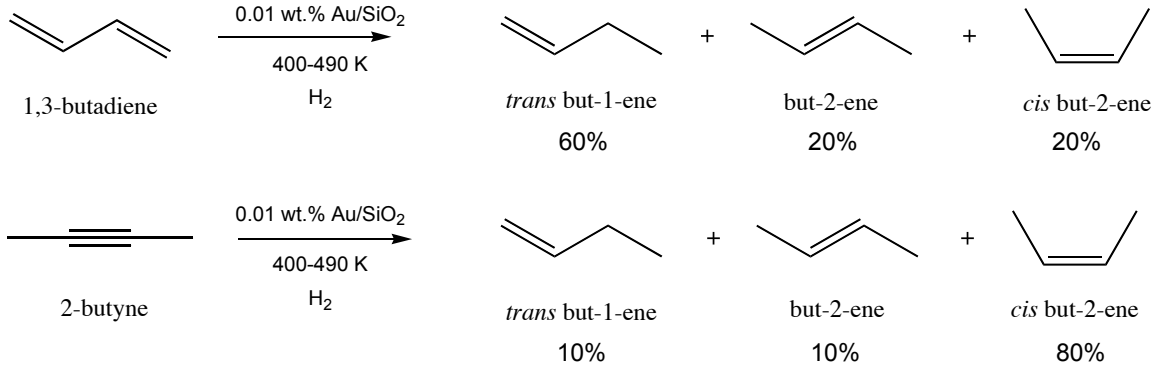

Figure 4.4. **Reaction scheme to shown the catalytic conversion of 1,3-butadiene and 2-butyne by gold supported on silica.[133]**

More recently, gold nanoparticles supported on cerium oxide have demonstrated extremely high selectivity for the hydrogenation of triple bonds in alkene-alkyne mixtures.[134] Selectivities as high as 95% for propyne hydrogenation in propyne-propene mixtures were found. Computational studies proved that this preference is due to only the triply bonded species being adsorbed onto the gold nanoparticle surfaces.

Despite heterogeneous gold-catalysed hydrogenation of unsaturated hydrocarbons being one of the oldest topics in gold catalysis history, only a relatively small amount of research has focused on this area. Of the work that has been carried out, no correlation can be made. This is because with each investigation, different supports, substrates, catalyst precursors and reaction conditions are used, making comparisons between different bodies of work very difficult.

Another area of heterogeneous gold catalysis that as been explored is the use of supported gold catalysts in the hydrogenation of α,β-unsaturated aldehydes.[135] In 1999 it was found that gold supported on ZnO or ZrO_2 was a highly selective catalyst that could be used to hydrogenate crotonaldehyde to crotyl alcohol.[136, 137] The catalyst displayed a selectivity of up to 81% for the hydrogenation of the C=O bond rather than the C=C bond. Both products could also be hydrogenated further to form butan-1-ol (see figure 4.5). It was found that the selectivity for the formation of the alcohol increased when larger particles of gold were present in the catalyst. These larger particles formed when the catalyst was calcined at higher temperatures. It was also demonstrated that the addition of a small amount of thiophene to the gold catalyst increased the selectivity of the unsaturated alcohol, but also lowered the overall conversion. The thiophene did not affect the gold morphology, but instead adsorped on to the surface of the gold particles and acted as an electronic promoter.

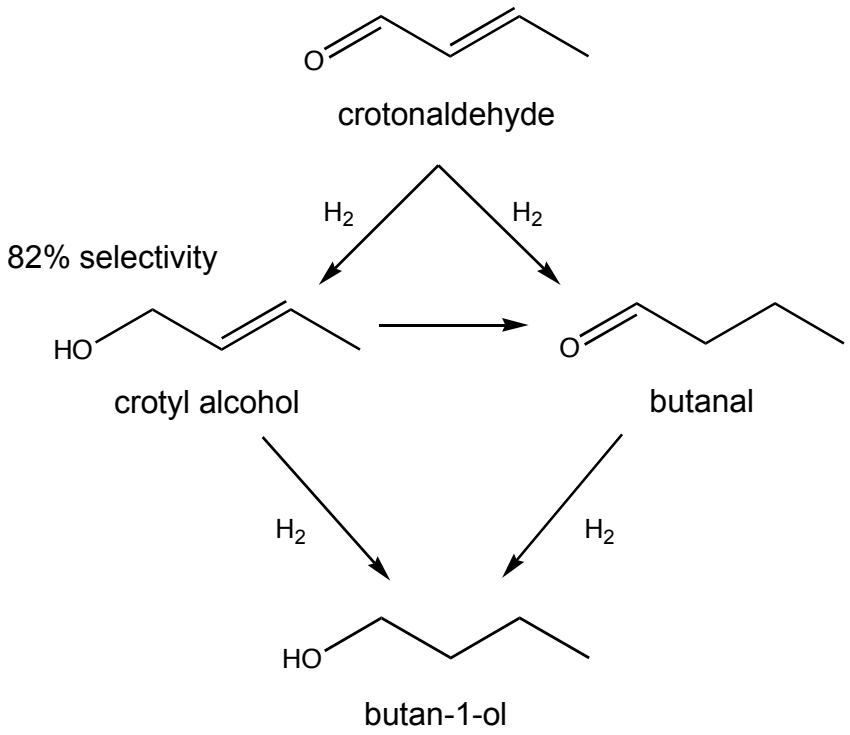

Figure 4.5. **Gold supported on ZnO at 400 °C has a selectivity of 82% for the hydrogenation of crotonaldehyde to form crotyl alcohol over butanal..**[136]

The use of gold catalysts for the hydrogenation of unsaturated organic molecules is just one potential application for this precious metal. Another area that has been explored is the use of gold in selective oxidation reactions.

4.1.1.2. Selective Oxidation

Gold catalysts have been found to be particularly effective for the epoxidation of alkenes and the oxidation of alcohols and this was demonstrated for the first time in 1998 when supported gold catalysts were used for the epoxidation of propene to propene oxide[138] (figure 4.6) by Haruta using gold nanoparticles deposited on to TiO_2. The reaction was found to occur in a vapour phase with H_2 and O_2 present. It was also found that when the particles of gold were between 2 and 4 nm in size, the propene was converted to propene oxide, but if the particle size was

less that 2nm, hydrogenation occurred and propane was formed. These reactions are potentially very useful as propene oxide is an important chemical in industry used for the production of resins such as polyurethane. It was later found that the initial low selectivity could be improved by changing the titanium support and consequently, gold catalysts were made where the gold was supported on TS1, Ti-zeolite-beta, Ti-MCM-41 and Ti-MCM-48.[139, 140]

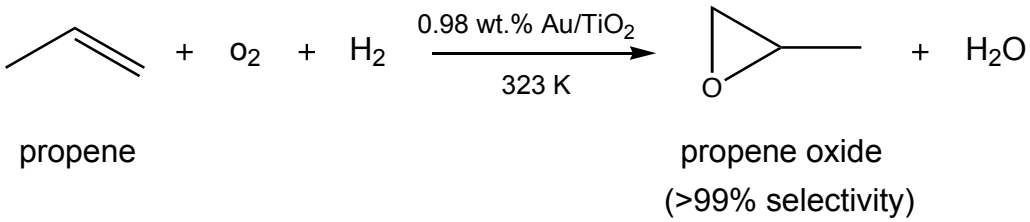

Figure 4.6. This reaction scheme shows the conversion of propene to propene oxide[138] using supported gold particles supported on TiO_2.

The oxidation of alcohols can also be achieved with gold. It was generally acknowledged that supported nanoparticles of palladium and platinum were effective catalysts for this process. However, they do not give good selectivity with complex substrates. In 2005 it was discovered that gold supported on cerium oxide could oxidise alcohols to aldehydes and ketones and even carry out further oxidation, converting the aldehydes to acids under mild conditions and without the need for a solvent.[141] The activity was shown to be higher than even the highest reported for palladium catalysts for the same process. The use of nanocrystalline ceria as a support increased the rate of reaction dramatically, giving selectivities and conversions >99%. This was carried out for a range of alcohols shown in table 4.1.

Table 4.1.Table showing the conversion of a selection of alcohols to ketones, aldehydes and acids after reaction with gold supported on CeO_2 nanoparticles.[142]

Substrate	Reaction Time (h)	Product	Conversion (%)	Selectivity (%)
3-octanol	3.5	3-octanone	97	>99
2-hydroylbenzyl alcohol	2	2-hydroxybenxaldehyde	>99	87
3,4-dimethoxybenzyl alcohol	2	4,3-dimethoxybenzylic acid	>99	>99
n-hexanol	10	Hexanoic acid	>99	>99
cinnamyl alcohol	3	cinnamylic acid	>99	98

The conversion of cyclohexane to cyclohexanol and cyclohexanone is one of the most important reactions carried out on the industrial scale with oxidised cyclohexane being essential to the production of nylon-6 and nylon-6,6, the worldwide production of which reaches 10^6 tonnes worldwide annually. Commercially this reaction occurs at ~150 ^oC using cobalt napthalene as an initiator for a radical oxidation process. This catalyst gives 70-85% selectivity and 4% conversion. Gold has been shown to activate cyclohexane at 150^oC and can give selectivities in excess of 90% when supported on MCM-41.[143, 144] However, as these catalysts of gold were reused, the selectivity shifted from cyclohexanone to cyclohexanol. This research gave evidence that gold catalysts could be used for C-H bond activation in alkanes, which could be of immense commercial significance.

Gold supported on activated carbon has shown good activity for the oxidation of glucose.[145] Glycolic acid was formed with up to 99% selectivity and 69% conversion, activity comparable with enzymatic systems. The catalysts were synthesised through the immobilisation of a pre-formed gold sol on the surface of the support and had an average particle size of 6.7 nm (0.7 wt.% loading). What was particularly interesting about this work was that the catalysts were synthesised in

batches of 80-500g, showing that large quantities of active gold catalysts could be prepared in single steps.

Oxidation reactions are of enormous industrial importance, especially in the synthesis of fine chemicals. Stoichiometric quantities of oxidizing agents such as permanganate are widely utilised in industrial oxidation reactions that lead to the accumulation of by-products. A green alternative would be a reusable (heterogeneous) catalyst that could oxidise a substrate without forming the side products. Oxygen sources such as hydrogen peroxide or molecular oxygen may be used to establish clean industrial oxidation methods[146, 147] that do not rely on stiochiometric oxidants.

4.1.1.3. H_2O_2 synthesis

Within the fine chemicals industry, there is no commercial method of producing hydrogen peroxide on a small scale when required. This means that the industry relies on obtaining the relatively small amount that it requires (e.g. for the production of epoxidised oils and hydroquinone) from large-scale manufacturers resulting in the need for transportation and storage . The possibility of using gold to catalyse the production hydrogen peroxide from H_2 and O_2 is an enticing concept to many chemical companies. For this reason, studies have been carried out into this area for a long time. It was recently found that gold supported on SiO_2 were effective for this reaction at only 283 K. What makes this process difficult to achieve is that the reaction conditions not only allow for the production of H_2O_2, but also promote its decomposition to water, its hydrogenation to water and sometimes the direct nonselective formation of water. However, it was found that the selectivity for H_2O_2 could be increased by supporting the gold either by itself or with palladium on Fe_2O_3[148] or on TiO_2[149] with palladium. The Au-Pd catalysts

had to be calcined at 400 ^{o}C to remain effective as catalysts calcined at lower temperatures gave higher initial activity but were unstable and lost activity over time. It was also found that the Fe_2O_3 supported gold catalysts had large gold particles (c.a. 48 nm) responsible for their activity whereas catalysts with smaller gold particles (c.a. 5 nm) had much reduced activity.

Another solution is to generate H_2O_2 *in situ* for immediate consumption. In oxidation reactions where oxidising compounds such as permanganate complexes are utilised, unwanted by-products are common. By generating the peroxide *in situ* for immediate usage, the only by-product from the oxidant would be water, making it ideal for implementation intoday's environmentally conscious society. Gold has been demonstrated as a suitable catalyst for this type of process for the oxidative desulphurization of thiophenes using H_2O_2 generated *in situ.*[150]

4.1.1.4. CO oxidation

For over two decades now one of the most highly researched areas of gold catalysis has been that of carbon monoxide oxidation.[151-159] In the 1980's Haruta found that that if the particles of gold are small enough, conversion of carbon monoxide to carbon dioxide may proceed, even at temperatures well below 0^{o}C.[155, 158, 159]

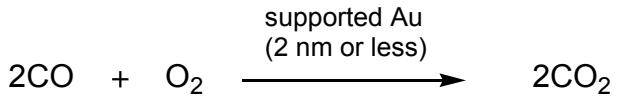

Figure 4.7. CO oxidation over a supported gold catalysts. This reaction can take place at temperatures as low as -66 ^{o}C.[152]

For this reaction, gold has a surprisingly high activity, one that is not replicated by other metals. When this activity was first discovered, it was initially attributed to some type of composite oxide catalyst from the support (α-Fe_2O_3) but it was later found that the most active catalysts had

gold particles present between 2 and 4 nm in diameter. Primarily, gold was supported on iron oxide, but later research suggested that the same high activity could be replicated by supporting gold on TiO_2. Much research has been carried out studying this catalyst. The main reason for this is that neither gold nor TiO_2 alone are active for CO oxidation, only when they are together is the high activity generated.

As so many research groups work in this area, each with their own experimental set ups and procedures, it makes it very difficult to directly compare results of one group to another. What is generally agreed upon is that it is necessary to have small particles of gold ≤4 nm on the surface of the support for activity, and the activity increases with decreasing particle size. The opposite effect is observed in gold catalysts for the direct synthesis of H_2O_2 where larger supported gold particles give higher activity catalysts than those with smaller particles. This makes the catalyst preparation method highly important as it greatly affects the size of the gold particles formed. Co-precipitation was initially used by Haruta to generate these catalysts, but now deposition precipitation is preferred. Impregnation is generally not used owing to the large gold particle sizes obtained. Table 4.2 compares the rates of CO oxidation for gold on TiO_2 catalysts prepared using different methods. It illustrates how high rates of oxidation can be obtained through the use of supported gold clusters.

Table 4.2. A table to show the activities for CO oxidation on supported nano-Au catalysts (DP= deposition precipitation, FD= photodecomposition, IMP= impregnation, IOH= impregnation of as-precipitated hydroxide, CVD= chemical vapour deposition).[158]

Gold precursor	Weight % Au on TiO_2	Preparation method	Av. gold particle diameter (nm)	Temperature (K)	Rate of CO oxidation (mmol/s/g_{Au})
$HAuCl_4$	2.3	DP	2.5	300	0.2
$HAuCl_4$	3.1	DP	2.9	300	0.6
$HAuCl_4$	1.0	FD	4.6	300	$2x10^{-5}$
$HAuCl_4$	1.0	IMP	-	300	$2x10^{-5}$
$HAuCl_4$	2.3	IMP	30	313	0.05
$Me_2Au(acac)$	4.6	CVD	2.9	262	0.05
$Me_2Au(acac)$	2.4	CVD	-	293	0.06
PPh_3AuNO_3	3.0	IOH	3	300	0.05
PPh_3AuNO_3	3.0	IMP	30	313	$6x10^{-3}$
$[Au_6(PPh_3)_6](BF_4)_2$	1.0	IMP	4.7	293	0.3

4.1.2. Gold catalyst preparation methods

There are a number of different methods of depositing gold on to supports. These will be discussed here:

Impregnation; involves metal nanoparticles particles or usually a gold precursor such as [$HAuCl_4$] being dissolved in an organic solvent and simply being stirred with the support until the solvent evaporates. This method is generally not used to prepare gold catalysts, as it tends to give relatively large gold particles (>10nm in size) on the surface of the support that are less active for catalytic reactions. Some of the earliest supported gold catalysts were prepared using this method,[160] where the concentration of the gold precursor solution was adjusted to give the

desired metal loading. After the solvent is removed, thermal treatment usually follows. One possible reason for the large particle sizes is the presence of Cl^- promotes mobility of the gold during heating. As this can also inhibit catalytic reactions, Cl^- can be removed through reduction with hydrogen or washing.[129]

Co-precipitation; This method requires an aqueous solution of $HAuCl_4$ and a metal nitrate to be poured into an aqueous solution of Na_2CO_3 containing either a hydroxide or carbonate co-precipitate. The precursor is then washed, dried and then calcined in air with the calcination temperature dependent on the support. This method was first reported in 1987[161] and is widely used as it is possible to obtain highly dispersed gold particles less than 10nm in size (see table 4.3). The main problem with this method is that a lot of the gold can be embedded within the support after precipitation, meaning that it inaccessible by the substrate for catalysis. With the high cost of gold, a method of catalyst synthesis that leaves part of the gold useless is undesirable.

Table 4.3. Table of gold particle sizes on different supports obtained through co-precipitation.[162]

Oxide Support	Gold Loading (wt.%)	Calcination Temp. (K)	Average gold particle diameter (nm)
MgO	2	473	<2
TiO_2	5	873	5
Fe_2O_3	5	673	4
Co_3O_4	5	673	6
NiO	10	673	8
ZnO	5	673	5
Al_2O_3	5	573	5
In_2O_3	5	673	5
SnO_2	5	673	3
SiO_2	5	573	20
Cr_2O_3	5	673	>30
CdO	5	295	21

Deposition-precipitation; An aqueous solution of $HAuCl_4$ is adjusted to a pH in the range of 6 to 10 before a metal oxide support is submerged in the solution. It is left in the solution for at least 1 hour which results in the deposition of $Au(OH)_3$ on to the metal oxide surface if the concentration and temperature are correct. The precursor is then washed, dried and calcined in air <523 K. The pH of the solution has a very large effect on the particle size. The relationship between the size of the gold particle and the pH can be seen in the graph below. This method has an advantage over co-precipitation because as the support surface acts as a nucleating agent for the gold particles, then all of the gold is deposited on to the surface of the support. This means that no gold is wasted through being trapped within the support as in co-precipitation. Figure 4.4 shows the change in gold particle diameter with the pH of the precursor solution.

At pH levels above 6, the main species on the solution is changed from $AuCl^-$ to $Au(OH)_n(Cl_{4-n})$ (n=1-3) and the mean particle size in the calcined catalyst becomes less than 4 nm.

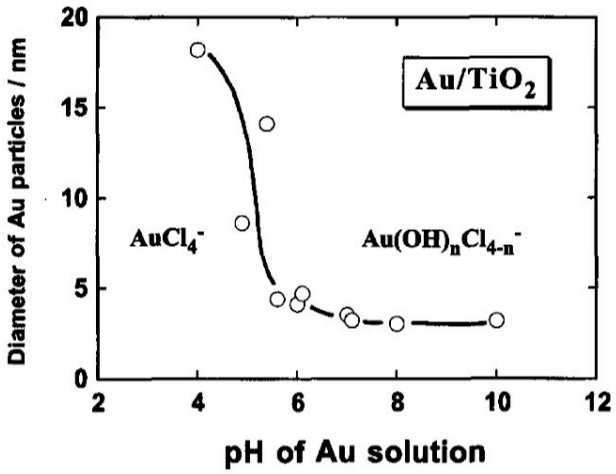

Figure 4.8. Graph relating the size of gold particles formed to the pH of the solution in deposition-precipitation.[163]

Co-sputtering; This method can be used to produce catalytically active gold films and requires magnetron sputtering equipment.[164] This process requires an atmosphere containing oxygen in which a gold plate and a metal oxide target such as Co_3O_4 are sputter deposited simultaneously onto a substrate to form a thin film, which is then annealed in air.

Chemical vapour deposition; In this method, the vapour of an organic gold complex such as $[Me_2Au(acac)]$ is introduced onto the surface of an evacuated metal oxide support.[165] The organic compound is then decomposed to form small gold particles through heating in air to 473-773 K. This method can give a larger range of gold particle sizes than deposition precipitation, though it can also give particles as small as 2nm (mean diameters= 7-9 nm). A similar method has been reported using gold nanoparticle suspensions instead of molecular gold precursors.[166] This gave gold particles of c.a. 50nm in size, which may not be as useful for the synthesis of catalytic gold films that require smaller particle sizes.

Anionic adsorption; this can be carried out using $HAuCl_4$ in aqueous solution and by lowering the pH of a solution containing a support to

below its point of zero charge to positively charge the support surface. The anionic gold precursor in solution can then bind to the support. The problem with this technique is that only about 20% of the gold in the solution gets deposited before equilibrium is reached giving a loading of about 1.5 wt. %. This method has been reported to give average particle sizes between 4 and 6nm[167] after calcination at 537 K.

Cation adsorption; This is a similar method to anionic adsorption but the pH of the solution containing the support is increased to past its isoelectric point so that the main surface species is O^-. This allows positively charged gold complexes such as $[Au(en)_2]^{3+}$ to adsorb onto the charged surface.[167] Following calcination at 573 K, metallic particles are left on the support surface. By increasing the aging time it is possible to get all of the gold in solution deposited on to the support.

Table 4.4. Table comparing cationic and anions adsorption of gold species on to TiO_2.[167]

Preparation Method	pH of reaction solution	Au precursor used	Au loading (wt. %)	Aging time (h)	Temp. (K)	Average particle size (nm)	Particle size distribution (nm)
Anionic adsorption	2	$AuCl_4^-$	1	1	353	5.6	2 - 8.3
Anionic adsorption	2	$AuCl_4^-$	1.5	15	353	4.4	2 - 7.5
Cationic adsorption	9.4	$Au(en)_2^{3+}$	1.1	1	353	2.1	1 - 3.5
Cationic adsorption	9.4	$Au(en)_2^{3+}$	6.1	16	353	4.1	1.7 - 6.4

These methods can be used to produce hemi-spherical gold particles on the flat planes of the metal oxide support that are more stable than spherical particles. Through the use of these preparation methods, the catalysts obtained are more highly active for different catalytic processes than unsupported gold.

4.1.3. Active site in catalysis

There is a lot of interest in the nature of the active species on gold catalysts. Activity has been attributed to cationic gold, metallic gold and interfacial gold-support atoms.

Model catalysts have been prepared to study the effect of particle size on the activity of TiO_2 supported gold.[168] Gold was deposited on to a TiO_2 (110) surface with varying coverage, affecting the size of the clusters formed. These surfaces were then analysed by scanning tunnelling electron microscopy and tested for catalytic activity for the oxidation of CO. The results of the study showed that the size of the gold particles did indeed have an effect on the catalytic activity, with activity peaking when clusters of 3.5 nm in size (and two layers of atoms thick) were present. This is in agreement with the work by Hutchings *et al.* on Fe_2O_3 supported bi-layer gold clusters.[53] The activity of the clusters increased as their size decreased from 6 to 3.4 nm. However, shrinking the clusters further led to a decrease in activity conflicting with Hutchings work. The decreasing particle size was correlated with a transition from metallic to non-metallic character by measuring the clusters' band gaps and it was concluded that this structure sensitivity originated from quantum size effects. This means that by careful selection of the support, the properties of the supported gold can be altered. Applying these findings to real support catalysts may be difficult due to the increased complexity of the support surface.

In 2004 Chen and Goodman prepared model catalysts of well ordered gold mono- and bi-layers on an ultrathin TiO_2 surface, grown on a molybdenum (111) surface.[169] The bi-layers were extremely active for CO oxidation whereas the mono-layers had much lower activity as seen in figure 4.9. What could be concluded from this investigation is that TiO_2 was acting as a promoter for the gold. The interfacing of the first layer of gold with Ti^{3+} is necessary for the activation of O_2.

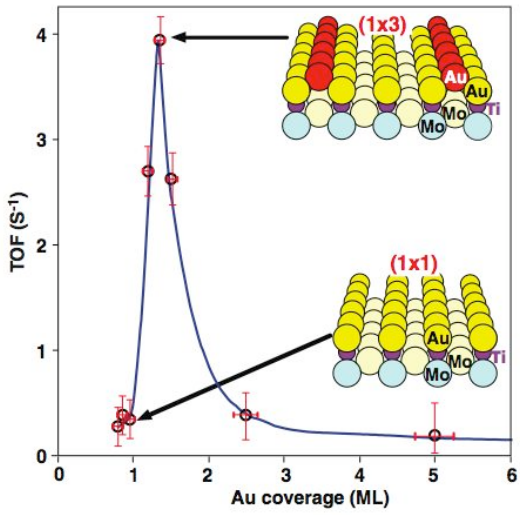

Figure 4.9. A plot showing the change in turnover frequency (TOF) with gold coverage of an ultrathin TiO_2 surface.[169]

In 2008, Hutchings and co-workers reported that two identically prepared Fe_2O_3 supported gold catalysts dried in different ways (one in static air, one in flowing air) gave slightly different average gold article sizes[53]. The catalyst dried in flowing air had an average gold particle size of 7 nm and the other, 5.4 nm. It was expected that the catalyst with the smaller mean particle size would have greater activity for CO oxidation at room temperature, but the opposite was observed. The catalyst dried in flowing air gave 100% CO conversion whereas the other gave only trace CO conversion. Investigation of the catalysts with aberration corrected high resolution scanning transmission electron microscopy found that both samples shared the presence of gold particles 2- 15 nm in size as well as individual gold atoms deposited on the Fe_2O_3 surface. What was present on the active sample, but missing from the inactive sample, was sub-nanometer gold clusters (0.2-0.5 nm in size) consisting of only a few gold atoms (figure 4.10). Calculations suggested that these tiny clusters only accounted for c.a. 1% of the gold on the surface of the support with c.a. 99% found in larger particles. The low frequency and extremely small size of these clusters makes them very difficult to detect through the usual techniques such as X-ray diffraction and EXAFS because of the cluster's

tiny signal contribution. Further investigation revealed that the activity may be attributed specifically to bi-layer clusters of about 0.5 nm in size. If more is to be learned about these clusters, then samples must be prepared with an increased frequency of clusters and a reduced frequency of larger gold particles.

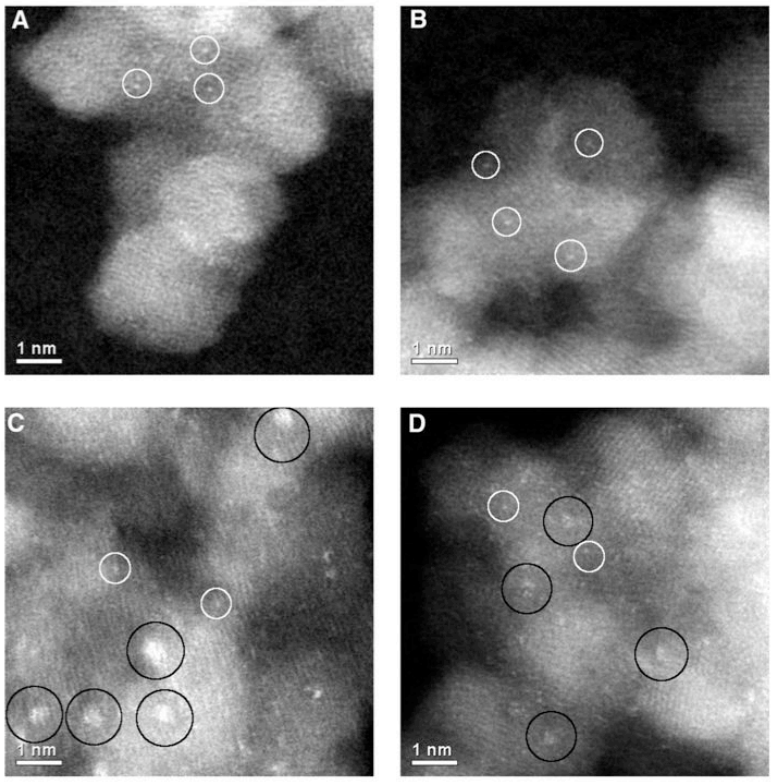

Figure 4.10. **HAADF STEM images of gold supported on Fe_2O_3.[53] Images A and B are of the inactive catalyst with individual atoms of gold highlighted by white circles. Images C and D are of the active catalyst and feature sub-nanometer gold clusters circled in black along with individual atoms of gold circled in white.**

A MgO supported gold catalyst was synthesised through the deposition of the molecular species $[Au(CH_3)_2(acac)]$ on to the partially dehydroxylated support.[152] After removing the methyl ligands, the catalyst was activated. Analysis of the active catalyst revealed small clusters composed of a few gold atoms on the surface of the support. XANES data showed these clusters to be cationic and that these particles were responsible for the activity observed for CO oxidation.

Another investigation of the active sites on gold catalysts looked at the effect of leeching off all the metallic gold from a lanthanum doped CeO_2 supported gold catalyst.[170] After leeching, the gold that remained was the cationic species on the surface defects of the support. Activity for the water gas shift reaction was enhanced upon the removal of the gold particles. This work, as well as many other papers,[171] gives clear evidence of the catalytic activity of cationic gold in various reactions. Activity cannot be ascribed exclusively to this species though, as evidence has also be given for the role of clusters and interfacial sites too.

FTIR spectroscopy was employed by Vindigi *et al*. to explore the relationship between the structure of the gold particles on the surface of metal oxide supports and their catalytic properties.[172] It was revealed that CO adsorbs on both corner and edge but not terrace sites on metallic gold particles 3-4 nm in size and on non-reducible oxides such as zirconia. For small non-metallic gold particles of 1.6 nm in size, CO adsorbs on the surface. This is very useful information for active catalyst design but it is extremely difficult to prepare a catalyst with only one specific size and shape of gold particle on the surface, especially using the popular deposition-precipitation and co-precipitation techniques. A method is needed whereby exact sized gold particles can be deposited on to the surface of a support without variation between them. This way, the effect of minor changes in gold particles varying from one catalyst to another could be observed through the catalysts' activity.

These are just a few examples of work on the active sites of gold catalysts. The debate as to what specifically enables gold to catalyse certain reactions will continue.

4.1.4. X-ray absorption spectroscopy

Catalyst characterisation is very important as it gives an insight into the nature of the active component. It is also important to understand the changes that a catalyst undergoes during pre-treatments such as calcination. X-ray absorption spectroscopy (XAS) is an invaluable tool in catalyst characterisation as it can be employed during any stage of the catalysts lifetime, from synthesis, pre-treatment, and even under reaction conditions. Due to the element specific nature of XAS, information on the structure of the active component of a supported heterogeneous catalyst, such as particle size, and other atoms bound to the absorbing atom, can be revealed.

Gates and co-workers[152] employed XAS to monitor the decomposition of magnesium oxide supported mononuclear gold complexes during calcination and in the presence of different reaction mixtures. EXAFS data confirmed the loss of ligands from the gold complex, resulting in the formation of bare gold clusters 5-6 atoms in size.

4.1.5. Current work

It is well known that both the size and shape of phosphine-stabilised molecular gold clusters can be easily tuned through a function of the size and donor properties of the phosphine employed. As previously discussed in Chapter 3, this allowed for manipulation of phosphine ligands to generate gold clusters with specific numbers of gold atoms at their core (either 6 or 9 atoms depending on the phosphine ligands used). The aim of this part of the project was to use the previously synthesised gold clusters to generate supported gold catalysts. Gold clusters were used as precursors to the active gold particles on the support. It was thought that it would be possible to have a high degree of control over the size of the gold particles formed on the catalyst as the gold is already grouped together in cluster of 6 or 9 atoms. As the clusters are all exactly the same size and shape when they are synthesised, the aim was to use them to create monodisperse distributions of gold particles on the surface of a support. Catalysts were prepared in this way and their catalytic activities evaluated. This way, it would be possible to directly compare clusters of different sizes to each other in terms of their catalytic activity. The effect of altering the loading of the gold, along with calcination temperature on the catalytic activity was also investigated.

4.2. Experimental methods

4.2.1. Deposition of $[Au_6(Ph_2P(o\text{-tolyl}))_6](NO_3)_2$ on to silica nanospheres

Silica nanospheres (1.00g, moles) in dry powder form was placed into a round-bottomed flask and a small amount of methanol (~3 ml) was added. The round-bottomed flask was then sealed and placed into an ultrasonic bath for 5 minutes to break up any aggregations of the silica spheres. To the slurry, a solution of $[Au_6(Ph_2P(o\text{-tolyl}))_6](NO_3)_2$ (mass dependent on required gold loading, see table 4.5) dissolved in methanol (~5 ml) was added and stirred for 1 hour in the sealed container. The container was then returned to the ultrasonic bath for 5 minutes before removing the methanol under vacuum. This left a brown solid on the inside to the round-bottomed flask, that was stored until calcination or use.

Table 4.5. Quantities of $[Au_6(Ph_2P(o\text{-tolyl}))_6](NO_3)_2$ needed to produce supported gold catalysts with varying gold loadings.

Desired gold loading of catalyst	Mass of $[Au_6(Ph_2P(o\text{-tolyl}))_6](NO_3)_2$ per gram of support material	Moles of $[Au_6(Ph_2P(o\text{-tolyl}))_6](NO_3)_2$ per gram of support material
0.1 wt. %	2.5 mg	8.44×10^{-7}
1.0 wt. %	25 mg	8.44×10^{-6}
4.0 wt. %	100 mg	3.37×10^{-5}

4.2.2. Deposition of $[Au_9(PPh_3)_8](NO_3)_3$ on to silica nanospheres

The same method used to deposit $[Au_6(Ph_2P(o\text{-tolyl}))_6](NO_3)_2$ on to the silica nanospheres was used to deposit $[Au_9(PPh_3)_8](NO_3)_3$. The mass of $[Au_9(PPh_3)_8](NO_3)_3$ used per gram of silica nanosphere support is shown in table 4.6.

Table 4.6. A table showing the quantities of $[Au_9(PPh_3)_8](NO_3)_3$ needed to produce supported gold catalysts with varying gold loadings.

Desired gold loading of catalyst	Mass of $[Au_9(PPh_3)_8](NO_3)_3$ per gram of support material	Moles of $[Au_9(PPh_3)_8](NO_3)_3$ per gram of support material
0.1 wt. %	2.3 mg	5.67×10^{-7}
1.0 wt. %	22.9 mg	5.67×10^{-7}
4.0 wt. %	91.5 mg	2.26×10^{-5}

4.2.3. Calcination of gold clusters supported on silica nanospheres

The silica nanosphere supported gold clusters (either $[Au_6(Ph_2P(o\text{-tolyl}))_6](NO_3)_2$ or $[Au_9(PPh_3)_8](NO_3)_3$) (1.00 g) were measured into a ceramic boat which was then placed into a furnace. The furnace was programmed with a ramp rate of 5 ^{o}C/min to the desired calcination temperature (either 300 or 500 ^{o}C). When the furnace reached the calcination temperature it was programmed to dwell at that temperature for 1 hour before deactivating and allowing the catalyst to cool to room temperature.

4.2.4. Catalytic Oxidation of Benzyl alcohol using supported gold catalyst

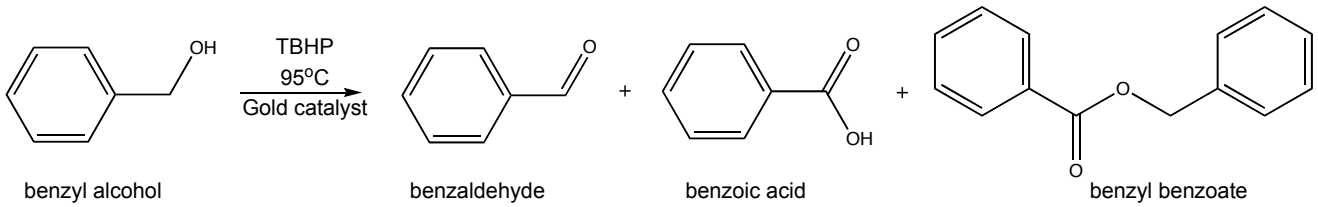

Figure 4.11. Reaction scheme of oxidation of benzyl alcohol

In a typical reaction, 0.25 g of catalyst was weighed into a reactor vessel. To this, 5.4 ml (26.06 mmol) of benzyl alcohol and 5.67 ml (5.0-6.0 M in decane) of tert-butyl hydroperoxide was added. After placing the reactor in the temperature controller, it was fitted with a condenser and a thermocouple connected to the temperature controller before being heated to 95^{o}C whilst being stirred. Samples of the reaction mixture were collected at t= 0, 0.25, 0.5, 0.75, 1, 2, 3 and 4 hours. After 4 hours, the reaction was stopped by cooling the mixture to 5^{o}C. The samples were analysed using a PerkinElmer Clarus 500 Gas Chromatograph.

4.2.5. *In situ* calcination EXAFS data collection

EXAFS data were collected, *in situ* whilst calcining the catalysts, at station 9.3 at the S.R.S. in Daresbury Laboratories using a specially designed furnace. For the calcination of $[Au_9(PPh_3)_8](NO_3)_3$ supported on silica nanospheres, the furnace was programmed with a ramp rate of 10 ^{o}C/min from room temperature up to 200^{o}C and then a rate of 5 ^{o}C/min up to 500 ^{o}C with a dwell time of 80 minutes before cooling down again. Heating $[Au_6(Ph_2P(o\text{-tolyl}))_6](NO_3)_2$ supported on silica nanospheres was also carried out using a temperature programmed furnace. The sample was heated from room temperature to 550 ^{o}C at a rate of 5 ^{o}C/min with a 30 minute pause before cooling. Au L_{III} XAS data was collected in the

range 11.8-12.7 keV using transmission geometry. The scan was collected over 344 seconds with a 60 second gap between each scan.

Background subtraction of the EXAFS data was carried out using VIPER[60]. Curve fitting analysis of the data was performed using EXCURVE [61].

XRD data was collected on a Bruker-AXS D4 powder X-ray diffractometer.

Electron microscope images were collected on a 100 keV Transmission electron microscope and a JEOL JSM-6301F Field Emission Scanning electron microscope.

TGA analysis of $[Au_6(Ph_2P(o\text{-tolyl})_6](NO_3)_2$ and $[Au_9(PPh3_{)8}](NO_3)_3$ was carried out using a Netsch DSC/TGA.

4.3. Results and discussion

Gold clusters of either 6 or 9 gold atoms stabilised by phosphines were deposited on to a silica nanosphere support with loadings of either 0.1, 1.0 or 4.0 weight % (wt.%) gold. In order to remove the phosphine ligands, the samples were calcined at either 300 or 500 ^{o}C. The uncalcined and calcined catalysts were then characterised using a range of techniques, including *in situ* EXAFS. The catalysts activities were then tested for the oxidation of benzyl alcohol. In this section, the result of the *ex situ* characterisation will first be discussed, followed by the *in situ* characterisation and finally the catalytic activity results.

4.3.1. TGA data

TGA of both $[Au_6(Ph_2P(o\text{-tolyl})_6)](NO_3)_2$ and $[Au_9(PPh_3)_8](NO_3)_3$ (see appendices 2 and 3) heated in air revealed that the there was a significant decrease in the mass of the complexes as the temperature increased from room temperature to 300 ^{o}C consistent with phosphine loss. The highest rate of change in the mass of $[Au_6(Ph_2P(o\text{-tolyl})_6)](NO_3)_2$ heated in air occurred at 300 ^{o}C whereas for $[Au_9(PPh_3)_8](NO_3)_3$ this occurred at 250 ^{o}C. This is in general agreement with the *in situ* XAS data, showing that decomposition of $[Au_9(PPh_3)_8](NO_3)_3$ occurs at a lower temperature than $[Au_6(Ph_2P(o\text{-tolyl})_6)](NO_3)_2$.

4.3.2. XRD and electron microscope data - size and distribution of the gold particles

Variations in the loading of the gold and calcination temperature gave a large range of conditions for gold particles to form on the surface of the

silica nanospheres. In order to gauge what size particles were being formed during calcination, powder XRD was carried out. The recorded spectra featured sharp peaks indicating the presence of large gold crystallites. By carrying out basic analysis and by using the Scherrer equation,[55] average gold particle sizes could be obtained for the catalysts. The average particle was calculated using the peak corresponding to gold (111) from the XRD spectra. Typical recorded XRD spectra is given in figure 4.12.

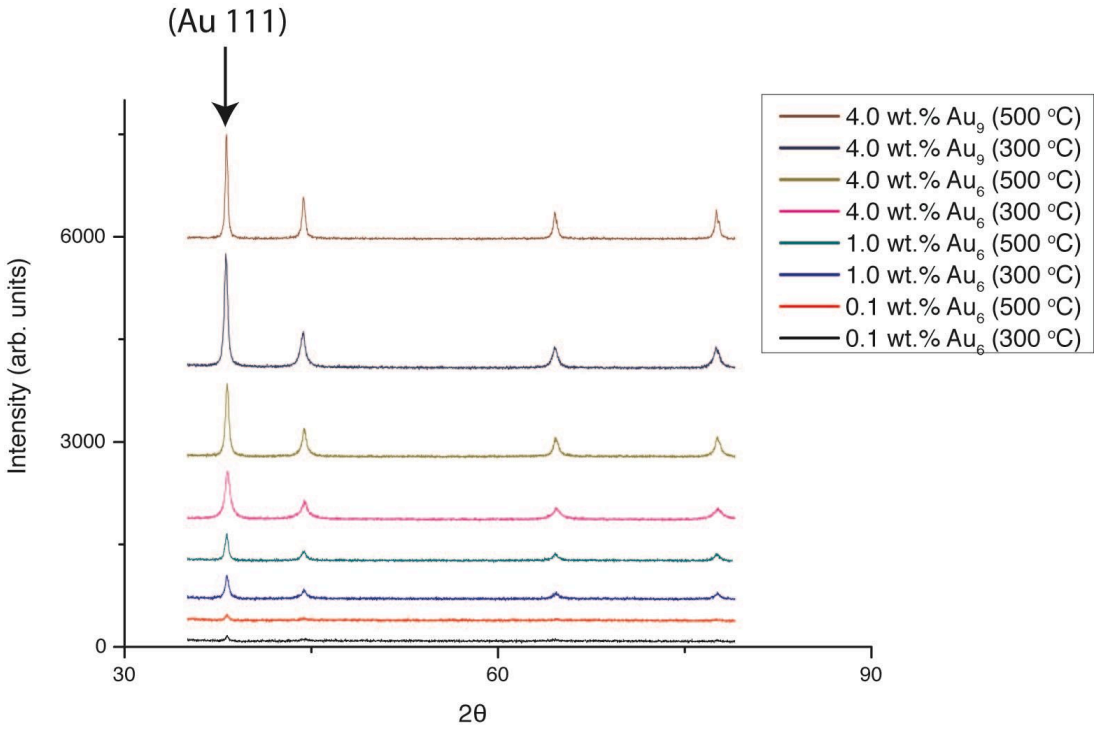

Figure 4.12. Typical XRD data recorded for gold clusters supported on silica nanospheres calcined to either 300 or 500 °C, where Au_9= $[Au_9(PPh_3)_8](NO_3)_3$ and Au_6= $[Au_6(Ph_2P(o\text{-tolyl}))_6](NO_3)_2$.

Table 4.7. A table showing the average gold particle size in $[Au_6(Ph_2P(o\text{-tolyl}))_6](NO_3)_2$ catalysts prepared with different gold loading and calcined to different temperatures.

	Uncalcined	300 ^{O}C	500 ^{O}C
0.1 wt. % Au	-	27 nm	25 nm
1.0 wt. % Au	-	18 nm	23 nm
4.0 wt. % Au	-	13 nm	19 nm

Table 4.7 presents the average particle sizes obtained for the catalysts synthesised from $[Au_6(Ph_2P(o\text{-tolyl}))_6](NO_3)_2$. This data highlights two points. Firstly, that apart from the 0.1 wt. % loaded catalysts, increasing the calcination temperature increases the average gold particle size. Secondly, increasing the gold loading of the catalyst gives smaller sized gold particles after calcination. No data is present for any of the uncalcined catalysts as the gold clusters are too small to have the long range order needed to scatter the X-rays enough for the instrument to detect. The XRD data from some of the catalysts made using $[Au_9(PPh_3)_8](NO_3)_3$ in table 4.8 shows that those calcined at 300 ^{o}C have a lower average particle size than those calcined at 500 ^{o}C.

Table 4.8. A table showing the average gold particle size $[Au_9(PPh_3)_8](NO_3)_3$ catalysts calcined to different temperatures.

	Uncalcined	300 ^{O}C	500 ^{O}C
4.0 wt. % Au	-	20 nm	29 nm

TEM and SEM investigations were carried out on a selection of samples to look at the distribution of the gold on the surface of the silica. The results are shown in figures 4.13 to 4.15.

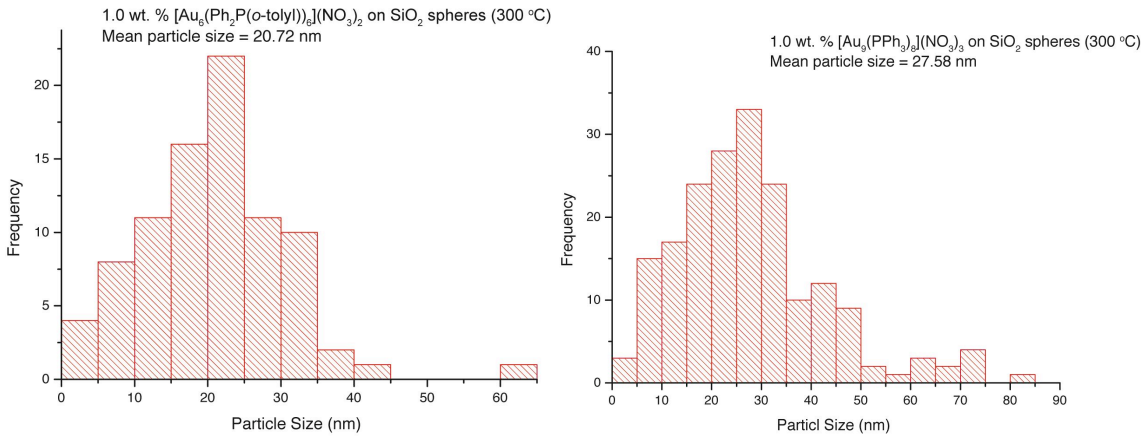

Figure 4.13. Histograms from TEM analysis to show the variation in gold particle size in catalyst synthesised from $[Au_6(Ph_2P(o\text{-toly}))_6](NO_3)_2$ or $[Au_9(PPh_3)_8](NO_3)_3$. Both of the catalysts were loaded with 1.0 wt. % gold and calcined to 300 °C.

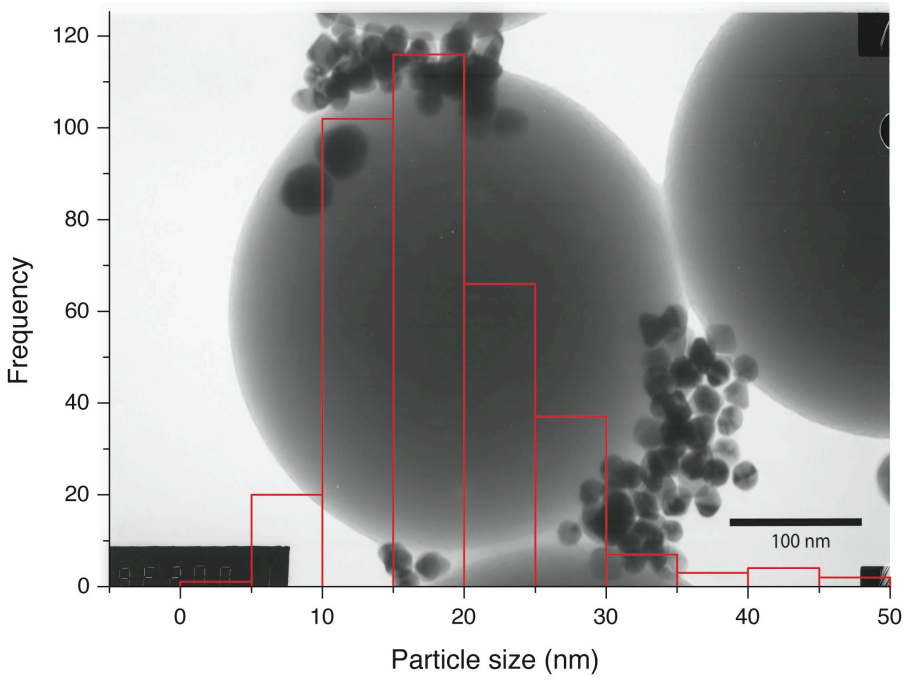

Figure 4.14. A TEM image and histogram to show the particle size distribution in $[Au_6(Ph_2P(o\text{-toly}))_6](NO_3)_2$ (4.0 wt. %) on silica nanospheres calcined at 300 °C (mean particle size = 18.31 nm).

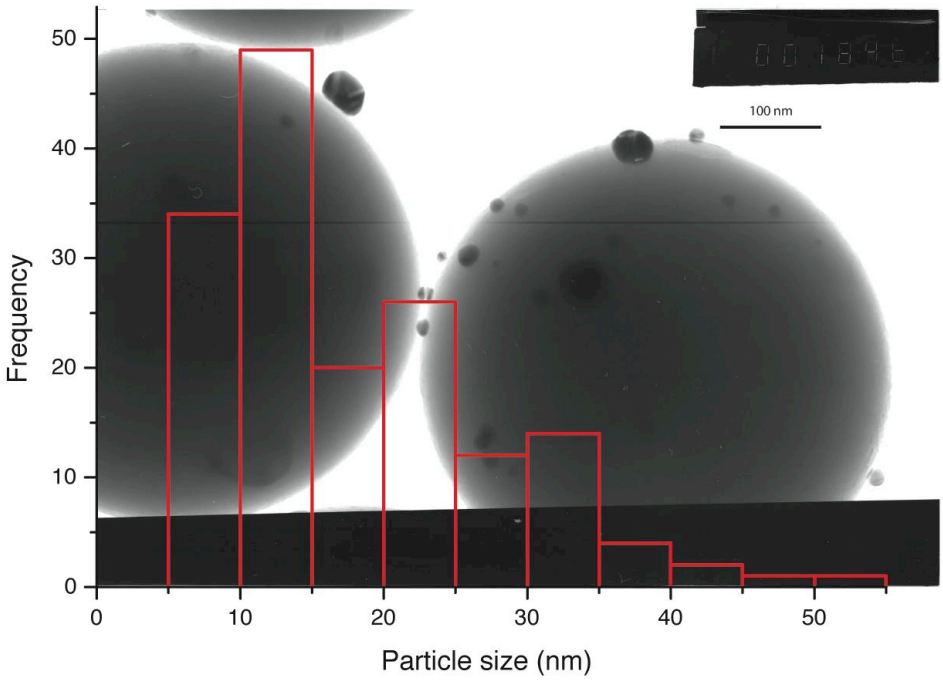

Figure 4.15. A TEM image and histogram to show the gold particle size distribution of $[Au_6(Ph_2P(o\text{-toly}))_6](NO_3)_2$ (4.0 wt. %) on silica nanospheres calcined at 500 °C (mean particle size = 22.69 nm)

The TEM results show the very broad size distributions of the gold particles in the catalysts. In agreement with the XRD data, the mean particle sizes are relatively large considering the initial size of the gold particles. This indicates that the gold is highly mobile on the surface of the silica during calcination and that there is not a strong gold-support interaction. Functionalising or pre-treating the support surface before the addition of the gold may rectify this.

4.3.3. XANES data

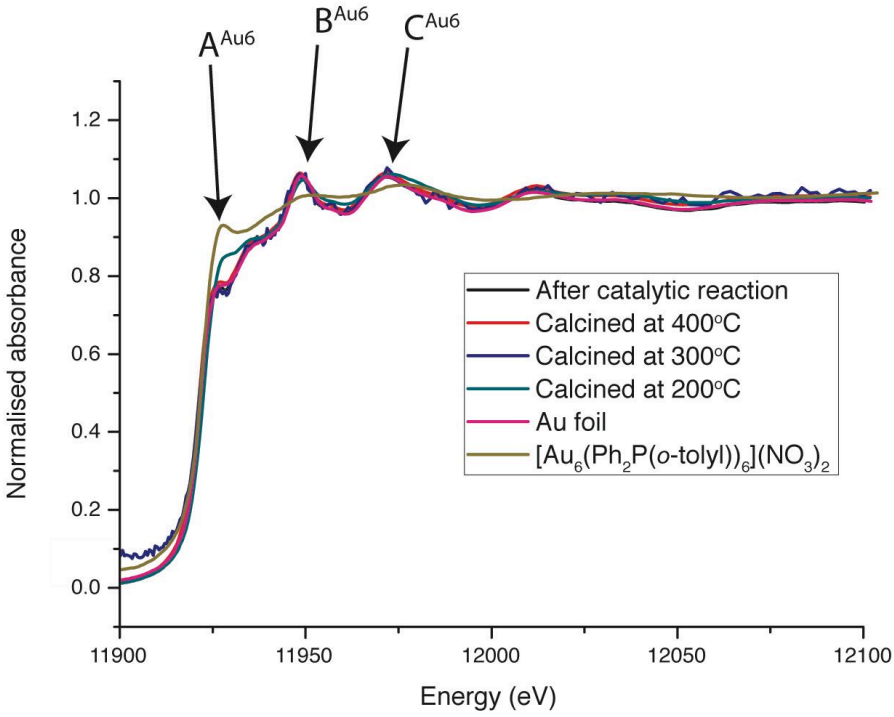

Figure 4.16. *Ex situ* Au LIII edge XANES data of $[Au_6(Ph_2P(o\text{-tolyl}))_6](NO_3)_2$ deposited on silica nanospheres (4 wt.% Au) after a range of treatments. Gold foil data is also presented.

The XANES data provides information relating to changes the gold undergoes in terms of oxidation state and coordination environment. The feature marked A^{Au6} in figures 4.16 and 4.17 is most prominent in the untreated cluster. Its presence indicates that the cationic charge distributed throughout $[Au_6(Ph_2P(o\text{-tolyl}))_6](NO_3)_2$ has not been completely lost. It is clear, that after calcination to 300 and 400 ^oC, and after uncalcined clusters deposited on the support have been used to carry out the catalytic reaction, that metallic gold is present with no charge. This is seen through the decrease in intensity of feature A^{Au6} and the presence of strong features marked as B^{Au6} and C^{Au6}, due to $gold^0$. After these treatments, the XANES spectra is very similar to that of metallic gold.

Temperature programmed *in situ* heating X-ray absorption experiments of the gold clusters supported on the silica nanospheres were carried out to

provide insight into the changes occuring gold during calcination. These experiments give us in depth detail about how the clusters of gold respond to different temperatures. With this information, it is possible to directly link the calcination conditions to the catalytic activity of the samples.

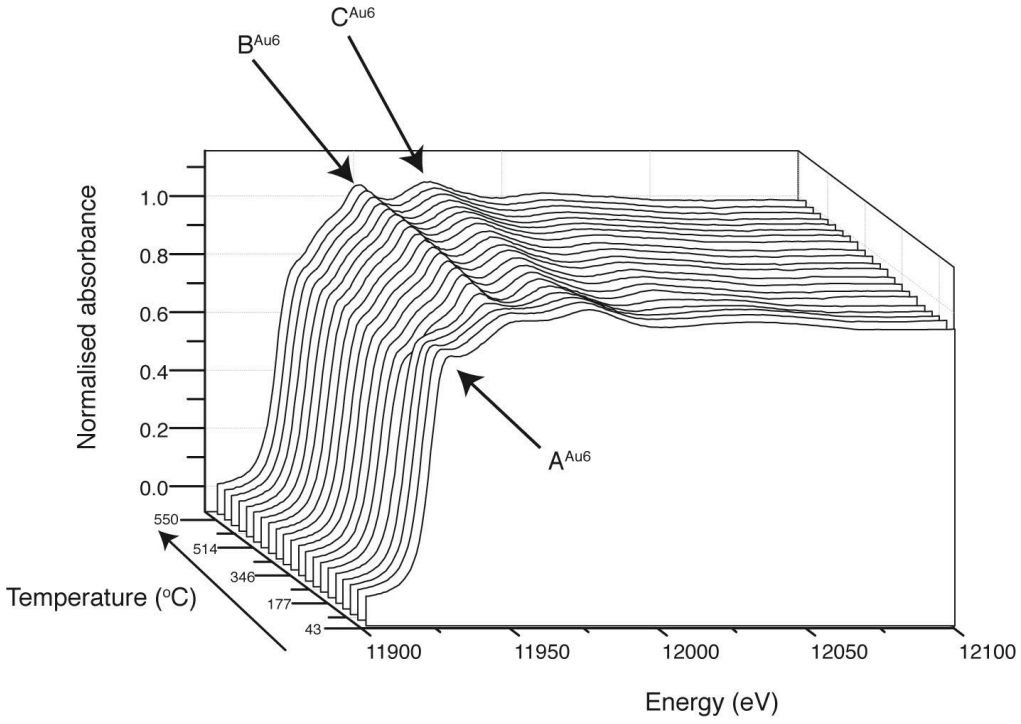

Figure 4.17. Au LIII edge XANES data following the temperature programmed calcination of $[Au_6(Ph_2P(o\text{-tolyl}))_6](NO_3)_2$ supported on silica nanospheres (4.0 wt. % Au) from 45 to 550 °C, at a rate of 5 °C/min.

The XANES data from the *in situ* calcination of $[Au_6(Ph_2P(o\text{-tolyl}))_6](NO_3)_2$ agrees with the *ex situ* data, in that the positive charge of the gold is lost and metallic gold particles are formed as the temperature increases to 550 °C. The *in situ* data shows the abrupt loss of the feature A^{Au6} (see figure 4.17) as the temperature goes from 212 °C to 245 °C. This is in agreement with TGA data that showed that the cluster rapidly loses the phosphines between 200 and 300 °C. As the temperature increased beyond 245 °C, a gradual increase in the intensity of features B^{Au6} and C^{Au6} is observed. As peaks B^{Au6} and C^{Au6} are observed in metallic gold

XANES spectra, their presence suggests that metallic gold particle formation occurs. This is highlighted in figure 4.18.

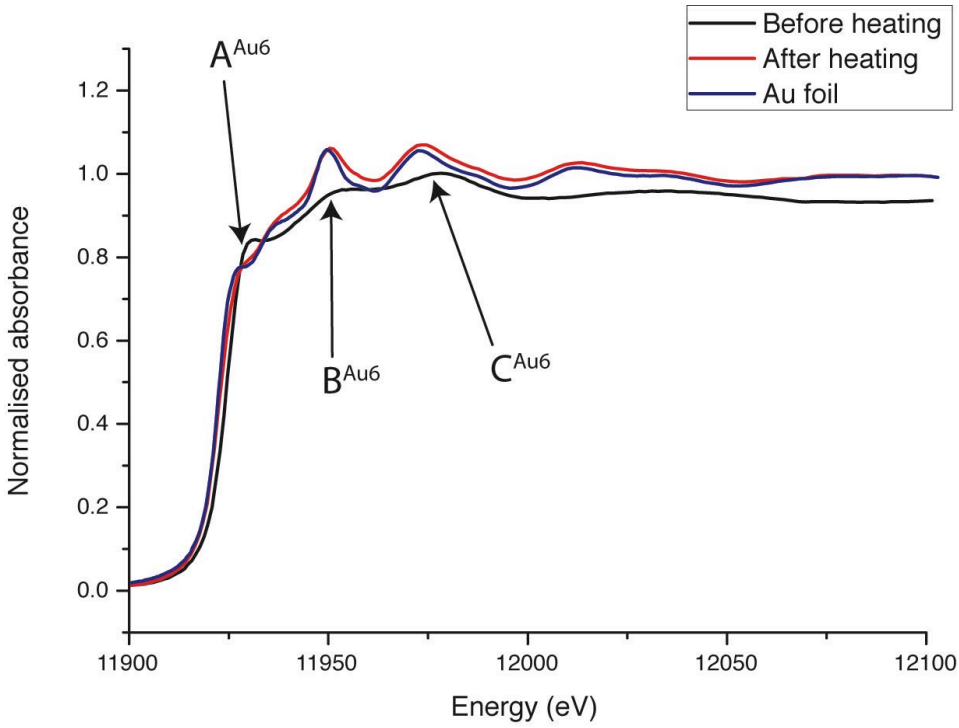

Figure 4.18. Au LIII normalised XANES data highlighting the differences between untreated $[Au_6(Ph_2P(o\text{-tolyl}))_6](NO_3)_2$ and after calcination at 550 ^oC. Gold foil data is also shown for reference.

The XANES data from the *in situ* heating of $[Au_9(PPh_3)_8](NO_3)_3$ shows the sudden loss of charge at about 200 ^oC, as the peak marked A^{Au9} (showing cationic charge) in figure 4.19 decreases in intensity. What then follows is an increase in intensity of features B^{Au9} and C^{Au9}, showing the clusters are converted into metallic gold particles, which carry these characteristic features in their XANES spectra. If the initial XANES spectra of $[Au_9(PPh_3)_8](NO_3)_3$ on the surface of the silica is compared with the final spectra after the calcination is complete (figure 4.20 below), it is clear that the structure of the cluster has been lost, along with the charge on the gold. After heating the clusters in air, the phosphine ligands are removed and metallic gold particles remain.

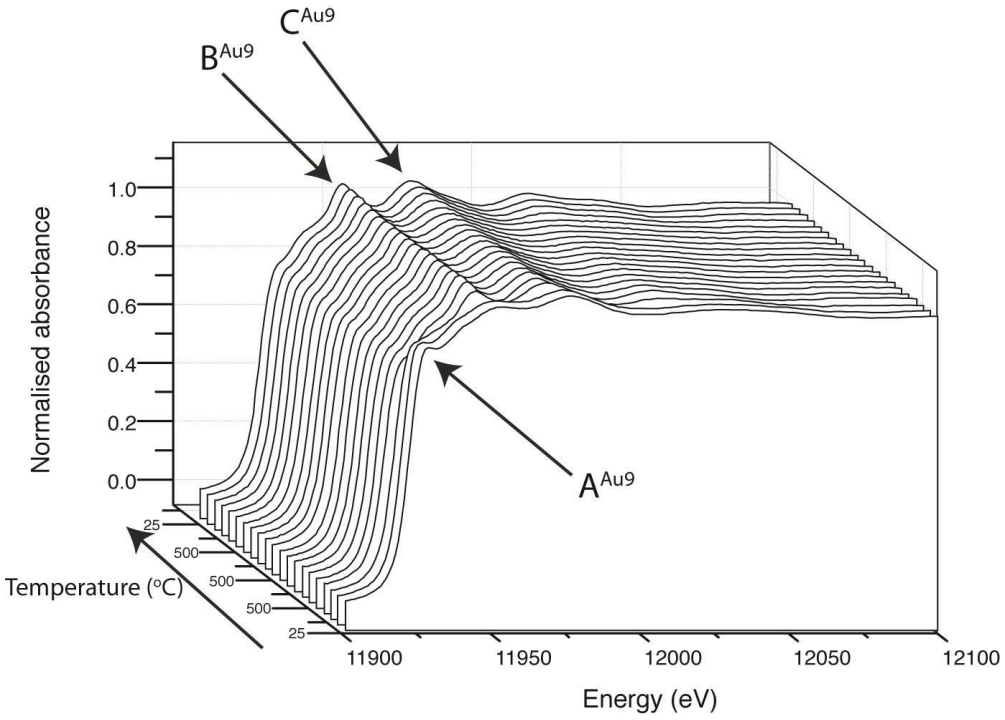

Figure 4.19. Au LIII normalised XANES data showing the temperature programmed calcination of $[Au_9(PPh_3)_8](NO_3)_3$ supported on silica nanospheres (4.0 wt. % Au).

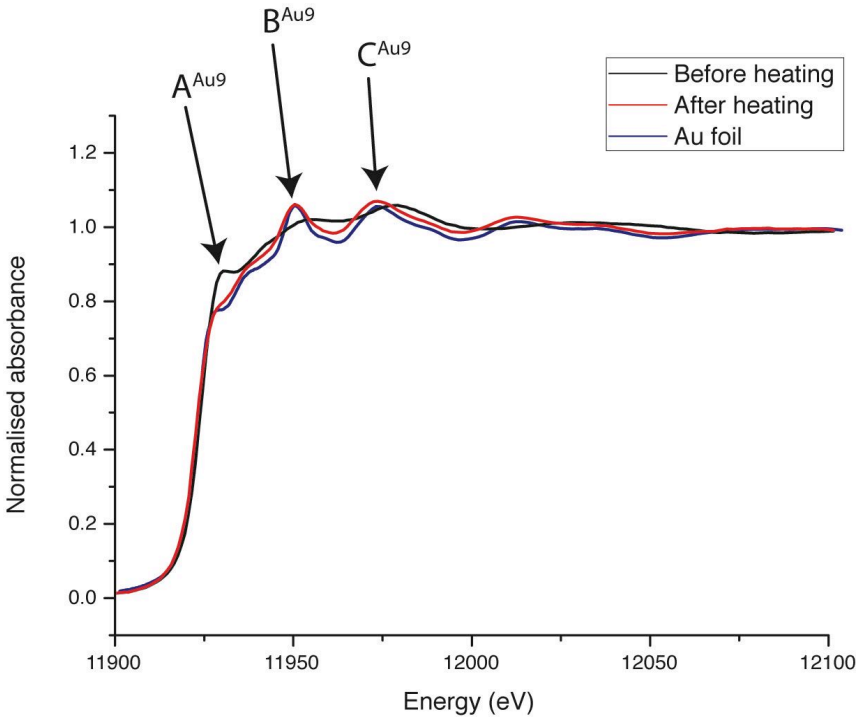

Figure 4.20. Au LIII normalised XANES data highlighting the difference between $[Au_9(PPh_3)_8](NO_3)_3$ supported on silica nanospheres before and after heating to 500 ^oC. Au foil XANES data is shown for reference.

The XANES data for both the $[Au_6(Ph_2P(o\text{-tolyl}))_6](NO_3)_2$ and $[Au_9(PPh_3)_8](NO_3)_3$ on silica nanospheres show that both of the supported clusters exhibit the same behaviour under high temperature treatment conditions. They both lose their cationic charge once they reach temperatures about 200 ^oC and then go on to form metallic gold particles. The data also shows that $[Au_9(PPh_3)_8](NO_3)_3$ loses it phosphine ligands at a lower temperature than $[Au_6(Ph_2P(o\text{-tolyl}))_6](NO_3)_2$. as PPh_3 is more readily oxidised then $Ph_2P(o\text{-tolyl})$.

4.3.4. EXAFS data

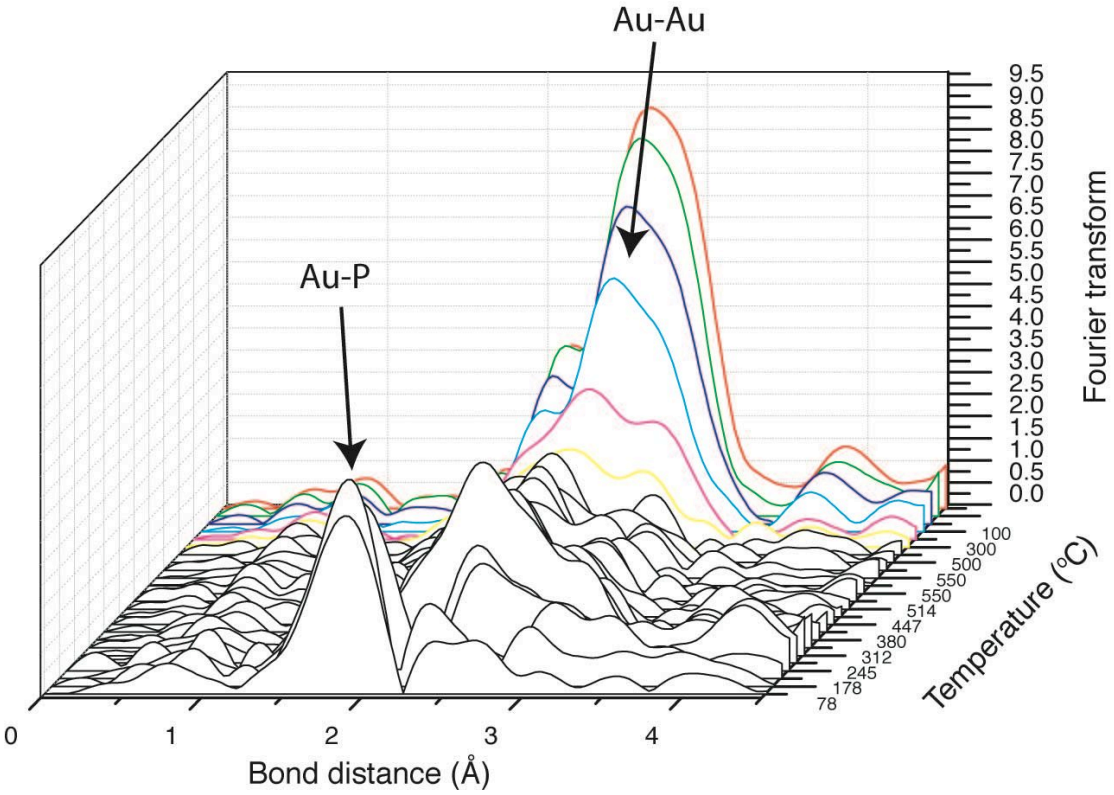

Figure 4.21. Phase shift uncorrected stacked Fourier transformed EXAFS data from the *in situ* heating of $[Au_6(Ph_2P(o\text{-tolyl}))_6](NO_3)_2$ (4.0 wt. % Au) supported on silica nanospheres. The coloured peaks indicate the cooling phase of the experiment.

The Fourier transformed Au L_{III} edge EXAFS data shown in figure 4.21 gives a good overall view of the transformation taking place in the sample. It can be seen that as the temperature increases, the intensity of the peak marked Au-P decreases due to the gradual loss of the phosphines. The peak marked as Au-Au shows little change up to 245 ^{o}C where it suddenly increases in intensity. It is only after the continued heating has ended that it increases further in intensity (during the cooling period). In agreement with the data obtained from the XANES, during the initial stages of heating the phosphine ligands are lost. The gold particles remaining then grow in size slightly, but stay at this size until the temperature reaches 500 ^{o}C when they marginally decrease in size. However, upon cooling, an increase in the intensity of the Au-Au peak is

observed which is due to a decrease in the thermal disorder. A small shift in the Au-Au peak position is also observed accounting for the general increase in Au-Au bond length as the gold is reduced from a cationic species to metallic.

Analysis of the Au L_{III} EXAFS data recorded during the *in situ* heating of $[Au_6(Ph_2P(o\text{-tolyl}))_6](NO_3)_2$ on silica nanospheres gave more insight into the XANES and FT data. Typical best fits of the calculated data to the experimental data are given in Appendix 2. As the temperature increased to 200 ^oC, there is little change in the Au-Au coordination number (figure 4.22). However, once the temperature exceeded 200 ^oC, the coordination number (CN) rapidly increased from ~3 to 9. As the temperature increases to 550 ^oC the CN stays around 9.5. Once the furnace was deactivated and the sample had cooled down, the final value for of the Au-Au CN was 8.6 (bulk metallic gold has a first shell CN of 12). This suggests that there is a definite increase in the size of the gold particle as the ligands are removed from $[Au_6(Ph_2P(o\text{-tolyl}))_6](NO_3)_2$ through calcination, but the particles are smaller than bulk gold.

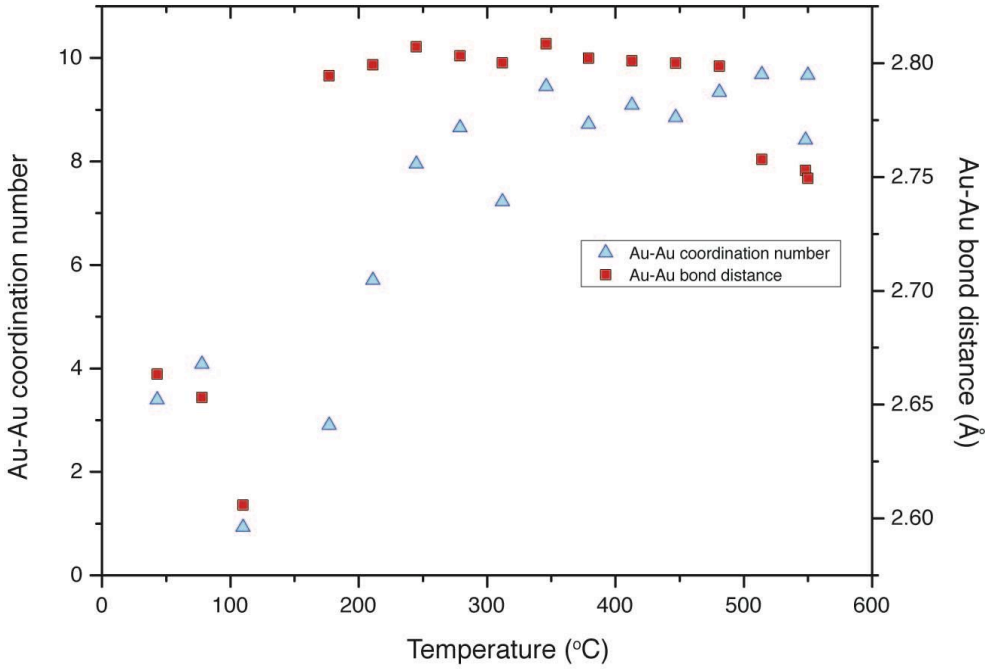

Figure 4.22. Variation of the Au-Au coordination number and Au-Au bond distance of $[Au_6(Ph_2P(o\text{-tolyl}))_6](NO_3)_2$ (4.0 wt. % Au) on silica nanospheres with increasing temperature (derived from EXAFS data).

Further evidence of the transformation of cationic gold to metallic gold is observed by looking at the Au-Au bond distance. As mentioned in section 3.1.2, in a cationic state, it is common for the Au-Au bond distance to be below 2.7 Å.[68, 72, 173] In an uncharged metallic state, the Au-Au bond distance is 2.88 Å (gold foil). In figure 4.22, it can be seen that as the temperature increases from 110 to 177 °C, the Au-Au bond distance jumps from 2.6 to 2.79 Å. As the temperature continued to increase up to 500 °C, the Au-Au bond length stayed at 2.79 Å, but when the temperature exceeded this (at 550 °C), the Au-Au bond distance started decreasing slightly to 2.75 Å. This could mean that at 550 °C, smaller particles of gold were formed than were present lower at temperatures. Upon cooling back down to room temperature (see figure 4.23), the Au-Au bond distance appears to increase to 2.82 Å. This value is slightly lower than that of bulk metallic gold due to the size of the gold particles,

as the Au-Au bond length in small particles (>50 nm) is lower than that observed in bulk.[174] The coordination fluctuates around 8 during cooling.

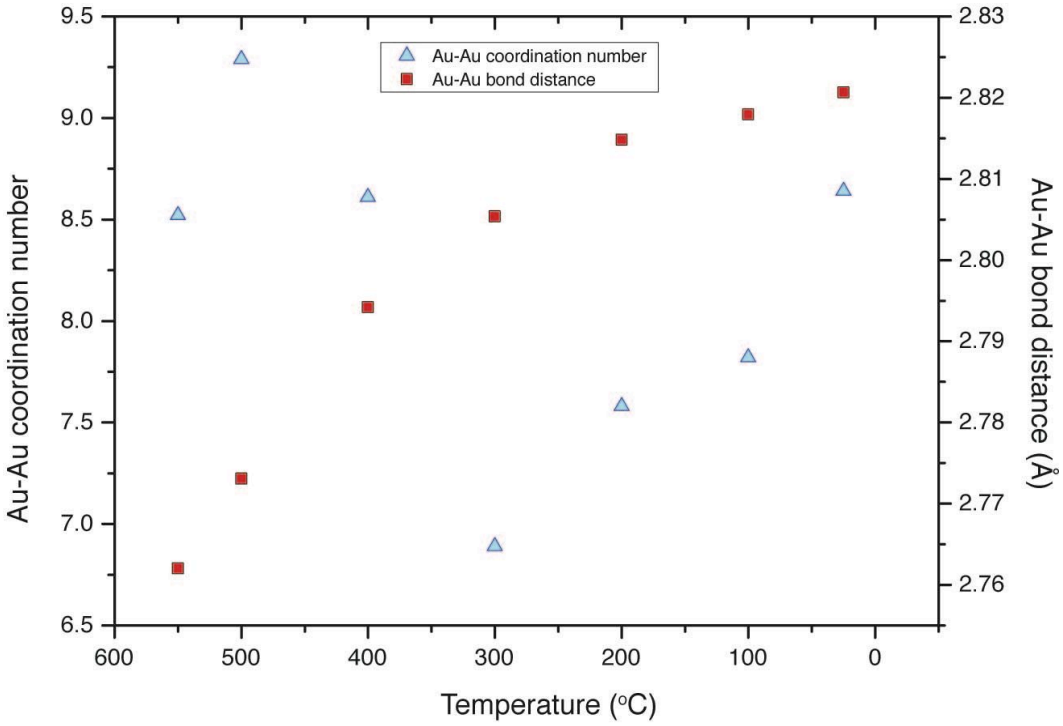

Figure 4.23. Variation of the Au-Au coordination number and Au-Au bond distance of $[Au_6(Ph_2P(o\text{-tolyl}))_6](NO_3)_2$ (4.0 wt. % Au) on silica nanospheres with decreasing temperature following calcination (derived from EXAFS data).

Considering the Au-Au bond distance before (2.66 Å) and after (2.82 Å) the calcination process, there is further evidence that calcination to 550 ^oC increases the size of the gold particles on the surface of the silica nanospheres. This is in good agreement with the Au-Au coordination number data described earlier.

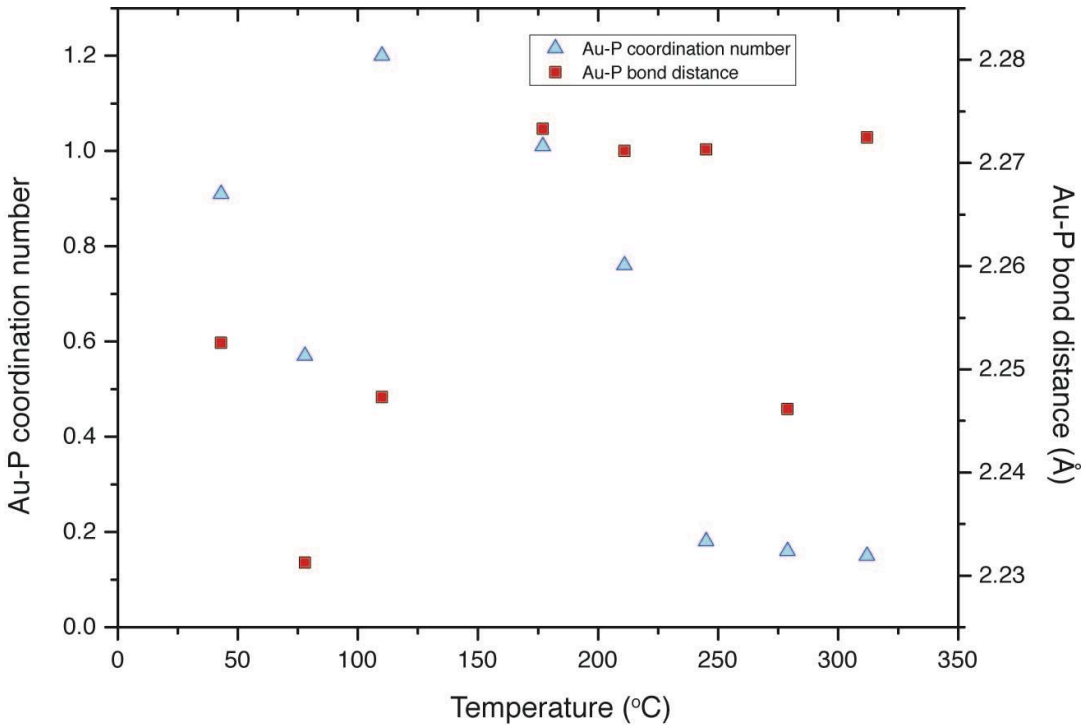

Figure 4.24. Variation of the Au-P coordination number and Au-P bond distance of $[Au_6(Ph_2P(o\text{-tolyl}))_6](NO_3)_2$ (4.0 wt. % Au) on silica nanospheres with increasing temperature (derived from EXAFS data).

Figure 4.24 shows how the Au-P coordination number generally started to decrease once the temperature inside the furnace exceeded 175 ^{o}C and by the time it had reached 225 ^{o}C, there was very little phosphorus remaining bound to the gold. It is also interesting to note the small changes in the Au-P bond distance as the temperature increases. As the temperature increased from room temperature to 175 ^{o}C, the bond length also increased slightly from 2.23 to 2.27 Å. As the accuracy of EXAFS data with respect to bond distance is ± 0.02 Å (whereas CN ± 10%), this small change is significant. This is due to the decrease in the stability of the bond as the temperature approaches that at which the bond is broken through oxidation of the phosphine. TGA data corroborated with the EXAFS data, showing that the phosphine ligands start to be lost at 175 ^{o}C.

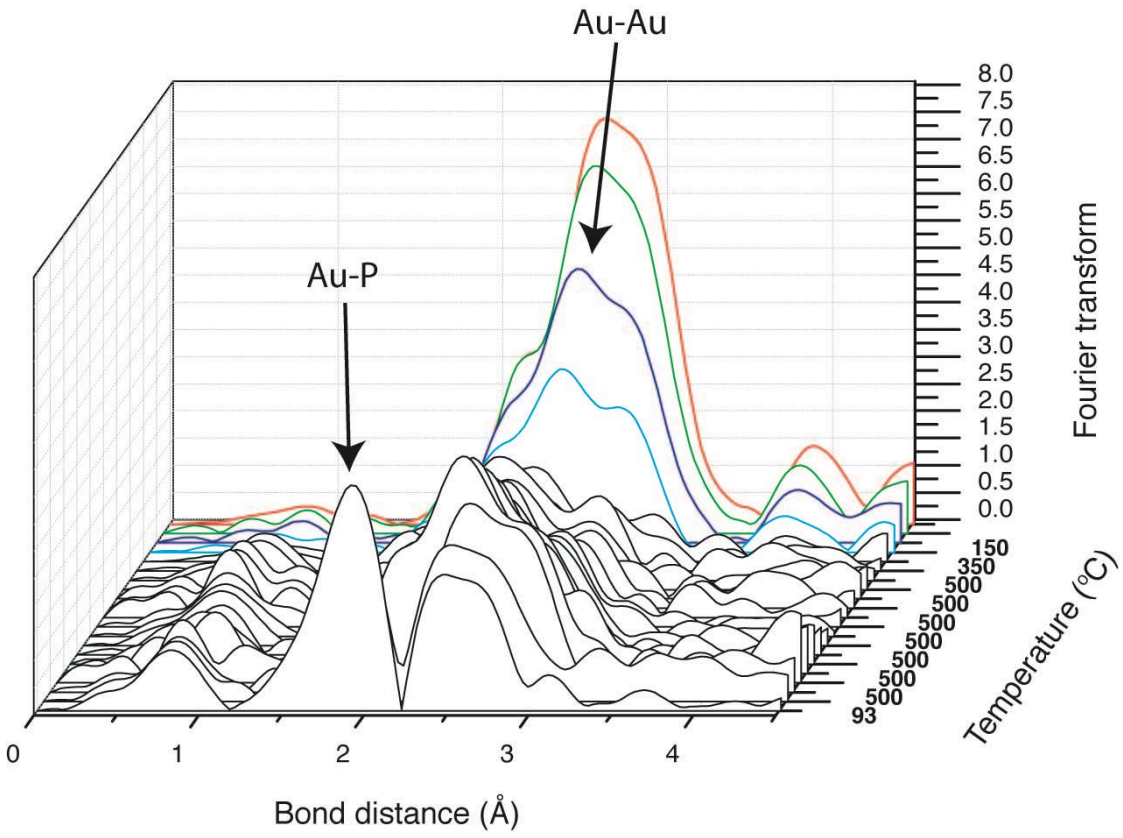

Figure 4.25. Phase shift uncorrected stacked Fourier transform EXAFS data for the *in situ* heating of $[Au_9(PPh_3)_8](NO_3)_3$ (4.0 wt. % Au) supported on silica nanospheres. The coloured peaks indicate the cooling period of the experiment.

The Fourier transform Au L_{III} EXAFS data taken from the *in* situ heating off $[Au_9(PPh_3)_8](NO_3)_3$ is shown in figure 4.25. The data shows the various stages of the transformation of the cationic gold cluster into metallic gold particles. Shortly after the start of the heating, the peak marked Au-P decreased rapidly in intensity as the phosphines were being removed from the cluster. Simultaneously, the peak marked Au-Au gradually increased in intensity, showing growth in the gold particle size. Once 500 ^{o}C was reached, there was little change in the intensity of the Au-Au peak, only a slight decrease in intensity, but once cooling started, the peaks began to grow in size, reflecting the decrease in thermal disorder. There was also a slight shift in the position of the Au-Au peaks as the Au-Au bond distance increased during the calcination process.

Analysis of the Au L_{III} edge EXAFS data recorded during the *in situ* heating of $[Au_9(PPh_3)_8](NO_3)_3$ (4.0 wt. % Au) on silica nanospheres showed that the clusters undergo a similar transformation to $[Au_6(Ph_2P(o\text{-tolyl})_6](NO_3)_2$ under the calcination conditions (see Appendix 3 for data fitting examples). Due to the relatively high ramp rate of the temperature program, less detailed information about what is happening to the gold at lower temperatures was obtained. What can be gleaned however, is information about what happens to the gold on the surface of the silica under prolonged heating at 500 ^{o}C and whether the length of time that the catalyst is exposed to this temperature make a difference to the particles formed.

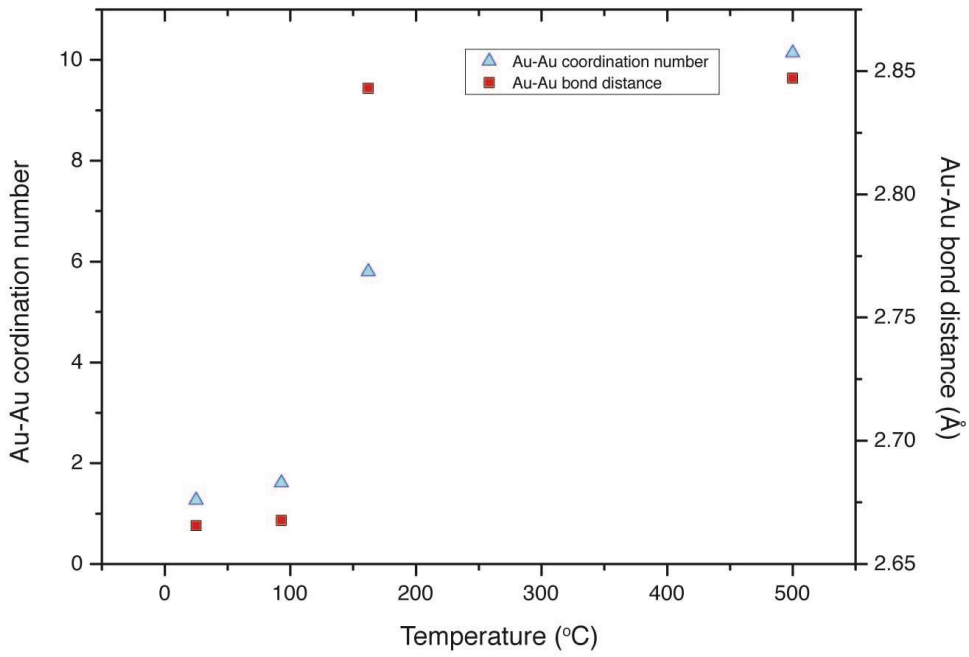

Figure 4.26. Variation of the Au-Au coordination number and Au-Au bond distance of $[Au_9(PPH_3)_8](NO_3)_3$ (4.0 wt. % Au) on silica nanospheres with increasing temperature (derived from EXAFS data).

Figure 4.26 shows that the Au-Au coordination number in $[Au_9(PPh_3)_8](NO_3)_3$ did not change much as the temperature increases from room temperature to 93 ^{o}C. However, once the temperature reached 162 ^{o}C, the Au-Au coordination number had risen dramatically to 5.8.

Once the target temperature of 500 °C had been reached, the Au-Au coordination number had reached 10.14. When the sample underwent prolonged heating at this temperature, there was little further change in Au-Au coordination number (generally staying at 9.25). This shows that on heating $[Au_9(PPh_3)_8](NO_3)_3$ on the silica to 500 °C, much larger particles of gold are generated.

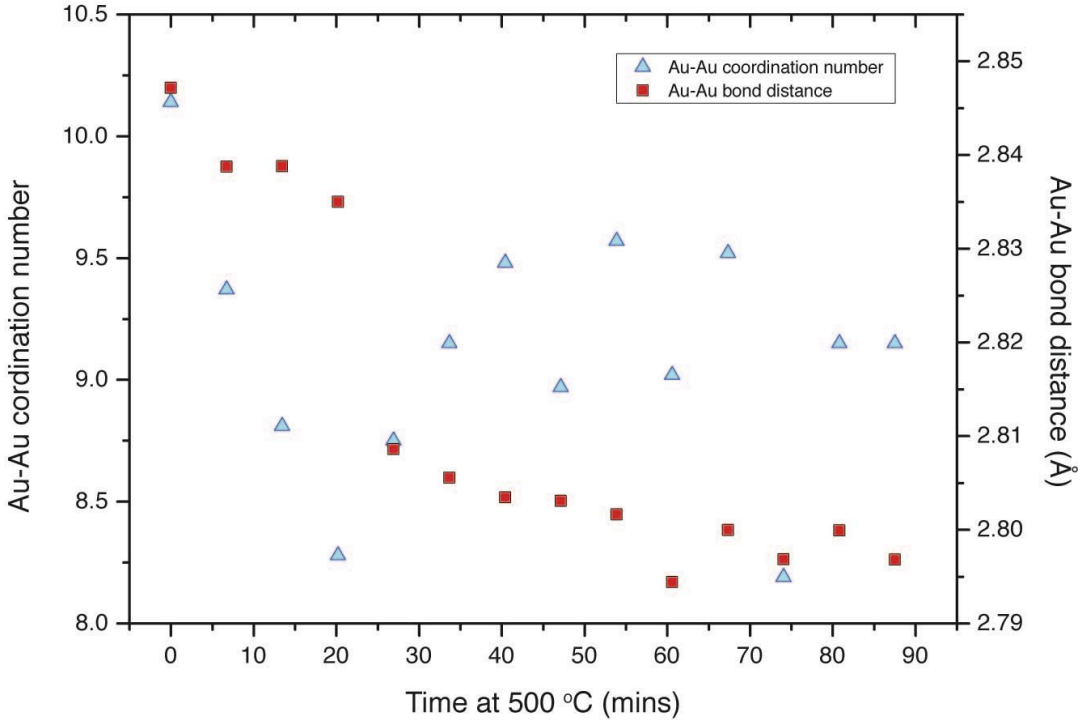

Figure 4.27. Change in the Au-Au coordination number and Au-Au bond distance of $[Au_9(PPH_3)_8](NO_3)_3$ (4.0 wt. % Au) on silica nanospheres at 500 °C (derived from EXAFS data).

Figure 4.27 shows that the Au-Au coordination number dropped to 7.7 and slowly increased before settling on 8.25. As the final datasets gave lower Au-Au coordination number values than the datasets recorded at 500 °C, this is further evidence to show that the particles decrease in size as the catalyst cools down after heating. Compared to the final Au-Au coordination number following the calcination of $[Au_6(Ph_2P(o\text{-tolyl})_6)](NO_3)_2$ on silica nanospheres, that observed for the calcination of $[Au_9(PPh_3)_8](NO_3)_3$ under similar conditions implies that smaller gold particles are obtained. This is because the final Au-Au coordination

number for the $[Au_6(Ph_2P(o\text{-tolyl})_6)](NO_3)_2$ sample is 8.6 whereas for the $[Au_9(PPh_3)_8](NO_3)_3$ sample it is 8.26. Considering that the gold particle in $[Au_9(PPh_3)_8](NO_3)_3$ starts off as being larger, and the PPh_3 ligands are lost at a lower temperature, it would have seemed more likely that it would produce larger gold particles. The difference in particle size could be due to the +50 ^oC difference in calcination temperature experienced by the $Au_6(Ph_2P(o\text{-tolyl})_6)](NO_3)_2$ sample.

As with the Au-Au coordination number data, the Au-Au bond distance also gives a clear picture of how the gold changes from $[Au_9(PPh_3)_8](NO_3)_3$ on the silica in its cationic state to small metallic particles. Mirroring the way that the gold in $[Au_6(Ph_2P(o\text{-tolyl}))_6](NO_3)_2$ behaved under calcination conditions, the bond distance increased dramatically once the temperature exceeded 150 ^oC. This is observed as an increase of almost 0.2 Å in the Au-Au bond as the gold loses it cationic character. At 500 ^oC, there was little variation in the Au-Au bond distance, the only change occurring being a negligible decrease of ~0.04 Å to 2.80 Å.

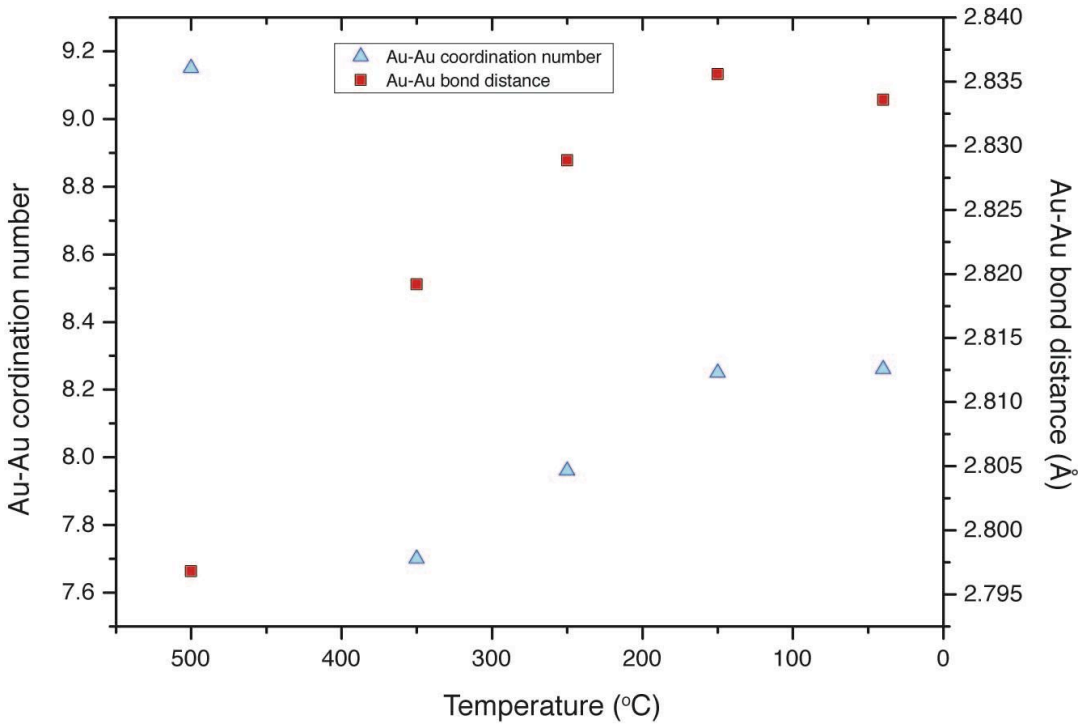

Figure 4.28. Variation of the Au-Au coordination number and Au-Au bond distance of $[Au_9(PPH_3)_8](NO_3)_3$ (4.0 wt. % Au) on silica nanospheres with decreasing temperature following calcination (derived from EXAFS data).

When cooling back down to room temperature, the Au-Au bond distance progressively increased to 2.83 Å. This shows that there is an overall change of + 0.17 Å in the Au-Au bond distance (figure 4.28). Again, the final value of the Au-Au bond length is less than that of bulk metallic gold, and again this is most likely due to the size of the small particles formed in this process. In agreement with the coordination number values obtained, there is further evidence that the gold particles formed from the calcination of $[Au_9(PPh_3)_8](NO_3)_3$ are smaller that those obtained from $[Au_6(Ph_2P(o\text{-tolyl})_6)](NO_3)_2$ under similar conditions as the final Au-Au bond length value is fractionally smaller.

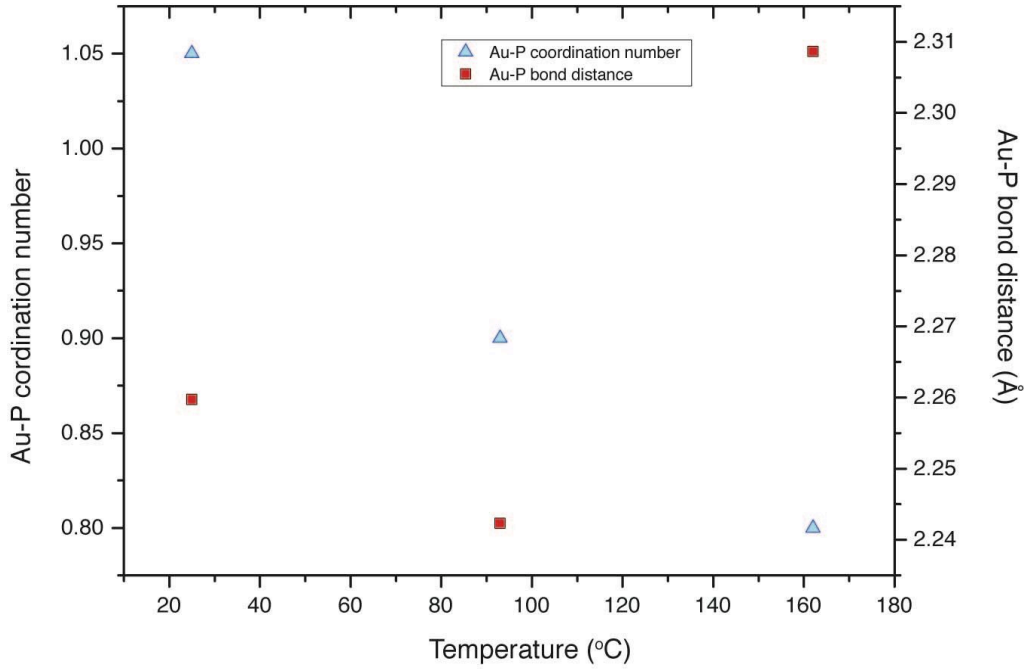

Figure 4.29. Au-P coordination number and Au-P bond distance with temperature before reaching 500 °C, at which point all the phosphines have been oxidised off.

The Au-P coordination number for $[Au_9(PPh_3)_8](NO_3)_3$ on silica nanospheres was observed to generally decrease as the temperature steadily rose (figure 4.29) and there were practically no Au-P bonds remaining once the temperature had reached 500 °C. As the coordination number decreased the Au-P bond length showed some slight variation. With the bond distance decreasing by ~0.2 Å after the coordination number had first dropped and then increasing by ~0.7 Å as the coordination number continued to decrease. This could give some detail about the transformation occurring, as the phosphines are lost from the surface of the cluster. The initial decrease in Au-P bond length occurs as the change in the oxidation state of the gold due to the partial loss of a phosphine ligand, resulting in a stronger and therefore shorter Au-P bond. Then, at a higher temperature and an even lower Au-P coordination number, the bond length has increased by almost 1 Å due to weakening of the Au-P bond as the rate of oxidation of the phosphines has started to increase. It is also worth noting that the PPh_3 groups appear to be lost

from $[Au_9(PPh_3)_8](NO_3)_3$ at a lower temperature than the Ph_2P(*o*-tolyl) groups are lost from $[Au_6(Ph_2P(o\text{-tolyl})_6](NO_3)_2$. This is because Ph_2P(*o*-tolyl) groups are slower to react with oxygen than PPh_3 groups.[175]

In agreement with the XANES data, the EXAFS data from the *in situ* heating of both $[Au_6(Ph_2P(o\text{-tolyl})_6)](NO_3)_2$ and $[Au_9(PPh_3)_8](NO_3)_3$ supported on silica nanospheres shows that the gold in both of the supported clusters undergo reduction to form metallic particles resulting form the loss of their stabilising phosphine ligands. The coordination number and average Au-Au bond distances show that the gold particles synthesised are much larger in size than the gold cores in the original clusters meaning that sintering is occurring during the calcination process. The temperatures at which phosphine loss occurs are in agreement with the TGA data.

The apparent increase in Au-Au bond distance as each of the supported cluster samples cooled is unlikely to attributed to growth in the size of the particle. It is also unlikely that the Au-Au bond distance would increase with decreasing temperature. These results are most likely an artefact of the EXAFS analysis procedure used. Anharmonic vibrations could cause the data to yield these results on cooling, but a discussion of this is not within the scope of this work.

The EXAFS, XRD and electron microscopy data have shown that calcination of the clusters on the surface of the support results in much larger gold particles being formed. The significant aggregation is a result of the high mobility of the gold on the surface of the silica support. Although it is possible to deposit gold on to the support surface using this method, it is clear that it cannot be used to remove the phosphine ligands off the gold in the clusters to leave small, uniformly sized gold particles. TEM analysis did show that despite many larger gold particles being present, there was still a presence of <10 nm sized particles. It is also likely that the very small (<2 nm) gold particles that could be present would be undetectable with the particular electron microscope used.

4.3.5. Catalysis data

In order to assess whether the different gold loading and heat treatments affected the activity of the catalyst, all of the catalysts were tested under the same conditions for the catalytic oxidation of benzyl alcohol. Tert-butyl hydroperoxide was used as an oxygen source. Full conversions and selectivities for each catalyst are given in figures 4.30 and 4.36. These are compared in other figures.

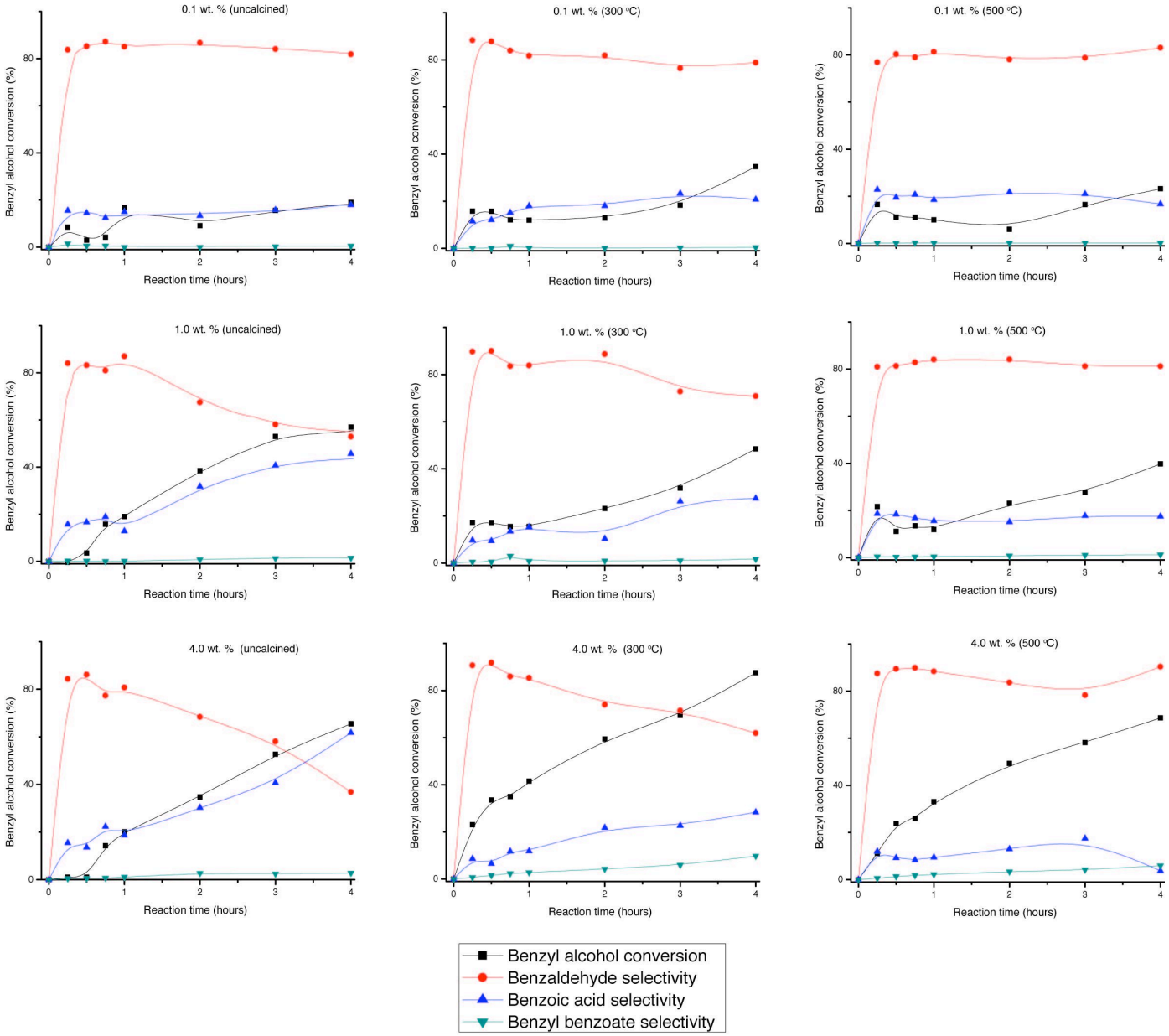

Figure 4.30. Catalysis data for $[Au_6(Ph_2P(o\text{-tolyl}))_6](NO_3)_2$ supported on silica nanospheres as catalysts for the oxidation of benzyl alcohol.

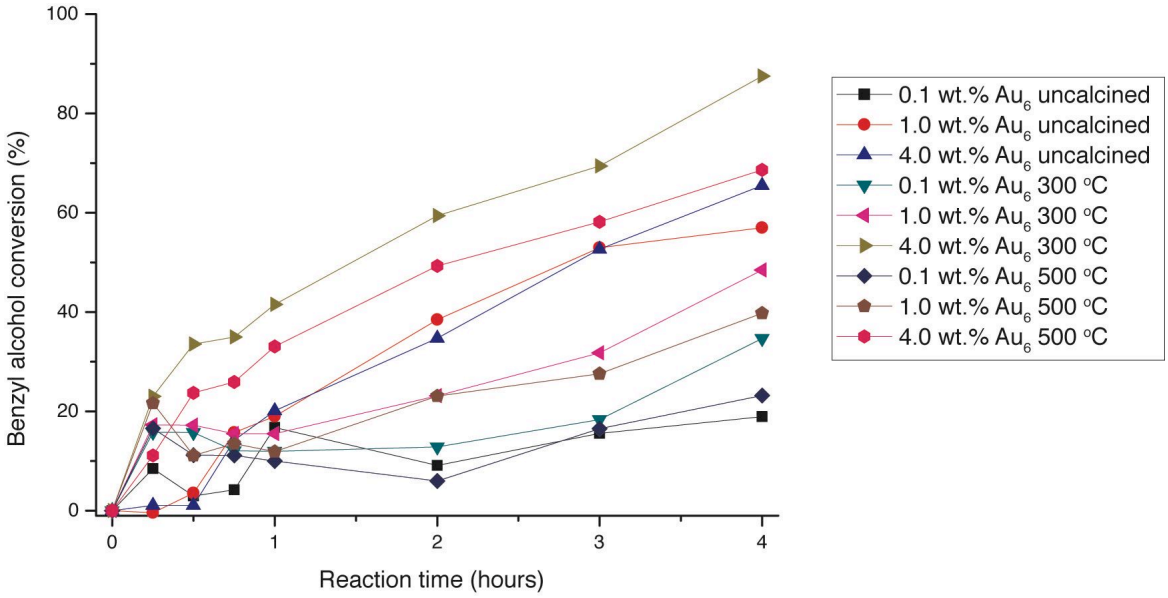

Figure 4.31. Conversion of benzyl alcohol over $[Au_6(Ph_2P(o\text{-tolyl}))_6](NO_3)_2$ (Au_6) supported on silica nanospheres.

By looking at the individual reactions with their variations in conversion and selectivity for different products, insight into the reaction pathways can be gained. With reference to figure 4.31 above, the 0.1 wt. % $[Au_6(Ph_2P(o\text{-tolyl}))_6](NO_3)_2$ ($0.1/Au_6$) loaded catalysts gave the lowest conversion of benzyl alcohol of all of the catalysts made using this cluster. Those calcined at 300 and 500 ^oC had higher rates of conversion than the uncalcined catalyst. The 1.0 wt. % catalysts gave higher rates of conversion and though the initial rate of conversion for the uncalcined catalyst was low, after 2 hours it had converted more benzyl alcohol than the catalysts $0.1/Au_6^{300C}$ and $0.1/Au_6^{500C}$. The catalysts with a 4.0 wt. % loading ($4.0/Au_6$) gave the highest conversions. As with the uncalcined 1.0 wt.% Au catalyst, ($1.0/Au_{6u}^{ncal}$) the uncalcined 4.0 wt. % Au catalyst ($4.0/Au_6^{uncal}$) had very low conversion during the first 45 minutes of the reaction. Only after that period did it start to show significant activity. 4.0 wt. % Au catalyst calcined at 300 ^oC ($4.0/Au_6^{300C}$) had a higher initial rate of conversion than that calcined at 500 ^oC ($4.0/Au_6^{500C}$). In fact, for each gold loading (0.1, 1.0 and 4.0 wt. %), the catalysts calcined at 300 ^oC gave higher conversions than those calcined at 500 ^oC. Often, the

uncalcined catalysts would start converting slowly, but by the time 4 hours had passed, the catalyst had reached a similar conversion to the catalyst calcined at 500 ^{o}C.

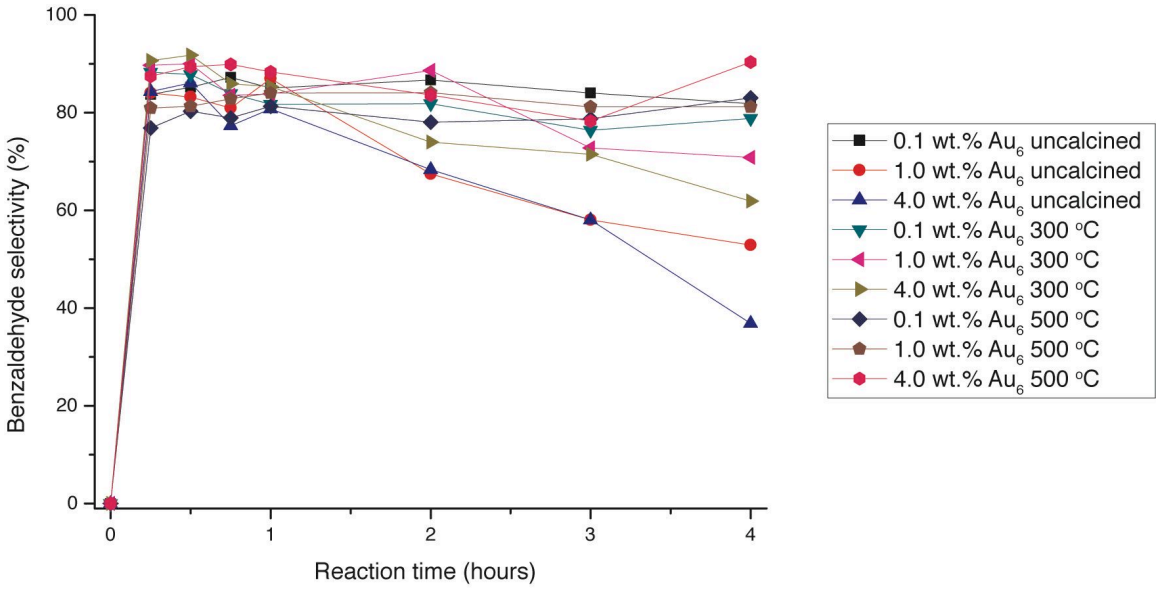

Figure 4.32. Selectivity for benzaldehyde during the catalytic oxidation of benzyl alcohol over $[Au_6(Ph_2P(o\text{-tolyl}))_6](NO_3)_2$ (Au_6) supported on silica nanospheres.

Figure 4.32 shows how the selectivity for benzaldehyde is seen to vary depending on the gold loading and calcination temperature. Catalysts with very low gold loading (0.1 wt. %), give very high selectivities. Also, it seems that regardless of the loading or calcination temperature, all of the catalysts give initial selectivities of 83-85%. However, for the uncalcined catalysts and those calcined at 300 ^{o}C, as the gold loading increases, their selectivity for benzaldehyde decreases. The most dramatic drop is seen in 4.0/Au_6^{uncal}, where after 4 hours, the selectivity for benzaldehyde is only 37%, less than half its initial value. Only the catalysts that were calcined at 500 ^{o}C give a consistently high selectivity for benzaldehyde for the duration of the reaction.

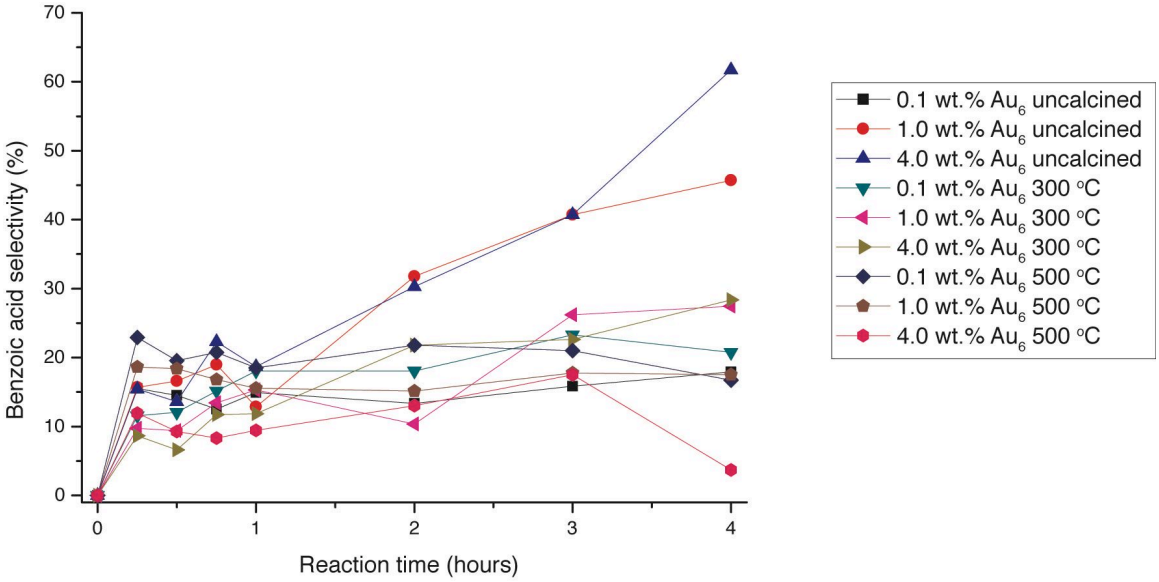

Figure 4.33. Selectivity for benzoic acid during the catalytic oxidation of benzyl alcohol over $[Au_6(Ph_2P(o\text{-tolyl}))_6](NO_3)_2$ (Au_6) supported on silica nanospheres.

The selectivity for benzoic acid also varies greatly depending on the gold loading and calcination temperature and this is illustrated in figure 4.33. For the $1.0/Au_6$ catalysts, there was little change in the benzoic acid selectivity throughout the reaction. The same is generally observed in with the catalysts with $1.0/Au_6^{300C}$, $1.0/Au_6^{500C}$, $4.0/Au_6^{300C}$, and $4.0/Au_6^{500C}$, though unusually the selectivity decreases to 4% after 4 hours with $4.0/Au_6^{500C}$. For catalyst $1.0/Au_6^{500C}$, and more so for $4.0/Au_6^{500C}$, the selectivity started to increase after 1 hour. In fact the selectivity for benzoic acid is higher than the selectivity for benzaldehyde at the end of the reaction for catalyst $4.0/Au_6^{uncal}$.

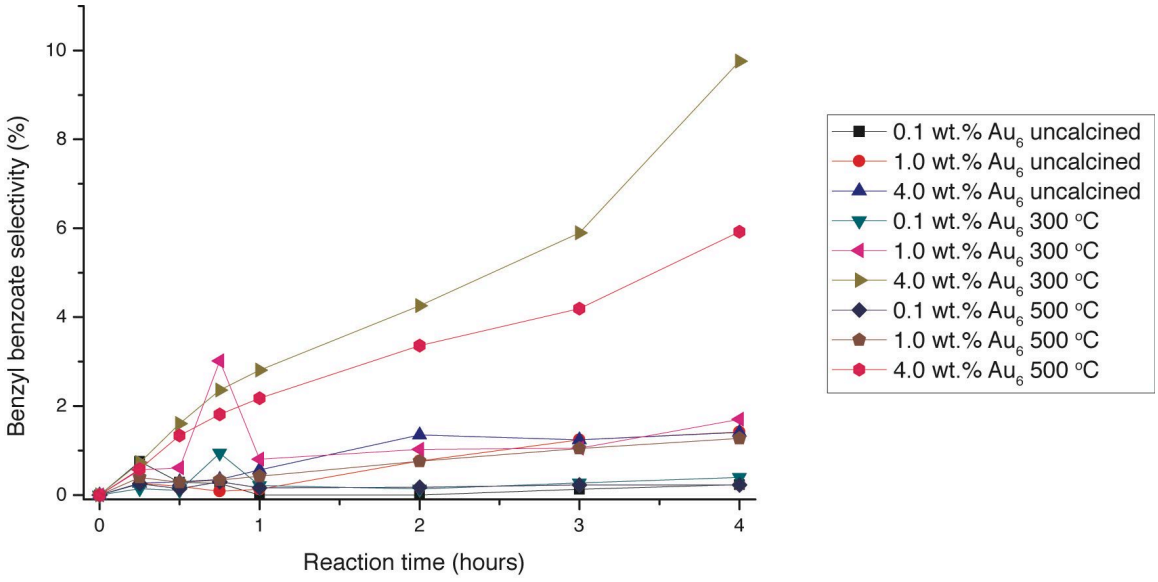

Figure 4.34. Selectivity for benzyl benzoate during the catalytic oxidation of benzyl alcohol over $[Au_6(Ph_2P(o\text{-tolyl}))_6](NO_3)_2$ (Au_6) supported on silica nanospheres.

Benzyl benzoate selectivity was generally very low for all of the catalysts (figure 4.34). Only catalysts $4.0/Au_6^{300C}$ showed any significant increase in selectivity for benzyl benzoate. This is associated with the catalyst's high benzyl alcohol conversion and decreasing benzaldehyde selectivity.

Based on the catalytic activity data, it is clear that a transformation is occurring in the gold clusters in the uncalcined catalysts. The delay in benzyl alcohol conversion observed with catalysts $1.0/Au_6^{uncal}$ and $4.0/Au_6^{uncal}$ at the start of the reaction suggests that the clusters undergo a change before the catalytic reaction can start. Also, as increasing the gold loading from 1.0 to 4.0 wt. % increases the length of the conversion delay at the start of the reaction, it can be assumed that the process is dependent on the amount of $[Au_6(Ph_2P(o\text{-tolyl}))_6](NO_3)_2$ present to begin with. It was also observed that the uncalcined catalysts would turn from being light brown, to maroon in colour after a catalytic reaction. This is similar in colour to the catalysts that had undergone calcination, so it may be inferred that a ligand removal process is occurring at the start of the catalytic reaction with catalysts $1.0/Au_6^{uncal}$ and $4.0/Au_6^{uncal}$.

It can be seen from the results of the catalytic oxidation of benzyl alcohol reactions, that the gold loading and calcination temperature both have a large influence on the catalysts activity. For $[Au_6(Ph_2P(o\text{-tolyl}))_6](NO_3)_2$ supported on silica nanospheres, it is apparent that increasing the gold loading increases the conversion of benzyl alcohol.

Figure 4.35 shows how increasing the loading from 0.1 to 1.0 wt. % increased the conversion by 37%. However, this increase in conversion was accompanied by a decrease in selectivity for benzaldehyde by 30%. The same is observed when the loading increases from 1.0 to 4.0 wt. %, with a 7% increase in conversion but a 16% decrease in selectivity.

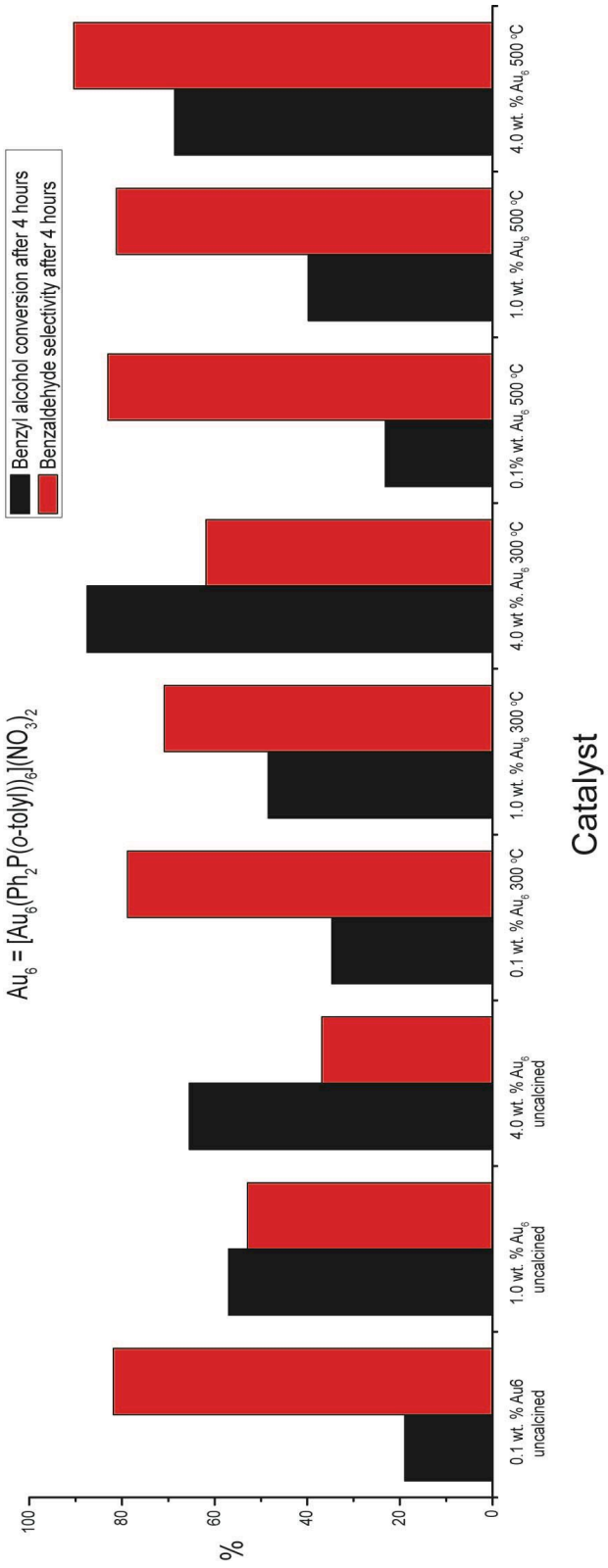

Figure 4.35. Results of catalytic oxidation of benzyl alcohol results after 4 hours using supported $[Au_6(Ph_2P(o\text{-tolyl}))_6](NO_3)_2$.

A similar trend was observed in the catalysts calcined at 300 ^{o}C. 0.1 wt.% $[Au_6(Ph_2P(o\text{-tolyl}))_6](NO_3)_2$ catalyst gave 35% conversion and 79% selectivity. Increasing the loading to 1.0 wt. % resulted in 48% conversion and 71% selectivity. A dramatic increase in conversion was observed using a 4.0 wt. % catalyst, giving 89% conversion of benzyl alcohol with 62% selectivity for benzaldehyde. The catalysts calcined at 500 ^{o}C differed from the trends observed for the other catalysts. These catalysts gave some of the lowest conversions coupled with the highest selectivities.

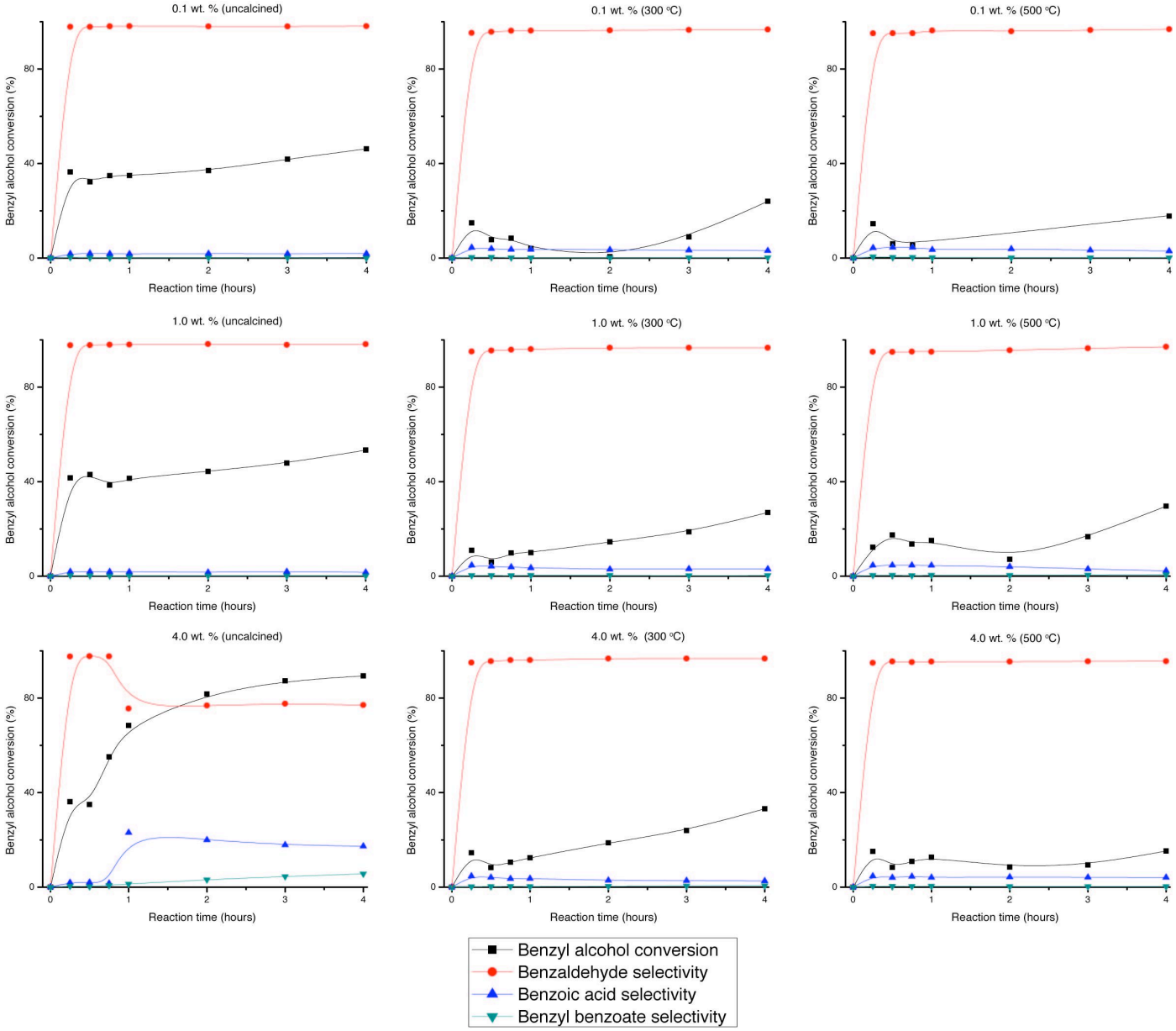

Figure 4.36. Catalysis data for $[Au_9(PPh_3)_8](NO_3)_3$ supported on silica nanospheres as catalysts for the oxidation of benzyl alcohol.

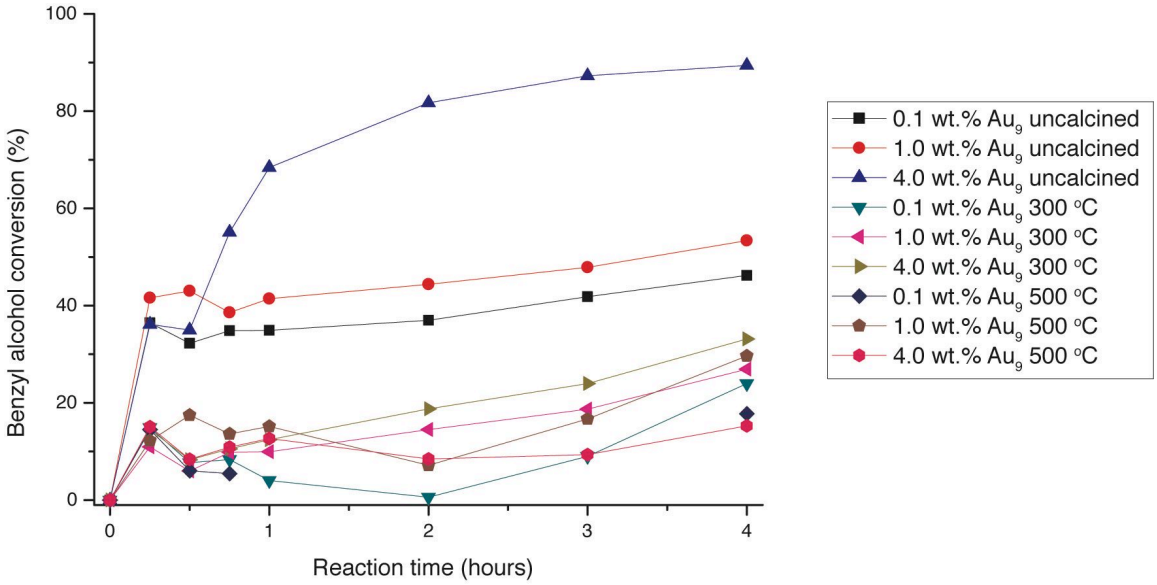

Figure 4.37. Conversion of benzyl alcohol over $[Au_9(PPh_3)_8](NO_3)_3$ (Au_9) supported on silica nanospheres.

Figure 4.37 compares the catalytic activities of the $[Au_9(PPh_3)_8](NO_3)_3$ loaded catalysts to each other. It is apparent that the activity of the calcined catalysts is far lower than the uncalcined catalysts. The calcined catalysts all converted only 20-30% of the benzyl alcohol after 4 hours and little increase is seen as the gold loading increases. The uncalcined catalysts exhibited good conversions. Increasing the loading of the gold from 0.1 to 1.0 wt. % only increases the conversion from 46% to 53%. When the gold loading is 4.0 wt. %, the conversion of benzyl alcohol is 89% after 4 hours. Also, no delay in activity is observed in the uncalcined $[Au_9(PPh_3)_8](NO_3)_3$ catalysts, unlike the $[Au_6(Ph_2P(o\text{-tolyl}))_6](NO_3)_2$ loaded catalysts. This could be due to the slightly higher susceptibility of PPh_3 to oxidation, whereas $Ph_2P(o\text{-tolyl})$ is more stable. All of the uncalcined catalysts gave very high initial rates of conversion. The extent of the final conversion of benzyl alcohol is dependent on the gold loading.

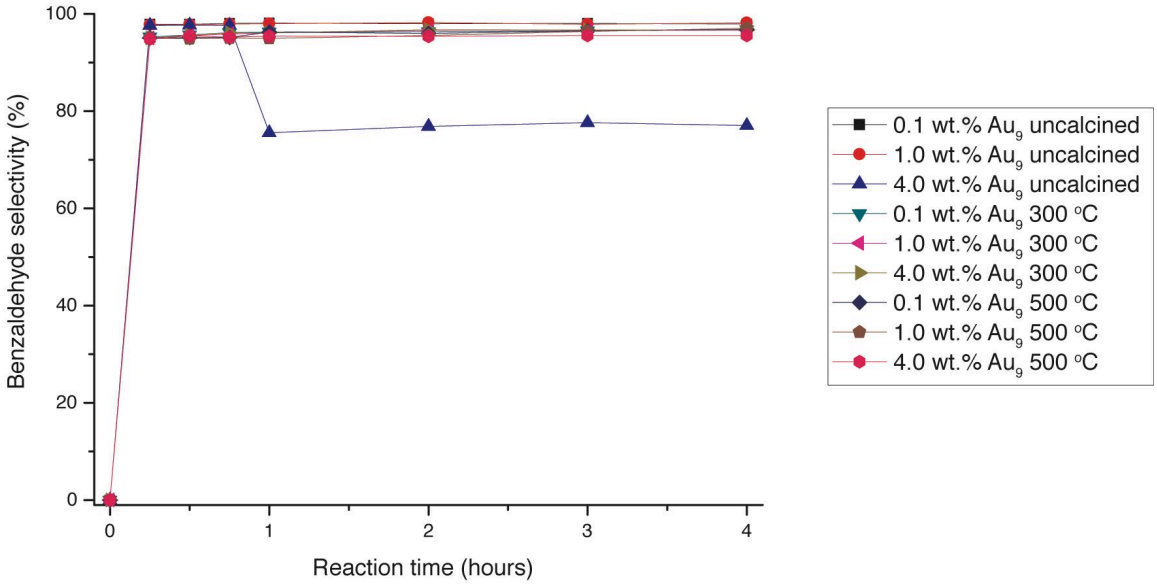

Figure 4.38. Selectivity for benzaldehyde during the catalytic oxidation of benzyl alcohol over $[Au_9(PPh_3)_8](NO_3)_3$ (Au_9) supported on silica nanospheres.

All of the $[Au_9(PPh_3)_8](NO_3)_3$ loaded catalysts showed very high selectivity for benzaldehyde (> 95%, see figure 4.38) and maintained this selectivity throughout the reaction except for catalyst $4.0/Au_9^{uncal}$. $4.0/Au_9^{uncal}$ started the reaction with this very high selectivity, but as the reaction proceeded and the conversion of benzyl alcohol exceeded 55%, the selectivity for benzaldehyde decreased to 76% and stayed at this for the remainder of the reaction. All but one of the catalysts made using supported $[Au_9(PPh_3)_8](NO_3)_3$ exhibited >95% selectivity for benzyaldehyde after 4 hours. Although this catalyst, $4.0/Au_9^{uncal}$, showed a slightly lower selectivity (77 %), it gave the highest conversion of benzyl alcohol, almost 90 %. This value is far higher than any of the other $[Au_9(PPh_3)_8](NO_3)_3$ catalysts.

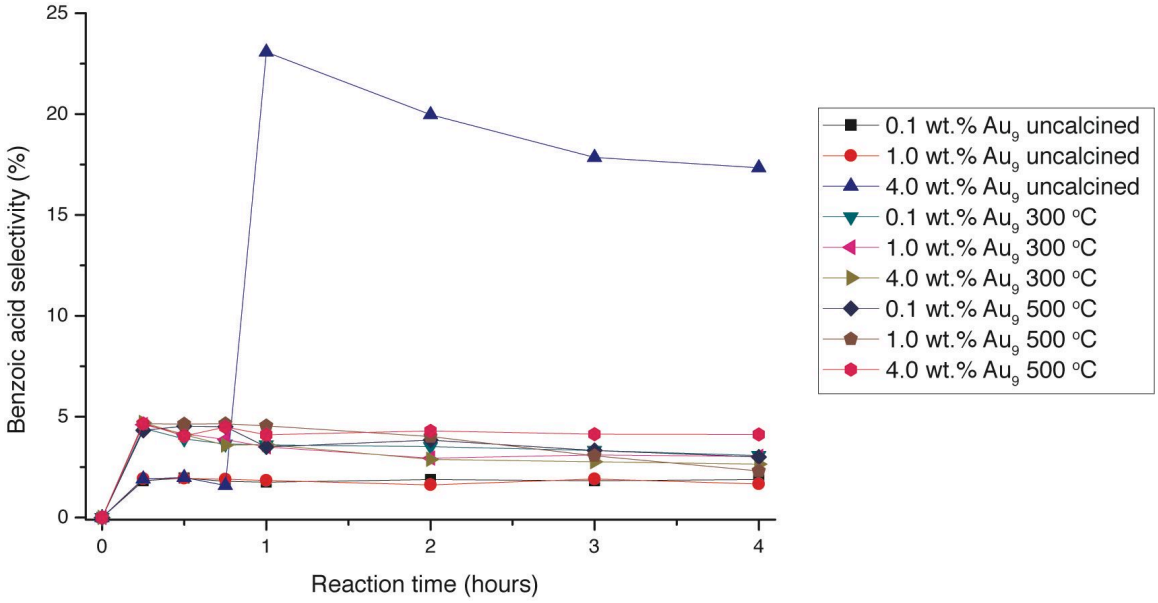

Figure 4.39. Selectivity for benzoic acid during the catalytic oxidation of benzyl alcohol over $[Au_9(PPh_3)_8](NO_3)_3$ (Au_9) supported on silica nanospheres.

Generally, the selectivity for benzoic acid for all of the $[Au_9(PPh_3)_8](NO_3)_3$ loaded catalysts was very low (<5%, see figure 4.39). The only one that differed was catalyst $4.0/Au_9^{uncal}$ which started with this low selectivity but it increased once the conversion of benzyl alcohol went beyond 55%. A similar trend is observed in the selectivity for benzyl benzoate. All of these catalysts had extremely low selectivities for benzyl benzoate (<1%, see figure 4.40) except for $4.0/Au_9^{uncal}$. Again, this catalyst started with this low selectivity, but as the reaction progressed, the selectivity increased.

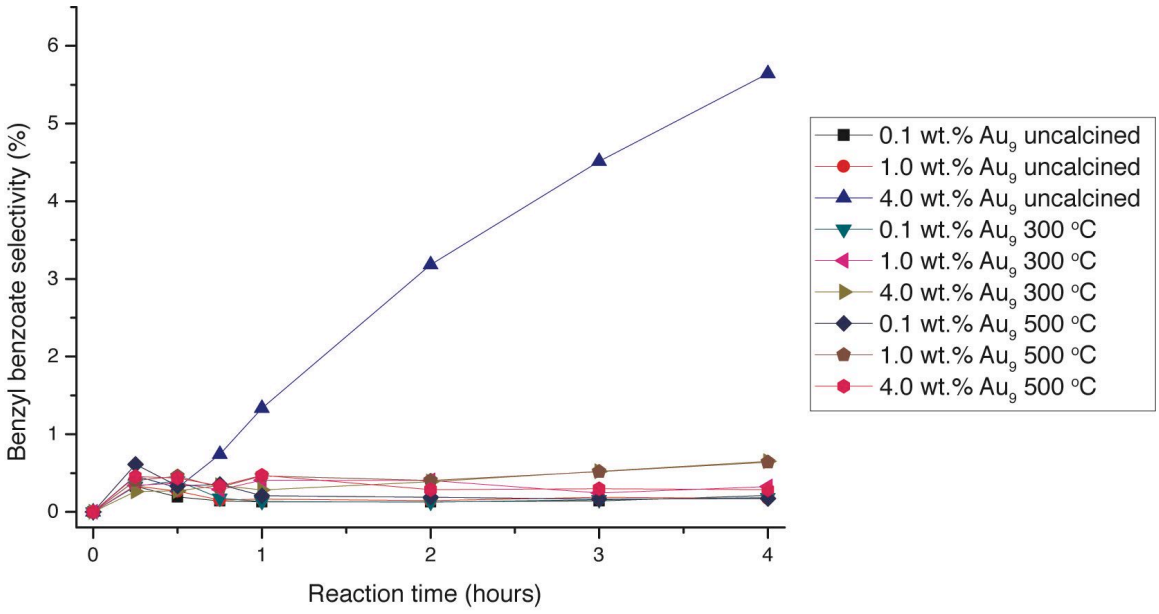

Figure 4.40. Selectivity for benzyl benzoate during the catalytic oxidation of benzyl alcohol over $[Au_9(PPh_3)_8](NO_3)_3$ (Au_9) supported on silica nanospheres.

By considering the relative concentrations of the reactants inside the reactor, the change in selectivity of catalyst $4.0/Au_9^{uncal}$ can be explained; as the reaction proceeds and benzyl alcohol is converted, there is less available for the catalyst to convert so the selectivity for the oxidation of benzyl alcohol to benzaldehyde shifts. As the concentration of benzaldehyde in the reactor vessel increases and the concentration of the benzyl alcohol decreases, the benzaldehyde will start to be oxidised, giving benzoic acid and resulting in an increased selectivity for benzoic acid and a decreased selectivity for benzaldehyde.

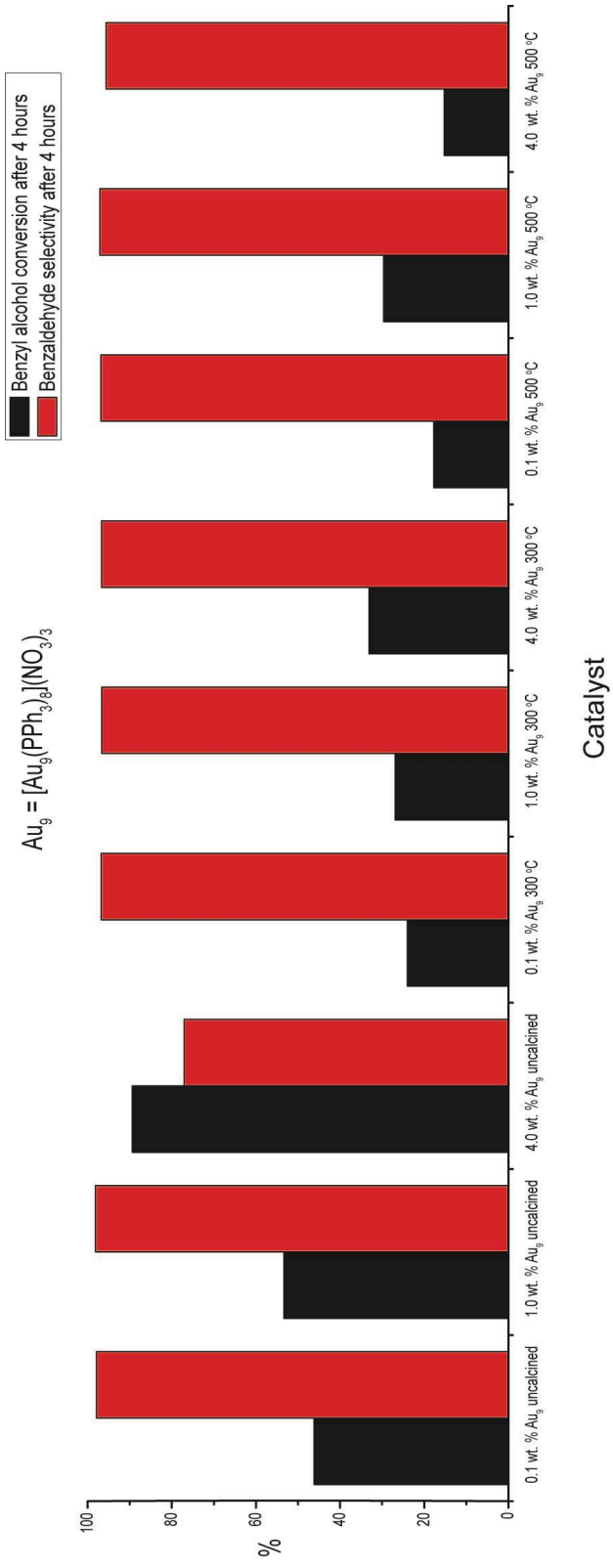

Figure 4.41. Results of catalytic oxidation of benzyl alcohol results after 4 hours using supported $[Au_9(PPh_3)_8](NO_3)_3$.

A leeching experiment to test the stability of the gold on the surface of the support revealed that the gold was able to leave the surface of the silica. After filtering the catalyst from the reaction mixture midway through a catalytic reaction, activity continued to be observed. This could be due to the filter paper having too large a pore size to withhold all of the nano-sized catalyst back from the rest of the solution. Perhaps a more accurate method would be to use a different filtration system to remove the catalyst.

Overall, the catalytic testing has shown that the silica nanosphere supported gold clusters can be highly active catalysts for the oxidation of benzyl alcohol. The catalysts are capable of high selectivity for benzaldehyde and high conversion of benzyl alcohol. However, trends suggest that there is a trade off between high selectivity for the desired product, benzaldehyde, and high conversion. Only the catalyst made from 4.0 wt. % of $[Au_6(Ph_2P(o\text{-tolyl}))_6](NO_3)_2$ calcined to 500 ^oC came close to offering both (69% conversion, 90% benzaldehyde selectivity after 4 hours).

There is also evidence to suggest that the catalysts synthesised from of $[Au_6(Ph_2P(o\text{-tolyl}))_6](NO_3)_2$ generally have higher activity but lower selectivity than those made using $[Au_9(PPh_3)_8](NO_3)_3$. Of the catalysts made using $[Au_6(Ph_2P(o\text{-tolyl}))_6](NO_3)_2$, those that have higher gold loading performed better in terms of benzyl alcohol conversion. Selectivity was generally superior in the catalysts synthesised from $[Au_9(PPh_3)_8](NO_3)_3$, though this most likely due to their lower conversion activity. The $[Au_9(PPh_3)_8](NO_3)_3$ catalyst that did show high conversion also showed that the high benzaldehyde selectivity decreased after a certain point in the reaction.

Calcining the $[Au_9(PPh_3)_8](NO_3)_3$ catalysts made little difference in terms of the selectivity for benzaldehyde, but higher calcination temperatures were detrimental to the amount of benzyl alcohol converted. The catalysts made using $[Au_6(Ph_2P(o\text{-tolyl}))_6](NO_3)_2$ generally showed

improved conversion and selectivity to benzaldehyde when calcined to 300 ^{o}C. Heating to 500 ^{o}C reduced the conversion but improved the benzaldehyde selectivity.

4.4. Conclusion

This work has demonstrated that the gold clusters $[Au_6(Ph_2P(o\text{-tolyl}))_6](NO_3)_3$ and $[Au_9(PPh_3)_8](NO_3)_3$ can be used as sources of gold in the synthesis of oxidation catalysts. By depositing these clusters on to a support and removing the phosphine ligands that envelope the gold core, the catalysts are activated. The temperature at which the phosphines are removed, as well as the gold loading, greatly affects the catalysts synthesised using $[Au_6(Ph_2P(o\text{-tolyl}))_6](NO_3)_3$, with the highest benzyl alcohol conversions obtained from the catalyst with a 4.0 wt. % loading calcined at 300 ^oC.

5. Low temperature ligand removal

Abstract

This chapter focuses on the use of tert-butyl hydroperoxide to facilitate the removal of the phosphine ligands from $[Au_6(Ph_2P(o\text{-tolyl}))_6](NO_3)_2$ at 95 ^oC as opposed to the higher temperatures required when heating in air. *In situ* quick EXAFS, along with other methods, was employed to monitor the gold in the cluster as it reacted with the peroxide. It revealed that the phosphines are lost with the formation of gold particles, but only once this had occurred did the catalyst started showing activity for the oxidation of benzyl alcohol.

5.1. Introduction

5.1.1. *In situ* characterisation

Characterisation methods that give information about a compound in an isolated, unreacting state are very useful for general purposes. But in cases where the active species is only present whilst participating in a reaction, these characterisation methods are less valuable. In catalytic reactions, it is often the case that the active component is only generated during the reaction, and that the catalytic metastable or transient species will revert back to its original state after the reaction. It is also highly likely that during catalyst preparation or pre-treatment that a process will occur which would provide a valuable insight into the catalyst. In order to observe these processes or transient species, *in situ* characterisation is essential.

There are a range of possible techniques that can be carried out under *in situ* conditions. Perhaps the most accessible is that of *in situ* IR spectroscopy.

5.1.1.1. *In situ* IR spectroscopy

IR spectroscopy can be used to study preparation of catalysts, catalytic reactions as they occur or analyse the interaction of surface adsorbed species. Specialised cells that allow gases or liquids to be fed into a solid catalyst under variable temperatures or pressures can be designed and built to fit standard IR spectrometers. The main problem with this technique is that interference can occur from gas phase and bulk contributions such as the metal oxide support, but this can be overcome by using specialised techniques.

5.1.1.2. In situ XRD

This can be used to observe the structural changes in bulk catalysts. Due to the necessity of long-range order in the sample being analysed, phase transitions occurring can be observed as well as the formation of crystalline materials. If the particles of a supported metal catalyst are large enough, then a change in crystallite size can be seen through a change in the line broadening of the peaks.

Though it is possible for *in situ* XRD data collection to be carried out in a standard laboratory diffractometer using a specially designed *in situ* cell, often long periods of time are required to obtain reasonable quality data. If a change in the catalyst occurs at high rate, then important data may be missed whilst time is spent scanning a sample. In order to increase the time resolution of the data collection, a more powerful source of X-rays must be used. A synchrotron can provide X-rays at intensities many orders of magnitude larger than that of a laboratory diffractometer. This means that *in situ* experiments can be carried out that record data in a matter of seconds rather than hours using specially designed detectors.

5.1.1.3. In situ XAS

As long-range order is not a requirement for XAS, it is an ideal technique for characterising a catalyst *in situ*, giving the coordination number, inter-atomic distances and types of atoms bound to the absorbing atom. This type of data would, in a working catalyst, be highly valuable as the structure of the catalyst could then be directly related to the activity. Conventional XAS techniques require at least several minutes to obtain reasonable quality data, which means that it cannot be used to monitor reactions that change over a short period of time. There are two methods that allow for data to be collected over shorter periods of time. These are

Energy dispersive X-ray absorption spectroscopy (EDXAFS) or Quick EXAFS (QEXAFS). Although they both obtain the same type of data, they do so in very different ways.[176]

5.1.1.4. EDXAFS

Whereas conventional EXAFS uses a motorised monochromator to step-wise scan through a range of X-ray energies that are focused on to the sample, EDXAFS uses a polychromated X-ray beam that allows the collection of whole energy ranges of X-rays using specialised detectors. A bent crystal polychromator disperses a range of X-ray energies on to a focal point where the sample is positioned. The X-rays then diverge on to a position sensitive detector. With detectors able to record full range scans between 2 and 100 ms, this technique can give very high time resolution data.[177] However, to improve the signal to noise ratio, 50-500 scans are recorded, but due to the very high data sampling rate, this means that it is still possible to record data in under a second. The potential problem with EDXAFS is that because the beam intensities before and after the sample are not recorded simultaneously, normalisation problems can occur if the X-ray beam should suffer any instabilities.[178]

5.1.1.5. QEXAFS

QEXAFS is an alternative to EDXAFS with a set up similar in arrangement to conventional EXAFS. The difference between QEXAFS and standard EXAFS data collection is that QEXAFS uses a monochromator that moves at a constant velocity instead of the stepwise.[176] This means that data can be collected in less than 1 minute and in sometimes <1 s in specialised setups. The data quality is not affected by the shorter period of time of the monochromator at each

energy, meaning that QEXAFS allows for high quality data to be recorded in very short time. This makes it ideal for studying dynamic systems.[179] This technique does not have the same sensitivity to beam instability as EDXAFS as ionization chambers are still employed. Figure 5.1 shows a schematic of a QEXAFS data collection setup.

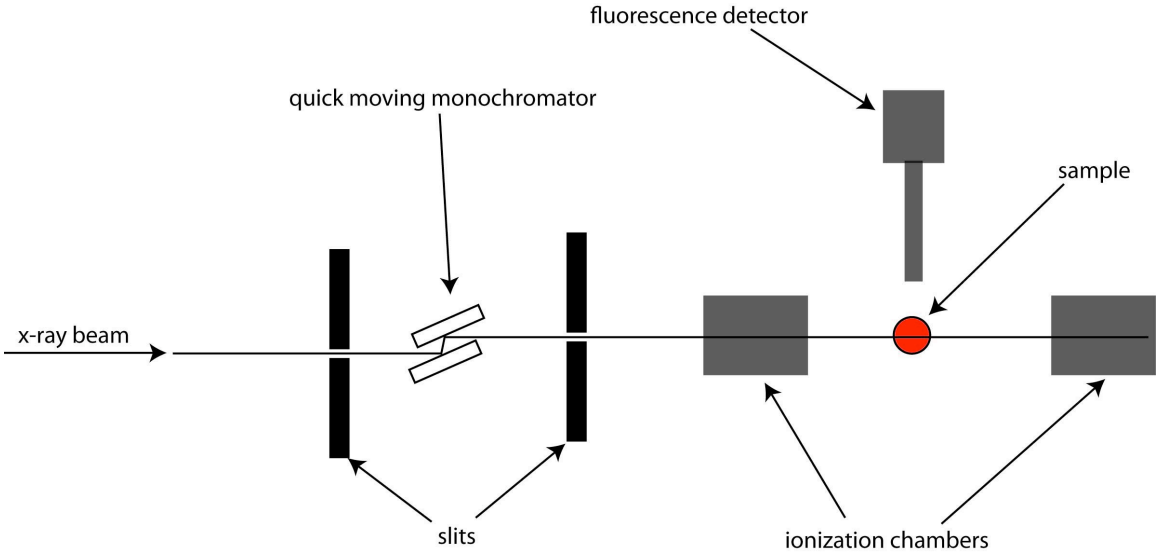

Figure 5.1. A schematic diagram for QEXAFS data collection.

5.1.2. Oxidation catalysts

Oxidation reactions are of enormous industrial importance, especially in the synthesis of fine chemicals. Stoichiometric quantities of oxidizing agents such as permanganate are widely utilised in industrial oxidation reactions that lead to the accumulation of by-products. A green alternative would be a reusable (heterogeneous) catalyst that could oxidise a substrate without forming the side products. As mentioned in chapter 4, oxygen sources such as hydrogen peroxide or molecular oxygen may be used to establish clean industrial oxidation methods.[146, 147]

Gold is recognised as being unique among the metals for its catalytic oxidation activity, specifically for the oxidation of CO to CO_2 at low

temperatures.[159, 161, 180] It has been established that there is a strong dependency of the activity of the gold catalyst on the size of the gold particles present.[163] Recently, it was found that the active component of the catalyst was not the large nanoparticles (>1nm) of gold, but was the small clusters of gold atoms only ~0.5nm or less in size.[53] Previously reported studies hinted at this when molecular clusters deposited on titania yielded highly active catalysts for oxidation of CO and in addition to this several organic substrates have been converted to their respective oxidised products using supported gold catalysts.[143-145, 181, 182] One reaction of particular interest is the oxidation of benzyl alcohol to benzaldehyde.[183-187]

A major limitation in the synthesis of supported gold nanoparticle catalysts is the lack of control over the size of the particles formed. One approach towards this problem is to use molecular clusters as catalyst precursors. This method has previously been successfully used to produce a variety of catalysts using mono and bimetallic[188-191] clusters, as previously mentioned in section 1.1.1.1 of the introduction. For example, Iwasawa and co-workers[192, 193] demonstrated the use of gold-phosphine precursors to generate supported gold nanoparticles, as have Lambert and co-workers[13] who used a 55 atom gold cluster to generate active oxidation catalysts.

As the results in Chapter 3 demonstrated, the size and shape of phosphine-stabilised gold clusters can be tuned as a function of the size and donor properties of the phosphine employed. This allowed for the synthesis gold clusters with specific numbers of gold atoms at their core, with either 4, 6 or 9 atoms depending on the steric bulk of the phosphine ligands used.

In Chapter 4, it was found that the uncalcined clusters were active for benzyl alcohol oxidation in the presence of TBHP. Those synthesised using $[Au_6(Ph_2P(o\text{-tolyl}))_6](NO_3)_2$ were initially less active than the calcined gold catalysts. When carrying out the catalytic reactions, it was

found that there was a significant induction period before the $[Au_6(Ph_2P(o\text{-tolyl}))_6](NO_3)_2$ catalysts showed activity; for the first 30 minutes of the reaction, little to no conversion of the benzyl alcohol was observed when the gold loading was 1.0 or 4.0 wt. %. This is thought to be due to the protective nature of the phosphine ligands that shroud the active sites. Once the gold cluster cores are exposed (by removing the phosphine ligands) to the reactants, the conversion begins.

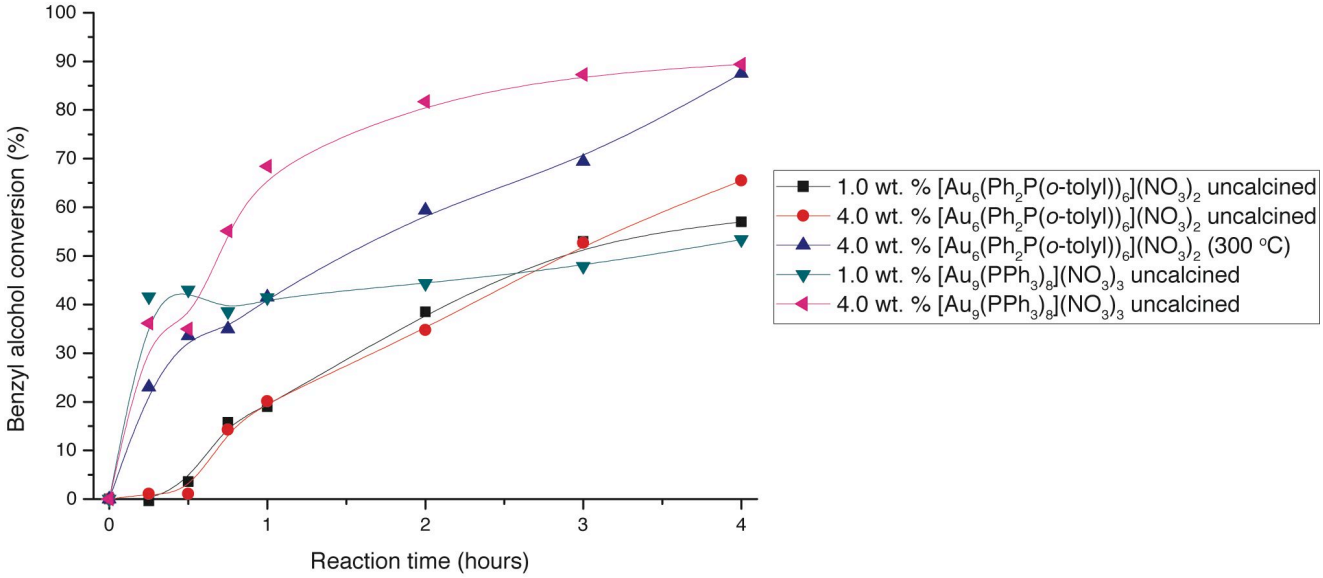

Figure 5.2. Comparing the catalytic activity of various uncalcined catalysts and one calcined catalysts for the oxidation of benzyl alcohol.

The uncalcined catalysts synthesised from $[Au_9(PPh_3)_8](NO_3)_3$ did not have this induction period (see figure 5.2) and this is most likely due to the PPh_3 ligands being more easily removed than $Ph_2P(o\text{-tolyl})$ ligands. They gave very high initial rates of reaction with as much as 40% benzyl alcohol conversion in the first 15 minutes of the reaction. It is possible that very small gold particles were generated this way. The particle formation process occurs too quickly in the uncalcined $[Au_9(PPh_3)_8](NO_3)_3$ catalysts so attention was instead focused on the reaction of uncalcined $[Au_6(Ph_2P(o\text{-tolyl}))_6](NO_3)_2$ with TBHP under catalytic reaction conditions.

5.1.3. Current work

In order to establish the ligand removal process takes place, using a specially designed *in situ* reactor cell together with synchrotron radiation, an experiment was designed that recreated the conditions experienced by the gold clusters in the reactor. *In situ* quick EXAFS were employed to monitor the gold in real time as the reaction was proceeding. This allowed for the high time resolution data to be recorded as the clusters gradually lost the stabilising phosphine ligands.

5.2. Experimental

5.2.1. Reaction of 4.0 wt. % $[Au_6(Ph_2P(o\text{-tolyl}))_6](NO_3)_2$ with tert-butyl hydroperoxide

11.3 ml (5.0-6.0 M in decane) of tert-butyl hydroperoxide was mixed with 0.5 g of 4.0 wt. % $[Au_6(Ph_2P(o\text{-tolyl}))_6](NO_3)_2$ supported on silica nanospheres in a round bottomed flask with a condenser fitted. The round bottomed flask was placed in an oil bath heated to 95 ^oC whilst stirred. After 40 minutes, 1 hour, 2 hour and 2.5 hours, the container was removed from the oil bath and a small sample of the solid catalyst was removed with a spatula and allowed to drain on some filter paper. The TBHP was rinsed off with hexane and the catalyst was allowed to dry. The sample was then stored for powder XRD analysis.

5.2.2. *In situ* peroxide assisted ligand removal QEXAFS data collection

This was carried out at BM29 of ESRF (which operates at 6GeV). In a typical experiment, 150 mg of self supporting wafers of supported gold cluster catalysts were placed into the *in situ* cell, TBHP (was added and the cell was sealed prior to placing the cell in a heating block; Kapton films were used as window material. The cell was heated to 95 ^oC at the rate of 6 ^oC/min and the data collection was started when the temperature of the cell was 30 ^oC. Au L_{III} XAS data was collected over the energy range of 11.6-13.0 keV, using transmission geometry. The whole scan was performed over 8 seconds and an additional 8 seconds was required to move the monochromator back to the starting position. A double crystal Si(111) monochromator was used for this work and ion chambers were employed to record incident (I_o) and transmitted beam intensities.

Background subtraction of the EXAFS data was carried out using VIPER software package[60]. Curve fitting analysis of the data was performed using DL_EXCURVE[61].

XRD data was collected on a Bruker-AXS D4 powder X-ray diffractometer.

5.3. Results and discussion

QEXAFS allowed the ligand removal process to be monitored in real time with scans of the sample being taken every 8 seconds. XAS experiments were performed in order to characterise the changes occurring in the cluster from the initial stages of degradation through to the formation of gold particles.

5.3.1. *Ex situ* XRD data

Table 5.1. A table to show the variation in gold particle size with time spent reacting with TBHP at 95 °C. These values are taken from XRD data of samples of $[Au_6(Ph_2P(o\text{-tolyl}))_6](NO_3)_3$ (4.0 wt. %) supported on silica nanospheres.

Time reacting with TBHP	Average gold particle size
40 minutes	3.2 nm
1 hour	3.2 nm
2 hours	3.6 nm
2 hours 30 minutes	3.9 nm

XRD analysis of the supported $[Au_6(Ph_2P(o\text{-tolyl}))_6](NO_3)_3$ (4.0 wt. %) catalysts sampled directly from a reaction with TBHP at different time intervals showed the average gold particle size at the time when the activity in the catalyst starts is 3.2 nm (see table 5.1). This is far smaller than the gold particle sizes observed in the calcined catalysts. These gold particles grow in size as the reaction proceeds and after 2.5 hours, they had reached an average size of 3.9 nm. The rate at which the gold particles increase in size is very low, indicating that this is a gradual process rather than one featuring a sudden increase in particle size as observed in the *in situ* calcination XAS experiments discussed in the previous chapter.

5.3.2. XANES data

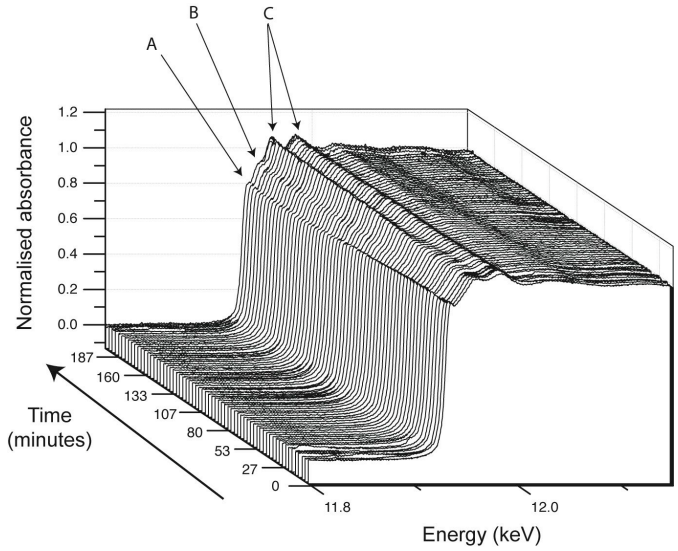

Figure 5.3. L_{III} edge XANES data highlighting the gradual loss of feature A, the development of feature B and the accentuation of features C.

Stacked Au L_{III} XANES data (normalised) recorded *in situ* is shown in figure 5.3. From this figure, and by comparing the data given in reference [120] with the previously discussed XANES data, it is clear that the features marked A and C at the start of the reaction are those of gold in a phosphine stabilised cationic cluster. During the course of the reaction these features undergo considerable changes; the appearance of a shoulder B occurs, whilst A decreases in intensity and C becomes more well-defined. The decrease in intensity of A indicates the gradual loss of cationic charge on the gold. The final spectrum after the reaction resembles that of metallic gold (see figure 5.4). These changes in the gold occur far more slowly than was observed for the *in situ* heating EXAFS data of the clusters undergoing calcination in Chapter 4.

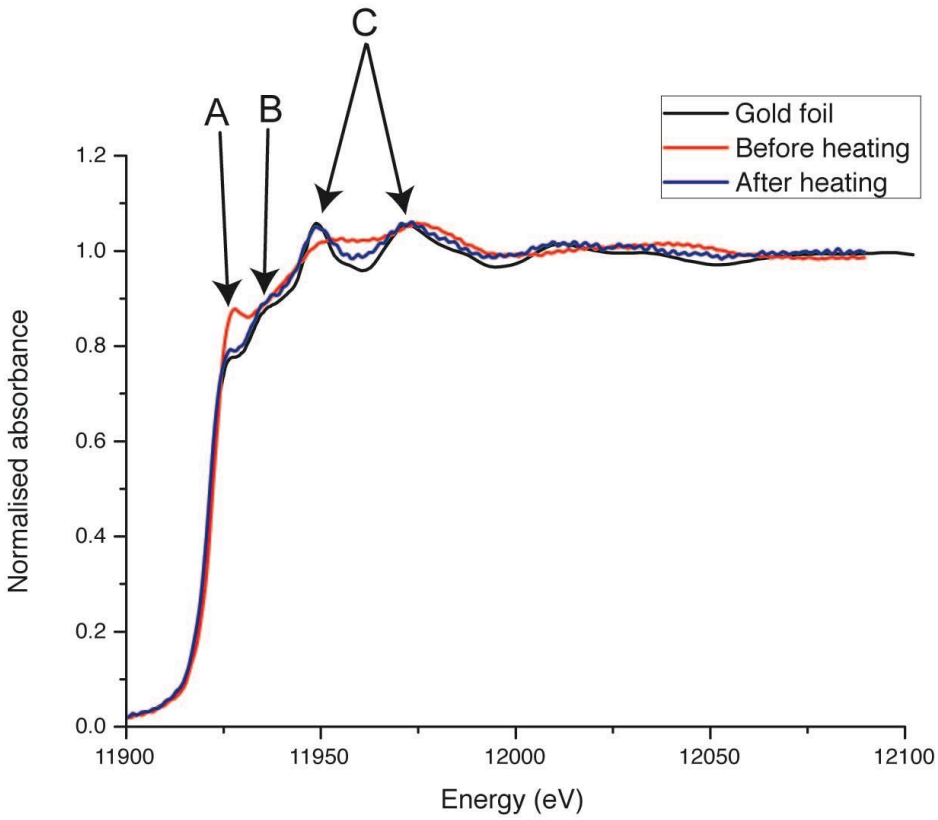

Figure 5.4. XANES data of the gold clusters before and after reacting with TBHP at 95 °C for 190 minutes. Gold foil XANES are shown for reference.

5.3.3. EXAFS data

The Fourier transformed Au L_{III} edge EXAFS data shows the gradual decrease in the intensity in the peak representing the Au-P bond. The position of the Au-Au bond peak also shifts, representing an increase in the Au-Au bond length. This is consistent with the loss of cationic charge shown in the XANES data, which would occur with an increase in the Au-Au bond length. This is illustrated in figure 5.5. Appendix 6 shows phase shift corrected Fourier transform data.

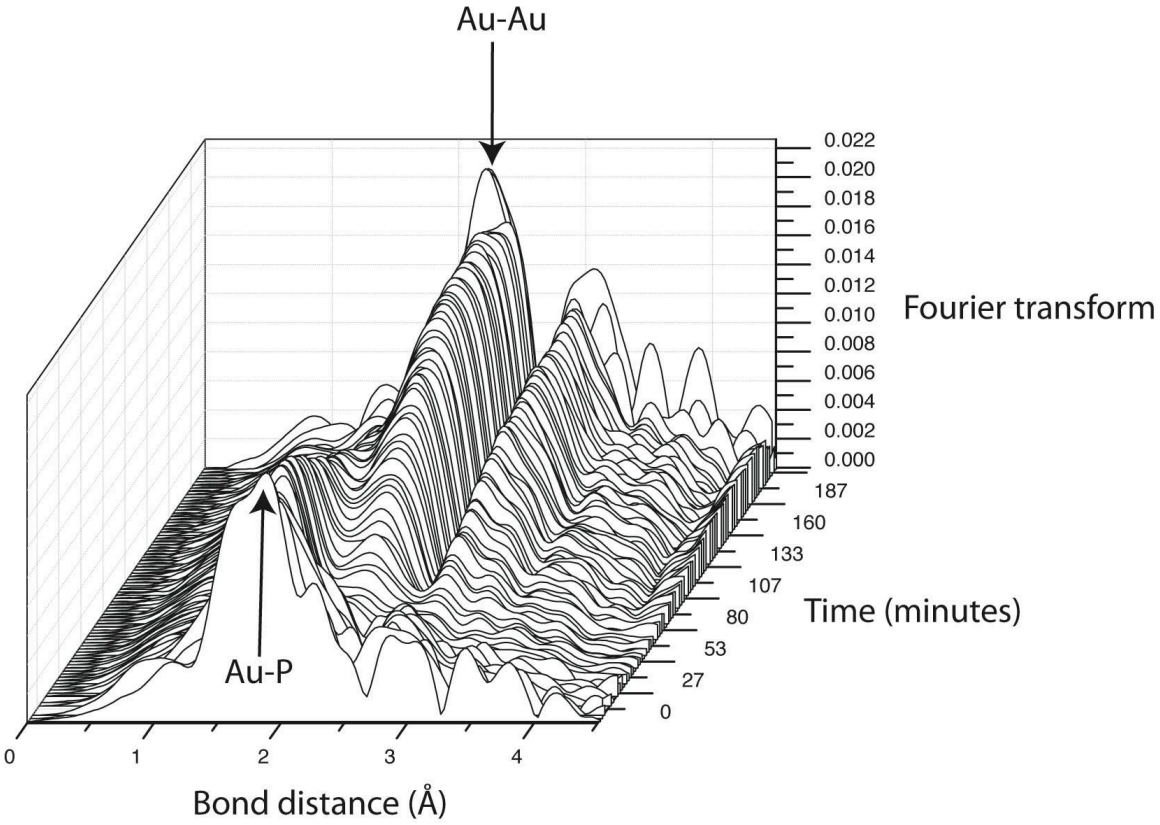

Figure 5.5. Phase- shift uncorrected Fourier transformed Au L_{III} edge QEXAFS data showing the changes Au-P and Au-Au bond distance and intensity over time reacting with TBHP at 95 ^{o}C.

To obtain a more quantitative picture of the changes that take place during the reaction, detailed EXAFS analysis was carried out. Typical fits of the recorded data to the calculated models are given in Appendix 7. Analysis of the EXAFS data revealed that both the Au-P and Au-Au coordination numbers remain almost constant (similar to the one found in $[Au_6(Ph_2P(o\text{-tolyl}))_6](NO_3)_3$) until the reaction time of about 40 mins (figure 5.6). After this time, the Au-P coordination number began to decrease and Au-Au started to increase. Closer examination of the Au L_{III} EXAFS data between 30 and 50 minutes of the reaction reveals further insight into the nature of ligand removal process. In particular, the Au-Au and Au-P distances were analysed (interatomic distance determination is more accurate than coordination number, since these are highly correlated with the disorder parameter).

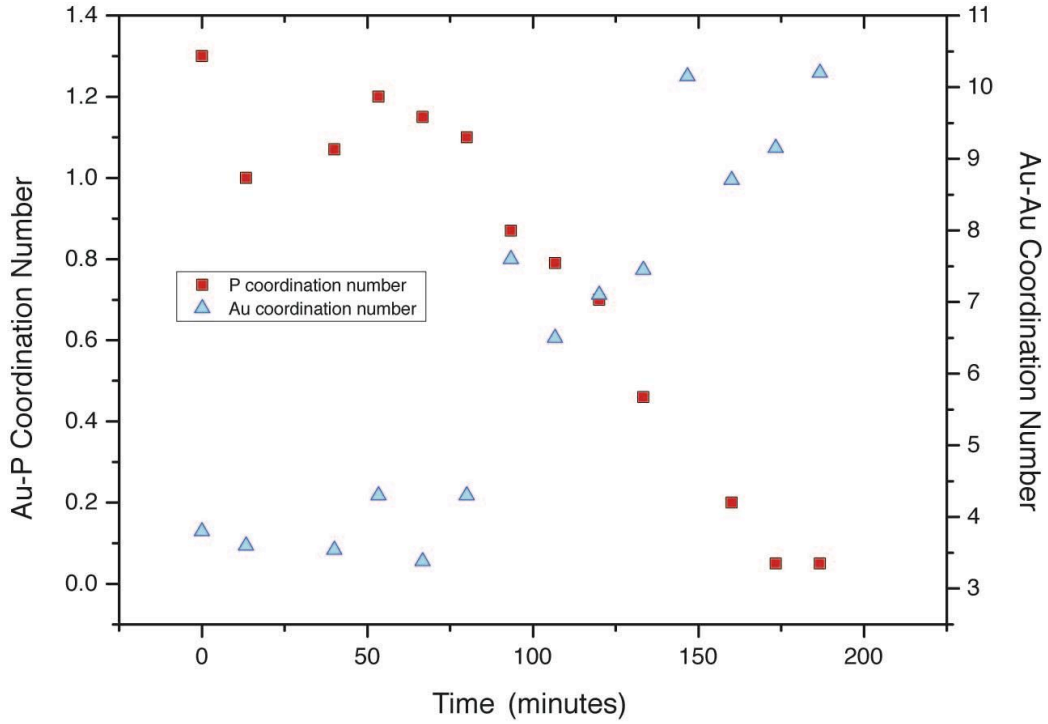

Figure 5.6. A plot of the change in Au-Au and Au-P coordination numbers with time, taken from analysed quick EXAFS during an *in situ* reaction of $[Au_6(Ph_2P(o\text{-tolyl}))_6](NO_3)_3$ (4.0 wt. %) supported on silica nanospheres.

In figure 5.7, the variation in Au-Au distance is plotted against time. In the first 30 minutes of the reaction, the average Au-Au distance is ca 2.7 Å, which is similar to the average distance obtained from the crystal structure of the $[Au_6(Ph_2P(o\text{-tolyl}))_6](NO_3)_3$ (see Chapter 3). However, after reacting for 30 minutes, the Au-Au distance slowly began to increase (at this point Au-P coordination began to decrease). This process appears to not be abrupt, but changes over a period of 15 minutes. During the course of this change it appears that Au-Au distance does not increase smoothly from 2.7 to 2.83 (typical of bulk Au-Au distance), instead an oscillatory change is seen. This could be due to partial removal of phosphine ligands at this stage.

The change in Au-P bond distance is also illustrated in figure 5.7. This is seen to generally increase from 2.2 Å to 3.3 Å as the reaction proceeds. This lengthening in bond distance could be due to the weakening of the Au-P bond as more phosphine ligands are removed from the gold. At the

time when the Au-Au bond distance increases at the highest rate, the Au-P bond distance fluctuates around 2.2 Å.

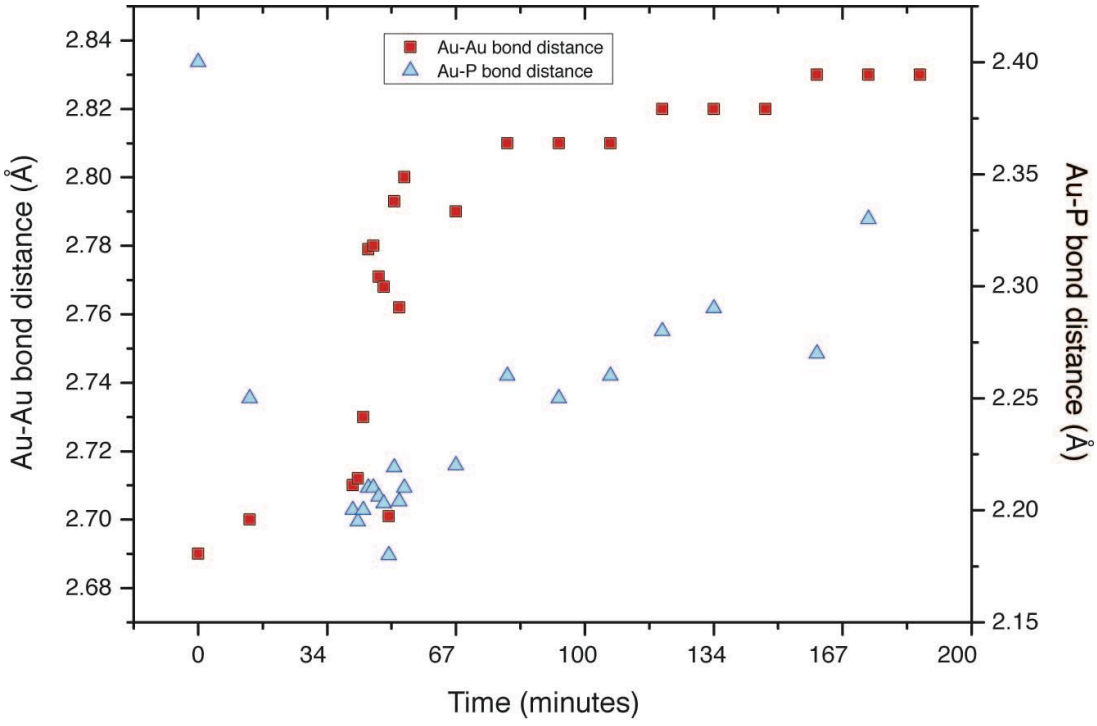

Figure 5.7. Variation in Au-Au and Au-P bond distance over time as the $[Au_6(Ph_2P(o\text{-tolyl}))_6](NO_3)_3$ reacts with TBHP at 95 °C.

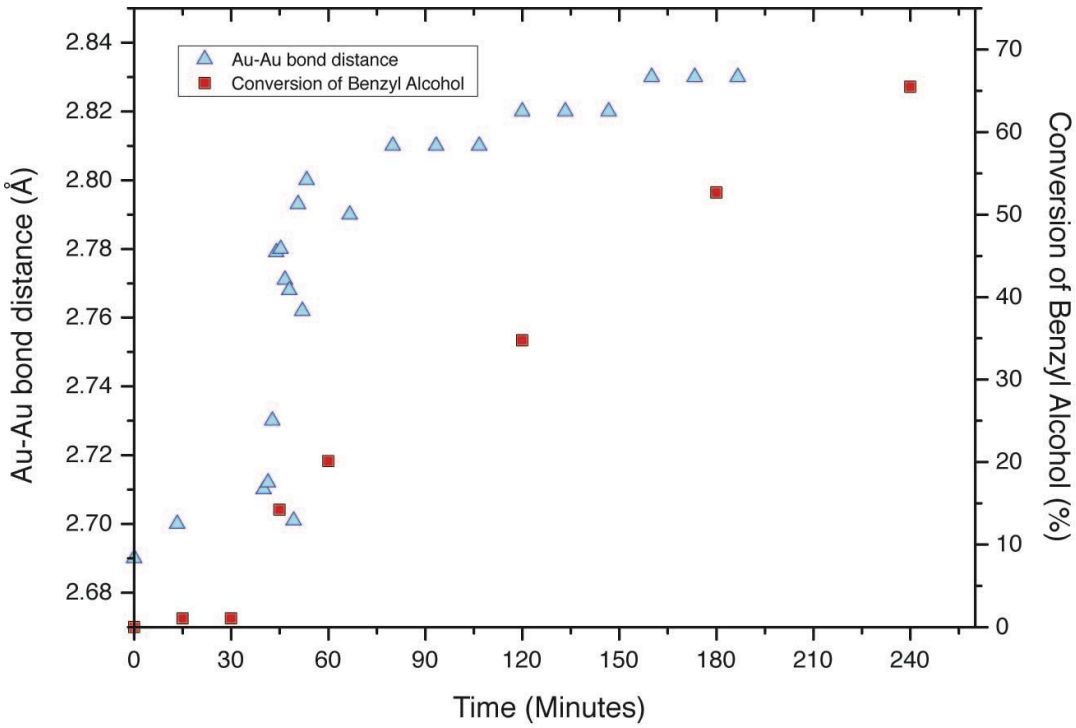

Figure 5.8. A plot of the variation in Au-Au bond distance in $[Au_6(Ph_2P(o\text{-tolyl}))_6](NO_3)_3$ (4.0 wt. %) supported on silica nanospheres taken from quick EXAFS data against the catalyst's activity in the oxidation of benzyl alcohol.

Figure 5.8 illustrates that there is a clear correlation between the formation of naked gold particles and the onset of catalytic activity. The initial activity is only observed once the Au-Au bond distance has increased slightly. This means that in order for the gold clusters to show catalytic activity for this reaction, there must first be a change in the structure of the cluster through the loss of a phosphine ligand (as seen from the change in the Au-P coordination number). Once this has occurred, a site is available on the surface of the gold cluster for catalysis to take place.

5.4. Conclusion

In summary, time-resolved *in situ* XAS studies clearly show that the presence of peroxide assists the removal of phosphine ligands thereby creating active gold catalysts for oxidation processes. This work not only shows detailed changes to the cluster during the induction period, but also how the exposed gold particles are formed during the catalytic reaction.

The correlation has been shown between the onset in activity in the uncalcined $[Au_6(Ph_2P(o\text{-tolyl}))_6](NO_3)_3$ (4.0 wt. %) catalysts and the time taken to begin removing the phosphines from the cluster. Complimentary *ex situ* data has also shown that smaller particles of gold are formed under theses lower temperature conditions than during calcination to either 300 or 500 ^{o}C, and the rate of particle growth is also very low.

6. Alternative catalyst supports

Abstract

This work focuses on preliminary catalysis data coupled with an *in situ* XAS investigation into the changes that titania supported phosphine stabilised gold clusters undergo during calcination.

6.1. Introduction

The metal oxide support is very important to the catalyst. Many catalysts can be tuned to give greater selectivity or a higher conversion through altering the support. Sometimes, even as subtle a difference as the phase of the support can make a difference. For example, it has been found that when highly dispersed gold is deposited onto the brookite, rutile and anatase phases of titania, a substantial difference in activity can be observed with brookite giving the most active catalyst for CO oxidation. Depending on the support that the gold is deposited on to, a range of catalytic reactions are accessible. Some of these are presented in table 6.1.

Table 6.1. **This table shows a selection of different catalysts available for different reactions. All the catalysts consist of gold particles on a support with the support being the only difference between each catalyst.**[163]

Reaction	Support	Notes
CO oxidation	TIO_2, Fe_2O_3, Co_3O_4, NiO, $Be(OH_2)$, $Mg(OH)_2$	active even at -70 ^oC
CH_4 oxidation	Co_3O_4	as active as Pd
$(CH_3)_3N$ oxidation	$NiFe_2O_4$	selective to N_2
$CH_3CH=CH_2 \rightarrow CHOCH=CH_2$	$Bi_2Mo_3O_{12}$	enhanced catalytic activity with unchanged selectivity
$CH_3CH=CH_2$ epoxidation	TiO_2	highly selective in the presence of H_2
$C_3H_8 \rightarrow (CH_3)_2CO$	TiO_2	selective in the presence of H_2
i-$C_4H_{10} \rightarrow (CH_3)_3COH$	TiO_2	
$C_5H_{11}OH \rightarrow C_4H_9CHO$	borosilicate glass	$NO_2 \rightarrow NO$
CO_2 or CO hydrogenation	ZnO, Fe_2O_3, ZrO_2	as active as Cu

Titanium dioxide, or titania, is a highly important semiconducting inorganic compound that is used in a range of applications. Chemically, it is most well known for its photocatalytic activity under UV light. This attribute has led to titania being used in self cleaning glass[194] and solar cells.[195] Aside from its photocatalytic properties, titania is also commonly used as a heterogeneous catalyst support.

6.1.1. Current work

This part of the project focussed on the deposition of $[Au_9(PPh_3)_8](NO_3)_3$ on to the surface of titania and mesoporous titania. These supports are already known to be active catalysts, and it has already been demonstrated that when coupled with gold, very highly active catalysts can be obtained.[169, 196] Many previously reported gold catalysts consisted of titania immobilised colloids of gold synthesised through conventional methods such as deposition precipitation. This work differs, as the gold is deposited on to the support as pre-formed phosphine stabilised clusters ($[Au_9(PPh_3)_8](NO_3)_3$) instead of forming metallic gold particles directly on the surface. As with Chapter 4, the gold clusters were deposited on to the titania surface using wet deposition and calcined to either 300 or 500 ^oC.

This work was carried out in collaboration with Dr. Andrea Sella and his student Fabian Carlson.

6.2. Experimental

6.2.1. Deposition of $[Au_9(PPh_3)_8](NO_3)_3$ on to mesoporous titania

Mesoporous titania (1.00g, 12.5 x 10^{-3} moles) was weighed into a round bottomed flask and covered with methanol (~ 3 ml). This slurry was placed in an ultrasonic bath for 5 minutes to break up any large aggregates of the support material. A solution of $[Au_9(PPh_3)_8](NO_3)_3$ (mass dependent on desired loading) in methanol (~3 ml) was added to the slurry and then the mixture was sealed and stirred for 1 hour 30 minutes. It was then placed in an ultrasonic bath for a further 5 minutes to ensure even dispersion of $[Au_9(PPh_3)_8](NO_3)_3$ before removing the methanol under vacuum. A brown solid was recovered from the round bottomed flask and stored until use. For 0.1 and 1.0 wt. % gold catalysts, 2.4 mg and 22.8 mg of $[Au_9(PPh_3)_8](NO_3)_3$ was added respectively per 1.00 g of titania.

6.2.2. Deposition of $[Au_9(PPh_3)_8](NO_3)_3$ on to other types of titania

The same method as described above was used, but with P25 Degussa or anatase titania in place of mesoporous titania.

6.2.3. Calcination of $[Au_9(PPh_3)_8](NO_3)_3$ on titania

The titania supported $[Au_9(PPh_3)_8](NO_3)_3$ (1.00 g) was measured into a ceramic boat which was then placed into a furnace. The furnace was programmed with a ramp rate of 5 K/minto the desired calcination

temperature (300 or 500 ^{o}C). When the furnace reached the calcination temperature it was programmed to dwell at that temperature for 1 hour before deactivating and allowing the catalyst to cool to room temperature.

6.2.4. Catalytic oxidation of benzyl alcohol

In a typical reaction, 0.1 g of catalyst was weighed into a 50 ml round-bottomed flask. 2.16 ml of Benzyl alcohol (10.42 mmol) and 4.54 ml of tert-butyl hydroperoxide (5.0-6.0 M in decane) was added to the container, which was then fitted with a condenser. This was lowered into an oil bath heated to 95 ^{o}C. The mixture was then stirred for 4 hours with samples of the reaction mixture collected at 0 hours and then every 15 minutes for the first hour and ever hour from then until 4 hours when the reaction was stopped by cooling the mixture to 5^{o}C. The samples were analysed using a PerkinElmer Clarus 500 Gas Chromatograph.

6.2.5. *In situ* calcination of 1.0 wt.% Au, $[Au_9(PPh_3)_8](NO_3)_3$ on anatase titania

In situ calcination EXAFS data was collected at station 9.3 at the S.R.S. in Daresbury Laboratories. A specially designed furnace was programmed with the following temperature program: room temperature to 100 ^{o}C at 2 ^{o}C/min, dwell at 100 ^{o}C for 20 mins, ramp to 200 ^{o}C at 2 ^{o}C/min, dwell for 20 mins, ramp to 300 ^{o}C at 5 ^{o}C/min, dwell for 20 min, ramp to 400 ^{o}C at 5 ^{o}C/min followed by cooling. Au L_{III} edge EXAFS were collected with 4 minute scans followed by 2 minute gaps, in the range 11.8-12.7 keV in transmission geometry.

6.3. Results and discussion

$[Au_9(PPh_3)_8](NO_3)_3$ was deposited on to various forms of titania with gold loading of either 0.1 or 1.0 wt. % gold. A 3.0 wt. % gold catalyst was also synthesised using rutile titania. They were tested for their catalytic activity for the oxidation of benzyl alcohol under conditions like those previously discussed in chapter 4. *In situ* XAS data was collected for 1.0 wt. % gold $[Au_9(PPh_3)_8](NO_3)_3$ supported on anatase titania to gain an insight to the changes occurring in the cluster during calcination.

6.3.1. *In situ* XANES data

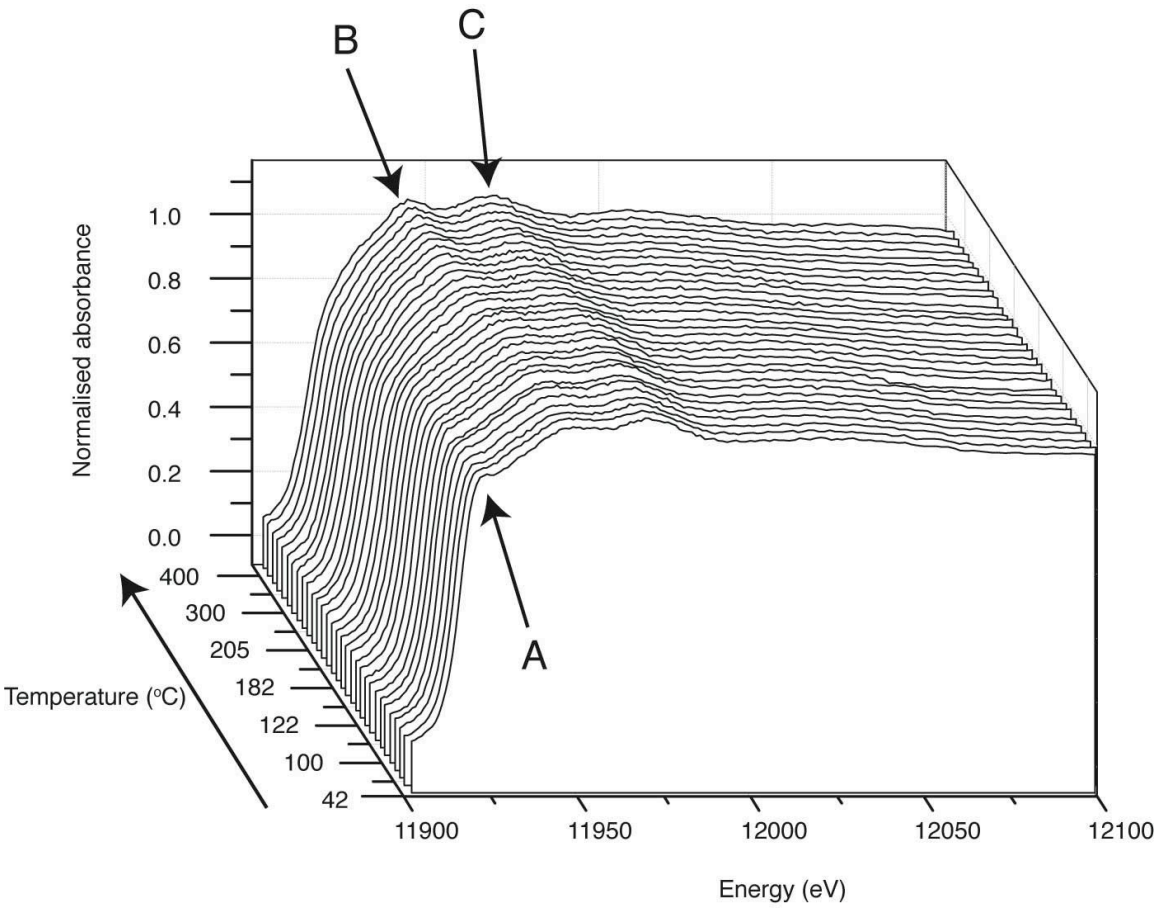

Figure 6.1. *In situ* XANES data following the calcination of 1.0 wt. % $[Au_9(PPh_3)_8](NO_3)_3$ to 400 °C.

Figure 6.1 illustrates the changes the XANES spectra as the temperature increases. As shown in XANES spectra in previous chapters, the presence of feature A indicates the presence of cationic charge on the gold. This feature decreases in intensity as the temperature increases showing a loss of charge from the gold. Features B and C increase slightly in intensity as the temperature increases due to the formation of metallic gold particles. The features in these XANES spectra are not as sharp as the features in XANES spectra in other chapters due to the low X-ray absorbance of the sample. Generally, the XANES data tells us that the gold cluster undergoes decomposition with the loss of cationic charge followed by the formation of metallic, uncharged gold particles on the surface of the support.

6.3.2. *In situ* EXAFS data

The Fourier transformed Au L_{III} edge EXAFS data showed a sudden decrease in the intensity of the peak representing the Au-P bond as the temperature increased reached 200 ^{o}C. A slight increase in the intensity of the peak assigned to the Au-Au bond is also observed. This is seen in figure 6.2.

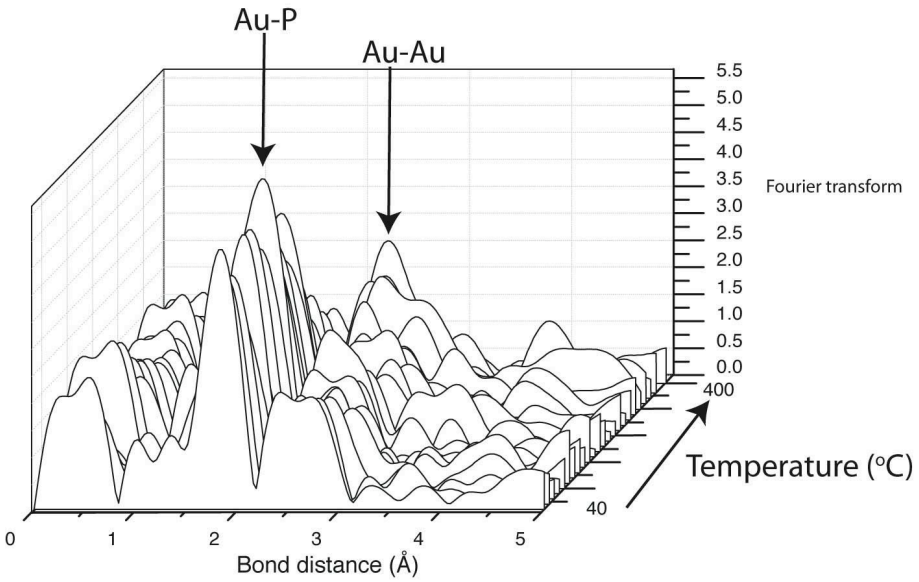

Figure 6.2. Fourier transformed Au L_{II} edge EXAFS data recorded from the *in situ* heating of 1.0 wt.% $[Au_9(PPh_3)_8](NO_3)_3$ supported on anatase titania.

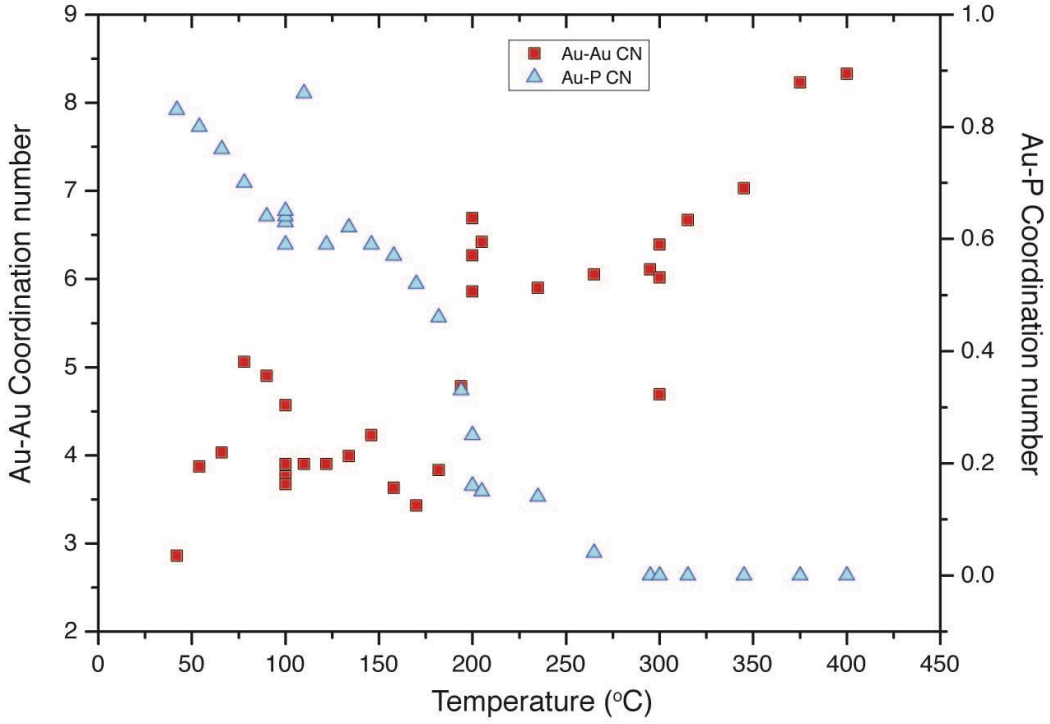

Figure 6.3. The variation in Au-Au coordination number and Au-P coordination number of 1.0 wt. % $[Au_9(PPh_3)_8](NO_3)_3$ to 400 °C from *in situ* EXAFS.

Analysis of the EXAFS data collected *in situ* yields more information into the changes undergone by the gold in the cluster during calcination.

Typical fits of the calculated structures to the recorded data are given in Appendix 8. Figure 6.3 shows that there is a general decrease in the Au-P coordination number as the temperature rises. The rate of change in the coordination number is highest as the temperature approaches 200 ^{o}C. This differs from previously mentioned TGA data (Appendix 3) of $[Au_9(PPh_3)_8](NO_3)_3$ which showed that the fastest rate of phosphine loss occurred at higher temperatures. It is possible that the presence of the support facilitates the loss of phosphines at lower temperatures. The Au-P coordination number reaches 0 at 300 ^{o}C, meaning metallic gold particles are left on the surface of the anatase.

The Au-Au coordination number steadily increases with the temperature once the temperature increases past 200 ^{o}C. Up until that point the Au-Au coordination number fluctuated around 3.8. There was a rapid increase in coordination number from 3.5 to 6.5 as the temperature rose from 175 to 200 ^{o}C. This change, along with the increasing coordination numbers up to 400 ^{o}C show that the gold particles continue to grow in size as the temperature rises.

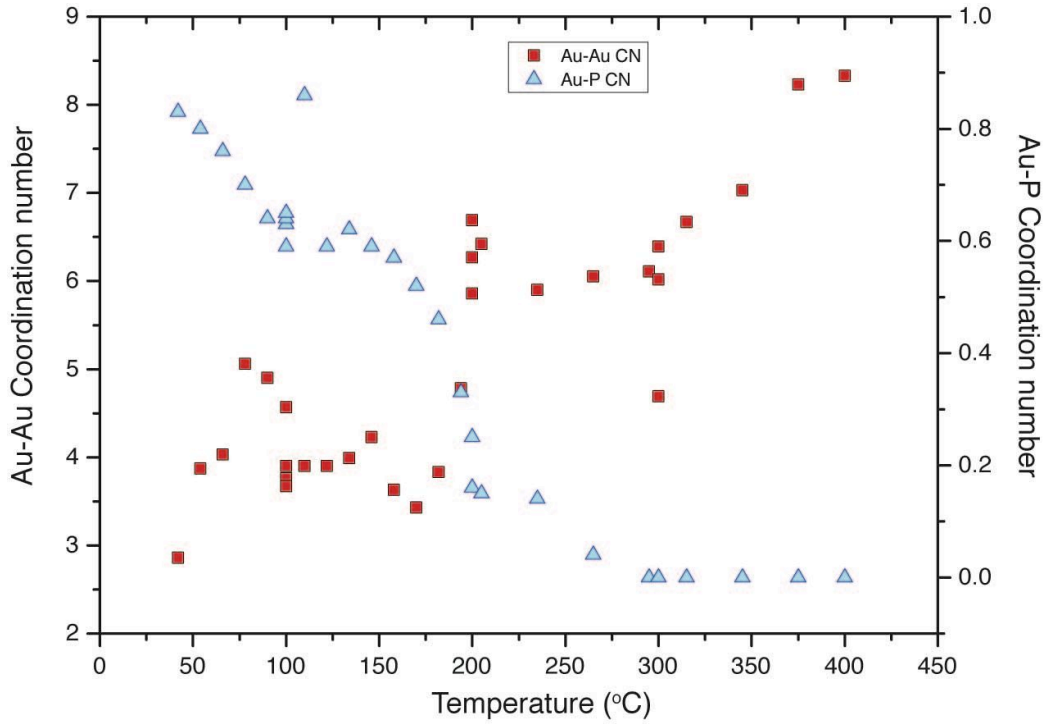

Figure 6.4. The variation of Au-Au and Au-P bond distance of 1.0 wt. % $[Au_9(PPh_3)_8](NO_3)_3$ to 400 °C from *in situ* EXAFS.

The Au-P bond distance (figure 6.4) generally fluctuates between 2.20 and 2.24 Å as the temperature approaches 200 °C. Beyond this temperature, there is a general increase in Au-P bond distance indicating the weakening of the bond due to phosphine loss and destabilisation of the cluster molecule. The Au-Au bond distance follow a similar trend, only it starts to steadily increase after reaching 150 °C. Before this temperature was reached, the Au-Au bond distance shifted between 2.67 and 2.73 Å. These contracted bond lengths are characteristic of cationic gold clusters. The gradual increase in Au-Au bond length is consistent with the loss of positive charge from the gold accompanying the loss of the phosphine ligands. The final bond length of 2.80 Å suggests that small (<50 nm) gold particles are present.

6.3.3. Catalysis data

It should be noted that one of the catalysts (3.0 wt. % $[Au_9(PPh_3)_8](NO_3)_3$ on anatase) had been prepared 2 years in advance. Although it had not undergone heat treatment, it was pink in colour, indicating the presence of gold particles. This was noticed for many other uncalcined anatase supported gold catalysts, but time did not permit further investigation of them. What was interesting with the uncalcined 3.0 wt. % $[Au_9(PPh_3)_8](NO_3)_3$ on anatase catalyst was that when the pink hue was first noticed, it was only on the outside surface of the powder. If the sample was disturbed, the pink colour would be replaced by the usual brown. Over time all of the sample gradually changed colour completely, and this is most likely due to a photocatalytic oxidation reaction occurring in the presence of the anatase titania. This photocatalytic reaction would be an interesting method of removing the phosphines from the clusters worthy of further investigation.

All of the other catalysts were prepared shortly before being tested for their catalytic activity but no noticeable change in colour was observed in the uncalcined catalysts. This could be due to the short-term light exposure of the catalysts.

Another issue with the TiO_2 supported catalysts arose when carrying out analysis of the gas chromatography data. It seemed as though the amount of decane that was present in the samples from the reactor vessel and used as an internal standard for the GC, decreased as the experiment proceeded, causing the data to present negative conversions of benzyl alcohol. It was soon identified that the TiO_2 was photocatalytically decomposing the decane to CO_2 and water. Linear decane was preferentially oxidised over aromatic benzyl alcohol or the branched tert-butyl hydroperoxide. In order to complete the GC analysis, tert-butyl hydroperoxide and its hydrolysis product, tert-butanol, were

together used as the internal standards under the assumption that their total amount would stay constant throughout the reaction.

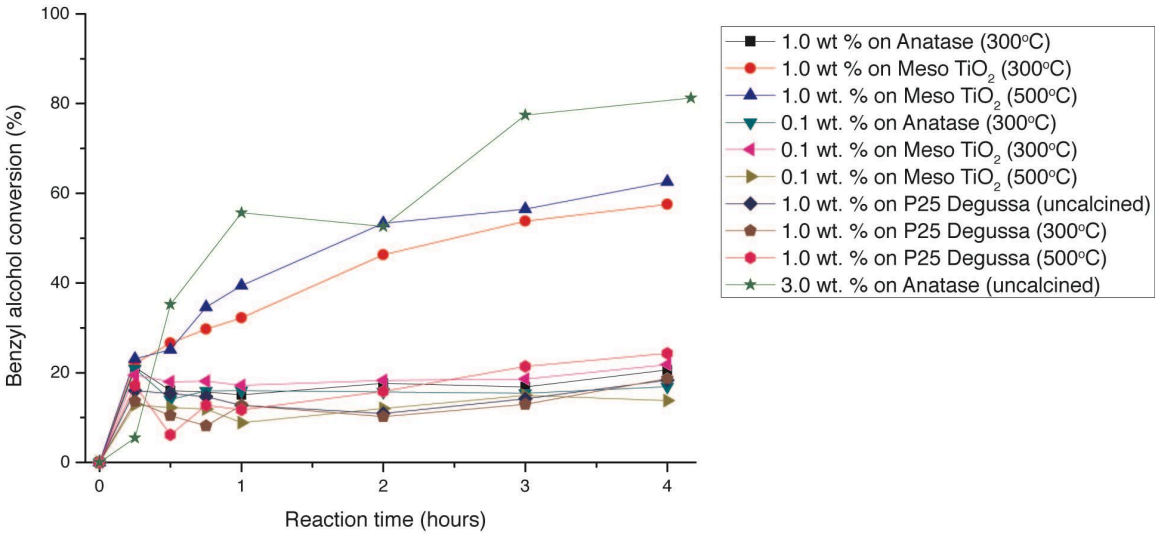

Figure 6.5. The conversion of benzyl alcohol during the catalytic oxidation of benzyl alcohol over $[Au_9(PPh_3)_8](NO_3)_3$ supported on various types of titania.

The catalytic oxidation of benzyl alcohol reactions revealed how active the catalysts were. Full conversions and selectivities for each catalyst are available in Appendix 9. The conversions of benzyl alcohol are shown in figure 6.5. The results indicate that the catalysts loaded with 0.1 wt.% gold are quite inactive for this reaction, with benzyl alcohol conversions of <20% after 4 hours. The conversion is very low regardless of the calcination temperature or the structure of titanium dioxide used as a support. The catalysts with 1.0 wt.% gold that are not supported on mesoporous titania gave also gave very low conversions. The catalysts that displayed high conversions of benzyl alcohol were those with gold loading of 1.0 wt.% supported on mesoporous titania and calcined to either 300 or 500 ^{o}C. The 3.0 wt.% gold loaded catalyst gave the highest conversion. This is consistent with the silica supported catalysts discussed in chapter 4 that converted more benzyl alcohol when the gold loading was higher.

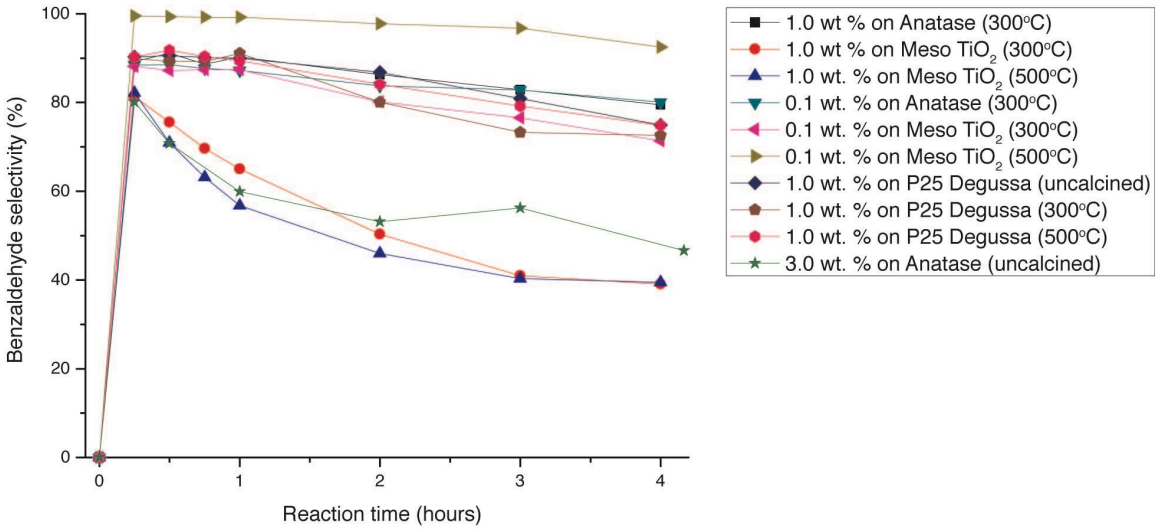

Figure 6.6. The selectivity for benzaldehyde during the catalytic oxidation of benzyl alcohol over $[Au_9(PPh_3)_8](NO_3)_3$ supported on various types of titania.

The selectivity for benzaldehyde is generally high (>80%) throughout the reaction for most of the catalysts (figure 6.6). The highest selectivity is seen in the 0.1 wt.% gold loaded catalyst supported on mesoporous titania calcined to 500 ^{o}C. The selectivity for benzaldehyde for this catalyst stays above 95% for most of the reaction. This is most like due to the very low conversion of benzyl alcohol by this catalyst. The catalysts that displayed the highest benzyl alcohol conversion also display the largest changes in selectivity. The initial selectivities of 80% gradually decrease to <50% by the end of the reaction. This is due to the reaction being carried out in a batch reactor which means that the when the concentration of the products builds up to a certain level, the products will start to be oxidised and the selectivity will therefore decrease.

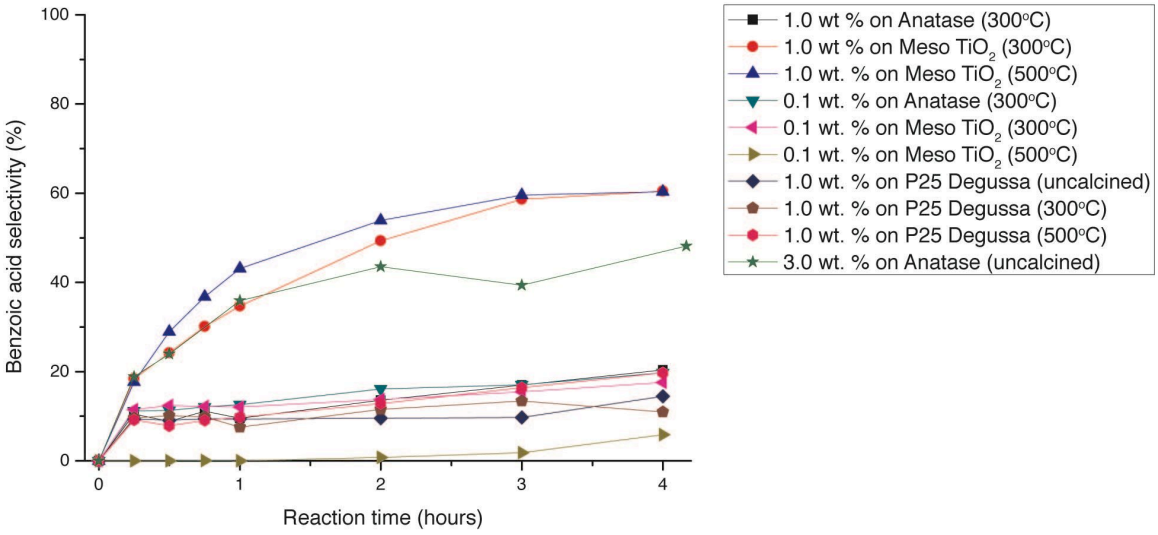

Figure 6.7. The selectivity for benzoic acid during the catalytic oxidation of benzyl alcohol over $[Au_9(PPh_3)_8](NO_3)_3$ supported on various types of titania.

Figure 6.7 shows the changes in selectivity for benzoic acid. All of the catalysts that displayed low conversions of benzyl alcohol have low selectivities for benzoic acid (~10%). The three catalysts that displayed high activities had selectivities for benzoic acid that increased throughout the reaction. After 4 hours, the active mesoporous titania catalysts had higher selectivities for benzoic acid (60%) than benzaldehyde (39%). This is also explained by the use of a batch reactor coupled with a highly active oxidation catalyst.

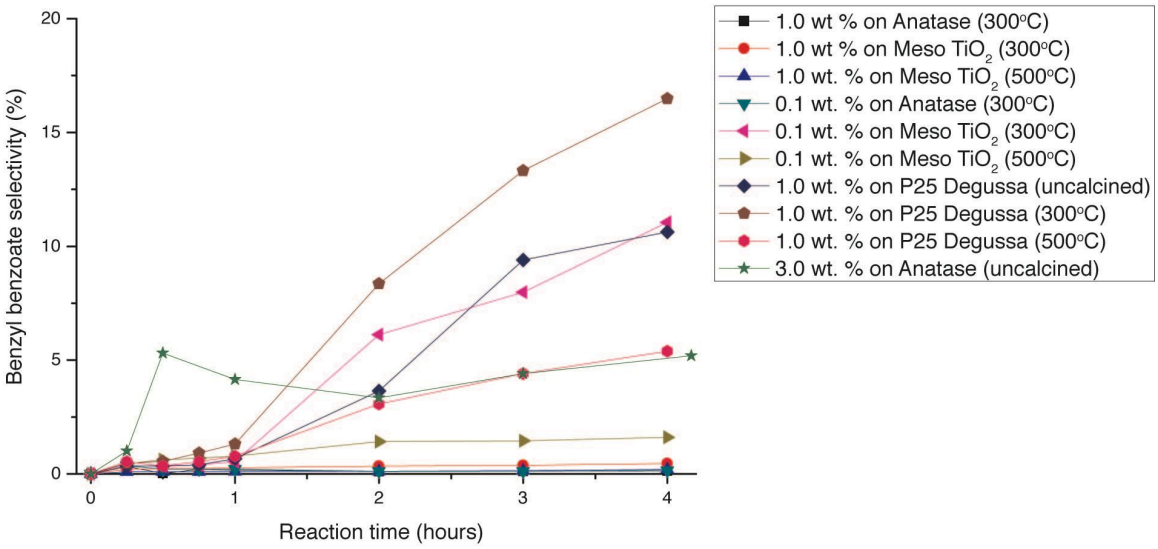

Figure 6.8. The selectivity for benzyl benzoate during the catalytic oxidation of benzyl alcohol over $[Au_9(PPh_3)_8](NO_3)_3$ supported on various types of titania.

The selectivity for benzyl benzoate shown in figure 6.8 is interesting as it shows that some of the catalysts that looked to be quite inactive display interestingly high selectivities for benzyl benzoate. All of the catalysts supported on the commercial P25 Degussa titania had the highest selectivities for benzyl benzoate. The P25 Degussa catalyst calcined to 300 ^{o}C had the highest selectivity for this product of all the catalysts discussed in this work. It is unusual for catalysts that display such low benzyl alcohol conversions to have such high selectivies for the ester product.

6.4. Conclusion

The *in situ* XAS experiment of the anatase supported gold clusters showed that the clusters undergo similar decomposition to those supported on silica. A temperature dependent loss of phosphines occurs, along with a loss of cationic charge. Metallic gold particles are formed, with evidence for sintering observed by the increase in the Au-Au coordination number and bond distances.

What is clear is how the structure of the support affects the activity or the catalyst. The mesoporous catalysts with 1.0 wt.% gold loadings gave a far higher conversion than the regularly structured catalysts with lower or equal gold loads. This is most likely due to the higher surface area of the mesoporous titania which allowed for a better distribution of the clusters during deposition. It is also likely that as a result of the clusters being separated by the pores of the support, less sintering occurred during calcination meaning smaller, more highly active particles of gold were present.

7. Conclusion

7.1. Cluster synthesis

It has been demonstrated that the number of gold atoms at the core of a phosphine stabilised cluster can be increased or decreased as a function of the steric bulk of the ligands. Evidence suggests that the novel clusters $[Au_4(P(o\text{-tolyl})_3)_4]^+$ and $[Au_4(Ph_2P(o\text{-tolyl}))_4]^+$ are obtained through the reduction of $[Au(P(o\text{-tolyl})_3)](NO_3)$ and $[Au(Ph_2P(o\text{-tolyl}))](NO_3)$ respectively using $NaBH_4$. The large cone angle ligands limit the size of the clusters formed, whereas if ligands with smaller cone angles are used, larger clusters with more gold atoms at their cores are obtained. This is seen through the formation of $[Au_6(Ph_2P(o\text{-tolyl}))_6](NO_3)_2$ and $[Au_9(PPh_3)_8](NO_3)_3$, which are stabilised by ligands with respective cone angles of 185^o and 145^o.

7.2. Catalyst preparation using calcination

$[Au_6(Ph_2P(o\text{-tolyl}))_6](NO_3)_2$ and $[Au_9(PPh_3)_8](NO_3)_3$ were used to prepare heterogeneous catalysts with a range of gold loadings. They were also calcined at either 300 or 500 ^oC. Calcination proved to be a counter-productive process for the removal of the stabilising phosphine ligands from the cluster as very large gold particles (10-60 nm in size) were generated this way. Aurophilicity and the elevated temperatures for calcination contributed to the agglomeration of the gold and the formation of these large particles.

Characterisation revealed that when $[Au_9(PPh_3)_8](NO_3)_3$ was dispersed on to the silica support with a gold loading equal to a supported $[Au_6(Ph_2P(o\text{-tolyl}))_6](NO_3)_2$ catalyst, following calcination to the same

temperature, the average gold particle size was larger than the $[Au_6(Ph_2P(o\text{-tolyl}))_6](NO_3)_2$ catalyst. This indicates that the size of the initial cluster before calcination is relevant to the size of the gold particles obtained after. The average gold particle size was generally seen to decrease with increased gold loading following calcination. Calcining the catalysts at 500 ^oC gave larger average particle sizes than those calcined at 300 ^oC due to the increased mobility of the gold on the surface of the silica at higher temperatures. A natural progression would be to either functionalise the surface of the silica to hold the clusters in place, or to use a higher surface area support that would allow for the clusters to be spaced further apart.

7.3. Catalytic activity

Despite the large size of the gold particles present, the catalysts supported on silica nanospheres generally displayed good activity for the oxidation of benzyl alcohol. Figure 7.1 correlates the size of the gold particles present in the catalysts with the conversion of benzyl alcohol. This shows how the smaller gold particles present in the catalyst give higher conversions. The highest conversion is obtained when the average gold particle size is 13 nm, whereas the lowest conversion is observed when the average gold particle size is 29 nm.

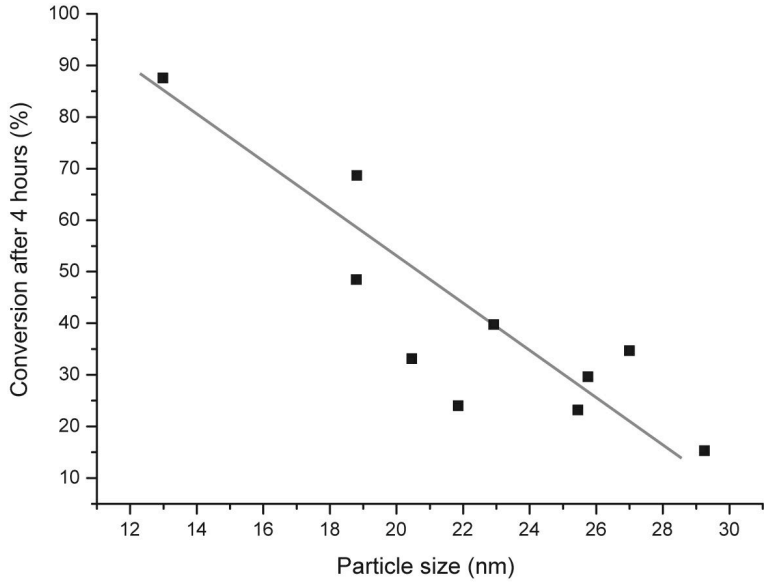

Figure 7.1. A plot of the catalysts average gold particle size (calculated from XRD data) against the catalysts conversion of benzyl alcohol after 4 hours.

Due to the nature of reactions in a batch reactor, the initial oxidation product from the oxidation of benzyl alcohol started to be oxidised further to benzoic acid. As the concentration of benzaldehyde increased inside the reactor when the most active catalysts were present, the selectivity decreased for the aldehyde and an increased for benzoic acid. A way to maintain the high selectivity throughout the reaction time would be to use a flow reactor whereby the oxidised products could be removed from the catalyst as they are generated to prevent further oxidation.[197] The decrease in selectivity for benzaldehyde with catalysts that offer higher benzyl alcohol conversions has also been noted before.[198]

A natural consequence of the most highly active catalysts was therefore a decrease in the selectivity of benzaldehyde once a significant proportion of the benzyl alcohol had been oxidised. Figure 7.2 shows an inverse trend to that seen for the conversion of benzyl alcohol against the average gold particle size on the catalyst. The figure shows that the selectivity after 4 hours is generally lower for when the average gold particle size is smaller and higher selectivity is obtained when larger gold particles are present.

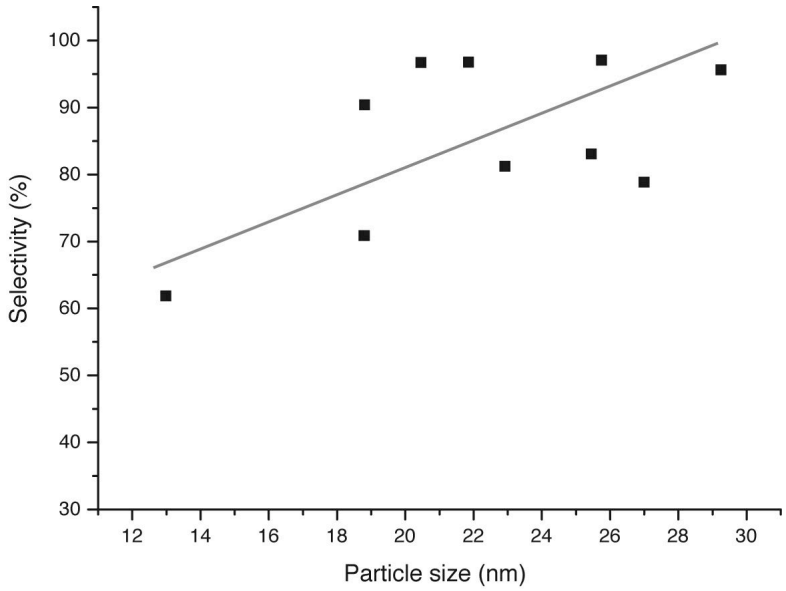

Figure 7.2. A plot of the average gold particle size (calculated from XRD data) against the catalysts selectivity for benzaldehyde after 4 hours for the catalytic oxidation of benzoic acid.

The method of benzyl alcohol oxidation using TBHP gives higher conversions in shorter periods of time than other groups using supported gold, and gold-palladium catalysts utilising pressurized oxygen as an oxidant[199] under higher temperature conditions. This is most likely due to the higher reactivity of the peroxide than molecular oxygen. The catalysts reported in this work generally give higher conversions of benzyl alcohol, with the more active catalysts giving lower benzaldehyde selectivities than other groups that also use TBHP as an oxidant.[147]

The deposition of $[Au_9(PPh_3)_8](NO_3)_3$ on to an alternative support, titania, yielded catalysts with generally lower activities. Though rutile loaded with 3.0 wt.% gold proved to have very high activity but low selectivity for benzaldehyde.

7.4. Peroxide assisted low temperature ligand removal

Perhaps the most widely applicable discovery of this work has been the development of a new method of removing the ligands at lower temperatures. *In situ* QEXAFS revealed that the phosphines are gradually lost from the clusters and the gold particles slowly increase in size as the reaction with TBHP proceeded. Where *in situ* XAS of the calcined catalysts showed that there was a fast increase in the Au-Au coordination number as the temperature rose, this process offers more control over the ligands removal process as it takes place at a lower rate. This method may prove to be viable for the activation of a range of ligand stabilised clusters and nanoparticles to form active catalysts.

7.5. Summary

This work has demonstrated that phosphine stabilised clusters can be employed to generate highly active catalysts for the oxidation of benzyl alcohol. The gold loading, calcination temperature support, and cluster type all affect the final catalysts activity. A new method of removing the phosphine ligands at a lower temperature has been discovered allowing more control over this process so that large particle formation may be avoided. This work is only scratching the surface of this area, and research must be continued to learn more about the potential uses of molecular clusters in the synthesis of heterogeneous catalysts, as it is likely that they offer a unique solution to the problem of obtaining homogeneously sized metal particles.

7.6. Future work

Further work could investigate the effect of pretreatment on the silica support surface. By charging the surface, it may be possible to deposit the clusters on to the surface more accurately than using wet deposition. Also, if the clusters are adsorbed on to the surface, rather than deposited, it may be possible to reduce the sintering occuring during calcination to give supported metal particles that are more similar to the clusters in size. It would also be interesting to repeat the low temperature ligand removl experiments using different gold cluster, and at lower temperatures. This might allow further control over the rate of cluster degredation to metal particles.

8. References

1. J. J. Berzelius, *Poggendorf's Annalen*, 1834, **31**, 273.
2. G. J. Sunley and D. J. Watson, *Catalysis Today*, 2000, **58**, 293.
3. G. Hutchings, *Journal of Materials Chemistry*, 2009, **19**, 1222.
4. *Catalysis*, Royal Society of Chemistry, 2005.
5. H. F. Rase, Handbook of Commercial Catalysts: Heterogeneous Catalysts, CRC Press, 2000.
6. J. Weitkamp, *Solid State Ionics*, 2000, **131**, 175.
7. C. J. Plank, W. P. Hawthorne and E. J. Rosinski, *Industrial & Engineering Chemistry Product Research and Development*, 1964, **3**, 165.
8. A. Corma, *Journal of Catalysis*, 2003, **216**, 298.
9. R. M. Heck and R. J. Farrauto, *Applied Catalysis A: General*, 2001, **221**, 443.
10. G. J. K. Acres and B. Harrison, *Topics in Catalysis*, 2004, **28**, 3.
11. O. S. Alexeev and B. C. Gates, *Industrial & Engineering Chemistry Research*, 2003, **42**, 1571.
12. D. S. Shephard, T. Maschmeyer, G. Sankar, J. M. Thomas, D. Ozkaya, B. F. G. Johnson, R. Raja, R. D. Oldroyd and R. G. Bell, *Chemistry-A European Journal*, 1998, **4**, 1214.
13. M. Turner, V. B. Golovko, O. P. H. Vaughan, P. Abdulkin, A. Berenguer-Murcia, M. S. Tikhov, B. F. G. Johnson and R. M. Lambert, *Nature*, 2008, **454**, 981.
14. Z. Hawass, Tutankhamum and the Golden age of the Pharaohs, National Geographic.
15. N. N. Greenwood and A. Earnshaw, *Chemistry of the Elements*, 2nd edn., Butterworth-Heinemann, 1997.
16. A. I. Yanson, G. R. Bollinger, H. E. van den Brom, N. Agrait and J. M. van Ruitenbeek, *Nature*, 1998, **395**, 783.
17. G. Humpston and D. Jacobson, *Gold Bulletin*, 1992, **25**, 132.
18. J. W. Sigler, G. B. Bluhm, H. Duncan, J. T. Sharp, D. C. Ensign and W. R. McCrum, *Annals of Internal Medicine*, 1974, **80**, 21.
19. N. Kaltsoyannis, Journal of the Chemical Society-Dalton Transactions, 1997, 1.
20. P. Pyykko, *Chemical reviews*, 1988, **88**, 563.
21. Modern Supramlecular Gold Chemistry, \wiley-VCH, 2008.
22. J. P. Desclaux, *Atomic Data and Nuclear Data Tables*, 1973, **12**, 311.
23. F. Scherbaum, A. Grohmann, B. Huber, C. Kruger and H. Schmidbaur, *Angewandte Chemie-International Edition*, 1988, **27**, 1544.
24. H. Schmidbaur, *Gold Bulletin*, 2000, **33**, 3.
25. H. Schmidbaur and A. Schier, *Chemical Society Reviews*, 2008, **37**, 1931.

26. E. Zeller and H. Schmidbaur, Journal of the Chemical Society-Chemical Communications, 1993, 69.
27. H. Beruda, E. Zeller and H. Schmidbaur, *Chemische Berichte-Recueil*, 1993, **126**, 2037.
28. H. Schmidbaur, *Chemical Society Reviews*, 1995, **24**, 391.
29. K. Angermaier and H. Schmidbaur, *Inorganic Chemistry*, 1995, **34**, 3120.
30. A. Schier, A. Grohmann, J. M. Lopez-De-Luzuriaga and H. Schmidbaur, *Inorganic Chemistry*, 2000, **39**, 547.
31. A. Grohmann, J. Riede and H. Schmidbaur, *Nature*, 1990, **345**, 140.
32. Dellamic.D and Calderaz.F, *Gazzetta Chimica Italiana*, 1973, **103**, 1099.
33. Z. Assefa, R. J. Staples and J. P. Fackler, Acta Crystallographica Section C-Crystal Structure Communications, 1996, **52**, 305.
34. W. M. Latimer and J. H. Hildebrand, *Reference Book of Inorganic Chemistry*, Third edn., 1953.
35. M. C. Gimeno and A. Laguna, *Chemical reviews*, 1997, **97**, 511.
36. M. Khan, C. Oldham and D. G. Tuck, *Canadian Journal of Chemistry*, 1981, **59**, 2714.
37. R. Roulet, N. Q. Lan, W. R. Mason and G. P. Fenske, *Helvetica Chimica Acta*, 1973, **56**, 2405.
38. U. M. Tripathi, A. Schier and H. Schmidbaur, Zeitschrift Fur Naturforschung Section B-a Journal of Chemical Sciences, 1998, **53**, 171.
39. J. C. Wang, N. I. Khan and J. P. Fackler, Acta Crystallographica Section C-Crystal Structure Communications, 1989, **45**, 1008.
40. R. J. Staples, C. King, M. N. I. Khan, R. E. P. Winpenny and J. P. Fackler, *Acta Crystallographica Section C-Crystal Structure Communications*, 1993, **49**, 472.
41. A. Hamel, A. Schier and H. Schmidbaur, Zeitschrift Fur Naturforschung Section B-a Journal of Chemical Sciences, 2002, **57**, 877.
42. P. G. Jones, Journal of the Chemical Society-Chemical Communications, 1980, 1031.
43. R. V. Parish and J. D. Rush, *Chemical Physics Letters*, 1979, **63**, 37.
44. L. Malatesta, L. Naldini, G. Simonetta and F. Cariati, *Coordination Chemistry Reviews*, 1966, **1**, 255.
45. R. C. Elder, E. H. K. Zeiher, M. Onady and R. R. Whittle, *Journal of the Chemical Society-Chemical Communications*, 1981, 900.
46. H. Schmidbaur, Angewandte Chemie-International Edition, 1976, **15**, 728.
47. R. J. Puddephatt, *The Chemistry Of Gold*, Elsevier Scientific Publishing Company, 1978.
48. M. L. Williams, *Inflammopharmacology*, 2008, **16**, 110.
49. K. J. Kilpin, W. Henderson and B. K. Nicholson, *Inorganica Chimica Acta*, 2009, **362**, 5080.

50. V. F. Duckworth and N. C. Stephenson, *Inorganic Chemistry*, 1969, **8**, 1661.
51. D. Safer, J. Hainfeld, J. S. Wall and J. E. Reardon, *Science*, 1982, **218**, 290.
52. A. A. Sousa, M. A. Aronova, Y. C. Kim, L. M. Dorward, G. Zhang and R. D. Leapman, *Journal of Structural Biology*, 2008, **161**, 336.
53. A. Herzing, C. Kiely, A. Carley, P. Landon and G. Hutchings, *Science*, 2008, **321**, 1331.
54. W. H. Bragg and W. L. Bragg, Proceedings of the Royal Society of London. Series A, Containing Papers of a Mathematical and Physical Character, 1913, **88**, 428.
55. A. L. Patterson, *Physical Review*, 1939, **56**, 978.
56. www.diamond.ac.uk.
57. J. J. Rehr and R. C. Albers, *Reviews of Modern Physics*, 2000, **72**, 621.
58. J. M. Thomas and G. Sankar, *Accounts of Chemical Research*, 2001, **34**, 571.
59. D. C. Koningsberger, B. L. Mojet, G. E. van Dorssen and D. E. Ramaker, *Topics in Catalysis*, 2000, **10**, 143.
60. K. V. Klementiev, *Journal of Physics D: Applied Physics*, 2001, **34**, 209.
61. N. Binsted, 1998.
62. Malatest.L, L. Naldini, Simonett.G and F. Cariati, *Chemical Communications*, 1965, 212.
63. McPartli.M, R. Mason and Malatest.L, Journal of the Chemical Society D-Chemical Communications, 1969, 334.
64. F. Cariati, L. Naldini, G. Simonetta and L. Malatesta, *Inorganica Chimica Acta*, 1967, **1**, 315.
65. F. Demartin, M. Manassero, L. Naldini, R. Ruggeri and M. Sansoni, *Journal of the Chemical Society-Chemical Communications*, 1981, 222.
66. J. W. A. Vandervelden, J. J. Bour, R. Pet, W. P. Bosman and J. H. Noordik, *Inorganic Chemistry*, 1983, **22**, 3112.
67. J. W. A. Vandervelden, J. J. Bour, F. A. Vollenbroek, P. T. Beurskens and J. M. M. Smits, *Journal of the Chemical Society-Chemical Communications*, 1979, 1162.
68. C. E. Briant, K. P. Hall, D. M. P. Mingos and A. C. Wheeler, *Journal of the Chemical Society-Dalton Transactions*, 1986, 687.
69. J. W. A. Vandervelden, J. J. Bour, J. J. Steggerda, P. T. Beurskens, M. Roseboom and J. H. Noordik, *Inorganic Chemistry*, 1982, **21**, 4321.
70. J. W. A. Vandervelden, P. T. Beurskens, J. J. Bour, W. P. Bosman, J. H. Noordik, M. Kolenbrander and J. Buskes, *Inorganic Chemistry*, 1984, **23**, 146.
71. J. W. A. Vandervelden, J. J. Bour, W. P. Bosman and J. H. Noordik, *Inorganic Chemistry*, 1983, **22**, 1913.

72. J. W. A. Vandervelden, J. J. Bour, W. P. Bosman and J. H. Noordik, *Journal of the Chemical Society-Chemical Communications*, 1981, 1218.
73. F. A. Vollenbroek, W. P. Bosman, J. J. Bour, J. H. Noordik and P. T. Beurskens, *Journal of the Chemical Society-Chemical Communications*, 1979, 387.
74. M. K. Cooper, G. R. Dennis, K. Henrick and M. McPartlin, *Inorganica Chimica Acta-Letters*, 1980, **45**, L151.
75. K. P. Hall, B. R. C. Theobald, D. I. Gilmour, D. Michael, P. Mingos and A. J. Welch, *Journal of the Chemical Society-Chemical Communications*, 1982, 528.
76. C. E. Briant, K. P. Hall and D. M. P. Mingos, *Journal of the Chemical Society-Chemical Communications*, 1984, 290.
77. P. L. Bellon, F. Cariati, M. Manassero, L. Naldini and M. Sansoni, *Journal of the Chemical Society D-Chemical Communications*, 1971, 1423.
78. F. Cariati and L. Naldini, Journal of the Chemical Society-Dalton Transactions, 1972, 2286.
79. F. Wen, U. Englert, M. Homberger and U. Simon, *Zeitschrift fur anorganische und allgemeine Chemie*, 2006, **632**, 2159.
80. F. Wen, U. Englert, B. Gutrath and U. Simon, *European Journal of Inorganic Chemistry*, 2008, 106.
81. C. E. Briant, K. P. Hall, A. C. Wheeler and D. M. P. Mingos, *Journal of the Chemical Society-Chemical Communications*, 1984, 248.
82. M. McPartlin, R. Mason and L. Malatesta, *Journal of the Chemical Society D-Chemical Communications*, 1969, 334.
83. C. E. Briant, B. R. C. Theobald, J. W. White, L. K. Bell and D. M. P. Mingos, *Journal of the Chemical Society-Chemical Communications*, 1981, 201.
84. B. K. Teo, X. SHI and H. Zhang, *Journal of the American Chemical Society*, 1992.
85. G. Schmid, R. Pfeil, R. Boese, F. Bandermann, S. Meyer, G. H. M. Calis and W. A. Vandervelden, *Chemische Berichte-Recueil*, 1981, **114**, 3634.
86. J. G. M. Vanderlinden, M. L. H. Paulissen and J. E. J. Schmitz, *Journal of the American Chemical Society*, 1983, **105**, 1903.
87. C. E. Briant, K. P. Hall, D. M. P. Mingos and A. C. Wheeler, *Journal of the Chemical Society*, 1986.
88. C. A. Tolman, *Chemical reviews*, 1977, **77**, 313.
89. A. M. M. Meij, A. Muller and A. Roodt, *Acta Crystallographica Section E*, 2003, **59**, m44.
90. V. G. Albano, P. L. Bellon, Manassero and M. Sansoni, *Journal of the Chemical Society-Chemical Communications*, 1970, 1210.
91. P. J. Dyson and D. M. P. Mingos, Homonuclear Clusters and Colloids of Gold: Synthesis, Reactivity, Structural and Theoretical Considerations in Gold; Progress in Chemistry, Biochemistry and Technology, Wiley, Chichester., 1999.

92. M. Fairbanksi, H. Benfield, R. Newportt and G. Schmida, *Solid State Communications,*, 1990, **73**, 431.
93. L. R. Wallenberg, J. O. Bovin and G. Schmid, *Surface Science*, 1985, **156**, 256.
94. G. Schmid, M. Baumle, M. Geerkens, I. Helm, C. Osemann and T. Sawitowski, *Chemical Society Reviews*, 1999, **28**, 179.
95. G. Schmid, *Chemical Society Reviews*, 2008, **37**, 1909.
96. D. M. P. Mingos, Journal of the Chemical Society-Dalton Transactions, 1976, 1163.
97. D. M. P. Mingos, Philosophical Transactions of the Royal Society of London. Series A, Containing Papers of a Mathematical or Physical Character, 1982, **308**, 75.
98. K. P. Hall, D. I. Gilmour and D. M. P. Mingos, *Journal of Organometallic Chemistry*, 1984, **268**, 275.
99. D. M. P. Mingos, *Polyhedron*, 1984, **3**, 1289.
100. D. M. P. Mingos, *Gold Bulletin*, 1984, **17**, 5.
101. D. M. P. Mingos, *Accounts of Chemical Research*, 1984, **17**, 311.
102. O. D. Haberlen, H. Schmidbaur and N. Rosch, *Journal of the American Chemical Society*, 1994, **116**, 8241.
103. A. Brodbeck and J. Strahle, *Acta Crystallographica Section A*, 1990, **46**, C.
104. M. Walter, J. Akola, O. Lopez-Acevedo, P. D. Jadzinsky, G. Calero, C. J. Ackerson, R. L. Whetten, H. Gronbeck and H. Hakkinen, *Proceedings of the National Academy of Sciences of the United States of America*, 2008, **105**, 9157.
105. M. Richter and J. Strahle, Zeitschrift fur anorganische und allgemeine Chemie, 2001, **627**, 918.
106. P. Jadzinsky, G. Calero, C. Ackerson, D. Bushnell and R. Kornberg, *Science*, 2007, **318**, 430.
107. Y. Shichibu, Y. Negishi, H. Tsunoyama, M. Kanehara, T. Teranishi and T. Tsukuda, *Small*, 2007, **3**, 835.
108. Y. Negishi, N. K. Chaki, Y. Shichibu, R. L. Whetten and T. Tsukuda, *Journal of the American Chemical Society*, 2007, **129**, 11322.
109. R. C. Price and R. L. Whetten, *Journal of the American Chemical Society*, 2005, **127**, 13750.
110. V. L. Jimenez, D. G. Georganopoulou, R. J. White, A. S. Harper, A. J. Mills, D. I. Lee and R. W. Murray, *Langmuir*, 2004, **20**, 6864.
111. G. L. Wang, T. Huang, R. W. Murray, L. Menard and R. G. Nuzzo, *Journal of the American Chemical Society*, 2005, **127**, 812.
112. M. Brust, M. Walker, D. Bethell, D. J. Schiffrin and R. Whyman, *Journal of the Chemical Society-Chemical Communications*, 1994, 801.
113. D. V. Leff, P. C. Ohara, J. R. Heath and W. M. Gelbart, *Journal of Physical Chemistry*, 1995, **99**, 7036.
114. G. Carotenuto and L. Nicolais, *Journal of Materials Chemistry*, 2003, **13**, 1038.

115. C. Battistoni, G. Mattogno and D. M. P. Mingos, *Journal of Electron Spectroscopy and Related Phenomena*, 1984, **33**, 107.
116. M. Levi Malvano, *Atti della Reale Accademia dei Lincei*, 1908, **17**, 857.
117. R. E. Benfield, A. Filipponi, D. T. Bowron, R. J. Newport and S. J. Gurman, *Journal of Physics-Condensed Matter*, 1994, **6**, 8429.
118. N. C. Baenziger, W. E. Bennett and D. M. Soboroff, *Acta Crystallographica Section B-Structural Science*, 1976, **32**, 962.
119. J.-C. Wang, M. N. I. Khan and J. P. Fackler, Jnr, *Acta Crystallographica Section C-Crystal Structure Communications*, 1989, **45**, 1008.
120. R. Benfield, D. Grandjean, M. Kröll, R. Pugin, T. Sawitowski and G. Schmid, *Journal of Physical Chemistry B*, 2001, **105**, 1961.
121. P. Bellon, M. Sansoni and Manasser.M, *Journal of the Chemical Society-Dalton Transactions*, 1972, 1481.
122. C. López-Cartes, T. Rojas, R. Litrán, D. Martínez-Martínez, J. De La Fuente, S. Penadés and A. Fernández, *Journal of Physical Chemistry B*, 2005, **109**, 8761.
123. S. n. Kéki, L. Nagy, G. De·k and M. Zsuga, *Journal of the American Society for Mass Spectrometry*, 2004, **15**, 1455.
124. W. A. Bone and W. Richard Vernon, Philosophical Transactions of the Royal Society of London. Series A, Containing Papers of a Mathematical or Physical Character, 1906, **206**, 1.
125. A. Couper and D. D. Eley, *Discussions of the Faraday Society*, 1950, 172.
126. R. J. Mikovksy, M. Boudart and H. S. Taylor, *Journal of the American Chemical Society*, 1954, **76**, 3814.
127. H. Wise and K. M. Sancier, *Journal of Catalysis*, 1963, **2**, 149.
128. G. Cocco, S. Enzo, G. Fagherazzi, L. Schiffini, I. W. Bassi, G. Vlaic, S. Galvagno and G. Parravano, *Journal of Physical Chemistry*, 1979, **83**, 2527.
129. P. A. Sermon, G. C. Bond and P. B. Wells, *Journal of the Chemical Society-Faraday Transactions I*, 1979, **75**, 385.
130. S. Naito and M. Tanimoto, Journal of the Chemical Society-Chemical Communications, 1988, 832.
131. R. O. C. Norman, W. J. E. Parr and C. B. Thomas, *Journal of the Chemical Society-Perkin Transactions 1*, 1976, 1983.
132. J. Erkelens, C. Kemball and A. K. Galwey, *Transactions of the Faraday Society*, 1963, **59**, 1181.
133. G. C. Bond, P. A. Sermon, G. Webb, D. A. Buchanan and P. B. Wells, *Journal of the Chemical Society-Chemical Communications*, 1973, 444.
134. Y. Segura, N. Lopez and J. Perez-Ramirez, *Journal of Catalysis*, 2007, **247**, 383.
135. P. Claus, *Applied Catalysis A: General*, 2005, **291**, 222.
136. J. E. Bailie and G. J. Hutchings, *Chemical Communications*, 1999, 2151.

137. J. E. Bailie, H. A. Abdullah, J. A. Anderson, C. H. Rochester, N. V. Richardson, N. Hodge, J. G. Zhang, A. Burrows, C. J. Kiely and G. J. Hutchings, *Physical Chemistry Chemical Physics*, 2001, **3**, 4113.
138. T. Hayashi, K. Tanaka and M. Haruta, *Journal of Catalysis*, 1998, **178**, 566.
139. R. J. Davis, *Science*, 2003, **301**, 926.
140. M. Comotti, C. Della Pina, R. Matarrese and M. Rossi, *Angewandte Chemie-International Edition*, 2004, **43**, 5812.
141. A. Abad, P. Concepción, A. Corma and H. García, *Angewandte Chemie-International Edition*, 2005, **44**, 4066.
142. A. Abad, P. Concepcion, A. Corma and H. Garcia, *Angewandte Chemie-International Edition*, 2005, **44**, 4066.
143. G. M. Lu, R. Zhao, G. Qian, Y. X. Qi, X. L. Wang and J. S. Suo, *Catalysis Letters*, 2004, **97**, 115.
144. R. Zhao, D. Ji, G. M. Lv, G. Qian, L. Yan, X. L. Wang and J. S. Suo, *Chemical Communications*, 2004, 904.
145. M. Comotti, C. Della Pina, R. Matarrese, M. Rossi and A. Siani, *Applied Catalysis A: General*, 2005, **291**, 204.
146. I. Arends and R. A. Sheldon, *Topics in Catalysis*, 2002, **19**, 133.
147. V. Choudhary, D. Dumbre, V. Narkhede and S. Jana, *Catalysis Letters*, 2003, **86**, 229.
148. J. K. Edwards, B. Solsona, P. Landon, A. F. Carley, A. Herzing, M. Watanabe, C. J. Kiely and G. J. Hutchings, *Journal of Materials Chemistry*, 2005, **15**, 4595.
149. J. K. Edwards, B. E. Solsona, P. Landon, A. F. Carley, A. Herzing, C. J. Kiely and G. J. Hutchings, *Journal of Catalysis*, 2005, **236**, 69.
150. H. Y. Song, G. Li, X. S. Wang and Y. J. Xu, *Catalysis Today*, **149**, 127.
151. L. Wang, Q. Liu, X. Huang, Y. Liu, Y. Cao and K. Fan, *Applied Catalysis B: Environmental*, 2009, **88**, 204.
152. Y. Hao and B. C. Gates, *Journal of Catalysis*, 2009, **263**, 83.
153. P. George, A. Gedanken, N. Perkas and Z. Zhong, *Ultrasonics Sonochemistry*, 2008, **15**, 539.
154. V. Aguilar-Guerrero and B. C. Gates, *Chemical Communications*, 2007, 3210.
155. S. Overbury, V. Schwartz, D. Mullins, W. Yan and S. Dai, *Journal of Catalysis*, 2006, **241**, 56.
156. W. T. Wallace and R. L. Whetten, *Journal of the American Chemical Society*, 2002.
157. J. Hagen, L. D. Socaciu, M. Elijazyfer and U. Heiz, *Physical Chemistry Chemical Physics*, 2002.
158. T. Choudhary, C. Sivadinarayana, C. C. Chusuei, A. K. Datye, P. Fackler and D. W. Goodman, *Journal of Catalysis*, 2002, **207**, 247.
159. M. Haruta, S. Tsubota, T. Kobayashi, H. Kageyama, M. J. Genet and B. Delmon, *Journal of Catalysis*, 1993, **144**, 175.
160. G. C. Bond and P. A. Sermon, *Gold Bulletin*, 1973, **6**, 102.
161. M. Haruta, T. Kobayashi, H. Sano and N. Yamada, *Chemistry Letters*, 1987, 405.

162. M. Haruta, H. Kageyama, N. Kamijo, T. Kobayashi, F. Delannay and T. Inui, in *Studies in Surface Science and Catalysis*, Elsevier, Editon edn., 1989, vol. Volume 44, pp. 33.
163. M. Haruta, *Catalysis Today*, 1997, **36**, 153.
164. T. Kobayashi, M. Haruta, S. Tsubota, H. Sano and B. Delmon, *Sensors and Actuators B-Chemical*, 1990, **1**, 222.
165. M. Okumura, K. Tanaka, A. Ueda and M. Haruta, *Solid State Ionics*, 1997, **95**, 143.
166. R. G. Palgrave and I. P. Parkin, *Journal of the American Chemical Society*, 2006, **128**, 1587.
167. R. Zanella, S. Giorgio, C. R. Henry and C. Louis, *Journal of Physical Chemistry B*, 2002, **106**, 7634.
168. M. Valden, X. Lai and D. W. Goodman, *Science*, 1998.
169. M. S. Chen and D. W. Goodman, *Science*, 2004, **306**, 252.
170. Q. Fu, H. Saltsburg and M. Flytzani-Stephanopoulos, *Science*, 2003, **301**, 935.
171. J. C. Fierro-Gonzalez and B. C. Gates, *Chemical Society Reviews*, 2008, **37**, 2127.
172. F. Vindigni, M. Manzoli, A. Chiorino and F. Boccuzzi, *Gold Bulletin*, 2009, **42**, 106.
173. S. A. Yurin, D. A. Lemenovskii, K. I. Grandberg, I. G. Il"ina and L. G. Kuz"mina, *Russian Chemical Bulletin*, 2003, **52**, 2752.
174. J. T. Miller, A. J. Kropf, Y. Zha, J. R. Regalbuto, L. Delannoy, C. Louis, E. Bus and J. A. van Bokhoven, *Journal of Catalysis*, 2006, **240**, 222.
175. B. G. Jacobi, D. S. Laitar, L. Pu, M. F. Wargocki, A. G. DiPasquale, K. C. Fortner, S. M. Schuck and S. N. Brown, *Inorganic Chemistry*, 2002, **41**, 4815.
176. A. J. Dent, *Topics in Catalysis*, 2002, **18**, 27.
177. Y. Iwasawa, *Journal of Catalysis*, 2003, **216**, 165.
178. S. Pascarelli, T. Neisius and S. De Panfilis, *Journal of Synchrotron Radiation*, 1999, **6**, 1044.
179. K. Okumura, K. Yoshino, K. Kato and M. Niwa, *Journal of Physical Chemistry B*, 2005, **109**, 12380.
180. R. M. Finch, N. A. Hodge, G. J. Hutchings, A. Meagher, Q. A. Pankhurst, M. R. H. Siddiqui, F. E. Wagner and R. Whyman, *Physical Chemistry Chemical Physics*, 1999, **1**, 485.
181. S. Carrettin, P. McMorn, P. Johnston, K. Griffin and G. Hutchings, *Chemical Communications*, 2002, 696.
182. M. Hughes, Y. Xu, P. Jenkins, P. McMorn, P. Landon, D. Enache, A. Carley, G. Attard, G. Hutchings, F. King, E. Stitt, P. Johnston, K. Griffin and C. J. Kiely, *Nature*, 2005, **437**, 1132.
183. G. Li, D. I. Enache, J. Edwards, A. F. Carley, D. W. Knight and G. J. Hutchings, *Catalysis Letters*, 2006, **110**, 7.
184. D. I. Enache, D. W. Knight and G. J. Hutchings, *Catalysis Letters*, 2005, **103**, 43.
185. T. Choudhary and D. Goodman, *Applied Catalysis A: General*, 2005, **291**, 32.

186. V. R. Choudhary, R. Jha and P. Jana, *Green Chemistry*, 2007, **9**, 267.
187. N. Dimitratos, J. A. Lopez-Sanchez, D. Morgan, A. F. Carley, R. Tiruvalam, C. J. Kiely, D. Bethell and G. J. Hutchings, *Physical Chemistry Chemical Physics*, 2009, **11**, 5142.
188. J. M. Thomas, R. Raja, B. F. G. Johnson, S. Hermans, M. D. Jones and T. Khimyak, *Industrial & Engineering Chemistry Research*, 2003, **42**, 1563.
189. F. Li and B. C. Gates, *Journal of Physical Chemistry C*, 2007, **111**, 262.
190. A. M. Argo, J. F. Odzak, J. F. Goellner, F. S. Lai, F. S. Xiao and B. C. Gates, *Journal of Physical Chemistry B*, 2006, **110**, 1775.
191. J. M. Thomas, B. F. G. Johnson, R. Raja, G. Sankar and P. A. Midgley, *Accounts of Chemical Research*, 2003, **36**, 20.
192. Y. Z. Yuan, K. Asakura, H. L. Wan, K. Tsai and Y. Iwasawa, *Catalysis Letters*, 1996, **42**, 15.
193. A. I. Kozlov, A. P. Kozlova, H. Liu and Y. Iwasawa, *Applied Catalysis A: General*, 1999, 9.
194. I. P. Parkin and R. G. Palgrave, *Journal of Materials Chemistry*, 2005, **15**, 1689.
195. M. Zukalova, A. Zukal, L. Kavan, M. K. Nazeeruddin, P. Liska and M. Gratzel, *Nano Letters*, 2005, **5**, 1789.
196. T. V. Choudhary and D. W. Goodman, *Topics in Catalysis*, 2002, **21**, 25.
197. M. G. Buonomenna and E. Drioli, *Organic Process Research & Development*, 2008, **12**, 982.
198. V. R. Choudhary, A. Dhar, P. Jana, R. Jha and B. S. Uphade, *Green Chemistry*, 2005, **7**, 768.
199. D. I. Enache, J. K. Edwards, P. Landon, B. Solsona-Espriu, A. F. Carley, A. A. Herzing, M. Watanabe, C. J. Kiely, D. W. Knight and G. J. Hutchings, *Science*, 2006, **311**, 362.

Appendix

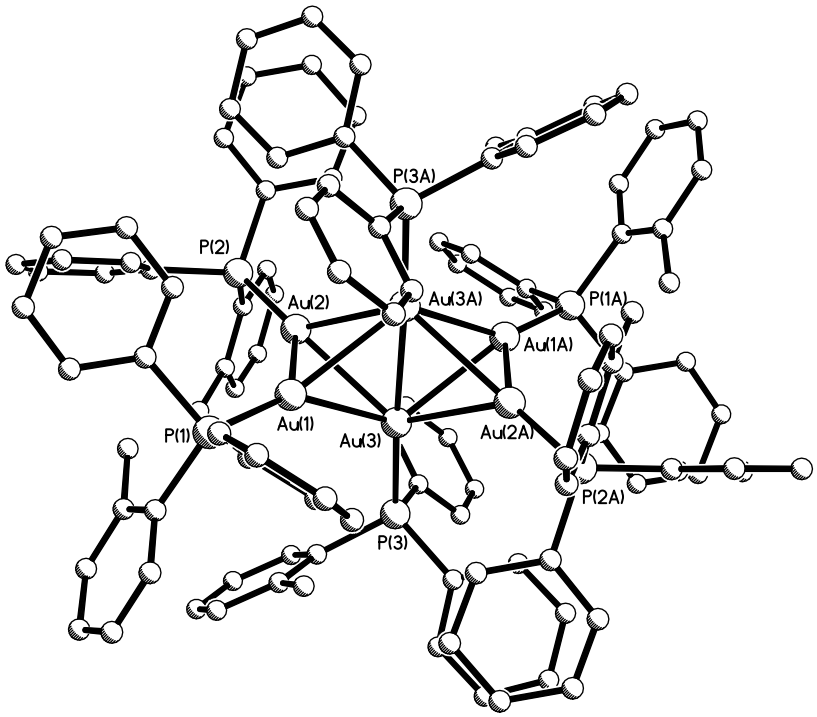

Chemical formula	$C_{57}H_{51}Au_3F_6P_4$	
Formula weight	1564.76	
Temperature	150(2) K	
Radiation, wavelength	MoKa, 0.71073 Å	
Crystal system, space group	monoclinic, P21/c	
Unit cell parameters	a = 13.568(3) Å	a = 90°
	b = 15.509(3) Å	b = 99.276(4)°
	c = 28.089(6) Å	g = 90°
Cell volume	5834(2) $Å^3$	
Z	4	
Calculated density	1.782 g/cm^3	

Selected bond lengths [Å] and angles [°]

Au(1)–P(1)	2.296(3)	Au(1)–Au(2)	2.6457(7)
Au(1)–Au(3)	2.8016(7)	Au(1)–Au(3A)	2.8244(7)
Au(2)–P(2)	2.284(3)	Au(2)–Au(3)	2.7723(7)
Au(2)–Au(3A)	2.8011(6)	Au(3)–P(3)	2.302(2)
Au(3)–Au(3A)	2.6165(8)	Au(3)–Au(2A)	2.8011(6)
Au(3)–Au(1A)	2.8244(7)		

Appendix 1. Selected crystallographic data for $[Au_6(Ph_2P(o\text{-tolyl}))_6](PF_6)_2$.

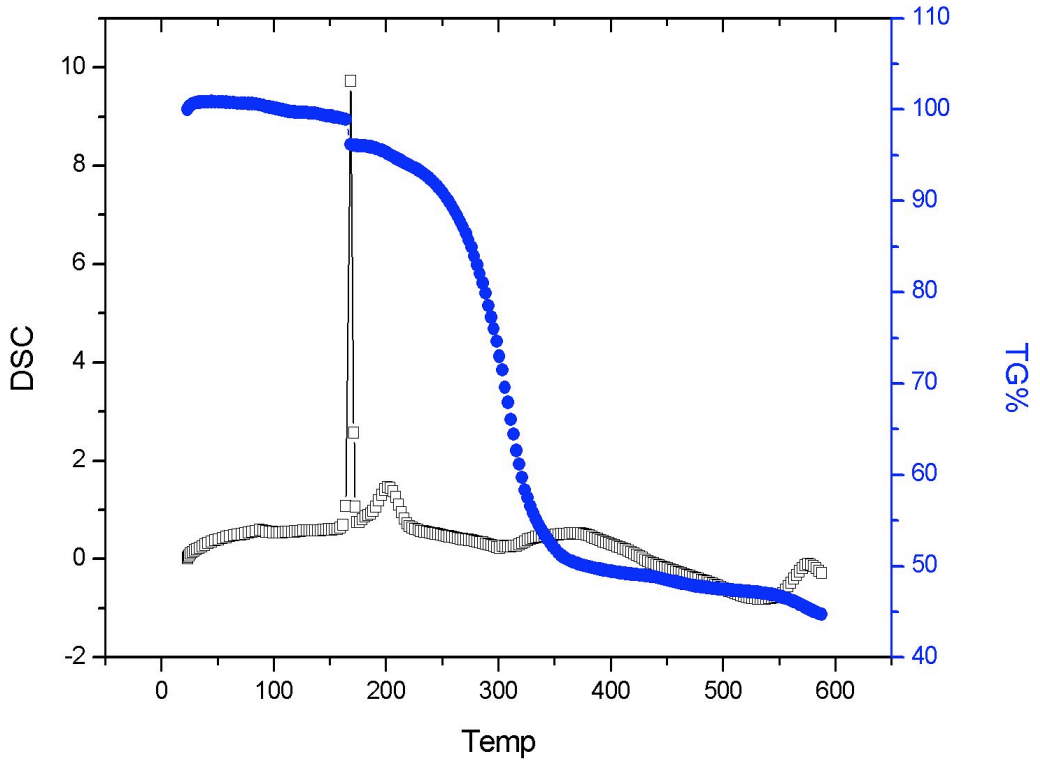

Appendix 2. TGA/DSC data for $[Au_6(Ph_2P(o\text{-tolyl}))_6](NO_3)_2$ heated in air.

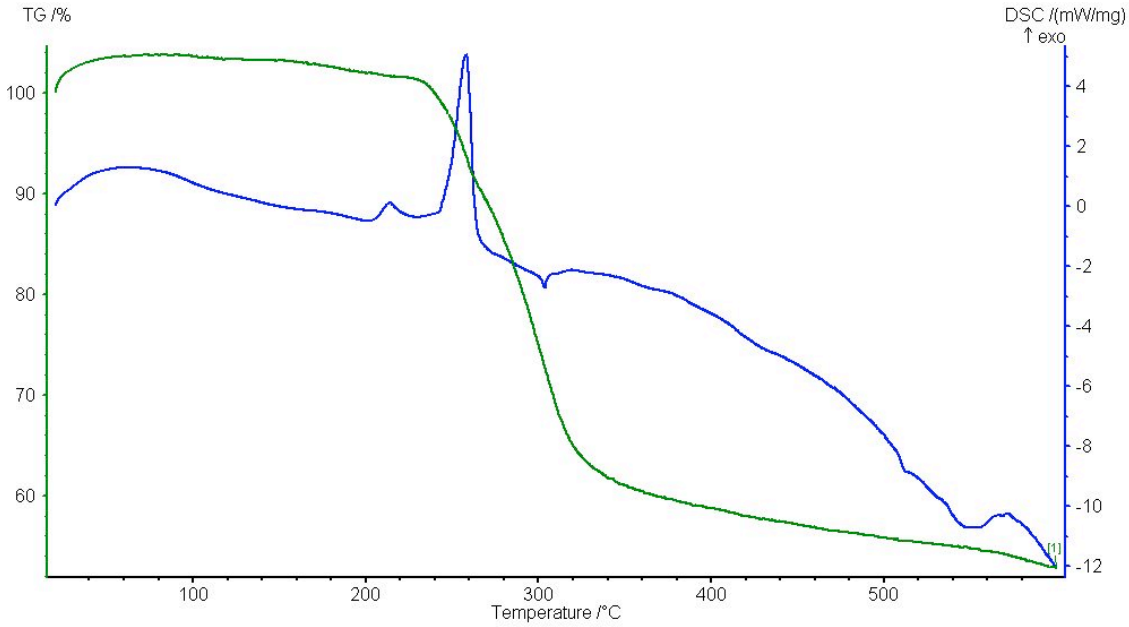

Appendix 3. TGA/DSC data for $[Au_9(PPh_3)_8](NO_3)_3$ heated in air.

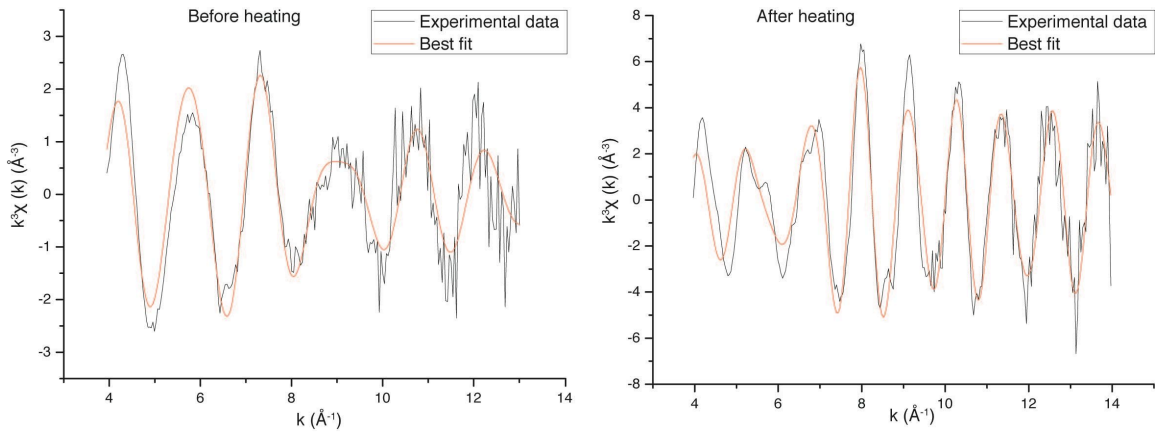

Appendix 4. Typical calculated and recorded EXAFS data fits for data recorded during the *in situ* heating of 4.0 wt.% $[Au_6(Ph_2P(o\text{-tolyl}))_6](NO_3)_2$ supported on silica nanospheres.

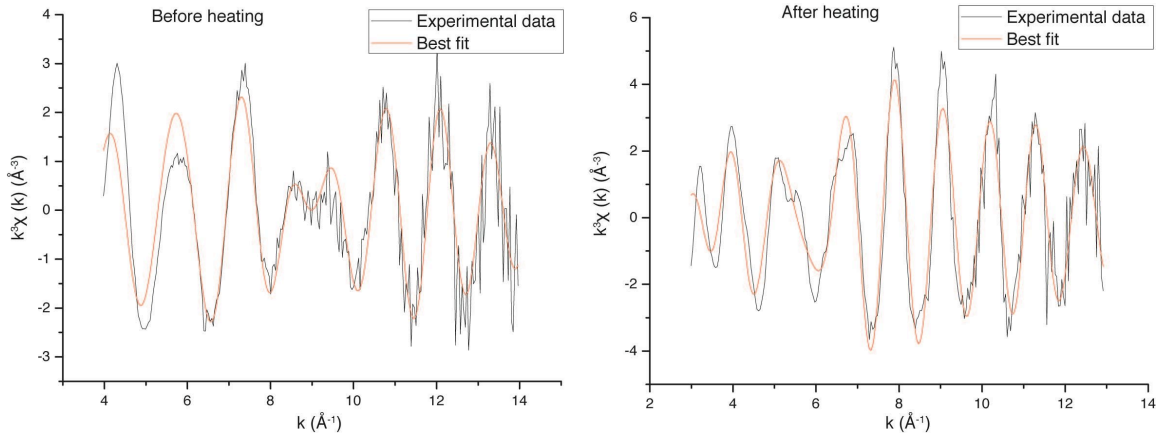

Appendix 5. Typical calculated and recorded EXAFS data fits for data recorded during the *in situ* heating of 4.0 wt.% $[Au_9(PPh_3)_8](NO_3)_3$ supported on silica nanospheres.

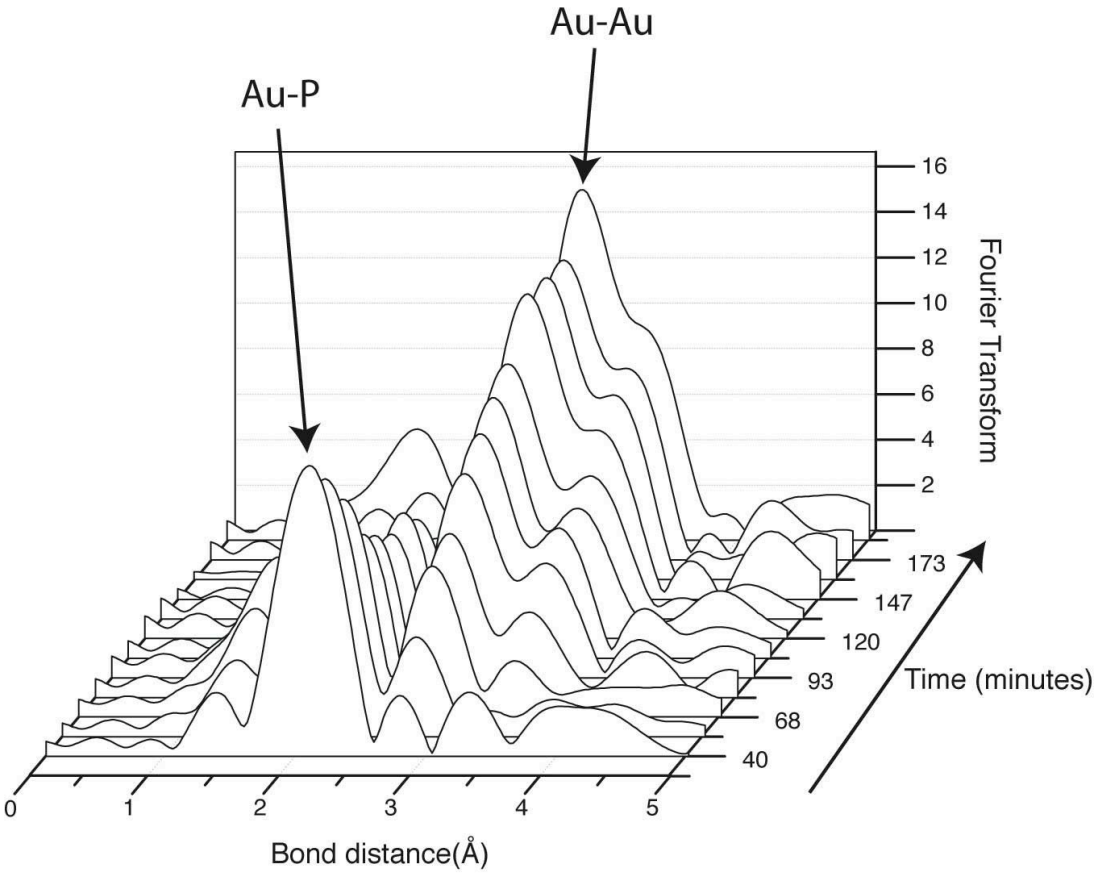

Appendix 6. Phase shift corrected Fourier transform data Au L_{III} edge QEXAFS collected *in situ* as 4.0 wt.% gold $[Au_6(Ph_2P(o\text{-tolyl}))_6](NO_3)_2$ supported on silica nanospheres reacted with TBHP at 95 ^oC.

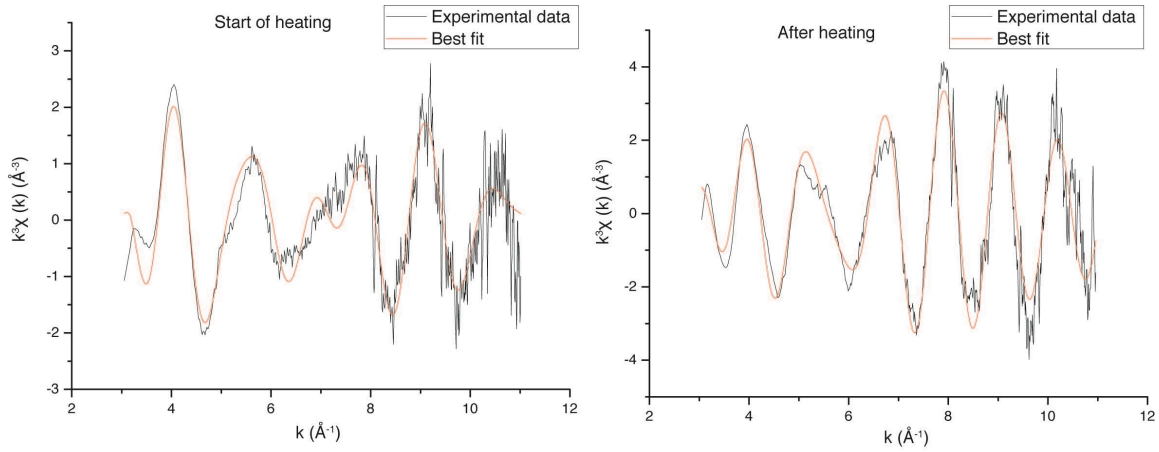

Appendix 7. Typical calculated and recorded EXAFS data fits for data recorded *in situ*, following the reaction of 4.0 wt.% $[Au_6(Ph_2P(o\text{-tolyl}))_6](NO_3)_2$ supported on silica nanospheres with TBHP at 95 ^oC.

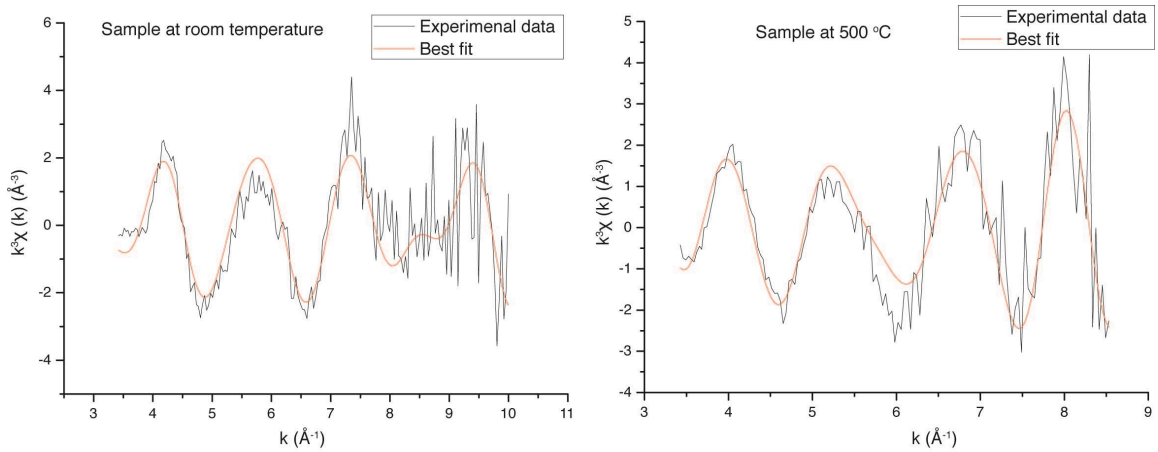

Appendix 8. Typical calculated and recorded EXAFS data fits of data recorded during the *in situ* heating of 1.0 wt.% $[Au_9(PPh_3)_8](NO_3)_3$ supported on anatase titania.

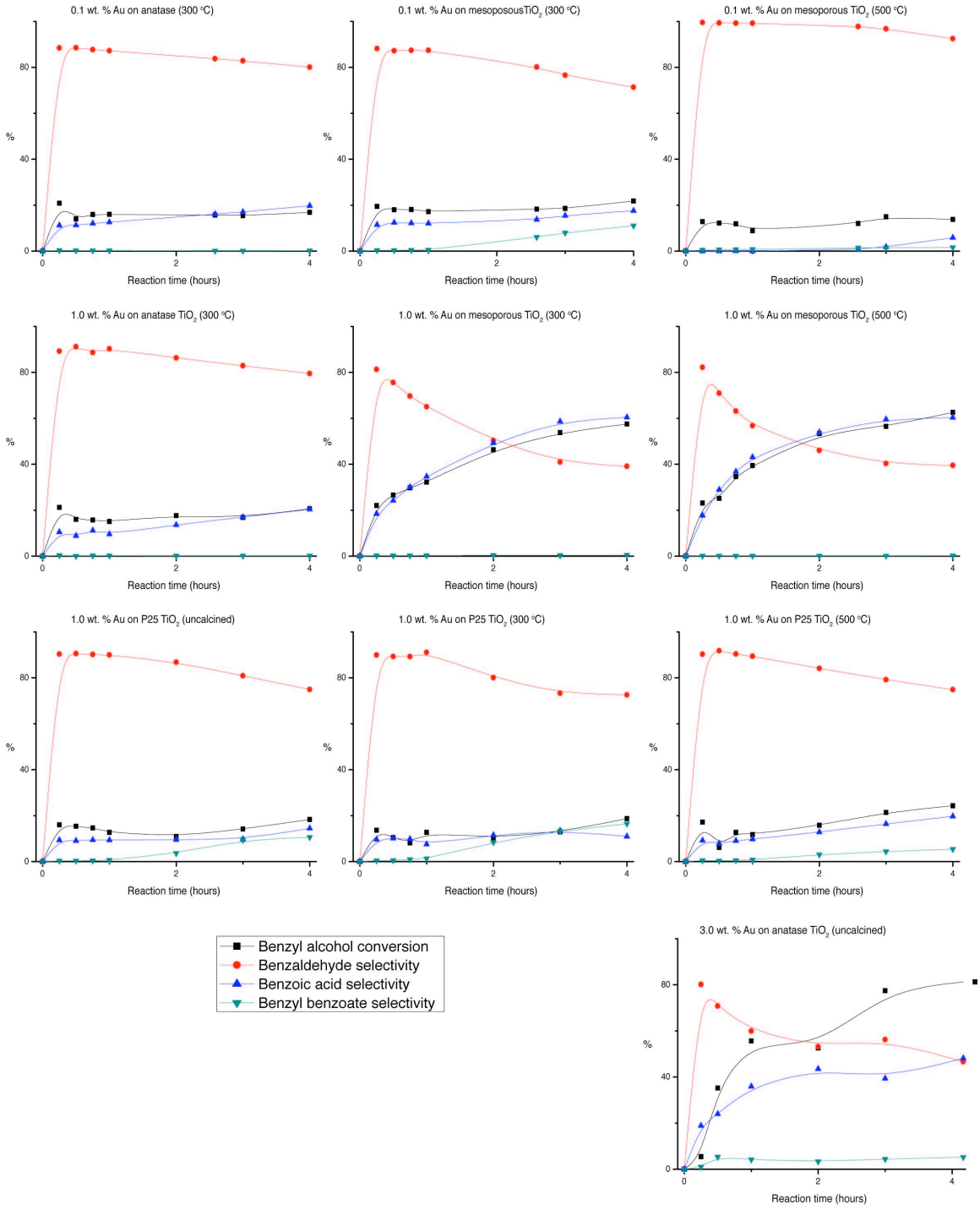

Appendix 9. Catalysis data for $[Au_9(PPh_3)_8](NO_3)_3$ supported on various types of titania as catalysts for the catalytic oxidation of benzyl alcohol.